

Investigation of fique fibre mechanical properties and its use as polymer reinforcement

Beatriz Casares Fernández

Submitted in fulfilment of the requirements
for the degree of Doctor of Philosophy

Advanced Composites Group
Mechanical and Aerospace Engineering Department
University of Strathclyde, Glasgow

September 22, 2026

This thesis is the result of the author's original research. It has been composed by the author and has not been previously submitted for examination which has led to the award of a degree.

The copyright of this thesis belongs to the author under the terms of the United Kingdom Copyright Acts as qualified by University of Strathclyde Regulation 3.50. Due acknowledgement must always be made of the use of any material contained in, or derived from, this thesis.

Abstract

Natural fibres have been part of goods manufacturing for centuries, also as reinforcement of composite materials. Technology and the discovery of new materials displaced them, but challenges of disposal and recyclability of materials, pushed by Western countries' legislation is making them one of the possible answers in these societies following the example of traditional uses. Their renewability and biodegradability alongside their light weight is making them the focus of research enable them to be used in high technical value applications. Understanding their behaviour and challenges is paramount to bring them as common reinforcements for composite materials.

In this work, the aim is to deepen the understanding of fique fibres, in both their physical structure and morphology, and their mechanical properties.

It is well known that the cross-sectional area varies from fibre to fibre. Understanding if and how it changes along the same fibre is important for creating models to analyse mechanical behaviours. This is done by an X-ray CT-scan to analyse how the fibre area varies along its length. With the CT-scan this is explored and also used to quantify the porosity of the fibre, obtaining what is the proportion of cell walls in fique. As part of the study of the mechanical properties, the fibre cross-sectional area is calculated in two ways, which gives a further insight on different fibre morphologies and leads to suggestions on what are the better approaches when modelling the fibre shape, showing that although the circularity assumption can be used, it is inaccurate, and how that can impact on the calculation of the mechanical properties.

Mechanical properties in natural fibres in general and fique fibre in particular have values that can differ significantly from one another or are calculated from small samples. Not having a value for mechanical properties is a challenge when creating models

and predicting properties for composite materials. In measuring the mechanical properties, besides comparing how the two area measurement approaches affects that, the introduction of a direct strain measurement technique to be applied to natural fibres is presented, showing how in shorter fibres induced errors from the equipment become more significant, as well as making non-linearities in the fibres become significant enough to amplify errors in the measured mechanical properties. This leads to recommendations on using longer fibres when possible, especially if using indirect strain measurement techniques. If fibres are short, a direct strain measurement technique is recommended, with direct cross-sectional area measurement to increase accuracy when measuring mechanical properties via tensile testing of single fibres.

Wettability of raw fique and chemically and physically treated fique is also studied by the calculation of polar and dispersive components of the surface energy as well as by the measurement of the contact angle between the matrix and the different types of fibres. Recycled polypropylene is the chosen matrix in this work to study fibre-matrix interaction.

In order to use fique fibres as reinforcement, they are also thermo-chemically characterized, as is the recycled polypropylene used as matrix. The interfacial properties between the two components are tested via the single fibre fragmentation test with raw fique fibres as well as chemically and physically treated fique fibres, that had also been previously thermo-chemically characterized. The relevance of this lies on the need to understand the interface behaviour and how it can be affected to be improved. The influence of chemical and physical treatments on the composition and the thermal stability of fibres is investigated as well as how that influences their interaction and load transfer capability when in contact with the matrix.

Publications

As part of this PhD a conference poster and a journal paper have been presented.

Journal paper

A peer reviewed journal paper has been published in the Journal of Natural Fibers on December 2024, with the title *Effect of gauge length, cross sectional area and strain measurement methods on stiffness characterisation of Fique natural fiber*, B. Casares B. Casares Fernández and M. Jalalvand.

Conference poster

A conference poster was presented at the CompTest 2021, 10th International Conference on Composite Testing and Model Identification, with the title *Single natural fique fibre tensile test: compliance theory versus direct strain measurement*, B. Casares Fernández, M. Jalalvand, and J. Kelly.

Acknowledgements

The process of getting to this thesis has been a long and winding road, with unexpected turns. It has also been rewarding to some extent, and a great learning opportunity in many ways.

For this, I want to thank Dr. Meisam Jalalvand, who gave me the opportunity of starting a PhD in natural fibres and trusted me till the end, while being encouraging and hopeful. Thankful to the Royal Academy of Engineering and the Newton Fund: Industry - Academia Partnership Programme, IAPP1/100149 in collaboration with the National University of Colombia, for the funding provided to this project.

For Chapter 2, Computed Tomography scanning was supported by the National Research Facility for Lab X-ray CT (NXCT) at the µ-VIS X-ray Imaging Centre, University of Southampton, through EPSRC grant EP/T02593X/1. Without the invaluable help and knowledge from Dr. Kate Dobson from the Department of Civil & Environmental Engineering and the Department of Chemical & Process Engineering at University of Strathclyde the data analysis would not have been possible.

I would have never gotten this far without the alumni and members of the ACG group, starting with José Luis Rudeiros and Fiona Gentles, who I have never met, but have been guiding lights on my path with their works on natural fibres. David Bryce, Georgios Xypollas, Shima Darian, and other past members of the ACG group that showed me there was a light at the end of the tunnel and whose success has kept inspiring me. Ross Minty has had a great influence in leading me to this final piece of work, by supporting me through laughs, tears, and full honesty. Ashlee Espinoza has been, on top of this, a true friend that has inspired me beyond limits, showing me what resilience and endurance look like.

Mr. James Kelly and his kindness, along with good coffees, chat and music has to be mentioned, alongside with his help and diligence with sample preparation, observation, and measurements.

I want to mention here Govanhill Library in Glasgow and Juan Compañel library in my home town, both public, where I have spent a lot of time writing this thesis. Thank you to these places where we can go and exist.

Further from University, I would not be writing this without the lessons learnt through my rugby refereeing and the guidance of Bob Easton, whose lessons I have been able to apply when pursuing this PhD and writing this thesis.

I have built this thesis as if I was crocheting a blanket for my niece Candela, who inspired me to never give up, making a square at a time to see them all coming together to form something unique. For that inspiration I am thankful.

To my father, who has his own way of showing support, but I truly believe never lost hope in me getting to this point. And to him, for inspiring me to prove I can. I need to prove nothing no more.

And last but not least, to my soul mate and best friend. I am forever thankful to the person who believes in me before I even try anything. To Luis, for not letting me give up when it may have been the easiest option,

but definitely not the most reasonable. I am sorry I did not take your advice in not pursuing a PhD, but I thank you for being with me during all this.

Graciñas to all.

Contents

Abstract **iii**

Acknowledgements **vi**

List of Figures **xi**

List of Tables **xix**

Acronyms **xxii**

Nomenclature **xxiii**

1 Natural Fibres and fique: history, characteristics, and uses **1**

1.1 Background 1

1.1.1 Natural fibres: types, structure, properties and extraction 1

1.1.2 Natural fibre chemistry 3

1.1.3 Lignocellulosic fibre structure 6

1.1.4 Fibre extraction, separation and processing 9

1.1.5 Fique 10

1.1.6 Traditional uses and future 14

1.2 Project objectives 17

1.3 Thesis outline 18

Bibliography 19

2 Porosity and cross-sectional area characterisation along the fibre length through X-ray CT **28**

2.1 Introduction 28
2.2 Literature review 28
2.2.1 CT-scan: history, equipment, and process 28
2.2.2 Composites and fibre characterisation through CT-scan 30
2.2.3 Natural fibres characterised using CT-scan 31
2.3 Methodology 33
2.3.1 Materials and sample preparation 34
2.3.2 CT-scan analysis 35
2.4 Results 37
2.4.1 Fibre area variation 37
2.4.2 Fibre porosity 39
2.5 Conclusions and future work 43
Bibliography 44

3 Mechanical characterisation of fique: Single fibre tensile test 47
3.1 Introduction 47
3.2 Literature review 47
3.2.1 Single fibre tensile test 47
3.3 Experimental 66
3.3.1 Materials and equipment 66
3.3.2 Sample preparation 67
3.3.3 Area measurement approaches 68
3.3.4 Indirect strain measurement 69
3.3.5 Direct strain measurement 70
3.4 Results and discussion 75
3.4.1 Cross section area 75
3.5 Conclusions 88
Bibliography 90

4 Thermo-chemical characterisation of fique and its chemical modifications 95

4.1 Introduction . . . 95
4.2 Literature review . . . 95
4.2.1 Natural fibres FT-IR analysis . . . 98
4.2.2 Thermogravimetric analysis of natural fibres . . . 106
4.2.3 Differential Scanning Calorimetry (DSC) of natural fibres . . . 113
4.3 Experimental . . . 118
4.3.1 Materials . . . 118
4.3.2 Methods . . . 120
4.4 Results and discussion . . . 121
4.4.1 Fourier Transformed Infrared Spectroscopy (FT-IR) . . . 121
4.4.2 Thermogravimetric analysis . . . 127
4.4.3 Differential Scanning Calorimetry (DSC) . . . 133
4.4.4 Conclusions . . . 135
Bibliography . . . 136

5 Fique fibre and matrix interaction: fique-recycled polypropylene 145
5.1 Introduction . . . 145
5.2 Literature review . . . 146
5.2.1 Polypropylene and recycled polypropylene . . . 146
5.2.2 Fibre-matrix interface . . . 151
5.3 Experimental . . . 168
5.3.1 Materials . . . 168
5.3.2 Methods . . . 169
5.4 Results and discussion . . . 178
5.4.1 Polypropylene and recycled polypropylene FT-IR . . . 178
5.4.2 Polypropylene and recycled polypropylene DSC . . . 181
5.4.3 Contact angle and wettability of fique fibres . . . 183
5.4.4 Fique-PP contact angle . . . 186
5.4.5 Single fibre fragmentation test . . . 189
5.5 Conclusion . . . 193
Bibliography . . . 195

6 Conclusions and future work **206**

6.1 Key findings 206

6.1.1 The future of fique 212

6.2 Future work 212

6.2.1 Cross-sectional area of fique and other natural fibres 212

6.2.2 Mechanical behaviour of fibres 212

6.2.3 Interfacial properties 213

6.2.4 Natural fibre reinforced composites 213

I Appendix A: MATLAB code for direct strain measurement as part of the mechanical characterization of fique. **214**

6.3 Main: Inputs, variables, output files definition and different functions call. 215

6.3.1 Function tracking points 217

6.3.2 Function Identifying breaking points 229

6.3.3 Function Interpolation force elongation 235

List of Figures

1.1 Types of natural fibres classified as mineral, animal and plant, with examples for each case. 3

1.2 Cellulose chains showing hydrogen bonds as well as the molecule structure showing the glycosidic bond [7]. 4

1.3 Lignin monomers chemical structure [10]. 5

1.4 (a) shows the structure of the wall of a plant cell, with the primary and secondary walls and lumen, as well as the microfibril angle [25], while (b) shows the intertwined structure formed by cellulose microfibrils bound together by the adhesive formed by lignin and hemicellulose [13]. 7

1.5 Fique plants, with trunk as described (a), [35], and still on the ground (b). 11

1.6 (a) Fique leaves being cut [38], (b) fique leaves being defibrillated [39], (c) and (d) showing the drying process of fique, where is hung out to dry, and goes from the green leafy colour to the yellowish colour [35, 40]. . . . 13

1.7 Heckling of fique using a heckling comb [35]. 14

1.8 (a) detail of the traditional Japanese joining method, the Blind Miter Doveltail and (b) view of LignoSat's structure showing the relationship among wooden panels, aluminium frames, and stainless-steel shafts [48]. 16

1.9 Curved surface manufactured on bamboo reinforced PLA mimicking the process of small blade manufacturing [49]. 16

2.1 Reconstructed 3D image of the scan where both, cross and longitudinal sections of a fibre can be seen. 30

2.2 Zeiss 160 kVp Versa 510 equipment [15]. 34

2.3 X-ray CT-scan preparation diagram with (i) showing a fibre being cut into smaller pieces, and (ii) showing how these pieces are stuck to the transparent tape consecutively. 35
2.4 The rolled preliminary sample next to a Sharpie pen for scale. 35
2.5 (a) Showing how the area of the fibre is selected, (b) selection of every 100 slices, (c) interpolation along the 100 slices to have the fibre reconstructed. 37
2.6 (a) Area (μm^2) for fibre *a*, whole, fibre walls and lumen in blue circles, yellow squares and green diamonds respectively; (b) Same for fibre *b* in purple, orange, and grey respectively. 39
2.7 Reconstructed cross-section image of the CT-scan where both fibres *a* and *b* are shown, showcasing the shape difference, with fibre *a* presenting a kidney like shape while fibre *b* presents a more circular section. 40
2.8 (a) Porosity (%) for fibre *a* shown in blue circles for each piece, with the average value in a green line across; (b) Porosity (%) for fibre *b* shown in orange circles for each piece, with the average value in a grey line across. 40

3.1 Calculation of the fiber's Young's Modulus adapted from the standard ASTM-C1557-20 2021 [3] to highlight the requirement of at least three different gauge lengths. 50
3.2 Fique fibre on arrival state (a) and after being brushed and washed in lukewarm water (b) to remove organic residues left from the leave extraction process, with a visible colour change as well as more disentangled. . 67
3.3 Sample preparation for single fibre tensile test where double sided tape is placed in the card (1), fique fibre with inserted and attached green beads stuck to the tape (2), and two components epoxy resin drops placed on top of the tape to reduce slippage (3). 67
3.4 Apparent diameter transverse measurement along a fibre (a), and direct cross-section area measurement (b), at x100 and x200 magnification respectively. 68

3.5 Sample preparation for cross section area observation (a), two pieces from each fibre stuck into a cardboard numbered with the correspondent fibre test numbers x, for the first two pieces closer to the number, and y for the two pieces further corresponding to a second fibre, to allow tracking them properly; (b),three cards embedded in Epofix transparent resin, through which the numbers can still be seen, and the cross section area of the fibres can be photographed with x200 magnification for later measurement. 69

3.6 Flowchart of the MATLAB code for tracking the two beads attached to each tested fiber, where n and m are the number of points identified on each bead. 71

3.7 Graphs explaining the step-by-step process of matching the information gathered by the equipment with the information on displacement gathered from the video recording. 73

3.8 Typical curves seen during the experimental part. Green curves, solid and dashed, are successful cases for long and short gauge lengths respectively; while red curves, solid and dashed, are representative of not valid samples due to breaking at the card edge (which has a perfect normal curve and is discarded due to visually seeing where the breaking happens) and pull out respectively. 74

3.9 Fiber's cross sectional area frequency intervals for the two area estimation approaches, assuming circularity from the apparent diameter and measuring the cross-sectional area at the failure point. 77

3.10 Comparison between the cross section area values calculated by using the apparent diameter and assuming circularity of the fibres and the cross section area measured at the microscope with its fitted line to compare it with the y=x that would follow if both values were the same. 78

3.11 Feret's diameters definition. 79

3.12 Different shapes found in fique area's measurement, with (a) showing the closest to a circular cross section, (b) showing an elongated shape resembling more an ellipse, and (c) shwoing a bean like section considered an extreme shape. 80
3.13 Feret's diameters definition. 80
3.14 Solidity definition, where A is the measured area and B is the area of the convex region. 80
3.15 (a) shows the compliance theory applied by using area from apparent diameter using circularity assumption of the fiber; (b) shows the compliance theory applied by using the cross-sectional measured area of the fibers. The Young's modulus of the fibers is the inverse value of the fitted slope, giving very close values for both cases, 17.3 and 17.1 GPa respectively. Coefficient of determination R^2 is higher when using the cross-sectional area measured, suggesting a better fit for this case. 82
3.16 Stress-strain curve obtained from the direct strain measurement method, where the initial slope of the curve is used to calculate the Young's modulus of the fibre by fitting a line of which slope is taken as the Young's modulus, represented by a on the line equation. 83
3.17 Two typical stress-strain curves of 10 and 100 mm fiber lengths for comparison. Both (a) and (b) show the differences between the direct strain measurement (solid line) vs. the equipment cross head displacement (dashed line), in both cases using the cross-sectional area (CSA). 84
3.18 Average tensile strength for each gauge length for both methods of area calculation, AD= apparent diameter at the left hand side (in a blue circle) of every gauge length and CSA=cross section area observation at the right hand side (in a burgundy diamond) of every gauge length. . . . 86
3.19 Average tensile strain (%) for each gauge length for both methods of strain measurement, equipment=indirect in blue circles to the left hand side of every gauge length and MATLAB=direct in pink circles to the right hand side of every gauge length. 88

4.1 Untreated fibre (i) and alkaline treated fibre (ii), showing the effects on removal of surface components as well as its effects on cellulose and lignin removal [2]. 98
4.2 TGA curves of different natural fibres and cellulose from [30], adapted with the thermal degradation stages identified in the literature for natural fibres. 109
4.3 Weight loss (a) and DTG (b) curves of fique at 10°C/min heating under nitrogen flow as presented in the work by Hidalgo-Salazar et al. [37], showing the hemicellulose and α-cellulose peak degradation temperatures. 112
4.4 Weight loss and DTG curves of fique dust (a) and fique alkaline dust (b) at 20°C/min heating under nitrogen flow as presented in the work by Salinas et al. [8], showing the shoulder disappearance for the alkaline dust associated with hemicellulose and the increased thermal instability for the treated dust. 113
4.5 Diagram of the functioning principle of the DSC technique [38]. 113
4.6 DSC and TGA of retted flax and cellulose from [39], where the cellulose endothermic peak can be clearly seen in contrast with the more flat evolution for the flax case. 114
4.7 DSC of fique treated with softener from [43], where the different transitions are identified for this case. 117
4.8 FT-IR results of washed fique (F) ready to use, and alkaline (FA), alkaline and high intensity ultrasonication (FA+HIUS), hydrolysis (FH), and hydrolysis and high intensity ultrasonication (FH+HIUS) treated fibres with lines highlighting the main areas of the analysis. 121
4.9 Washed fique (F) with both alkaline (FA) treated fibres and alkaline plus high intensity ultrasonication (FA+HIUS) treated fibres (a), with a zoom into the peak differences (b) to better evaluate how the fibre composition is affected. 124
4.10 Zoom into two regions to explore the peak differences between the cleaned fique and both, hydrolysis and hydrolysis+HIUS treated fibres. 126

4.11 TGA and DTG results for the washed fique and the different treatments, showcasing the differences among them and how different treatments affect when peak degradation happens to different treated fibres. These curves are specific to each test, and do not represent the average values represented in the tables. 128
4.12 TGA results for the washed fique (a) and the different treatments: mercerised (b), mercerised+HIUS (c), hydrolysed (d), and hydrolysed+HIUS (d), showcasing the differences among them and how they affect fibre degradation. These curves are specific to particular tests but the values on each figure are the averaged ones. 132
4.13 DSC curves for washed fique and the different treatments, showing the differences especially in the shift from endothermic to exothermic peak upon the mercerisation treatment. 135

5.1 FTIR spectrum of isotactic and atactic polypropylene, showcasing how the structural chemical differences can be appreciated through FTIR. . . 148
5.2 Virgin and recycled PP FT-IR spectra from [10], showing the 1730 cm^{-1} in the recycled material. 149
5.3 Second heating DSC results from [23] on recycled polypropylene from technological waste and the peak at 109°C suggesting the presence of low density polyethylene. 151
5.4 Contact angle measurement approach through fibres bridged with water from [38] with the radius of curvature of meniscus formed by water signalled. 157
5.5 Micromechanical tests: (a) pull-out, (b) microbond, (c) fragmentation, and (d) push-out from [44]. 161
5.6 Schematic and example of the fracture modes on single fibre fragmentation tests from [51, 53], with (a) disk crack indicating high adhesion, (b) double cone crack indicating intermediate adhesion, and (c) debonding indicating weak adhesion. 166
5.7 Bags made of polypropylene (a), and the pellets resulted from the recycling of those bags (b). 169

5.8 Diagram showing the forces acting on the fibre when immersed in the different liquids, with advancing and receding angles identified [61]. . . . 171
5.9 Least squares method applied to the three liquids used to measure the contact angle of differently treated fique fibres, in this case for delignified fique, showing how the line interception allows for calculation of the dispersive component of the surface energy, while the slope allows for the calculation of the polar component. 172
5.10 (a)Shows the fibre hung and how the rePP filament is made a knot around it; (b) shows the sample finished with the cement drops to keep the fibre in place when subjected to temperature. 173
5.11 (a) Shows how 5 points around the droplet are selected; (b) shows the software fitting the best match between an ellipse and a circumference and giving the contact angle θ as an outcome. 174
5.12 Schematic of the single fibre fragmentation test [48]. 175
5.13 Specimen for the SFFT where the sand paper has been glued to both ends of the sample to prevent sliding in the clamping area. 175
5.14 Exploded diagram with different parts identified of the mould used in the manufacturing of the SFFT samples [58]. 177
5.15 FTIR absorbance bands with identified peaks of fabric and recycled PP in black at the bottom and in red at the top respectively. 179
5.16 DSC results of fabric and recycled PP with melting peaks identified for the second heating cycle. 182
5.17 DSC of polypropylene homopolymer, block copolymer and random copolymer, showcasing how the chemical structure impacts the melting behaviour, from [70]. 182
5.18 DSC results of fabric and recycled PP with crystallization peaks identified for the second cooling cycle. 183

5.19 Graph obtained directly from the OneAttension measuring equipment, where the hysteresis between advancing and receding angle can be seen between the first immersion and the retraction, as well as for the second cycle. 184
5.20 Surface energy and its polar and dispersive components for the untreated fique and the different treatments, showing how these impact the polarity of the fibres. 185
5.21 (a) and (d) show a rPP knot around washed and hydrolysis treated fique respectively, (b) and (e) show how the rPP starts melting, and (c) and (f) show how a droplet is finally formed around the fibre. 186
5.22 Graph showing the evolution of the contact angle of rPP on the different treated fique fibres. 187
5.23 (a) Washed fique and a rPP well formed droplet; (b) mercerized fique with rPP, with a gap between polymer and fibre; (c) mercerized+HIUS treated fibre with matrix visible on the fibre's surface; (d) hydrolysed fique with rPP on the fibre surface; (e) hydrolysed+HIUS fique with rPP matrix showing a discontinuous matrix surface on top of the fibre. . . . 188
5.24 (a) Initial specimen with some fragments signalled by black arrows after testing, (b) initial specimen with no fragments after testing, with bubbles pointed out by blue arrows, (c) tested specimen with some fragments signalled by black arrows with visible stress whitening, and (d) failed specimen, with no fragmentation and a visible superficial defect signalled by a blue arrow. 190

List of Tables

1.1 Different fibres with their composition and MFA. 8
1.2 Fique fibre composition. 13
1.3 Natural and synthetic fibres industrial purchase price in $/kg. 17

2.1 Area values for the whole fibre *a* and the corresponding walls and lumen with the standard deviation for each of them, as well as the final average. 41
2.2 Area values for the whole fibre *b* and the corresponding walls and lumen with the standard deviation for each of them, as well as the final average. 42

3.1 characterisation of fibres from different studies; ms: measured, cr: corrected 63
3.2 Number of tested fibres and valid tests corresponding to each gauge length and the total. 75
3.3 Area obtained from the apparent diameter (AD) approach assuming circularity compared to the area measured by the cross-sectional area (CSA) observation. 77
3.4 Parameters for figures in Fig. 3.12 showing the differences between the shapes found. 81
3.5 Young's modulus values, standard deviation, and coefficient of variation for different gauge lengths from the direct strain measurement method . 85
3.6 Tensile strength values of fique fibres. AD=Area from apparent diameter, CSA=Cross section area. 86

4.1 FT-IR band assignment for the fique fibres analysed, including washed fique, fique treated with alkaline solution, fique treated with hydrolysis, and fique fibres treated chemically and exposed to high-intensity ultrasonication. 127
4.2 Thermogravimetric analysis with temperature peaks on the DTG as identified in Fig. 4.11c and Fig. 4.11d. 129
4.3 Weight loss at the different stages identified from the TGA and DTG for the washed fique and each treatment, following nomenclature as used in Fig. 4.12. 130
4.4 DSC results with peak temperatures (°C) of events and their nature. . . 134

5.1 Surface free energy for natural fibres. 159
5.2 Summary of surface tension and the polar and dispersive components of the liquids used in the wettability characterisation of fique 172
5.3 FT-IR band assignment for the fabric and recycled PP. 180
5.4 Advancing contact angles (°) for fique and its different treatments for the four used liquids 185
5.5 Advancing contact angles (°C) for fique and its different treatments with recycled polypropylene with temperature increase. 186
5.6 Critical fibre length (mm) and shear strength (MPa) for different fibre treatments. 191

Acronyms

AD apparent diameter

CSA cross-sectional area

CT computed tomography

DSC Differential Scanning Calorimetry

DTG Derivative Thermogravimetric Analysis

FT-IR Fourier Transform Infrared Spectroscopy

HIUS High Intensity Ultrasonication

MaPE maleic anhydride modified high-density polyethylene

MaPP maleic anhydride grafted polypropylene

$NaClO_2$ sodium chlorite

NaOH sodium hydroxide

PP polypropylene

rPP recycled polypropylene

SEM Scanning Electron Microscope

TGA Thermogravimetric Analysis

VTMO vinyl tri-methoxy silane

3D three dimensions

Nomenclature

Greek symbols

$\overline{\sigma_f}$	Averaged tensile strength of fique	MPa
Δ	Variation	
ϵ	Elongation	
γ or γ_{LV}	Liquid surface tension	mN/m
γ_{LV}^d	Liquid surface tension dispersive component	mN/m
γ_{LV}^p	Liquid surface tension polar component	mN/m
γ_{SL}	Surface tension between two phases	mN/m
γ_{SV}	Solid surface tension	mN/m
γ_{SV}^d	Solid surface tension dispersive component	mN/m
γ_{SV}^p	Solid surface tension polar component	mN/m
ϕ	Fibre diameter	μm
ρ	Density	kg/m^3
σ	Tensile strength	MPa
θ	Contact angle	$^\circ$
θ_A	Advancing contact angle	$^\circ$

θ_R	Receding contact angle	°

Roman symbols

A	Area	
$\overline{A}$	Average area	
C_s	System compliance	
CV	Coefficient of variation	%
E	Young's or elastic modulus	GPa
$\overline{E}$	Average Young's or elastic modulus	GPa
F	Force	
F_p	Force at peak	
g	Acceleration of gravity	m/s^2
h	Immersion depth	mm
H_m	Heat (enthalpy) of fusion	J/g
H_m^0	Heat (enthalpy) of fusion of 100% crystalline polymer	J/g
kVp	Peak tube voltage	kV
m	Fibre mass	g
M	Mol	
MFA	Microfibril angle	°
N	Total number of	
P	Perimeter	mm
p/v	Percentage per volume	%

s	Seconds	
s	Standard deviation	
T	Temperature	°C
W	Watt	
wt	weight	
w/v	Weight per volume	%
X_c	Crystallinity	%

Chapter 1

Natural Fibres and fique: history, characteristics, and uses

In this chapter a look at composites history and progression is taken, focusing on natural fibres, and more specifically plant fibres and fique.

1.1 Background

Natural fibres have been part of composites from the beginning, with the example of straw reinforced clay as a starting point. But they can also be part of the future. Their renewability, compostability, low or negative carbon emissions, safety on use and low abrasion to equipment, besides their mechanical properties and low density make them the target of many investigations to lead onto a more sustainable future. In here, we are going to explore the different types of natural fibres, with uses, structure, and properties. Extraction of natural fibres and how they are obtained to be used as reinforcement for composites materials is also explored before focusing on fique, its habitat, traditional uses and extraction process.

1.1.1 Natural fibres: types, structure, properties and extraction

Fibres can be synthetic (human made) or naturally occurring. Natural fibres can be classified depending on their origin, as shown in Fig. 1.1. Mineral, animal or plant

are the three main categories, and each of them has specific properties derived from their composition. The most common mineral fibre naturally occurring is asbestos, which has been widely used in construction and found to be carcinogenic, leading to its use being banned in many countries around the world [1, 2]. Asbestos is characterised for being a very fine fibre, 2000 times thinner than human hair. There are different forms of asbestos, but the most commonly found is chrysotile form which occurs in serpentine rock, which is a type of metamorphic rock. Animal fibres are protein based, and to this category belong widely used fibres like wool, cashmere, and silk, all with different properties and different applications, but deeply connected to what humanity has traditionally used to cover their body. Plant fibres, instead of a protein based structure, have a cellulose based structure, making this component the most available organic polymer on Earth [3]. Depending where the fibre is extracted from, plant fibres can be classified further into seed, bast, also referred as skin in the literature, or leaf fibres. Although other classifications also include fruit, which would separate coconut and cotton into different categories; and stalk fibres, such as straws of wheat, rice, or other crops like bamboo, which is sometimes put also under the bast label [4]. Cotton is a well known seed fibre, extensively used for textiles, but also coir fibre, characterised for being strong and rough, making it ideal for rope, brushes and doormats. Bast fibres include hemp, flax or jute. Hemp is one of the oldest domesticated plants by humans, with woven clothing dating back to the 6200 BC in Central Asia. It has been extensively used for textile making, for sailing equipment and papermaking, also valued for the oil in its seeds, similarly to flax, which has also extensively used for similar applications [5]. Sisal and other agave family plants like henequen, banana, pineapple, and fique produce leaves from which the fibres are extracted.

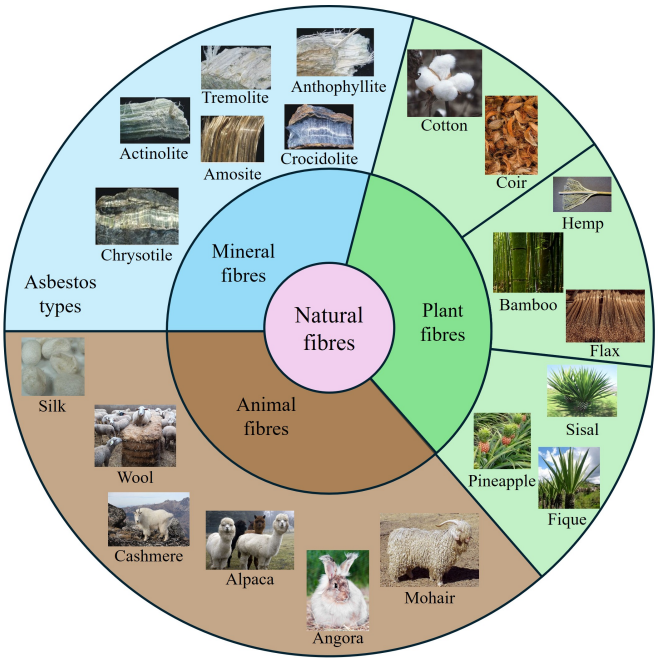


Figure 1.1: Types of natural fibres classified as mineral, animal and plant, with examples for each case.

1.1.2 Natural fibre chemistry

Mineral fibres such as asbestos have a silicate chemical composition which varies from type to type. Animal fibres have a chemical composition which is protein based, in contrast with the cellulose based composition of plant fibres. The protein based composition of animal fibres is primarily based on α-keratin proteins, consisting of 18 aminoacids, and making these types of fibres polar, with great affinity for water [6]. In the case of plant fibres, they are composed of cellulose, hemicellulose, and lignin, with the presence of these components varying depending on the type of plant fibre, but also from fibre to fibre.

Cellulose

Cellulose is the main component of lignocellulosic plant cell walls. And cellulose is a complex carbohydrate, a polysaccharide, with a chemical formula of $C_6H_{10}O_5$, discovered in 1838 by Anselme Payen. The β-D-glucose molecules connected by glycosidic bonds lead up to long chains of hundreds to thousands of monosaccharide units, as shown

in Fig. 1.2. The hydrogen bonds between cellulose molecules contribute to stabilising the structure, thus contributing to the mechanical strength of the cellulose microfibrils that they form together. Four types of crystallinity of cellulose have been identified so far, these being cellulose type I, II, III, and IV.

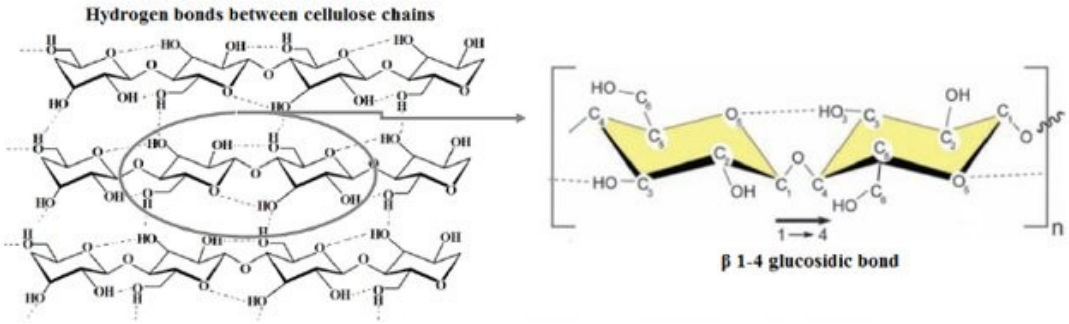


Figure 1.2: Cellulose chains showing hydrogen bonds as well as the molecule structure showing the glycosidic bond [7].

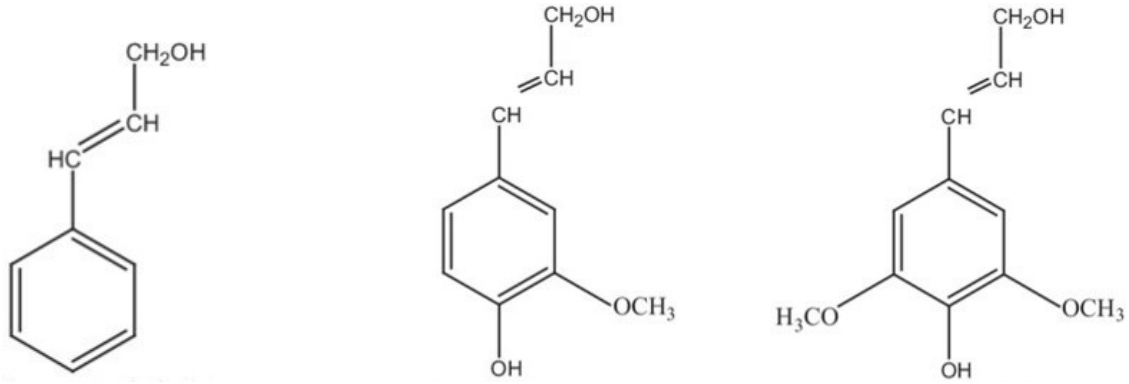
Hemicellulose

Hemicellulose is as cellulose a complex polysaccharide, but unlike cellulose, it is a copolymer formed of pyranose and furanose sugar units, including predominantly of 1→4-linked monosaccharides of β-D-glucose, β-D-glucuronic acid, D-xylose, β-D-mannose, β-D-galactose, α-L-fucose, and α-L-arabinose [8,9]. If cellulose is formed by long chains that bond to each other giving place to microfibrils, hemicellulose is form of short chains, and while cellulose is the main load bearing component in plant fibres, hemicellulose is meant to be responsible for the interfibre adhesion through a broad hydrogen bonding network [9], also acting as the matrix of cell walls. Hemicellulose, as cellulose, has a different composition depending on the fibre type.

Lignin

Lignin is the second most abundant organic substance on Earth and is often described as a non-regular polymer due to the absence of a unique repeating unit; however, it is an amorphous macromolecular polyphenolic biopolymer, and its biosynthesis occurs through enzymatic dehydrogenation of three phenylpropanoid monomers: p-coumaryl alcohol, coniferyl alcohol, and sinapyl alcohol, which structures are shown in Fig. 1.3

[10], which form both C–O and C–C bonds, leading to a heterogeneous and a three-dimensional structure [11]. Lignin plays a crucial role in allowing plants to grow high and compete for sunlight [12], since it gives the cell walls the necessary compressive strength to do so. Lignin acts as a binder between cellulose and hemicellulose, being this bond physical and chemical, filling the space between cellulose and hemicellulose and acting as an adhesive. Cellulose microfibrils are embedded in a hemicellulose matrix within a pool of lignin [13]. Depending on factors like type of plant, plant organ or type of tissue different types of lignin occur, but in any case its hydrophobic nature contributes to the waterproofing of the cell walls as well as protecting the cell against microbial pathogens while contributing to the mechanical strength [13].



(a) p-Courmararyl alcohol (b) Coniferyl alcohol (c) Sinapyl alcohol

Figure 1.3: Lignin monomers chemical structure [10].

Pectin

Pectin is a heteropolysaccharide, making it more complex than polysaccharides like cellulose and hemicellulose [14]. The role of pectin in cell walls is helping to limit or prevent the aggregation of cellulose microfibrils by binding indirectly to cellulose via xylan. This contributes to wall porosity, increased hydration, and enhanced flexibility [15]. Pectin degradation is one of the key parts of fibre retting [16].

Lipids

Lipids are organic compounds that contain hydrocarbons mainly formed by esters of fatty acids with alcohols and polyols, and can be classified into fixed oils, fats, and

waxes. The main role of waxes in plants is to protect them from foreign organisms and desiccation of the plant [17]. Main above the ground organs of plants are covered by a continuos extracellular membrane composed of cutin and waxes called cuticle. Many cuticle properties are based on waxes, and, among other things, act as a water transpiration barrier as well as influencing the wettability, self-cleaning behaviour, and light reflection. The hydrophobicity seen in plant leaves is a direct consequence of them [18].

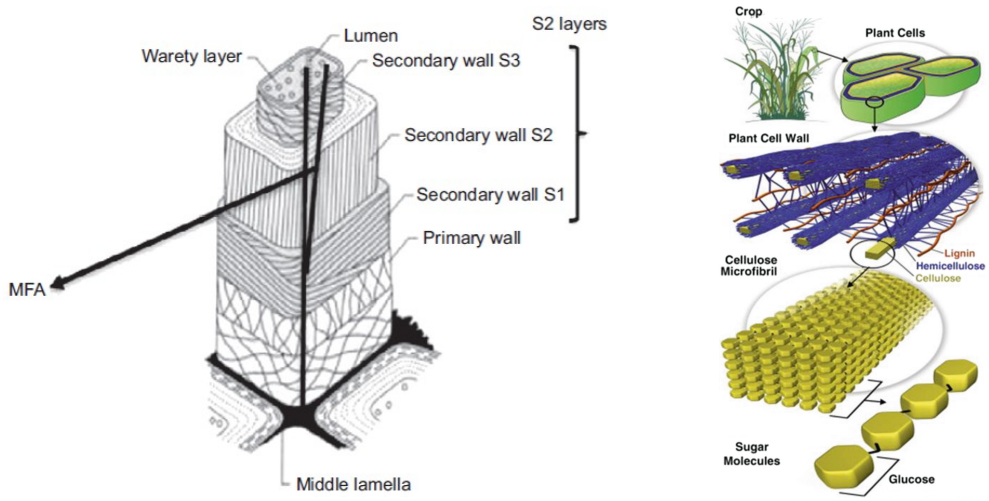
1.1.3 Lignocellulosic fibre structure

Plant fibres as we see them are refined composite materials themselves. Each fibre is formed by a bundle of elementary fibres, which are individual plant cells. Cell walls of these elementary fibres or fibrils have a layered hollow structure that consists on a primary layer and three secondary layers named S1, S2, and S3, from the outer to the innermost, as shown in Fig. 1.4a, although references with the secondary wall layers named reversely are also found [19, 20], with the lumen being the hollow part. The middle lamella is the outermost part in the cell and it is the physical connection between cells, physically adhering to each other. The middle lamella is pectin and lignin rich [21]. The cell wall structure and its function are intimately connected, with great variation between structural dimensions depending on the function, age, and position of the cell in the plant, with chemical variation depending on growth conditions, geographical factors and method of extraction [22]. The outermost layer is the oldest, with cellulose content increasing from the outermost to innermost layer, while lignin increases following the reverse pattern [23].

The primary wall consists mainly of pectin, cellulose and hemicellulose, while the secondary wall consists mainly of cellulose, hemicellulose, and lignin [24]. Both hemicellulose and lignin form an adhesive that keeps membranes and cellulose microfibrils linked inside each layer, Fig. 1.4b, and that allows for all the layers to swollen and shrink together throughout moisture variations without stress being created in the structure [23].

While hemicellulose content remains constant throughout the layers, other components vary, and this is deeply connected with each layers functionality, being the S2 in

the secondary wall the thickest layer and the one with highest cellulose content, being responsible for most of the mechanical performance of the fibre. In the secondary wall, cellulose microfibrils are arranged in an helicoidal way around the different layers in this secondary wall. The angle of this cellulose microfibrils around the S2 layers in respect to the longitudinal axis of the fibre, as defined in Fig. 1.4a, is called the microfibril angle (MFA), and is another parameter that contributes to the mechanical properties of natural fibres, varying from one to another, with tensile strength increasing with microfibril angle reduction [22–24]. In Table 1.1, the chemical composition of some natural fibres is shown along their MFAs.



(a) (b)

Figure 1.4: (a) shows the structure of the wall of a plant cell, with the primary and secondary walls and lumen, as well as the microfibril angle [25], while (b) shows the intertwined structure formed by cellulose microfibrils bound together by the adhesive formed by lignin and hemicellulose [13].

Table 1.1: Different fibres with their composition and MFA.

Fibre (type)	Cellulose (%)	Hemicellulose (%)	Lignin (%)	Pectin, wax and others (%)	MFA (°)	Ref.
Abaca (leaf)	56–63	15–25 20–25	7–9 7–12.4	-	20–25	[22, 26]
Agave americana (leaf)	68.5, 59.5	18.4, 17.4	6.1, 13.6	3.9	-	[22, 27]
Agave sisaliana (leaf)	47–78	10–24	7–11	13	10–22, 10–25, 20–25	[22, 23, 25, 28]
Bamboo (bast)	26–73.8, 228.8– 56.7	12.5–31, 17.2–43.8	10.2– 36.9, 21–31	2.4	2–10	[22,25,26]
Banana (bast)	60–65	5–10 10–24	6–19 5–10	-	11–12	[25,26,29]
Coir (seed)	32–43	0.15–0.25	40–45	-	30–49	[25, 26]
Cotton (seed)	82.7-92	5.7	0	0–1.6	20-30	[23,26,30]
Curaua (leaf)	73.6 77.2–85.7	9.9 6.8–7.3	7.5 6.4–8.7	3.8	-	[22, 31]
Flax (bast)	71 64.1–75	18.6–20.6 10.37–20.6	2.2 2–5	-	6–10 5-10	[22, 23, 25, 26]
Hemp (bast)	57–77	14–22.4	3.7–13	2.5	6.2, 6	[22,23,25]
Henequen (leaf)	77.6 70–77.6	4–8 4–20	13.1 8–13.1	-	-	[22, 26]
Jute (bast)	64.4 45–71.6 41–48 61–71	11.8 13.6–21 18–24 13–20.4	12 21–26 21–24 5–13	1.2 0.8	8, 8.1	[22, 23, 25, 26, 29]
Kenaf (bast)	31–57 37–49 31–72	20.3–33.9 18–24 20–33.9	9–21.2 15–21 8–21.2	2.5 2–4 2–6.2	9–15 7.1	[22,26,32]
Pineapple (leaf)	81 70–82	12.7 18	12–14 5–12.7	-	14	[22, 25, 26, 30]
Ramie (bast)	68.6–91 61.9–85	5–16.7 3–7.6	0.6–0.7 0.5–9.1	2.2	8, 7.5 69–83	[22,25,26]

1.1.4 Fibre extraction, separation and processing

Fibre extraction from seed, bast or leaves can significantly impact the later properties of the fibre , from mechanical properties to fibre structure or chemical composition. The fibre extraction is done in order to separate the technical fibres from the woody tissue in the rest of the plant part, through detachment, disintegration, and deterioration of pectins, gums, and different adhesive substances. This process is called retting and it can be biological, mechanical, physical or chemical [33, 34].

Biological retting

Biological retting can be natural or artificial. In the first type dew retting and cold water retting are found. Dew retting consists on spreading the harvest on field after being cut, and leave microorganisms to separate the fibres from cortex and xylem. Plants are turned around periodically, ensuring retting happens homogenously, and need to be monitored to ensure quality of the fibres. This method requires particular conditions of humidity and temperature, that makes it not available everywhere, and depending on conditions it can take between 3 and 6 weeks. The cold water retting process consists of putting the harvest under water in rivers, lakes, or tanks, for anaerobic microorganisms to break down pectin. If tanks are used, water is changed every two days, and the process can take between 7 and 14 days, depending on water type, temperature, and bacteria function. Despite this process giving a higher quality fibre type than dew retting, the amount of water needed alongside the pollution in the waste water makes it not ideal, with legislation preventing it around Europe. In the artificial biological retting group, there is the warm water retting, which mimics an accelerated cold water retting, in tanks, at temperatures between 28 and 40 °, reducing the duration to 3 to 4 days, but carrying the same drawbacks [33, 34].

Mechanical or green retting

Mechanical retting consists of separating the fibres from the woody materials via mechanical means after the material has been field dried or marginally retted. It is called green retting because the plant is fed into the machine when still green, when it is

more flexible. This is especially used for bast fibres, where there is no fibre value in the leafy parts of the plant, which are discarded in the process. After that the stem is split and the outer bark layer peeled, with the bark being ribboned. Although pectin and other substances are not fully removed, they are significantly degraded, and ribbons are bundled together into fibre bundles [33, 34].

Physical retting

Physical retting includes processes like ultrasound and steam explosion. In the first case, fibres are crushed and cleaned, and then put into hot water while high intensity ultrasonication is applied at 40 kHz, leading to fibre separation. In the steam explosion process fibres undergo high pressures and high temperatures, leading to fibre separation, this being a good alternative to the conventional retting process, leading to fine fibres with good mechanical properties [33].

Chemical retting

In chemical retting processes, the part of the plant from the fibres are to be extracted from is submerged in tanks with water solutions of sulphuric acid, chlorinated lime, sodium or potassium hydroxide, and soda ash to dissolve the pectin component. Although it can lead to good quality fibres, the cost is higher than other methods due to the use of chemicals and the higher energy requirement [33, 34].

1.1.5 Fique

The name fique is used to refer to a plant whose taxonomy is as follows:

- **Phylum**: Magnoliophyta (Angiosperms)
- **Class**: Liliopsida (Monocots)
- **Order**: Asparagales
- **Family**: Asparagaceae
- **Subfamily**: Agavoideae

- **Genus**: Furcrarea



(a) (b)

Figure 1.5: Fique plants, with trunk as described (a), [35], and still on the ground (b).

This includes more than 400 species. The most common cultivated species are *Furcrarea gigantean* known as common tunosa, *Furcrarea macrophylla* known as uña de águila, *Furcrarea cabuya*, known as ceniza, *Furcrarea castilla* known as bordo de oro, and *Furcrarea andina* known as rabo de chucha. Common names for fique include cabuya, penca, fique perulero, maguey, cabui, cabuya blanca (white cabuya), chuchao, and cocuiza. In general, what characterizes these species is that they are upright stem plants, with height varying from 2 to 7 metres, with green leaves between 1 to 3 metres long arranged radially as can be seen in Fig. 1.5. In some species the leaves are toothed, but in general they are fleshy, pointed, channelled and spiny, with a width between 10 to 20 cm, making them relatively narrow. As the plant grows, it develops a short trunk. The root system these plants develop makes them a good species to prevent soil erosion. Added to this, flowers are only produced once during an individual plant's life cycle. Typical life span for these plants is between 10 and 20 year, with them becoming suitable for fibre production between 3 and 6 years depending on growing conditions [36, 37].

1.1.5.1 Fique habitat, production, and composition

Fique is considered a rustic plant, meaning that although it requires tropical conditions, it can adapt to diverse agro-ecological conditions. Requiring semi-humid conditions, warm and sun exposure for good development, it can grow in arid conditions with

soils poor in nutrients. It originated from the tropical area in the Andean regions of Colombia and Venezuela, but that has spread to the eastern coast of Brazil and the West Indies. Taken to Mauritius in the XVII century by the Dutch from Brazil, it has spread naturally there. In Colombia, it grows from the coastal regions to regions elevated above 3,000 m [36].

Fique leafs are cut from the plant, removed by their base, and a dethorning process of cutting the edges is done before defibering the leaf. This process can be seen in Fig. 1.6a. At least 20 leafs have to be left on the plant to ensure survival for a further cut. Ripped leafs or those that are no longer pointing upwards are the ones chosen [38]. The defibering process, Fig. 1.6b, consists of removing the cortex of the leaf from the fibres, and can be done mechanically or manually. When done mechanically, a calibrated shredder is used, with the base and thickest part of the leaf being introduced first up to 1/4 of the leaf. After that, the leaf is taken out, inverted, and introduced from the tip, leading to fibre obtention. After the fibre has been obtained, a fermentation process takes place, aiming to clean the fibres, removing pulp, sap, and gums mainly, leading to a change in colour, from green to the characteristic yellowish colour of the dry fique. This fermentation process is done in tanks, where the fibres are stretched through the length and the fique covered in water. After the fermentation process is done, the fibre is hung to dry after it has been wrung out, Fig. 1.6c and Fig. 1.6d. After having been dried, the fibre is packed, without mixing different lengths, and with a humidity content lower than 12% [36, 37].

Table 1.2: Fique fibre composition.

	Cellulose (%)	Hemicellulose (%)	Lignin (%)	Pectin, wax, and others (%)	Ref.
Fique	73.8	10.5	11.3	2.6	[36, 37]
	70.0	-	10.1	-	[41]
	57	29	13	-	[42]
	68.4	16.7	7.2	0.7	[43]
	58.3± 17.5	14.6±7.9	7.2±3.1	16.5±5.9	[44]
	42.1	13.0	18.2	26.7	[45]
	55.8	18.6	14.2	11.4	[38]



(a)



(b)



(c)



(d)

Figure 1.6: (a) Fique leaves being cut [38], (b) fique leaves being defibrillated [39], (c) and (d) showing the drying process of fique, where is hung out to dry, and goes from the green leafy colour to the yellowish colour [35, 40].

The extracted fique fibre comprises only 4% of the total weight of the leaf [36], and its composition varies depending on the source, as presented in Table 1.2. It could be said that cellulose is between 55 and 70% of the fibre content, while hemicellulose and lignin sit between 10 and 20%, with pectin, wax, ashes and humidity accounting for the difference.

Once the fibre is received to be worked with, a heckling process takes place, by which the fibre is passed through different sizes of heckling combs, Fig. 1.7, to remove final contaminants and untangle the fibres. Normally, a small addition of an emulsion of vegetable oils and water is used, to ensure a good heckling and texture before the fibre is threaded and/or woven to be converted into products.



Figure 1.7: Heckling of fique using a heckling comb [35].

1.1.6 Traditional uses and future

Fique, as many other natural fibres in different locations around the world like jute, flax or hemp, has been used to manufacture all sorts of daily objects and handcrafts, as well as textiles. For fique, the long fibres are used in packaging, ropes and braids, handcrafts, erosion control blankets, fabrics, backpacks, and home accessories like lamps, curtains, carpets, as well as hats and footwear [36]. Its most iconic use is in Colombian coffee sacks, as well as cocoa, rice, maize, potatoes and other tubers, and for all sort of cereals.

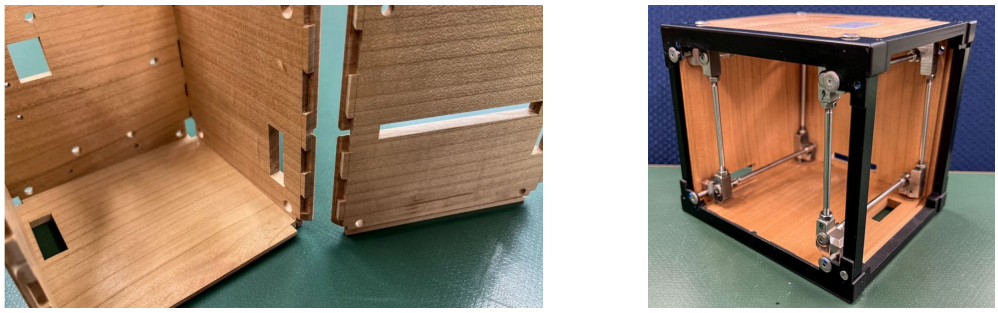
The use of natural fibres like fique in more technical fields like composites is also not new, since composites and natural fibres have been linked since the beginning, starting with the adobe and straw bricks, but also lime concrete, as a particle reinforced composite and already described by Vitruvius in his ten books on architecture [46]. Not only there, but how natural fibres like flax became a reinforcement in composite materials when an aluminium shortage was expected during World War II, and phenolic resin reinforced with flax skein was used to develop and manufacture the Spitfire fuselage,

although the aluminium shortage never happened. In this context, the use of honeycomb core material using balsa wood or kraft paper in the DH Albatross airliner and the Mosquito show how natural fibres have been present in structural components [47].

Development of polymers at the beginning of the XX century with Bakelite being discovered in 1907 slowly built into the launch of glass fibre reinforced polymers in the 30s decade, with Owens Corning leading a revolution in lightweight composites. Carbon fibre was first patented in 1961, contributing to the development of industries like maritime and air traffic. The massive use of composites for structural applications like wind turbine blades begins in the 1990s and 2000s. The contribution of synthetic fibre reinforced composites to technology advancements is invaluable, but its mass use and the lack of prevision around their whole life cycle has lead to the need of research development in composite structures' recycling, remanufacturing or reusing. But not only this, also the look for other materials that can enhance sustainability of materials by digging in the origins, with the use of natural fibres. One example is the recent launch of a wooden satellite by the Japanese Aerospace Exploration Agency in collaboration with the Kyoto University to explore the viability of the use of this material in space research. This satellite made of magnolia wood (*Hoonoki* in Japanese) panels assembled with a Japanese wood-joinery method is the paradigm of connection between groundbreaking research and tradition for a more sustainable future Fig. 1.8 [48]. But this is not the only one. Manufacturing of a small turbine blade of bamboo fibre reinforced PLA, as shown in Fig. 1.9, as part of the development of robust manufacturing processes of biodegradable structural parts [49] drives in the same direction of connecting traditional and future uses of materials that have been around and can help shape a more sustainable future.

The use of natural fibres as reinforcement for composite materials has some drawbacks, since due to their natural origin, moisture absorption impacts the interface bonding between fibre and matrix, leading to deterioration of mechanical properties. Added to this is the limited maximum temperature under which natural fibres can be processed in the manufacturing of composites, alongside their poor fire resistant properties when talking about plant fibres. But the advantages they possess keep pushing them as sustainable and renewable materials, with low or negative carbon footprint and good

thermal and acoustic insulating properties. Their low cost added to their low specific weight keep them as a good option to replace glass fibre reinforced composites where structural requirements are not essential, as some components in the automotive industry, where the weight reduction is still relevant [4]. In Table 1.3 a number of fibres and their purchased prices have been collected, but it is important to take into account that the price per kilogram of natural fibres may be higher if the fibres require further chemical treatments or processing in order to get a higher grade for composite applications. The use of new tools like Life Cycle Assessments (LCAs) can help in the assessment of energy and water use to understand the differences between natural and synthetic fibres, but the end of life opportunities and the renewability and biodegradability of natural fibres have to be accounted for beyond economical costs as part of the fibre's processing, especially given the times we are living in, where environmental cost has been neglected for so long.



(a) (b)

Figure 1.8: (a) detail of the traditional Japanese joining method, the Blind Miter Doveltail and (b) view of LignoSat's structure showing the relationship among wooden panels, aluminium frames, and stainless-steel shafts [48].

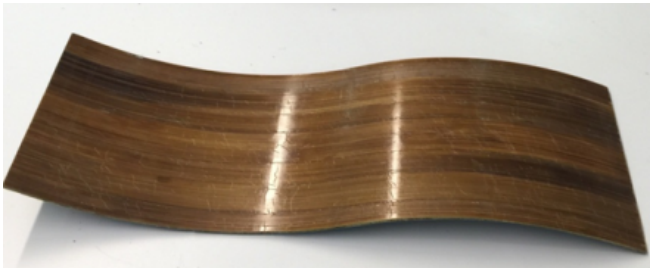


Figure 1.9: Curved surface manufactured on bamboo reinforced PLA mimicking the process of small blade manufacturing [49].

Table 1.3: Natural and synthetic fibres industrial purchase price in $/kg.

Fibre	Purchase price US$/kg	Ref.
Abaca	1.55-2.55	[50]
Bamboo	0.25-0.50	[50]
Banana	0.1	[50]
Coir	0.20-0.84	[50]
Cotton	1.71-5.06	[50]
Curaua	0.44	[50]
Fique	0.36-0.45	[51]
Flax	3.79-6.42	[52]
Hemp	2.20-5.00	[53]
Jute	0.25-0.50, 0.55-1.15	[50, 53]
Kenaf	0.30-0.65	[50]
Sisal	0.35-1.30	[50]
Carbon	30-85	[54]
Glass	0.75-3	[54]
Polypropylene	1.50	[54]

1.2 Project objectives

In that same spirit, this work is born to answer some questions about natural fibres, more specifically fique fibre, to help find higher end applications through the study of the fibre.

The main objective of this research is to create a deeper understanding of natural fibres and natural fibre composites. In this case, fique fibre with recycled polypropylene as matrix is of special interest for the use of a biodegradable material alongside a recycled one. Both fique and recycled PP are supplied by Compañía de Empaques via the Universidad Nacional de Colombia, who has also supplied all treated fique fibres.

The first detailed objective is about the shape and dimensions of fique fibre, as this affects the later calculation of mechanical properties as tensile strength, and will define where these fibres can be used. Understanding how fibre dimensions changed along the fibres when used as reinforcement of long fibre composites (from 20 mm for long fibre reinforced thermoplastics to 6 m in high performance components) is essential in order to understand their performance. Alongside this, how the cross-sectional area is

measured and how accuracy can be increased, as well as studying the assumption of circularity for the case of fique, are part of this first objective.

The second detailed objective is to provide with a direct strain measurement technique, as one of the gaps found in the literature has been how fique mechanical properties are measured and the need to increase accuracy by removing uncertainties. As part of this objective a comparison to the most used indirect strain measurement technique is also done and the number of fibres tested significantly increased compared to what is found in the literature. Part of removing uncertainties is looking at how the cross-sectional area is obtained and how it affects the obtention of the fibre mechanical properties.

The third detailed objective is connected with how fique fibre interacts with recycled polypropylene. For this, chemically and physically treated fique fibres have also been used. These fibres have been studied to understand better the chemical changes of their composition after the treatments and how wettability is modified due to those changes.

The fourth detailed objective is directly linked with the quality of the fibre-matrix interface, and how changes in the fibre composition may affect the interface behaviour between the fique and the recycled polypropylene, measuring the interfacial shear strength via the single fibre fragmentation test.

1.3 Thesis outline

Within this spirit of linking tradition while looking at the future, this thesis is born, working on fique fibre and on its characterisation to find appropriate applications where this fibre can be used, pushing for a more sustainable use of materials in structural applications.

After the introduction to natural fibres and to fique and its uses in particular in this first chapter, giving a background within natural fibres classification, composition, extraction, and uses, in chapter 2 the fique fibre is studied.

Chapter 2 includes the CT-scan of two fique fibres, with the reconstruction and measuring methodologies detailed. This chapter comprises the 3D reconstruction of the scans, and the measuring of the cross-sectional area along two fibres, and how it varies.

Chapter 3 is the core part of this work, where the mechanical characterisation of fique via two different methods is presented. Indirect and direct strain measurement techniques are used in obtaining the mechanical properties of this fibre via tensile testing. Two different approaches to measuring the cross-sectional area of the fibre are also presented, and how the approach selected affects the calculation of the said mechanical properties is also studied.

Chapter 4 includes the thermo-chemical study of fique, and the variation this fibre suffers under treatments like mercerization, hydrolysis or high intensity ultrasonication, and how its thermal stability and composition are affected.

Chapter 5 covers the thermo-chemical characterisation of recycled polypropylene alongside the study of the contact angle and wettability of fique for the different treated fibres. This is done by directly measuring the contact angle of the recycled polypropylene with the fibres, and by the study of the polar and dispersive components of the surface energy of the fibres. To finish this chapter, the measurement of the interfacial shear strength by the single fibre fragmentation test is done, to study the load transfer and how different treatments on the fibre may impact this.

Chapter 6 presents a review and summary of key observations and findings gathered throughout this work, drawing main conclusions alongside recommendations for future work.

Bibliography

[1] C. Roux and J. Robertson, *FIBERS | Types*, pp. 838–854. Elsevier, 2000. https://doi.org/10.1006/rwfs.2000.0513.

[2] UK Health Security Agency, UK goverment, "Asbestos: general information," March 2024. https://www.gov.uk/government/publications/asbestos-properties-incident-management-and-toxicology/asbestos-general-information.

[3] E. Marinho, "Cellulose: A comprehensive review of its properties and applications," *Sustainable Chemistry for the Environment*, vol. 11, 9 2025. https://doi.org/10.

1016/j.scenv.2025.100283.

[4] F. I. Mahir, K. N. Keya, B. Sarker, K. M. Nahiun, and R. A. Khan, "A brief review on natural fiber used as a replacement of synthetic fiber in polymer composites," *Materials Engineering Research*, vol. 1, pp. 88–99, 2019. https://doi.org/10.25082/MER.2019.02.007.

[5] L. Pinsard, *Immersion au sein de la chaîne de valeur du chanvre textile : du choix de la variété jusqu'au textile.* PhD thesis, Institut National Polytechnique de Toulouse (Toulouse INP), 2023. https://doi.org/10.70675/c3703237z1523z49e9za64fz8a76f3d7ba9e.

[6] B. A. McGregor, *Physical, chemical, and tensile properties of cashmere, mohair, alpaca, and other rare animal fibers*, pp. 105–136. Elsevier, 1 2018. https://doi.org/10.1016/B978-0-08-101272-7.00004-3.

[7] M. Poletto, V. Pistor, and A. J. Zattera, *Structural Characteristics and Thermal Properties of Native Cellulose.* InTech, 8 2013. https://doi.org/10.5772/50452.

[8] J. Rao, Z. Lv, G. Chen, and F. Peng, "Hemicellulose: Structure, chemical modification, and application," 5 2023. https://doi.org/10.1016/j.progpolymsci.2023.101675.

[9] V. Chibrikov, P. M. Pieczywek, J. Cybulska, and A. Zdunek, "The effect of hemicelluloses on biosynthesis, structure and mechanical performance of bacterial cellulose-hemicellulose hydrogels," *Scientific Reports*, vol. 14, 12 2024. https://doi.org/10.1038/s41598-024-72513-w.

[10] S. Gea, Y. A. Hutapea, A. F. R. Piliang, A. N. Pulungan, R. Rahayu, J. Layla, A. D. Tikoalu, K. Wijaya, and W. D. Saputri, "A comprehensive review of experimental parameters in bio-oil upgrading from pyrolysis of biomass to biofuel through catalytic hydrodeoxygenation," 3 2023. https://doi.org/10.1007/s12155-022-10438-w.

[11] R. Katahira, T. J. Elder, and G. T. Beckham, "A brief introduction to lignin structure," in *Lignin Valorization: Emerging Approaches*, The Royal Society of Chemistry, 4 2018. https://doi.org/10.1039/9781788010351-00001.

[12] M. Abhilash and D. Thomas, *Biopolymers for Biocomposites and Chemical Sensor Applications*, pp. 405–435. Elsevier Inc., 2017. https://doi.org/10.1016/B978-0-12-809261-3.00015-2.

[13] E. I. Akpan, *Chemistry and Structure of Lignin*, pp. 1–50. Cham: Springer International Publishing, 2019. https://doi.org/10.1007/978-3-030-18792-7_1.

[14] A. Roman-Benn, C. A. Contador, M.-W. Li, H.-M. Lam, K. Ah-Hen, P. E. Ulloa, and M. C. Ravanal, "Pectin: An overview of sources, extraction and applications in food products, biomedical, pharmaceutical and environmental issues," *Food Chemistry Advances*, vol. 2, 2023. eLocator 100192 https://doi.org/10.1016/j.focha.2023.100192.

[15] K. T. Haas, R. Wightman, A. Peaucelle, and H. Höfte, "The role of pectin phase separation in plant cell wall assembly and growth," *The Cell Surface*, vol. 7, p. 100054, 2021. eLocator 100054 https://doi.org/10.1016/j.tcsw.2021.100054.

[16] W. Meijer, N. Vertregt, B. Rutgers, and M. van de Waart, "The pectin content as a measure of the retting and rettability of flax," *Industrial Crops and Products*, vol. 4, no. 4, pp. 273–284, 1995. https://doi.org/10.1016/0926-6690(95)00041-0.

[17] D. S. Seigler, *Plant Waxes*, pp. 51–55. Boston, MA: Springer US, 1998. https://doi.org/10.1007/978-1-4615-4913-0_4.

[18] K. Koch and H.-J. Ensikat, "The hydrophobic coatings of plant surfaces: Epicuticular wax crystals and their morphologies, crystallinity and molecular self-assembly," *Micron*, vol. 39, no. 7, pp. 759–772, 2008. https://doi.org/10.1016/j.micron.2007.11.010.

[19] C. Baley, F. Busnel, Y. Grohens, and O. Sire, "Influence of chemical treatments on surface properties and adhesion of flax fibre-polyester resin," *Composites Part A:*

Applied Science and Manufacturing, vol. 37 (10), pp. 1626–1637, 10 2006. https://doi.org/10.1016/j.compositesa.2005.10.014.

[20] S. Bhowmik, S. Kumar, and V. K. Mahakur, "Various factors affecting the fatigue performance of natural fiber-reinforced polymer composites: a systematic review," *Iranian Polymer Journal*, vol. 33, 11 2023. https://doi.org/10.1007/s13726-023-01243-z.

[21] V. Brulé, A. Rafsanjani, D. Pasini, and T. L. Western, "Hierarchies of plant stiffness," *Plant Science*, vol. 250, pp. 79–96, 2016. https://doi.org/10.1016/j.plantsci.2016.06.002.

[22] A. Karimah, M. R. Ridho, S. S. Munawar, D. S. Adi, Ismadi, R. Damayanti, B. Subiyanto, W. Fatriasari, and A. Fudholi, "A review on natural fibers for development of eco-friendly bio-composite: characteristics, and utilizations," *Journal of Materials Research and Technology*, vol. 13, pp. 2442–2458, 2021. https://doi.org/10.1016/j.jmrt.2021.06.014.

[23] S. Nautiyal, S. Dimri, I. Riyal, H. Sharma, and C. Dwivedi, "Natural fibres and their composites: a review of chemical composition, properties, retting methods, and industrial applications," *Cellulose*, vol. 32, pp. 3497–3527, 4 2025. https://doi.org/10.1007/s10570-025-06487-x.

[24] T. H. Mokhothu and M. J. John, "Review on hygroscopic aging of cellulose fibres and their biocomposites," *Carbohydrate Polymers*, vol. 131, pp. 337–354, 2015. https://doi.org/10.1016/j.carbpol.2015.06.027.

[25] S. R. D. Petroudy, *Physical and mechanical properties of natural fibers*, pp. 59–83. Elsevier Inc., 2017. https://doi.org/10.1016/B978-0-08-100411-1.00003-0.

[26] I. Elfaleh, F. Abbassi, M. Habibi, F. Ahmad, M. Guedri, M. Nasri, and C. Garnier, "A comprehensive review of natural fibers and their composites: An eco-friendly alternative to conventional materials," *Results in Engineering*, vol. 19, 9 2023. https://doi.org/10.1016/j.rineng.2023.101271.

[27] T. T. Gebretsadik, A. H. Tesfay, A. G. Gebru, E. Assayehegn, Y. H. Desta, K. H. Gebremedhin, H. Gebrehiwet, and T. B. Teklemedhin, "Characterization and comparative insights on agave americana and agave sisalana leaf fibers for high-performance applications," *Journal of Natural Fibers*, vol. 20, 2023. https://doi.org/10.1080/15440478.2023.2246648.

[28] X. Lu, M. Q. Zhang, M. Z. Rong, G. C. Yang, and H. M. Zeng, "Sisal reinforced polymer composites," *Fuhe Cailiao Xuebao/Acta Materiae Compositae Sinica*, vol. 19, pp. 1–6, 10 2002. https://doi.org/10.1016/b978-0-12-818983-2.00003-7.

[29] M. Puttegowda, S. M. Rangappa, M. Jawaid, P. Shivanna, Y. Basavegowda, and N. Saba, *Potential of natural/synthetic hybrid composites for aerospace applications*, pp. 315–351. Elsevier, 1 2018. https://doi.org/10.1016/B978-0-08-102131-6.00021-9.

[30] R. Arjmandi, I. Yıldırım, F. Hatton, A. Hassan, C. Jefferies, Z. Mohamad, and N. Othman, "Kenaf fibers reinforced unsaturated polyester composites: A review," *Journal of Engineered Fibers and Fabrics*, vol. 16, p. 15589250211040184, 2021. https://doi.org/10.1177/15589250211040184.

[31] A. E. de Freitas, F. de J. Padilha, S. de S. Barros, T. M. Khan, B. Pereira, W. T. Barbosa, J. D. Barbosa, F. L. Calderaro, S. da Silva, M. G. Quirino, and F. A. de Freitas, "Curauá fiber from plants produced by tissue culture: thermal, mechanical, and morphological characterizations," *Cellulose*, vol. 30, pp. 2841–2858, 3 2023. https://doi.org/10.1007/s10570-023-05067-1.

[32] T. T. D. Silva, P. H. P. M. D. Silveira, M. P. Ribeiro, M. F. Lemos, A. P. D. Silva, S. N. Monteiro, and L. F. C. Nascimento, "Thermal and chemical characterization of kenaf fiber (hibiscus cannabinus) reinforced epoxy matrix composites," *Polymers*, vol. 13, 6 2021. https://doi.org/10.3390/polym13122016, issn = 20734360.

[33] M. Ramesh, *Hemp, jute, banana, kenaf, ramie, sisal fibers*, pp. 301–325. Elsevier, 1 2018. https://doi.org/10.1016/B978-0-08-101272-7.00009-2.

[34] S. A. Mohamed, E. S. Zainudin, S. M. Sapuan, M. D. Azaman, and A. M. Arifin, *Introduction to Natural Fiber Reinforced Vinyl Ester and Vinyl Polymer Composites*, pp. 1–25. Elsevier, 1 2018. https://doi.org/10.1016/B978-0-08-102160-6.00001-9.

[35] "El fique: conoce esta fibra natural y su trabajo artesanal (Fique: get to know this natural fibre and its crafting)." https://vivoboreal.com/el-fique-conoce-esta-fibra-natural-y-su-trabajo-artesanal, 2018. Accessed January 28, 2026.

[36] Ministerio de Ambiente, Vivienda y Desarrollo territorial de Colombia (Ministry of Environment, Housing and Territorial Development of Colombia), "Guía ambiental del subsector fiquero (Environmental guide of the fique subsector)," 2006. www.minambiente.gov.co.

[37] United Nations Conference on Trade and Development (UNCTAD), "Biotrade – designer's toolkit 1. fique or cabuya furcraea spp., sustainable materials for the fashion industry, biodiversity/ecosystems/community impact review," *Fique or Cabuya Furcraea spp.*, p. 12, 2014.

[38] L. Rendón-Castrillón, M. Ramírez-Carmona, C. Ocampo-López, V. Pinedo-Rangel, O. Muñoz-Blandón, and E. Trujillo-Aramburo, "The industrial potential of fique cultivated in colombia," 1 2023. https://doi.org/10.3390/su15010695.

[39] "Video sobre defibrilado de fique (Defibrillating fique video)." YouTube: https://www.youtube.com/watch?v=_MW-LqinZOM, 2020. Accessed January 28, 2026.

[40] "Promueven el uso del fique como alternativa a plásticos de un solo uso (Promoting the use of fique as an alternative against single use plastics)." https://diariodelhuila.com/promueven-el-uso-del-fique-como-alternativa-a-los-plasticos-de-un-solo-uso/, 2024. Accessed January 28, 2026.

[41] S. Delvasto, E. F. T. Perea, F. Perdomo, and R. M. de Gutiérrez, "An appropriate vacuum technology for manufacture of corrugated fique fibre reinforced cementi-

tious sheets," *Construction and Building Materials*, vol. 24, pp. 187–192, 2010. https://doi.org/10.1016/j.conbuildmat.2009.01.010.

[42] C. G. Hoyos, V. A. Álvarez, P. G. Rojo, and A. Vázquez, "Fique fibers: Enhancement of the tensile strength of alkali treated fibers during tensile load application," *Fibers and Polymers*, vol. 13, pp. 632–640, 5 2012. https://doi.org/10.1007/s12221-012-0632-8.

[43] M. F. Muñoz-Velez, M. Á. Hidalgo-Salazar, and J. H. Mina-Hernández, "Fique fiber an alternative for reinforced plastics. influence of surface modification," *Biotecnología en el Sector Agropecuario y Agroindustria*, vol. 12 (2), pp. 60–70, 12 2014. https://www.researchgate.net/publication/317501110_FIQUE_FIBER_AN_ALTERNATIVE_FOR_REINFORCED_PLASTICS_INFLUENCE_OF_SURFACE_MODIFICATION.

[44] T. Gómez, S. Zuluaga, M. Jiménez, M. A. Navacerrada, M. M. Barbero-Barrera, D. de la Prida, A. Restrepo-Osorio, and P. Fernández-Morales, "Evaluation of colombian crops fibrous byproducts for potential applications in sustainable building acoustics," *Polymers*, vol. 13 (1), 101, 2020. https://doi.org/10.3390/polym13010101.

[45] K. G. Bastidas, M. F. R. Pereira, C. A. Sierra, and H. R. Zea, "Study and characterization of the lignocellulosic Fique (Furcraea Andina spp.) fiber," *Cellulose*, vol. 29, pp. 2187—-2198, 2022. https://doi.org/10.1007/s10570-021-04377-6.

[46] V. Šerifi, M. Tarić, D. Jevtić, A. Ristovski, and M. Šahinagić Isović, "Historical development of composite materials," *ANNALS OF THE ORADEA UNIVERSITY. Fascicle of Management and Technological Engineering.*, vol. Volume XXV, 2018. https://doi.org/10.15660/auofmte.2018-3.3392.

[47] D. H. Middleton, "Composite developments in aircraft structures — part 1," *Aircraft Engineering and Aerospace Technology*, vol. 64, pp. 2–8, 1992. https://doi.org/10.1108/eb037234.

[48] "Jaxa's first wooden satellite deploys from space station." https://www.nasa.gov/image-article/jaxas-first-wooden-satellite-deploys-from-space-station/, 2025. Accessed January 29, 2026.

[49] A. Pozo, A. Fernández-López, and A. Güemes, "Diseño y fabricación de una pala de aerogenerador mediante material compuesto biodegradable (Design and Manufacturing of a small wind turbine with biodegradable composite materia)," *Revista de la Asociación Española de Materiales Compuestos - Matcomp17 Proceedings - Applications and multifunctional composites*, vol. 2, pp. 1–7, 2018. https://doi.org/10.23967/r.matcomp.2018.04.001.

[50] T. Eleutério, M. J. Trota, M. G. Meirelles, and H. C. Vasconcelos, "A review of natural fibers: Classification, composition, extraction, treatments, and applications," *Fibers*, vol. 13, no. 9, 2025. https://www.mdpi.com/2079-6439/13/9/119, doi: 10.3390/fib13090119.

[51] S. Neves Monteiro, F. Salgado de Assis, C. L. Ferreira, N. Tonini Simonassi, R. Pondé Weber, M. Souza Oliveira, H. A. Colorado, and A. Camposo Pereira, "Fique fabric: A promising reinforcement for polymer composites," *Polymers*, vol. 10, no. 3, 2018. https://www.mdpi.com/2073-4360/10/3/246, doi: 10.3390/polym10030246.

[52] Alliance of European flax, linen & hemp, "European flax fibre market for 2025." https://allianceflaxlinenhemp.eu/en/flax-linen-hemp-economic-observatory/flax-linen-and-hemp-economic-observatory-figures-2025, 2025. Accessed September 21, 2026.

[53] Textile Tech Insight, "Global fibre prices 2026: Cotton, polyester, viscose, nylon, wool & recycled fibres." https://textiletechinsight.com/article/global-fibre-prices-2026/, September 2026. Accessed September 21, 2026.

[54] M. J. Keith, B. Al-Duri, T. O. McDonald, and G. A. Leeke, "Solvent-based recycling as a waste management strategy for fibre-reinforced polymers: Cur-

rent state of the art," 4 2025. https://www.mdpi.com/2073-4360/17/7/843 doi:10.3390/polym17070843.

Chapter 2

Porosity and cross-sectional area characterisation along the fibre length through X-ray CT

2.1 Introduction

In Chapter 2 a short introduction to X-ray computed tomography (CT) scan is done, along with a literature review on the use of this technology in characterising fibre reinforced composites as well as natural fibre specifically. Other procedures used to characterised porosity on natural fibres are also mentioned for relevance in the study of porosity of fique fibres as part of this chapter.

Experimental details like materials, sample preparation and image analysis are detailed just before results on fibre porosity and cross-sectional area (CSA) variation are reported.

2.2 Literature review

2.2.1 CT-scan: history, equipment, and process

Computed tomography main characteristic is that it is a non-destructive three dimensions (3D) imaging technique, based on the different X-ray attenuation of materials as

studied by Allan Cormack in the 1950s. But X-ray imaging story begins much earlier, in the 1895 with the discovery of X-rays by Wilhelm Conrad Roentgen. Cormack would win the Nobel prize in 1979 along with Sir Godfrey Hounsfield for the development of computer assisted tomography. Hounsfield was an engineer at Electric and Musical Industries (EMI), and after applying for funding to develop a top system to scan phantoms and cadaveric specimens, he demonstrated the ability to image the inside of a brain specimen. In 1971, and in collaboration with neuroradiologist James Ambrose, the first CT examination of a patient with a lesion in the right frontal lobe took place [1, 2]. This brought a revolution into medicine in general, and neurology in particular. But while in medicine, nowadays, the object of study, the patient, remains steady and is the scan which rotates around the patient capturing the images, when studying materials or inert samples, normally is the object what is rotated. Based on that premise, the working principles of X-ray CT-scan starts with the sample mounted on a rotator, which is hit by an X-ray beam. A series of N radiographs are recorded, corresponding to N angular positions of the sample. Those radiographs are later used by the reconstruction software to produce a 3D map of the linear X-ray attenuation coefficient μ within the sample under study. A 3D image is then formed with that distribution, with the reconstruction of slice by slice, as shown in Fig. 2.1, and in it the voxel is the elementary unit, which can be viewed with the right visualization software, and in which one can take measurements by knowing the image resolution, i.e. how to translate from voxel -3D pixels- to mm^3 [3]. The resolution will depend on the size of the specimen, with a smaller size giving higher resolution. The analysis of the 3D reconstructed image can be done using different software like ImageJ, Dragonfly or Avizo. In any case, image segmentation will be used for the analysis. The reconstructed image is in the grey scale (0-255), which means that brightness or colour intensity varies along this grey scale with the material density. The brighter the grey, the higher the density. This equates to black being air in the CT-image, while a material like a natural fibre will have a lighter grey or a brighter white depending on the segmentation used. In the case of natural fibres is common to see the fibre structure in light grey while the lumen is black, as it is filled with air, permitting the analysis of fibre porosity.

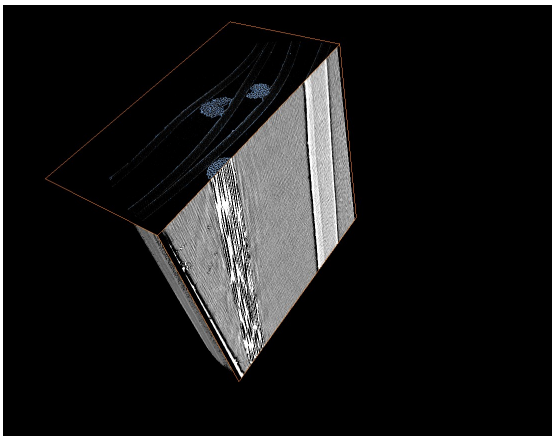


Figure 2.1: Reconstructed 3D image of the scan where both, cross and longitudinal sections of a fibre can be seen.

The three software mentioned earlier are used for visualisation and computation of data sets. ImageJ is an open sourced software which permits visualization of the 3D scan images, but computations and further analysis are better done in any of the other two, given the size of the data, which requires more robust analysing tools. Avizo or Dragonfly are exactly that.

2.2.2 Composites and fibre characterisation through CT-scan

Given how CT-scanning is a non-destructive technique and how microstructure and interaction between fibre-fibre and fibre-matrix define the material or component mechanical properties, a lot of research is being done in fibre reinforced materials. This is either by the development of new analysis techniques that help with porosity evaluation and void identification [4, 5], automate analysis process [6], or that help explaining material behaviour by understanding the underlying microstructure and stress state [7]. The study of CT-scan parameters impact on the analysis and results has also been studied, showing the potential and relevance of CT-scan in identifying internal defects despite showing that the smaller the defect the higher the errors [8], but also noise is reduced when longer scan time and higher resolution are used, leading to an image with increased quality [9].

Gao *et al.* [3] presented a review on the application of CT-scan in fibre reinforced

composites, highlighting some of the challenges of using this technology in the materials field. When applying it to fibre reinforced composites it can contribute to recognise better all constituent phases, helping to identify better defects that can be introduced during manufacturing as well as understanding damage from in-service accumulation. Real geometry of composites obtained through the CT imaging can be used to successfully model mechanical properties, with detailed inner structure examination, as well as microstructure, defect population, and damage distribution. The high resolution of micro-CT allows for fibre centre lines definition leading to generating a micro-scale finite element model with high fidelity of carbon or other types of fibres. But not only the fibres, but also how fibres interact with one another by looking at fibre arrangement in cross-section, 3D fibre waviness pattern, or contacting frequency between fibres, as this has an impact in the overall performance of the composite. Despite this, some challenges still remain. Sample size is one of them, since composite components are rather large compared to the accepted sample size to study through imaging. And when larger components can be scanned, poor phase contrast and long acquisition times are still barriers.

2.2.3 Natural fibres characterised using CT-scan

Bensadoun *et al.* [10] use micro-CT scan to study a variety of natural fibres like flax fibres composites, hemp and silk fibres, and palm tree skin and core as well as dry and wet cone scale. Woven flax yarns are embedded into three different types of thermoset matrices: epoxy, bio-polyester and bagasse-based furan resin. For this case, main features are observed and the textile geometry parameters can be used for modelling. One clear challenge is raised: the attenuation factors from epoxy and the bio-based matrices are very similar to the fibre's, making it very hard to differentiate them. When this is the case, finding the optimal scanning parameters is essential. For the case of hemp fibre and the analysis of its internal structure, the reconstructed elementary fibres from the CT-scan are shown to be hollow, while in the observation through Scanning Electron Microscope (SEM) they are full. This divergence can be explained by the large density variation between the different elements in the hemp fibre, where the internal elements

are expected to be of a much lesser density than the shell components, showing that information is lost during the CT-scan, requiring again a more optimal set of scanning parameters to try to solve this problem. For the case of the analysed silk, this is embroidered with metallic silver and golden threads, which have very high attenuation and can create artefacts, i.e. a fault in digital CT-scan images. Despite this and with CT-scanning being a non-destructive technique, it can still be useful in reconstructing historical textiles. The kernel of palm leaves was scanned to visualize the internal structure, with both the core and the skin. Its structure is like foam reinforced with unidirectional fibres, these being the core and the skin structures respectively. In this case, different powers were required to get the skin and the core due to the density differences. The pine cone is studied as part of the work of self-shaping materials since pine cones remain closed when attached to the tree or under wet conditions and they open up in dry conditions in order to release the seeds. The perpendicular fibres in the outer layer contract due to water loss, while the fibres oriented parallelly in the inner layer will induce lateral contraction, creating different degrees of shrinkage leading to internal stresses. This effect is the reason for the CT-scan under both, wet and dry conditions.

Tran *et al.* [11] have a closer look to coir fibres through a X-ray microtomography in SEM (SEM-CT) and SEM imaging to study the fibre's internal structure and its porosity. The porosity values are compared with those measured through SEM imaging of three cross-section per fibre. In the SEM-CT-scan a volumetric data set is used to measured this porosity. From the SEM imaging, values between 22 to 30% porosity are obtained, while using the SEM-CT method these values are increased to 27 to 40%, with one outlier presenting a 46% porosity. There is an argument to suggest that SEM-CT calculated porosity is overestimated. This is because the quality of the obtained images is based on the density difference between the fibre and the air surrounding it. In the case of coir this difference is not large, and if to that is added the fact that coir fibres consist of various thin organic tissues that might not be well detected, an overestimation of porosity is considered and a more accurate calculation is hypothesised to be done via SEM imaging alone.

Seghini *et al.* [12] used CT-scan in flax reinforced resins to measured the debonding length and correlate how the bigger the debonding length, the weaker the fibre-matrix interaction, which correlated perfectly with the interfacial shear strength measurements made on the flax reinforced vinylester and epoxy resins. In the vinylester case the interfacial shear strength calculated is lower than for the epoxy case, with smaller values of critical length for the flax/epoxy system, showing a better adhesion when flax is used as reinforcement of the epoxy matrix. In this case, the use of micro-CT scan helps to the length measurement being more accurate, reducing the dispersion of data, and helping to predict the level of adhesion between the two components.

Fibres like hemp, sisal, jute or kapok have been calculated porosities of 2.46%, 10.85%, 11.36%, and 73.95% respectively via SEM and image analysis. Porosity analysis of seagrass, alfa grass, and hemp done via mercury porosimetry shows values of 76.6%, 57.3%, and 74.8% [13].

Hidalgo-Salazar *et al.* [14] use a CT-scan on natural fibres, among which fique fibre is included to calculate the proportion of lumen over the total area, distinguishing it from the fibre area. It is not mentioned here how many fibres of each type are scanned, but given the amount of resources needed it is expected a low number. Despite this, a calculation of correction factors when measuring natural fibres cross-sectional areas is presented. This is done by measuring the fibres apparent diameter (AD), calculating the area from it assuming a circular cross-section and comparing it from the area measured through the CT-scan. This leads to correction factors for different fibres, although it may be relevant to have a wider pool of data to finely tune them appropriately. Area correction factors go from 1.46 for hemp fibre to 10.24 for toquilla straw, with fique presenting a value of 2.86.

2.3 Methodology

Studying the fibre cross-section variations along its length as well as the proportion of lumen and fibre walls are the aims of the experiment carried out in this piece of work.

To determine fibre cross-sectional changes and porosity, X-ray micro-CT (X-CT) im-

ages were acquired using a Zeiss Xradia 510 Versa micro-focus system at the University of Southampton, as the one shown in Fig. 2.2.

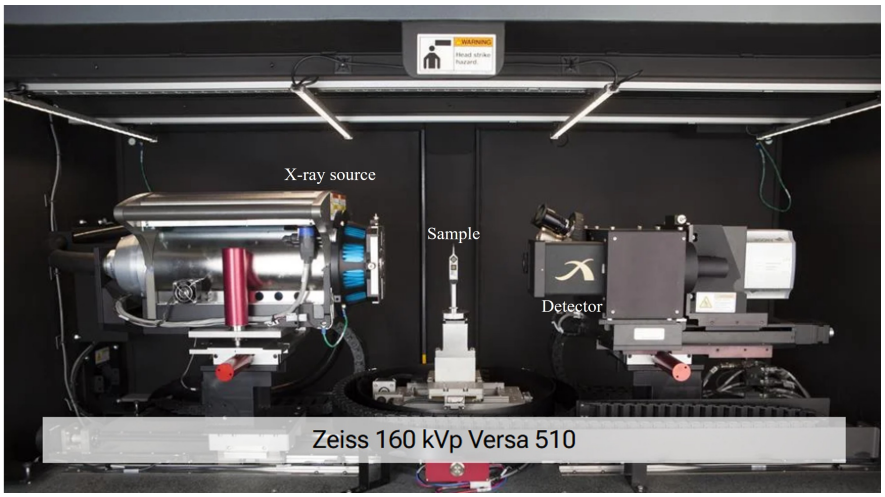


Figure 2.2: Zeiss 160 kVp Versa 510 equipment [15].

.

The source settings were 80 kVp, 7 W and non filter with 1 s exposure time per frame and one frame per projection. A number of 3001 projections were acquired throughout a 360°C sample rotation, yielding a 1.4966 reconstructed voxel resolution with the aid of 4× magnification optics. A 1.6 × 3.0 × 7.1 mm^3 field of view was achieved by performing three vertically overlapping scans per X-CT acquisition. This ensured that the full length of the sample could be captured within the X-CT volume. The analysis of the fibre/lumen area has been done using Avizo.

2.3.1 Materials and sample preparation

As commented earlier, the best sample shape is cylindrical, but it also requires that the mounting material has a different enough density from the fibres analysed [10], so this can be successfully distinguished from the CT-scan data. Consideration of sample length is relevant too, since there is a time limit for scanning and also only as much that can be scanned at once. The aim was to scan two different fibres for the longest length possible. For this to be done, each fibre was cut into 2 cm length pieces, and stuck in order of cutting one after each other onto the transparent tape, as shown in

Fig. 2.3. So, two fibres with a total length of 11 and 13 cm were cut into 2 cm pieces, then stuck on the transparent adhesive tape in a known order. Three overlapped scans of 7 mm high covered the full length of all pieces.

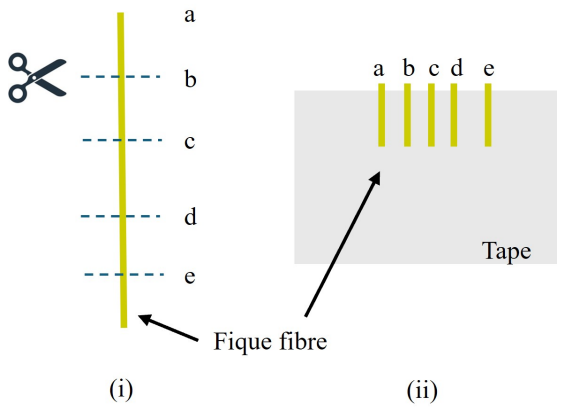


Figure 2.3: X-ray CT-scan preparation diagram with (i) showing a fibre being cut into smaller pieces, and (ii) showing how these pieces are stuck to the transparent tape consecutively.

To show the scale of the sample, in Fig. 2.4 a first sample test shows the rolled transparent tape with fibres as long as the width of the tape, stuck inside it next to a marker. The final sample looked like that with fibres cut into pieces, as described earlier.



Figure 2.4: The rolled preliminary sample next to a Sharpie pen for scale.

2.3.2 CT-scan analysis

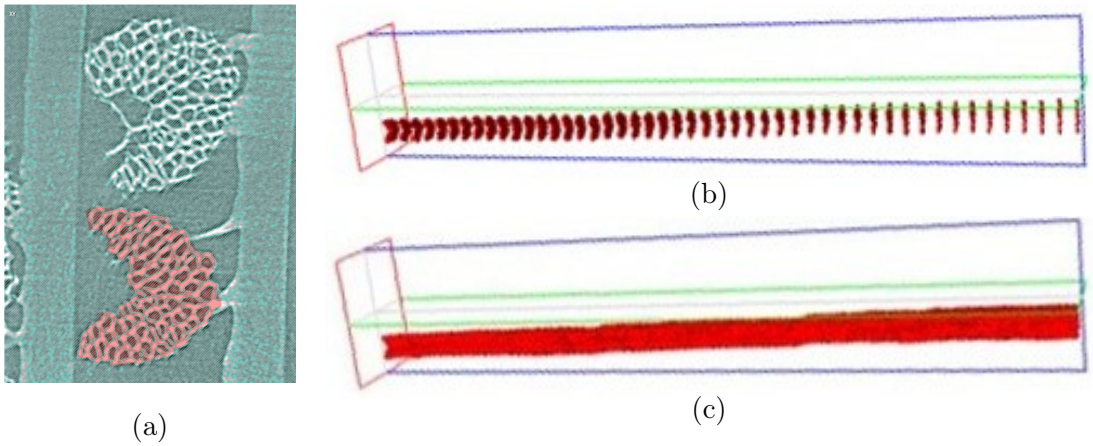
Here, the software used is Avizo. The data is input in Avizo, where the resolution information is required when loading the data set. The data set can be cropped, to allow for faster computation if, for example, the analysis consists on measuring over individual fibres, these can be cropped separately. Segmentation can be done in many

different ways in Avizo, but thresholding is one of the most common tools used, which shows the distribution of pixels intensity as an histogram. The thresholding tool is then used to select what is displayed and what is filtered.

The CT-scan data was worked on by the CT-scan facility at University of Southampton before being shared. This work meant changing the files from 16 bit to 8 bit; cropped the overlap of each scan; scaled the histogram to match with each image; image concatenation; the outside of the image was cropped, so only the fibres are in the field of view (FOV); the contrast was enhanced using a pixel saturation of 0.3%; lastly the histogram was redistributed to use all the greyscale values (from 0 to 255). As explained earlier in Section 2.2, these greyscale values are associated with the density of the materials within the object of study. The brighter the higher the density. In the case worked here, the different fibre bits are cropped individually to ease the computation requirements and analysed independently. Because the density of the natural fibre is very close to the tape's density, a first thresholding is made and then a manual selection of the fibre area is done. This is done every 50 slices, and later interpolated to get the whole piece in 3D on its own for the approximately 4000 sections in total, as shown in Fig. 2.5. After interpolation, every slice is revised to see that the selection is good, and corrected if required, which only happens if the fibre was not straight at some point, which is rare. Once the fibre is selected, the final thresholding is done. In this case, the threshold is applied at 140 in the 0-255 scale. This means that only pixels in the 140 threshold are selected from the previously selected area, corresponding to the fibre walls. Finding this value was done through trial and error, using other values and comparing how well it would fit the walls selection. Knowing the total area as selected in the first step and the area corresponding to the fibre walls, the porosity of the fibres can then be calculated with a subtraction per slice, as shown in Eq. (2.1), and the percentage later calculated of what corresponds to the lumen area over the total area of the cross-section, Eq. (2.2), with data exported into a .csv file. Added to this, the area variation along the fibre can also be measured. This is done per slice, and the porosity is presented as an average values from all the slices measured.

$$\text{Lumen area} = \text{Total area - Fibre walls area} \tag{2.1}$$

$$\text{Porosity (\%)} = \text{Lumen area / Total area} \tag{2.2}$$



(a) (b) (c)

Figure 2.5: (a) Showing how the area of the fibre is selected, (b) selection of every 100 slices, (c) interpolation along the 100 slices to have the fibre reconstructed.

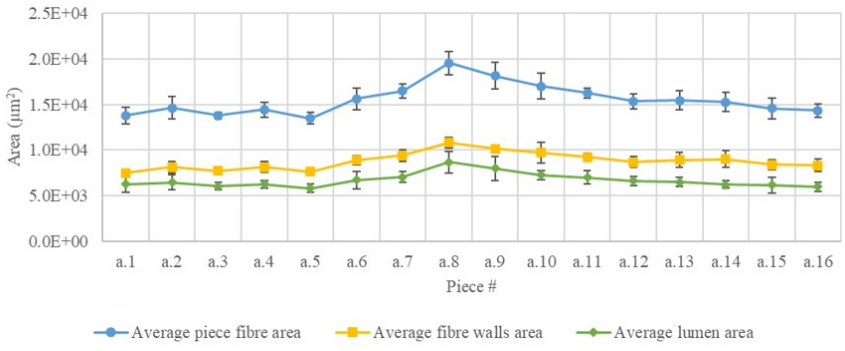
2.4 Results

Results from the CT-scan analysis are broken down into two different subsections here, so fibre porosity is first commented, followed by fibre cross section area variation. It is worth mentioning here that the two fibres that were scanned had no visible differences at the naked eye, but they proved to have very different shape, one being more bean shape and the other one being closer to a circular cross section, proving immediately the point that at least cross section shape can vary from fibre to fibre.

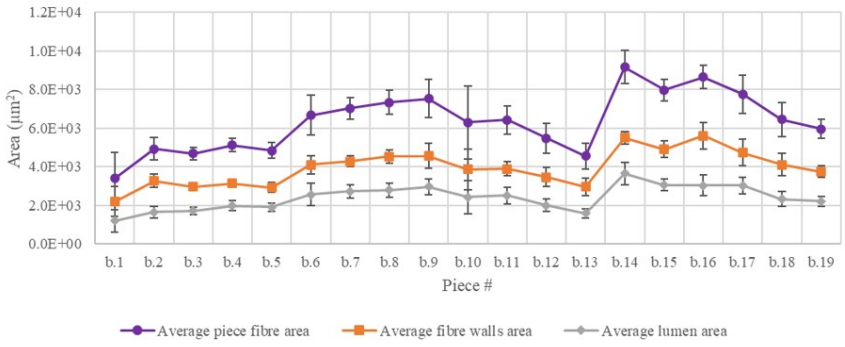
2.4.1 Fibre area variation

For each small piece, the area was calculated per section and then averaged. This averaged value is presented for each bit in Fig. 2.6 (a) and (b), where it corresponds to the mean area of each of the two fibres for the total cross-section, the fibre walls, and the lumen with error bars indicating the standard deviation for each case. The

average value for the whole cross-section of fibre a is $1.5 \times 10^4\,\mu\text{m}^2$, while for fibre b it is $6.3 \times 10^3\,\mu\text{m}^2$, showing a significant area difference. The averaged wall area values are $8.8 \times 10^3\,\mu\text{m}^2$ and $3.9 \times 10^3\,\mu\text{m}^2$, whereas the lumen areas are $6.7 \times 10^3\,\mu\text{m}^2$ and $2.4 \times 10^3\,\mu\text{m}^2$ for fibres a and b, respectively. These values were used to calculate the porosity and, as mentioned before, correspond to approximately 40% of the total fibre area. The apparent diameters corresponding to these area values, assuming circular cross-sections, are $140.2\,\mu$m and $89.8\,\mu$m, respectively. On top of the average values given, the averaged area values for each fibre piece are shared in Table 2.1 and Table 2.2 for fibres a and b respectively, with the standard deviation showing in numbers what is shown on Fig. 2.6, where variability in area values can be seen. It is well known that fibre area changes from fibre to fibre, but with this, it shown that it can be a difference of at least one order of magnitude. What is not so well known is how much the area along the fibre can change, and that is what is presented here quantifying how the fibre area changes along the same fibre, and how walls and lumen change proportionally. Along 11 cm of fibre there is a variation of 6.2% and 12.2% in the measured area for fibres a and b respectively, while this variation is 6.6% and 11.8% for fibre's walls area, and 10.2% and 16.8% for fibre's lumen area.



(a)



(b)

Figure 2.6: (a) Area (μm^2) for fibre *a*, whole, fibre walls and lumen in blue circles, yellow squares and green diamonds respectively; (b) Same for fibre *b* in purple, orange, and grey respectively.

2.4.2 Fibre porosity

The study of the porosity shows averaged values of 43% and 37% for fibres *a* and *b* respectively, with this being calculated from the measured lumen area over the total area of the fibre and averaged over the 7 mm length of each piece of fibre, and then averaged for the whole length. For fibre *a*, the highest porosity value is 41.0%, while the highest value is 45.3%. For fibre *b* these values are 33.4% and 39.5% respectively. As commented in Section 2.2.3, a great variety of values is found in the literature for natural fibres, showcasing their variety and variability. This result, with both values being relatively close, shows that despite the difference in shape and size between both fique fibres studied here, as shown in Fig. 2.7, porosity changes proportionally to each fibre cross-section size.

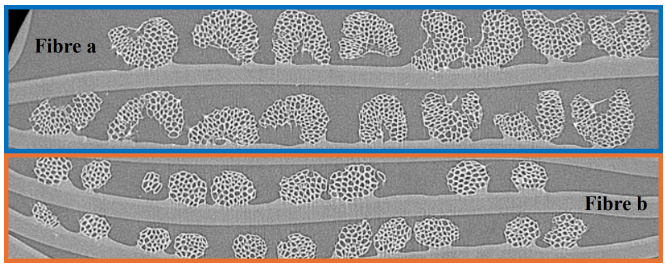
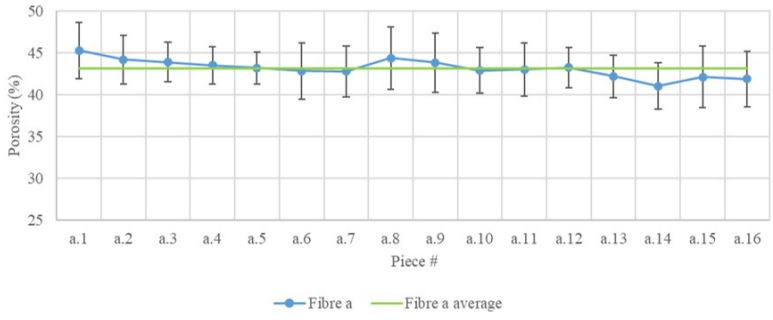
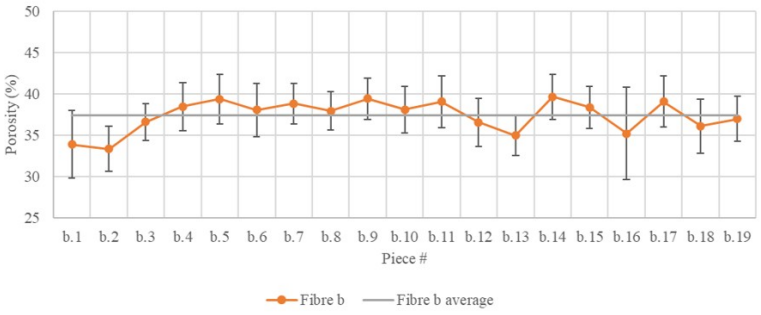


Figure 2.7: Reconstructed cross-section image of the CT-scan where both fibres *a* and *b* are shown, showcasing the shape difference, with fibre *a* presenting a kidney like shape while fibre *b* presents a more circular section.

Fig. 2.8 shows the porosity along all the 16 and 19 fibre pieces studied with the standard deviation for each piece represented on the error bars. It is worth noting how for fibre b, the porosity changes between wider limits, while being slightly lower itself. This might be explained by the lower whole area, where small changes have a higher impact.



(a)



(b)

Figure 2.8: (a) Porosity (%) for fibre *a* shown in blue circles for each piece, with the average value in a green line across; (b) Porosity (%) for fibre *b* shown in orange circles for each piece, with the average value in a grey line across.

Table 2.1: Area values for the whole fibre a and the corresponding walls and lumen with the standard deviation for each of them, as well as the final average.

Piece #	Whole fibre a (x$10^3\mu m^2$)	Standard deviation (x$10^3\mu m^2$)	Walls (x$10^3\mu m^2$)	Standard deviation (x$10^3\mu m^2$)	Lumen (x$10^3\mu m^2$)	Standard deviation (x$10^3\mu m^2$)	Porosity (%)	Standard deviation (%)
a.1	13.79	0.91	7.52	0.25	6.27	0.85	45.28	3.36
a.2	14.61	1.22	8.14	0.63	6.47	0.79	44.18	2.93
a.3	13.79	0.35	7.74	0.34	6.06	0.39	43.89	2.36
a.4	14.42	0.79	8.15	0.59	6.27	0.42	43.49	2.22
a.5	13.49	0.66	7.66	0.38	5.83	0.44	43.18	1.89
a.6	15.62	0.12	8.90	0.53	6.71	0.96	42.82	3.36
a.7	16.49	0.75	9.43	0.64	7.06	0.61	42.79	3.04
a.8	19.53	1.27	10.83	0.58	8.69	1.18	44.37	3.72
a.9	18.14	1.48	10.14	0.34	7.99	1.29	43.84	3.56
a.10	16.99	1.42	9.72	1.14	7.27	0.49	42.89	2.71
a.11	16.26	0.55	9.25	0.38	7.01	0.70	43.03	3.19
a.12	15.35	0.82	8.71	0.60	6.63	0.49	43.23	2.43
a.13	15.43	1.06	8.93	0.80	6.51	0.52	42.19	2.56
a.14	15.26	1.04	9.02	0.89	6.24	0.42	41.02	2.77
a.15	14.57	1.12	8.41	0.54	6.16	0.89	42.13	3.71
a.16	14.34	0.70	8.32	0.68	5.99	0.50	41.87	3.32
Average	15.51	0.96	8.81	0.58	6.69	0.68	43.14	2.94

Table 2.2: Area values for the whole fibre b and the corresponding walls and lumen with the standard deviation for each of them, as well as the final average.

Piece #	Whole fibre b (x$10^3\mu m^2$)	Standard deviation (x$10^3\mu m^2$)	Walls (x$10^3\mu m^2$)	Standard deviation (x$10^3\mu m^2$)	Lumen (x$10^3\mu m^2$)	Standard deviation (x$10^3\mu m^2$)	Porosity (%)	Standard deviation (%)
b.1	3.40	1.36	2.19	0.78	1.20	0.59	33.89	4.09
b.2	4.94	0.59	3.26	0.33	1.66	0.30	33.35	2.73
b.3	4.68	0.31	2.96	0.17	1.72	0.19	36.62	2.24
b.4	5.12	0.34	3.14	0.15	1.98	0.26	38.49	2.94
b.5	4.84	0.41	2.93	0.27	1.91	0.23	39.39	3.03
b.6	6.67	1.03	4.09	0.48	2.57	0.59	38.11	3.23
b.7	7.03	0.56	4.29	0.27	2.74	0.35	38.86	2.43
b.8	7.34	0.63	4.55	0.34	2.79	0.35	37.97	2.33
b.9	7.54	0.99	4.57	0.65	2.97	0.41	39.45	2.48
b.10	6.29	1.89	3.87	1.06	2.43	0.87	38.12	2.79
b.11	6.43	0.72	3.90	0.38	2.52	0.42	39.07	3.17
b.12	5.48	0.77	3.47	0.50	2.00	0.33	36.57	2.93
b.13	4.56	0.66	2.96	0.46	1.59	0.25	35.02	2.49
b.14	9.17	0.87	5.51	0.33	3.66	0.58	39.68	2.75
b.15	7.98	0.57	4.91	0.41	3.06	0.29	38.39	2.56
b.16	8.65	0.61	5.61	0.69	3.04	0.53	35.24	5.57
b.17	7.76	1.00	4.73	0.69	3.03	0.42	39.12	3.07
b.18	6.44	0.89	4.11	0.58	2.33	0.40	36.15	3.28
b.19	5.96	0.49	3.75	0.30	2.21	0.27	37.00	2.70
Average	6.33	0.77	3.94	0.46	2.39	0.40	37.39	2.99

2.5 Conclusions and future work

In this chapter, the exploration of the porosity of fique and the cross-section area variation along the fibre have been explored via a CT-scan and the corresponding image analysis using Avizo software. The porosity of the fibres has been calculated by diving the lumen area over the whole cross-section area after a thresholding step in the image analysis process, with porosity being lower than 45% for both fibres analysed. Both fibre shown here have different morphologies and different sizes, confirming what was expected on fibre to fibre variation. Quantification of fibre cross-sectional area variation along the same fibre is shows a 6.2% and 12.2% variation for fibres a and b respectively along the whole area, while this is 6.6% and 11.8% for fibre's walls area, and 10.2% and 16.8% for fibre's lumen area.

Having the opportunity to analyse via CT-scan and a more traditional method like SEM or microscopic analysis the cross-sectional area of the same fibres can bring light to how much under or overestimation is done through the different methods and allow for an accurate obtention of a correction factor when calculating the fibre area through more accessible approaches assuming a circularity that is not real, but which facilitates significantly the area calculation for further mechanical properties analysis, as will be explained in the next chapters of this thesis.

Bibliography

[1] L. Vásárhelyi, Z. Kónya, Kukovecz, and R. Vajtai, "Microcomputed tomography–based characterization of advanced materials: a review," *Materials Today Advances*, vol. 8, 12 2020. https://doi.org/10.1016/j.mtadv.2020.100084.

[2] C. H. McCollough and P. S. Rajiah, "Milestones in CT: Past, present, and future," *Radiology*, vol. 309 (1), 10 2023. https://doi.org/10.1148/radiol.230803.

[3] Y. Gao, W. Hu, S. Xin, and L. Sun, "A review of applications of ct imaging on fiber reinforced composites," *Journal of Composite Materials*, vol. 56 (1), pp. 133–164, 1 2022. https://doi.org/10.1177/00219983211050705.

[4] L. Zhuang, H. S. Shin, S. Yeom, C. N. Pham, and Y. J. Kim, "A novel method for estimating subresolution porosity from ct images and its application to homogeneity evaluation of porous media," *Scientific Reports*, vol. 12 (1), 12 2022. https://doi.org/10.1038/s41598-022-20086-x.

[5] Y. Tao, Z. Wang, and S. A. Hadigheh, "Enhancing x-ray micro-ct analysis for detecting voids and carbon fibre features in fibre-reinforced cementitious composites using advanced 3d gaussian filtering," *Measurement: Journal of the International Measurement Confederation*, vol. 249, 5 2025. https://doi.org/10.1016/j.measurement.2025.117018.

[6] A. Grießer, R. Westerteiger, E. Glatt, H. Hagen, and A. Wiegmann, "Identification and analysis of fibers in ultra-large micro-ct scans of nonwoven textiles using deep learning," *Journal of the Textile Institute*, vol. 114 (11), pp. 1647–1657, 2023. https://doi.org/10.1080/00405000.2022.2145429.

[7] G. Chiesura, G. Luyckx, E. Voet, N. Lammens, W. van Paepegem, J. Degrieck, M. Dierick, L. van Hoorebeke, P. Vanderniepen, S. Sulejmani, C. Sonnenfeld, T. Geernaert, and F. Berghmans, "A micro-computed tomography technique to study the quality of fibre optics embedded in composite materials," *Sen-*

sors (Switzerland), vol. 15 (5), pp. 10852–10871, 5 2015. https://doi.org/10.3390/s150510852.

[8] P. Hermanek and S. Carmignato, "Porosity measurements by x-ray computed tomography: Accuracy evaluation using a calibrated object," *Precision Engineering*, vol. 49, pp. 377–387, 7 2017. https://doi.org/10.1016/j.precisioneng.2017.03.007.

[9] P. Gálvez-Hernández, R. Smith, K. Gaska, M. Mavrogordato, I. Sinclair, and J. Kratz, "The effect of x-ray computed tomography scan parameters on porosity assessment of carbon fibre reinfored plastics laminates," *Journal of Composite Materials*, vol. 57 (29), pp. 4535–4548, 12 2023. https://doi.org/10.1177/00219983231209383.

[10] F. Bensadoun, M. Barburski, I. Straumit, N. L. Q. Tran, C. Fuentes, J. Zenina, O. Shishkina, G. Pyka, I. Verpoest, A. W. V. Vuure, M. Wevers, and S. V. Lomov, "Challenges of x-ray tomography technique on natural fibre-based composites," *11th European Conference on Non-Destructive Testing (ECNDT2014)*, 10 2014. www.ndt.net/?id=16510.

[11] L. Q. Tran, T. N. Minh, C. A. Fuentes, T. T. Chi, A. W. V. Vuure, and I. Verpoest, "Investigation of microstructure and tensile properties of porous natural coir fibre for use in composite materials," *Industrial Crops and Products*, vol. 65, pp. 437–445, 3 2015. https://doi.org/10.1016/j.indcrop.2014.10.064.

[12] M. Seghini, F. Touchard, F. Sarasini, D. Mellier, J. Tirillò, M. Seghini, F. Touchard, F. Sarasini, and D. Mellier, "Interfacial adhesion assessment in flax / epoxy and in flax / vinylester composites by single yarn fragmentation test : Correlation with micro-ct analysis.," *Composites Part A: Applied Science and Manufacturing, Elsevier*, vol. 113, pp. 66–75, 2018. https://doi.org/10.1016/j.compositesa.2018.07.015.

[13] M. Ayadi, C. Segovia, A. Baffoun, R. Zouari, V. Fierro, A. Celzard, S. Msahli, and N. Brosse, "Influence of anatomy, microstructure, and composition of natural

fibers on the performance of thermal insulation panels," *ACS Omega*, vol. 8 (51), pp. 48673–48688, 12 2023. https://doi.org/10.1021/acsomega.3c02481.

[14] M. A. Hidalgo-Salazar, J. P. Correa-Aguirre, A. J. Román, R. Gonzalez, R. Vera, and T. A. Osswald, "Colombian natural fibers: Potential applications in sustainable natural fiber reinforced composites materials," *Polymer Composites*, vol. 46 (6), pp. 5599–5617, 4 2025. https://doi.org/10.1002/pc.29313.

[15] University of Southampton, "Submicron resolution and versatility." https://muvis.org/equipment/zeiss-160-kvp-versa-510. Accessed: 2025-10-31.

Chapter 3

Mechanical characterisation of fique: Single fibre tensile test

3.1 Introduction

3.2 Literature review

Tensile test of single fibres is the most obvious way of testing the mechanical properties of a material. Consisting on pulling from the fibre ends until it breaks, will give the Young's modulus and tensile strength of the fibre as the most important outcomes. These properties are essential in being able to understand materials behaviour and to predict the properties of the final material where they are use. The fibre's mechanical properties directly affect composite materials mechanical properties which are one of the key parameters in design and analysis of structures. A good understanding of this properties is paramount if natural fibres are to be used as reinforcement for composite materials, and finding the appropriate applications is directly linked to their mechanical performance.

3.2.1 Single fibre tensile test

Single fibre tensile test was previously covered by D3379 Standard test method [1], which was aimed for high-modulus ($> 21 \times 10^9$ Pa) single filament materials. This

standard was withdrawn in the 1998. There are two more standards under which the single fibre tensile test falls. The D3822 [2] covers the characterisation for textile fibres, either synthetic or natural. The C1557 [3] is the successor of the D3379 and covers the tensile characterisation of single fibre, either obtained from a fibre bundle or a spool. Advanced ceramic, glass, carbon, and other fibres are covered by this test standard, applied to single fibres for engineering applications, being the one applied in this work of fique tensile characterisation.

The tensile test of single fibres consists on attaching the fibre to a card tab which is loaded in the direction of the fibre until fracture of the fibre occurs. The fibre is attached on its ends via cement, wax, or as in this case, double sided tape to keep it in place and avoid twisting of the fibre. The card tab is cut before the test is started, when load is applied at the defined speed rate. Both direct and indirect strain measurement techniques are contemplated in the standard, although because of ease of use indirect strain measurement is most commonly used. This is single tensile test, which works well when covering synthetic fibres, but when it comes to natural fibres single fibres as such are not easy to obtain and handle, so the concept of single technical fibres is introduced. Technical fibres consist of a composite structure of many elementary fibres assembled together [4], but can be considered the smaller unit for measurement of mechanical properties when it comes to natural fibres.

3.2.1.1 Indirect strain measurement of single fibres

According to the standard used in this work, the compliance of the system is defined as "the contribution by the load train system and specimen-gripping system to the indicated cross-head displacement". This means that the displacement measured by the equipment does not account just for the fibre elongation. The elongation attributed to the fibre is calculated by subtracting the elongation attributed to the system compliance from the total cross-head displacement [3]. The recorded cross-head displacement is:

$$\Delta L = \Delta l + C_s F \tag{3.1}$$

where

ΔL = recorded cross-head displacement, m,

C_s = system compliance, m/N, and

Δl = elongation of the specimen gauge length, m.

Calculating the strain of the fibre is as follows:

$$\epsilon = \frac{\Delta l}{l_0} \tag{3.2}$$

where

l_0 = fibre gauge length

Using the definition of strain and the linear relationship with stress and Young's modulus of the fibre, it can be written:

$$\epsilon = \frac{\sigma}{E} = \frac{F}{EA} = \frac{\Delta l}{l_0} \tag{3.3}$$

Combining Eq. (3.1) and Eq. (3.3) a linear relationship for the force and cross-head displacement with the Young's modulus of the fibre and the compliance of the system is obtained:

$$\frac{\Delta L}{F} = \frac{\Delta l}{F} + C_s = \frac{l_0}{EA} + C_s \tag{3.4}$$

Assimilating that to a linear relationship, if plotting the cross-head displacement over the force against the initial gauge length over the area for at least three different gauge lengths, the inverse of the linear slope is the Young's modulus E and the cut with the axis is the system compliance C_s, as shown in Fig. 3.1, adapted from [3].

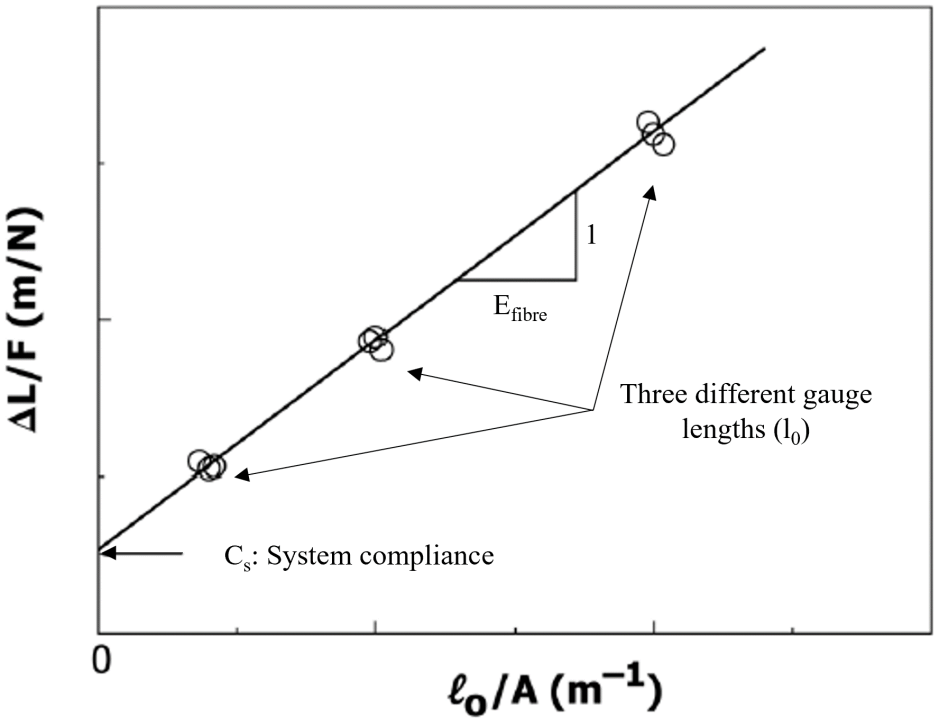


Figure 3.1: Calculation of the fiber's Young's Modulus adapted from the standard ASTM-C1557-20 2021 [3] to highlight the requirement of at least three different gauge lengths.

3.2.1.2 Indirect strain measurement of single fibres: natural and synthetic

Many studies have been done using indirect strain measurement for calculating single fibre's mechanical properties, both synthetic and natural.

Tomczak *et al.* [5] study the morphology and properties of curauá fibres in a very detailed work where the effect of diameter, test gauge length and strain at rate is presented, with 50 fibres tested for each of these parameters. Fibres of 26 and 64 μm diameter are used, showing that a diameter increase decreases the tensile strength value from 310 to 87 MPa, while Young's modulus decreases from 96.1 to 34 GPa, with no significant change in the strain at failure, it being 4.40 and 4.94% respectively. Increasing the gauge length lead to a decrease in both, the tensile strength from 223 to 173 MPa, and the strain at failure from 10.2 to 3.74%, while the Young's modulus increased from 26.6 to 51.8 GPa. The effect of increasing the strain rate from 5 to 50

mm/min does not affect the Young's modulus or the strain at failure, with values of 48.7 GPa and 4.57-4.49%, respectively, while tensile strength increases from 178 to 217 MPa.

One of the challenges to overcome when calculating the tensile strength of any natural fibre is their natural changing cross section area, as has been explored in Chapter 2. Applying to these natural fibres the conventional method of using an apparent diameter to calculate the area of the fibre by assuming its circularity in contrast with cross section area measurement, is explored in the work of Hu *et al.* [6]. Although ASTM D-3822-01 [2] was first designed for natural and man-made fibres stating that area of these is to be calculated with an integrated device or a planimeter, it is likely that technical difficulties lead to adopt assumption of circularity, which is closer to reality for the case of synthetic than for natural fibres. Three types of flax fibres: bast flax, flax retted by enzyme, and flax retted by water were tested. The most traditional approach of circularity assumption and direct cross section area observation via Scanning Electron Microscopy (SEM) approaches for area calculation are used, and mechanical properties results compared on the basis of the different area approach used. The method variation also includes a fibre selection for testing based on apparent defects visible under an optical microscope as well as contaminated fibres removal from the testing. A number of 20 fibres per type of fibre are tested, with 50 mm gauge length at cross head speed of 120 mm/min. Two apparent diameters are used for the area calculation assuming circularity: the first one is the average of the apparent diameter at five random locations (a); the second one is to measure the smallest apparent diameter along the fibre (b). For the direct cross section area measurement, this is taken at failure location (c), as fracture is considered brittle without great impact on fibre's area variation around that location. Tensile strength values for bast flax by using (a), (b), and (c) area calculation approaches are 205 ± 87 MPa, 339 ± 240 MPa, and 400.6 ± 40.8 MPa respectively. For enzyme retted flax 591 ± 249 MPa, 688 ± 225 MPa, and 456.5 ± 33.9 respectively. And for water retted flax 701 ± 224 MPa, 775 ± 186 MPa, and 354.4 ± 25.4 MPa respectively. Tensile modulus and strain at fracture for all these cases are presented in Table 3.1, with the main conclusion of this work being fibre selection and direct area

measurement of the fibre's cross section increases accuracy of mechanical properties characterisation, with the need to increase the number of samples used for this case, as in contrast with the traditional approach of apparent diameter.

Defoirdt *et al.* [7] made a study on coir (white and brown), bamboo and jute and their tensile characterisation. The method used is a non-direct strain measurement. Compliance and slippage are put together here and calculated as proportional to the applied force as a factor α. This is used to correct the strain and the tensile modulus, which are determined by drawing the stress vs. corrected strain curve. Corrected Young's modulus is determined from the extrapolated Young's modulus for an infinitely long test length, as for this infinite gauge length the displacement that comes from compliance and slippage can be ignored. This compliance and slippage factor would be constant for all measured test lengths for the same plant fibre, but this is not the case and a correction factor is plotted for each test for the same fibre and then a linear regression applied. The area of the different fibre types is calculated by means of the density method, giving a unique area value per fibre type. Tensile strength is reported here with two values plus their standard deviation, as the weakest and strongest test length as can be see in Table 3.1. Tensile strength decreases as the test length of the fibre increases for all the fibre types. This is attributed to the size effect, by which the larger the sample size the higher the number of flaws, which is also calculated as a matter of defect density, as the slope of the plot of the tensile strength vs. the test length, drawing the conclusion that steam explosion extraction of the bamboo fibres is more damaging than the mechanical extraction of white coir. As for the tensile modulus, the one extrapolated for infinitely long fibres corrected and uncorrected by the α factor accounting for compliance and slippage are presented, as reported in Table 3.1 later in this section. Corrected values for white and brown coir are 3.44 GPa and 4.94 GPa, while for bamboo and jute are 33.37 GPa and 26.25 GPa respectively. Tensile modulus characterisation main conclusion is that gauge length affects the measured modulus, with impact of the set up and slippage being higher the shorter the fibre.

In their work, Fidelis *et al.* [8] study the tensile behaviour of jute, sisal, curaua, coir and piassava fibres. The indirect strain method is applied, with the compliance of the

system calculated by testing six gauge lengths of sisal fibres, 10, 20, 30, 40, 50, and 60 mm while for the other fibres a gauge length of 40 mm was used. For all cases a 0.2 mm/min displacement rate is maintained and 15 fibres were tested for every gauge length. In this study, cross-sectional area is measured for each fibre. Young's moduli reported here are 63.7 ± 32.5 GPa for curaua, 43.9 ± 12.3 GPa for jute, 2.6 ± 0.7 GPa for coir, 3.8 ± 0.9 GPa for piassava, and 19.5 ± 4.5 GPa for sisal. Tensile strength in MPa is 543 ± 260, 249 ± 89, 90 ± 35, 131 ± 36, and 484 ± 135 respectively, also presented in Table 3.1. In this work, the fibres analysed are classified into two distinct groups. Curaua, sisal and jute are allocated to high performing fibres presenting Young's moduli higher than 19 GPa as well as tensile strengths above 249 MPa, while coir and piassava are deemed low performance fibres. Interestingly, sisal, coir and piassava presented a non linear region in their stress-strain curve, and in here it is deemed to be due to a degradation mechanism by which the weak primary cell walls collapse and delamination of fibre cells during the loading process.

When it comes to tensile characterisation of single fibres, and as commented before, when using an indirect strain measurement, the compliance of the system, which contributes to this measured strain is one of the things to consider. The question if this compliance is constant is not new, and different works have looked into this, in order to quantify this compliance and its impact on the mechanical properties to be measured via single fibre tensile test.

Jiang *et al.* [9] studied the compliance of two different testing equipment for the characterisation of carbon nanotube fibres. In doing this, the fibres were attached by means of cyanoacrylate glue (commonly known as instant glue) to a 210 g m^{-2} photo paper. From the two sets of equipment used, the main difference is the gripping systems, one pneumatic and another one with split-shim grips. The former is thought to cause the larger system compliance, while the latter set up shows a smaller system compliance. The effect of system compliance increases with the decrease of the gauge length, normally leading to over estimation of tensile strain. The recommendation is that for testing machines with large system compliance, fibre gauge length should be larger than 50 mm, and definitely longer than 10 mm, as shorter fibres could lead to

high strength values based on reduced number of defects in such fibres.

3.2.1.3 Direct strain measurement of single fibres: natural and synthetic

The standard C1557 also considers the case for which optical flags can be attached to the fibre, and the actual elongation of the fibre directly tracked. If the displacement of the optical flags is monitored, the stress-strain curve can be obtained for each fibre with the recorded force and the known area of each fibre, allowing for a direct calculation of the Young's modulus from the slope of the linear part of the curve.

Tensile test of single fibres has already a long sample preparation time, but the attachment of optical flags can make the sample preparation more complicated, and being not possible for small diameter fibres ($d < 5 \cdot 10^{-6}$m) [3].

Back in 1974, Moore and Lepper [10] described two methods to calculate the Young's modulus of Kevlar-49-II® strands impregnated in epoxy resin. The method named A in their work is a direct strain measurement method using a extensometer which consists of two linearly variable differential transformers (LVDT). These are connected to glass beads attached to the fibre. The voltage difference with increasing elongation is translated into displacement, after appropriate calibration. Known increments of displacement are made, and the elongation obtained. The method called B in their work, which uses a least squares analysis, is an indirect strain measurement with several gauge lengths and at a 12.7 mm/min cross-head speed rate. The tensile modulus obtained by these two methods, 138.52 and 144.52 GPa respectively, was compared to the value provided by a different study, 137.69 GPa. Averaged values of tensile modulus obtained by both methods differ by less than 5%, showing a very good agreement in tensile modulus between both methods, agreeing with the results obtained by the prior study taken as reference.

Depuydt *et al.* [11] calculate the tensile modulus of bamboo and flax fibres using also both, indirect and direct strain measurement methods. In order to prove the accuracy of the methods steel fibres, with known Young's modulus, were used as reference for both techniques. Measuring strain directly on the fibres required optical flags to be attached. These optical flags were approximately 3 mm in diameter and a black speckle pattern

was applied by spraying black paint on top of the white surface of the flags. Tests were recorded with a digital camera so tracking of the flags was possible in order to obtain the displacement of them, assimilated to be the same as the points of the fibres to where they were attached. Processing of the images was done with a correlation software to determine the fibre's strain from the relative pixels displacement. The area of the fibres was calculated by the density method, based on Eq. (3.5), which requires length, mass and density of the fibres considered to be measured. This is an average area value use for each type of fibre, i.e., steel, flax, and bamboo.

$$A = \frac{m}{\rho l} \tag{3.5}$$

where A is the average area of the fibres; m is the mass as measured by an analytical balance; ρ is the density, determined by a gas pycnometer; and l is the known length to which the fibres were cut. Four different fibre lengths, 10 mm, 20 mm, 35 mm and 50 mm, were used to test the robustness of the indirect strain measurement method with the steel fibres, while only 50 mm fibre lengths were used when applying the direct strain measurement method to the different fibres. Cross-head displacement for all cases was set to 1.5 mm/min. Results show that direct strain measurement of steel fibres is less biassed than the indirect strain measurement method. Direct strain measurement gives a Young's modulus for steel of 187 ± 12 GPa. While the three different approaches used based on the indirect strain measurement give 147 ± 4 GPa, 140 ± 2 GPa, and 150 ± 4 GPa. The actual Young's modulus is 193 GPa. Direct strain measurement method gives a value for bamboo Young's modulus of 51.8 ± 6.8 GPa, with 24 fibres tested, higher than values found in the literature. Flax fibres Young's modulus calculated by this method is in agreement with those found in the literature, 40 ± 11 GPa with 18 fibres tested. The conclusion of this work was that the measured Young's modulus from the indirect strain measurement method was 25% less than using the direct strain measurement method, arguing the inaccuracy of the assumption of a constant system compliance.

Huether *et al.* [12] developed a direct strain measurement technique for single glass

fibres, by developing a single fibre tensile testing device (SiFiT). In this device the fibre does not need to be mounted onto a card/paper tab, it is directly clamped to the device by rubber-coated aluminium parallel grippers and kept aligned by employing a Venturi nozzle. The Venturi nozzle sits in the lower gripper. The Venturi nozzle creates a local deinflation that keeps the fibre aligned without the need of touching it. The upper gripper has an angle that allows the fibre to be aligned with the help of tweezers. Polymeric fluorescent beads are manually attached to the glass fibres. This material goes into spherical shape due to the surface tension when in contact with the fibre, and is later exposed to ultraviolet light. Beads size is between 120 and 500 μm, so it is big enough to be tracked but not too big to impact the stiffness of the fibre. More than one bead applied to each fibre from both ends, leaving at least a 50 mm length free of beads with a gripping length of 80 mm. As opposed to other tensile test characterisation methods were the fibre is loaded until breakage occurs, in this work a stepwise in 0.04 N intervals testing method is applied, in order to allow time for high resolution and long exposure time pictures to be taken. Diameter determination is done after the test is completed in a Scanning Electron Microscope (SEM), with 15 measurements of the apparent diameter of each fibre with different micrographs and different positions per fibre. This method is compared with ASTM D3379 standard procedure, with five different lengths up to 50 mm and with the diameter measurement being done by the density method as explained before. For the direct strain measurement method 6 fibres are tested, while for the application of the standard 250, 50 fibres per each length (20, 30, 35, 40 and 50 mm), were tested. An average Young's modulus value of 82.6 GPa for the first case, as opposed to 91.47 GPa for the second case.

Adusumalli *et al.* [13] uses what is called in this work the paper frame technique to make the tensile characterisation of different types of fibres. This choice of technique comes down to have the same approach to keep consistency due to the different nature of the fibres, being these natural fibres as flax (cellulose based), hair (protein based) and synthetic fibres as Kevlar and glass. Other man-made cellulose fibres as lyocell and viscose are also tested along with pulp. Rubber jaws are used for gripping in this case. Tensile tests are carried out until failure at a cross-head displacement rate of 1mm/min.

A number of 50 fibres per fibre type where tested. Tensile strength, failure strains and Young's modulus are calculated, from the maximum value in the stress-strain curve the first two, and from the initial linear section, 1-2% strain, of the same plot the latter. From this, tensile modulus of Kevlar is between 65 and 90 GPa, while glass' has a value of 70 GPa. Strain to failure is less than 4% in both cases, confirming their brittle nature. Young's modulus of hair, the only protein based fibre in this study, is 2-4 GPa with a failure strain of 40-50%. Both, lyocell and viscose show elastic and plastic regions in their stress-strain plots, with a tensile modulus of 20-25 and 8-12 GPa respectively, with tensile strain of 6-7% and 15-20% also respectively. Pulp fibres show a tensile modulus of 3-6 GPa and a strain at fracture of 4-8%. Lastly, flax is found to have a Young's modulus of 28-40 GPa with a strain at fracture of 1.4%. Of all these fibres, Kevlar has highest tensile strength, 2800-3000 MPa, with glass, 2900 MPa, followed by flax, 500-900 MPa; Lyocell, 420-520 MPa; viscose, 400-420 MPa; and hair and pulp, both in the 200-350 MPa range.

3.2.1.4 Fique characterisation: work done on fique

Gañán and Mondragón [14] use fique bundles with surface modified treatments to reinforce a polyester resin when studying the potential of fique as matrix reinforcement. In this study, fique fibre is characterised previously to the composite manufacturing, untreated and with different surface modifications. An Instron machine with pneumatic clamps and a 10 N load cell is used here, at a 5mm/min deformation rate. Fibres are 50 mm length, and 30 fibres were tested per each surface treatment. The area of the fibres is assumed as circular for simplicity, estimated from a measurement of the transverse diameter made using an optical microscope. For untreated fibres the reported tensile strength and elastic modulus are 200 MPa and 8-10 GPa respectively. Fibre diameter values are reported between 80 and 200 μm.

Delvasto *et al.* [15] use fique fibre to reinforced Portland cement for the production of roof sheets, as opposed to asbestos reinforced cement. In their work, the properties and microstructure of fique fibre are discussed, although the experimental details are not described. Despite this lack of detail, this is one of the reference works when it

comes to fique properties, and because of that it is included here. The area of the fibre is calculated through the density approach, and an equivalent diameter is calculated. This equivalent diameter is the one the fibre would have if its cross-section was circular, and it is between 0.16 and 0.42 mm. The main components of fique fibre are presented as cellulose, on a 70%, and lignin, on a 10.1%. Mechanical properties of the fibre are presented, with a tensile strength between 43 and 571 MPa, with an average value of 132.4 MPa and a coefficient of variation of 40%. Strain at break is 9.8% and the tensile modulus has a range of 8.2-9.1 GPa. This great coefficient of variation in the tensile strength is attributed to the lack of consistency in the fibre geometry and fibre diameter, which vary from fibre to fibre and along the same fibre as discussed Chapter 2. This is justified here as the change needed according to the physical requirements of the fibres along the length of the leaf to sustain its weight.

Hoyos *et al.* [16] study the impact of alkali treatment on the mechanical and chemical characteristics of fique after 4 and 24 hour treatments. As part of this work, characterisation of fique not subjected to any treatment is also made following ASTM 3379-75 recommendations. This study reports the use of 20 fibres of 30 mm each, tested at 2 mm/min loading rate. Area of the fibres is assumed to be calculated following circular cross section assumption since the average diameter is reported to be 0.20 $\pm$ 0.04 mm. Tensile strength is reported to be 197 $\pm$ 65 MPa, while Young's modulus is 5.7 $\pm$ 1.8 GPa.

Muñoz-Vélez *et al.* [17] made a study of surface modification of fique fibres, and as part of it the characterisation of fique without treatment is done. A study on the cross-sectional area of the fibres is made, and the assumption of circularity of them leads to the calculation of an apparent diameter. The value obtained for the area is 0.036 $\pm$ 0.016 mm^2, and with the assumption of circularity the equivalent apparent diameter is calculated as 0.209 $\pm$ 0.050 mm. Regarding the mechanical properties, tensile strength is reported as 263.55 MPa, while Young's modulus is reported as 8.64 GPa for 50 mm test length. Mechanical tests are run on an Instron 3366, with a 100 N cell at a strain rate of 10% test length/min. A number of 15 fibres split among 5 fibre lengths (50, 25.40, 19.05, 12.70, and 6.35 mm) are tested.

Luna *et al.* [18] use fique to study how dry etching plasma treatment modifies the surface of the fibres and the tensile strength. They also apply the measurement technique to not treated fibres to understand such possible change in properties. In this case fibres are obtained from fabrics obtained in the local market, and individual fibres are cut to 100 mm length based on the space available for the plasma treatment. Tensile tests were carried out using an indirect strain measurement method with a paper tab, at 1.5 mm/min loading rate, so fibre failure would occur under 30 s. Tensile strength is calculated by using the failure load for each fibre over the area. The cross-sectional area for each fibre is obtained by using micrographs at the fracture planes after the test has been carried out. Tensile strength is calculated as an average from at least 5 specimens per treatment case, including untreated fibres. Tensile strength does not suffer alterations after the treatments, although surface roughness is increased suggesting a potential improvement in bonding mechanisms when fique is used in composites. The average value for tensile strength for untreated fique in this study is 80 MPa and average cross-sectional area values are not reported.

Souza *et al.* [19] use fique fibres to produce cellulose nanofibres for membrane manufacturing. Raw fique fibres are chemically treated before being ground via mechanical means. As part of this study, the fique fibres were mechanically characterised by applying the ASTM D3822. The distance between grips used here is 25 mm, at a 60 mm/min loading rate with a load of 1000 N. Measurement in five points of the diameter suggests that assumption of circularity is made in this case, but number of fibres is not reported. The tensile strength obtained in this study is is 320 $\pm$ 59 MPa.

As part of Low-Density Polyethylene (LDPE)-Al/Fique composite characterisation [20], a report on fique mechanical properties determined according to standard test method for tensile properties of single textile fibres (ASTM D3822-07) is done. Besides that no many details on cross-sectional area calculation, load cell use or cross-head speed are given. Maximum tensile strength is reported as 336.12 MPa and a tensile modulus of 5.44 GPa along with a 9.3% strain at failure are reported as part of the preliminary characterisation before going into the composites characterisation which is the main focus of this piece of research.

Gómez *et al.* [21] study the use of fique alongside with coir fibre for acoustic applications as building materials. Chemical composition as well as mechanical properties are calculated. Tensile tests are carried out in an Instron 5582 with a 50 N load cell, at a cross head speed of 5 mm/min. A number of 40 fibres with a 50 mm gauge length were tested for each type of fibre. It is acknowledge here that fique cross-sectional area is highly eccentric elliptical or ribbon-shaped, in contrast with the circular outline of coir fibre. Fibre's diameter is measured from microscopic images of the longitudinal section, and the density of the fibres is obtained by the gas displacement method. Despite this, if or how the cross-sectional area of the fibres is calculated is not specified. Chemical composition of fique fibre according to this study is 58% cellulose, 15% hemicellulose, 7%, while for coir is 47%, 8% and 33% respectively. Mechanical properties of fique are obtained, with tensile strength being 195 MPa while the elastic modulus is 4 GPa. For coir these values are 121 MPa and 2 GPa.

Bastidas *et al.* [22] study the chemical, structural and mechanical characterisation of chemically treated fique fibre, and as part of this the raw fibre is also studied. Mechanical characterisation is done via Dynamic Mechanical Analysis (DMA), with a 17.5 mm fibre. The value of the storage modulus is an average of three measurements for each sample, with this value being 24.31 GPa. The area used in this case appears to be calculated from an apparent diameter taken from the literature as 170 μm.

In the work by Muñoz Blandón [23] a mechanical characterisation of fique is done through tensile testing of 25 fibres of 50 mm gauge length with a 15 N load cell at a speed range of 0.01 to 40 mm/min. Area of the fibres is calculated from measurement of the apparent diameter and assumption of circularity of the cross-section. Apparent diameter values were obtained between 133 and 365 μm, with an average value of 235.05 μm. From the tensile test, values for tensile strength, Young's modulus, and elongation were calculated at 355.07 MPa, 11.54 GPa, and 8.7% respectively. A standard deviation of 15% for the elongation and up to 37% for the Young's modulus shows the inherent variability of the natural fibres and fique in particular. In this case, the statistical study shows that for the tensile strength and the Young's modulus the values obtained are closed to the mean, giving a standard distribution curve, while this is not the

case for the elongation, which presents asymmetry towards the lower values from the average. As part of this, a statistically significant relationship was found between the tensile strength and the Young's modulus with the fibre diameter, this being inversely proportional, showing that the smaller the fibre diameter the higher the values of the two mechanical properties.

Guzmán-López *et al.* [24] study the physical and mechanical properties of fique as part of exploring the use of fique in industrial processes as part of composites manufacturing. As part of this, the geometry of the fibres is studied in four to six fibres from 500 to 1000 mm of length by the measurement of the apparent diameter at both ends of the fibre and at midpoint, leading to average and minimum values, later used for the calculation of the mechanical properties. Diameter values range from 20.9 to 276 μm, with the fibre area calculated assuming circular cross-section. Tensile testing is done in a electromechanical machine of 10 kN load cell, at a speed of 3 mm/min. Two values of tensile strength and Young's modulus are calculated per sample batch, based on averaged and minimum area values, leading to average and maximum values. Tensile strength average values are between 72.02 and 208.13 MPa, while maximum values are within 79.25 and 233.57 MPa. For the Young's modulus average values are between 5.1 and 8.4 GPa, with maximum values between 5.3 and 10.3 GPa. Elongation ranges from 1.15 to 1.47%. With these results, the authors proposed a value of 70 MPa for tensile strength of fique and highlights how for all cases values of deformation below 1.5% are achieved.

To the best of the author knowledge, no work of direct strain measurement has been done on fique fibre.

While natural fibre variability is acknowledge in every study, the number of fibres tested do not always aim to showcase a full representation of this variability and how it can happen not only across different fibres, but along the same fibre depending on where apparent diameters are measured. It is deemed relevant to use the same number of fibres, and when possible the same fibres, when applying both methods of area calculation, so standard deviations can be somehow comparable. With the natural variation found in the fibres, having significantly different test numbers can lead to

great standard deviation differences giving the false understanding that lower numbers mean more accuracy because of lower standard deviation, when what it can mean is a misrepresentation.

Table 3.1: characterisation of fibres from different studies; ms: measured, cr: corrected

Fibre type	Method used			Area approach			Experimental characteristics				Mechanical properties			
	Indirect strain measurement	Direct strain measurement	Other	Apparent diameter (μm)	Cross section area ($\times 10^3 \mu m^2$)	Density (kg/m^3)	Number of fibres/ gauge length	Gauge length (mm)	Speed rate (mm/min)	Load cell (N)	Tensile strength (MPa)	Tensile modulus (GPa)	Strain at failure (%)	Reference
Kevlar-49-III		x				x	3					138.52		[10]
Kevlar-49-III	x					x	4,5, 4,5, 3,5, 5,5	76.2,101.6, 127,152.4, 177.8,203.2, 228.6,254	12.7			144.52		
Sisal	x				x			10,20,30, 40,50,60			484±135	19.5±4.5		
Jute	x				x			40			249±89	43.9±12.3		
Curaua	x				x		15	40	0.2		543±260	63.7±32.5		[8]
Coir	x				x			40			90±35	2.6±0.7		
Piassava	x				x			40			131±36	3.8±0.9		
Bamboo		x				x	24	50				51.8±6.8		
Flax		x				x	18	50	1.5			40±11		[11]
Steel		x				x	22	50				187±12		
Steel	x					x	17,20, 20,22	10–50				147±4; 140±2; 150±4		
Flax											500–900	28–40	1.4	
Hair											200–350	2–4	40–50	
Viscose											400–420	8–12	15–20	
Lyocell			Hybrid				50		1	50	420–520	20–25	6–7	[13]
Kevlar											2800–3000	65–90	1.5–3.5	
E-Glass											2900	70	3.4	
Pulp											200–350	3–6	4–8	
Glass		x		x			6	50				82.6		[12]
Glass	x					x	50	20,30, 35,40, 50				91.47		
Flax (bast)	x			x (5 random locations + smallest diam.)			20				205±87 339±240	48±29 78±32	1.71±0.94	
Flax (bast)	x				x		6	50	120		400.6±40.8	48.2±4.9	1.32±0.84	[6]
Flax (enzyme retted)	x			x (5 random + smallest diam.)			20				591±249 688±225	57±22 61±18	1.43±0.90	

Fibre type	Method used			Area approach			Experimental characteristics				Mechanical properties			
	Indirect strain measurement	Direct strain measurement	Other	Apparent diameter (μm)	Cross section area ($\times 10^3 \mu m^2$)	Density (kg/m^3)	Number of fibres/ gauge length	Gauge length (mm)	Speed rate (mm/min)	Load cell (N)	Tensile strength (MPa)	Tensile modulus (GPa)	Strain at failure (%)	Reference
Flax (enzyme retted)	x				x		6				456.5±33.9	57.1±7.2	1.35±0.68	
Flax (water retted)	x			x (5 random + smallest diam.)			20				701±224 775±186	54±23 56±15	1.75±1.94	
Flax (water retted)	x				x		6				354.4±25.4	57.1±7.2	1.08±0.92	
Coir (white/brown)	x				x	20–55	5–35	5	200		162±32– 192±37 / 186±55– 343±36	3.39 (ms) 3.44 (cr)/ 4.16 (ms) 4.94 (cr)	26.1±5.6– 42.4±14 / 24.5±6.8– 59.0±5.0	[7]
Bamboo	x				x	10–15	5–35	1	200		639±175– 813±94	33.87 (ms) 33.37 (cr)	2.0±0.6– 2.9±0.7	
Jute	x				x	10–15	5–35	0.1	5		307±84– 399±100	24.70 (ms) 26.25 (cr)	1.4±0.2– 1.6±0.3	
Fique	x			Φ=50–200		x	30	50	5	10	200	8–12	4–6	[14]
Fique	x			x Φ=160–420 (236 avg)		723					43–571 (132 avg)	8.2–9.1	9.8	[15]
Fique	x			x Φ=200			20	30	2		197±65	5.7±1.88		[16]
Fique	x			x Φ=209±50	(36±16)	1102	15	50,25.4,19.1, 12.7,6.35	10% test length/min	100	263.55–410	8.64–2.9	4.8–23	[17]
Fique	x				x		5	100	1.5		80			[18]
Fique	x			x				25	60	1000	320±59			[19]
Fique	x			x Φ=210±50		1100		25.4			336.12±27.9 (max)	5.44±0.45	9.3±0.7	[20]
Fique	x			Φ=236.0±63.0		720	40	50	5	50	194.8±165.1	4.0±3.3		[21]
Coir	x			Φ=252.0±61.3		820					120.8±67.2	1.8±0.9		
Fique			DMA	x Φ=170				17.5				24.31		[22]
Fique	x			Φ=235.05±43.58		1140	25	50	0.6–2400	15	355.07	11.54	8.7	[23]
Fique	x	x		x Φ = 197.39 Φ = 174.44 Φ = 137.74 Φ = 147.55 Φ = 131.59	x CSA = 16.9 CSA = 18.2 CSA = 19.1 CSA = 18.2 CSA = 13.3		24–49	10 20 40 100 200	5% test length/min	100	359 (AD) 329 (CSA)	17 (indirect) 6.9 // 9.5 7.9 // 8.3 16.6 // 13.1 17.8 // 18.7 18.5 // 18.4 (direct per length AD//CSA)	11–2.2 5.5–2.1	[25], this work

Fibre type	Method used			Area approach			Experimental characteristics				Mechanical properties			
	Indirect strain measurement	Direct strain measurement	Other	Apparent diameter (μm)	Cross section area ($\times 10^3 \mu m^2$)	Density (kg/m^3)	Number of fibres/ gauge length	Gauge length (mm)	Speed rate (mm/min)	Load cell (N)	Tensile strength (MPa)	Tensile modulus (GPa)	Strain at failure (%)	Reference
Fique	x			Φ=253.8			5	675	3	10000	93.46	8.03	1.15	[24]
				Φ=200.4			5	475			76.69	8.42	1.43	
				Φ=250.4			5	495			76.68	5.11	1.47	
				Φ=275.8			5	480			72.02	7.22	1.45	
				Φ=20.9			5	510			208.13	6.28	1.42	

3.3 Experimental

3.3.1 Materials and equipment

Fique fibres provided by Compañía de Empaques through Universidad Nacional de Colombia were used in this work. Fibres were brushed on arrival with different brushes thicknesses to remove organic residues and then washed in lukewarm water. After that, fibres were wrapped around a square metallic plate and dried in an oven for three hours at 80^{o}C. This helps to straighten the fibres and makes sample preparation for tensile test easier. In Fig. 3.2 the colour difference between the fique fibres pre and post brushed and washed process is clearly visible. Technical fibres, which are composite structures consisting of an assembly of many elementary fibres having a polygonal cross-section that allows them to fit closely together [26], were randomly selected after being cut to the approximate lengths to fit the 250 g/m^2 card size for the five different gauge lengths used in the characterisation process: 10, 20, 40, 100 and 200 mm. Green beads of 1 mm diameter were attached to the fibres for tracking purposes.

Tensile tests were carried out using a Testometric M250-2.5CT testing machine with a 100 N load cell. Strain rate was established at 5% strain per minute and kept constant for all gauge lengths, so the applied displacement per min was proportional to the fibre gauge length.

For each fibre tested, Windtest analysis software, which controls the Testometric testing machine recorded the load as a function of the cross-head displacement and time. Simultaneously, each test was recorded with a digital video camera Canon Legria HF G50 set up on a tripod at 50 cm from the sample, capturing 50 frames per second.

Results of fibres breaking very close to the beads or to the cardboard edges were discarded as well as those that showed slippage at the end tab during the test. This led to 24 fibres of 10 mm, 29 fibres of 20 mm, 50 fibres of 40 mm, 46 fibres of 100 mm and 49 fibres of 200 mm considered as valid tests (198) over a total of 306 fibres tested, with failed tests being concentrated on 10 and 20 mm gauge lengths mainly.

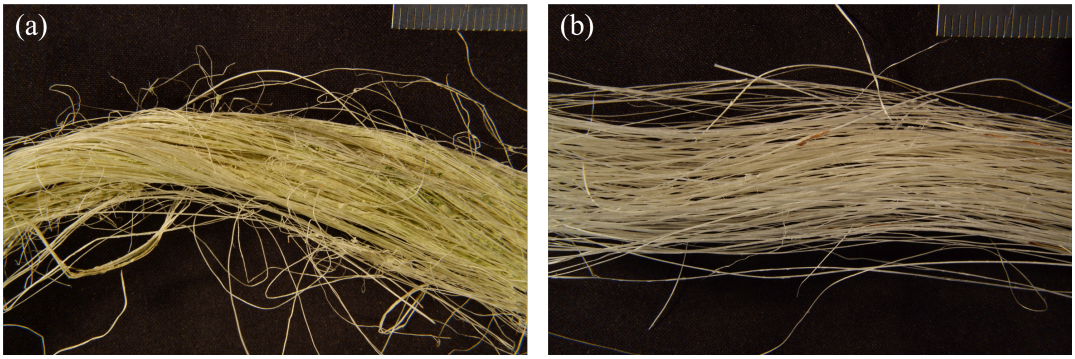


Figure 3.2: Fique fibre on arrival state (a) and after being brushed and washed in lukewarm water (b) to remove organic residues left from the leave extraction process, with a visible colour change as well as more disentangled.

3.3.2 Sample preparation

With fibres already cleaned, dried and cut to approximately the desired length, technical fibres were randomly selected and visually inspected to avoid fibres with obvious fraying or residue visible to naked eye. Fibres were inserted in two green beads and glued to them by using two components epoxy droplets deposited on the fibre by a thin wire. The attachment of the fibres to the card was done using double sided tape, later covered by the same two component epoxy resin to avoid slippage of the fibre during testing. The sample preparation process is shown in Fig. 3.3.

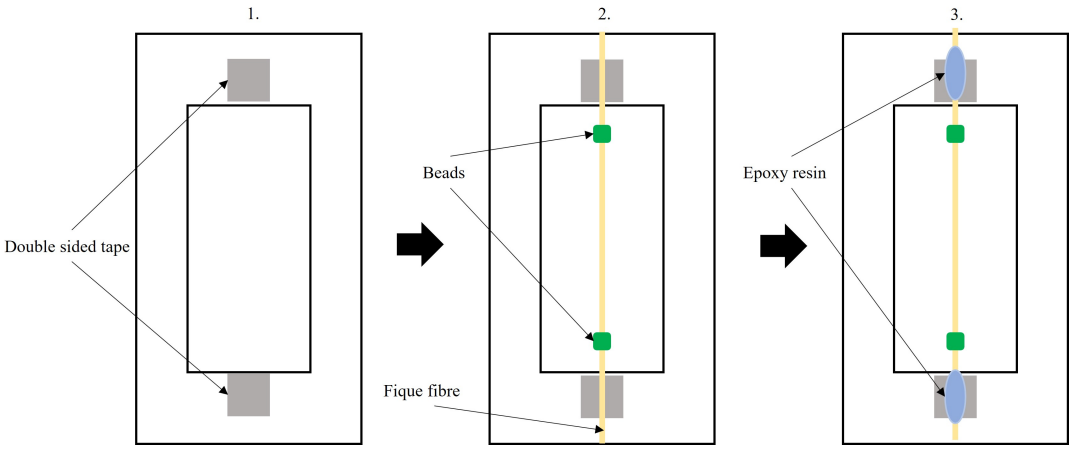


Figure 3.3: Sample preparation for single fibre tensile test where double sided tape is placed in the card (1), fique fibre with inserted and attached green beads stuck to the tape (2), and two components epoxy resin drops placed on top of the tape to reduce slippage (3).

3.3.3 Area measurement approaches

Once the samples were ready, the fibres were transversely placed under a Leica microscope and the image was captured at x100 magnification to obtain the apparent diameter of the fibres. The apparent diameter was later used to calculate the fibre's area by assuming circularity of its cross section. For the shortest fibre lengths, 10, 20 and 40 mm, one picture of the midpoint was taken, while for the two longest gauge lengths of 100 and 200 mm, three pictures at the top, middle and bottom of the fibres were taken due to the significant length increase and the possibility of variation of cross section along the length. On each picture, three measurements of the apparent diameter were done using ImageJ software, and then averaged. Fig. 3.4 (a) shows an example of three measurements taken from the transverse view. The area of the fibre was estimated using the average apparent diameter and assuming circular cross section by using Eq. (3.6).

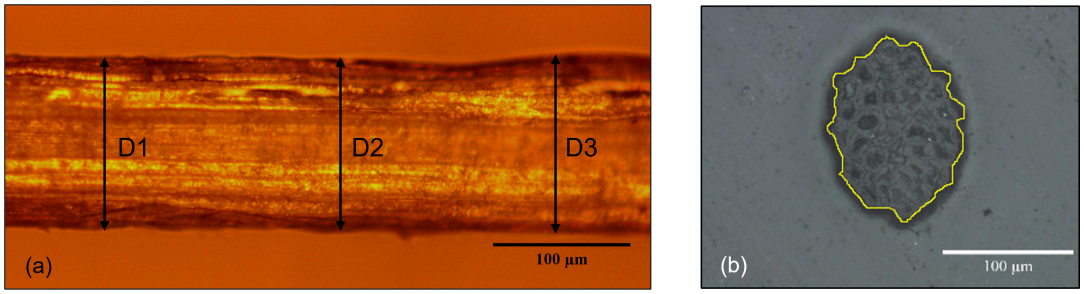


Figure 3.4: Apparent diameter transverse measurement along a fibre (a), and direct cross-section area measurement (b), at x100 and x200 magnification respectively.

$$A = \pi * \frac{d^2}{4} \tag{3.6}$$

where A is cross section area; and d is the averaged apparent diameter.

To find the true cross-sectional area (CSA) of the fibres, after the test, the two pieces of the broken fibres were cut out and glued to a card using LoctiteTM Gel Superglue. The cards with the fibres were later placed in a circular mould and transparent Epofix epoxy resin was poured into the mould to embed the fibres. After leaving the resin to cure for 24 hours at ambient temperature, the surface of the moulds with the embedded

fibres was ground at 300 rpm with progressively finer grit silicon carbide paper numbers 500, 800, 1200 and 2400. Polishing was done at 150 rpm, again with progressively finer diamond papers of 6, 3 and 1 micron(s) on a DP mol pad with DP lubricant. This preparation process for direct cross section observation is shown in Fig. 3.5.

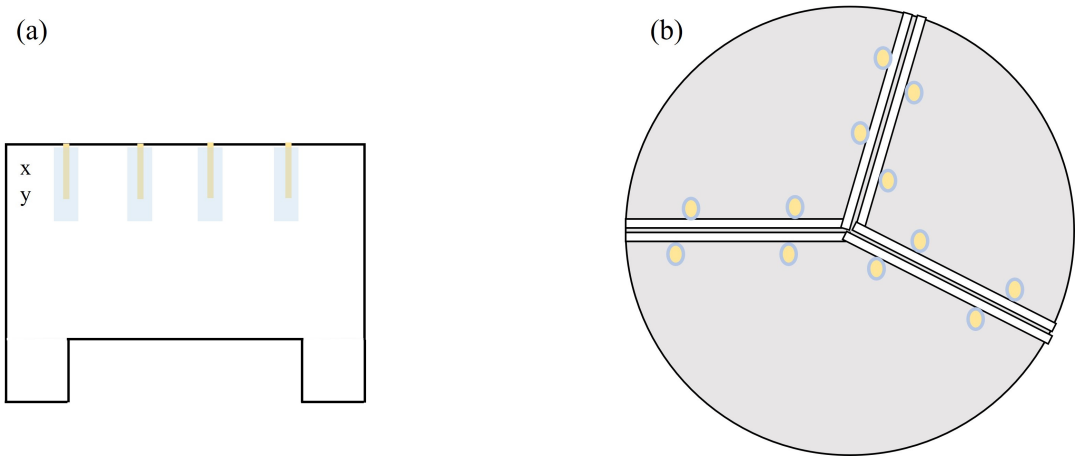


Figure 3.5: Sample preparation for cross section area observation (a), two pieces from each fibre stuck into a cardboard numbered with the correspondent fibre test numbers x, for the first two pieces closer to the number, and y for the two pieces further corresponding to a second fibre, to allow tracking them properly; (b),three cards embedded in Epofix transparent resin, through which the numbers can still be seen, and the cross section area of the fibres can be photographed with x200 magnification for later measurement.

Fibre cross sections were photographed using an Olympus GX51 microscope at x200 magnification and later measured using ImageJ software. Two measurements were done per fibre as shown in Fig. 3.4 (b) and using the fibre contour. An averaged value of the cross-sectional area was used for the modulus calculation, and it is also referred from now onwards as CSA.

3.3.4 Indirect strain measurement

Same fibres were used for both methods, with data retrieved from the equipment, force and cross-head displacement, used for calculating the Young's modulus via indirect strain measurement. As explained in Section 3.2.1.1 at least three gauge lengths are required to apply this method. In this case five gauge lengths of 10, 20, 40, 100, and 200

mm were used, giving five datasets to be plotted according to Eq. (3.4). This is done for both cross-sectional area calculation approaches to allow for comparison within the same method, so an observation on how the area approach followed affects the results can be made.

3.3.5 Direct strain measurement

The two beads on each fibre are assumed to move with the points on the fibre they are attached to, so by tracking their movement, the elongation of the fibre is captured. These beads, which are significantly shorter than the total length of the fibres, are assumed to be rigid solids. The beads movement on every fibre was video recorded and an in-house MATLAB code, which can be found in Part I, was developed to track the beads movement in a post processing stage of the captured videos. The video is opened in MATLAB and the area occupied by each bead is manually selected. The detectMinEigenFeatures function recognizes n and m number of points on each bead using minimum eigenvalue algorithm for all the video frames and calculates the average position for the top and bottom beads for every frame in pixels, as shown in Fig. 3.6. The position of each bead for every frame is tracked by the Kanade-Lucas-Tomasi (KLT) algorithm (MathWorks 2019).

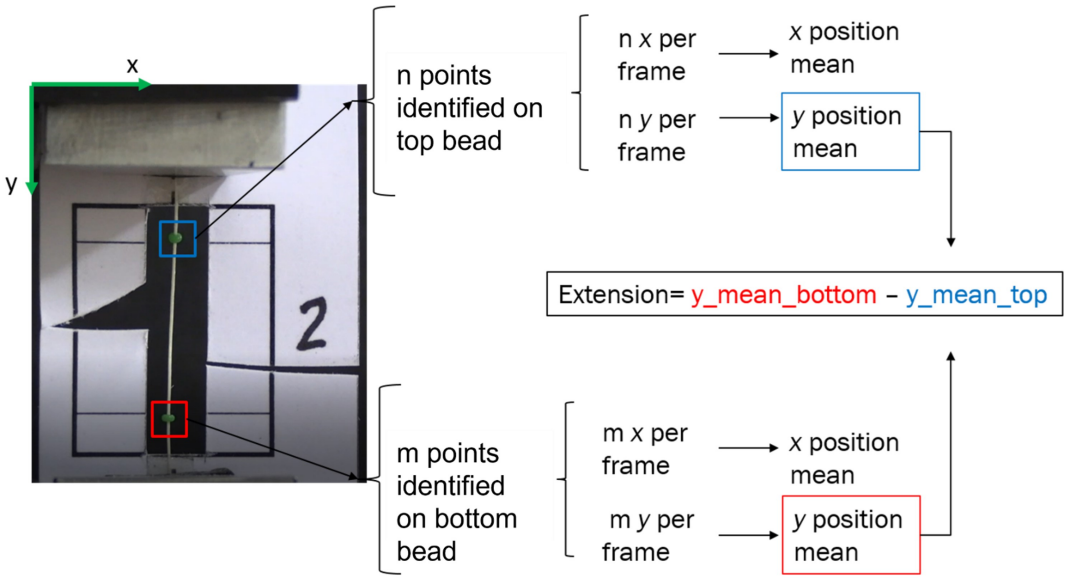
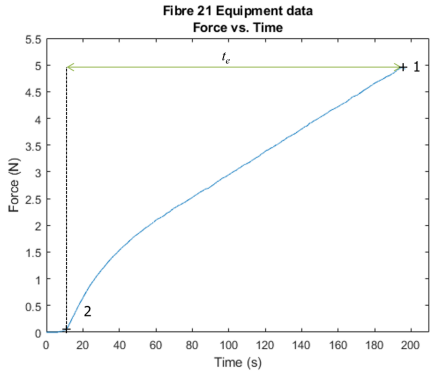


Figure 3.6: Flowchart of the MATLAB code for tracking the two beads attached to each tested fiber, where n and m are the number of points identified on each bead.

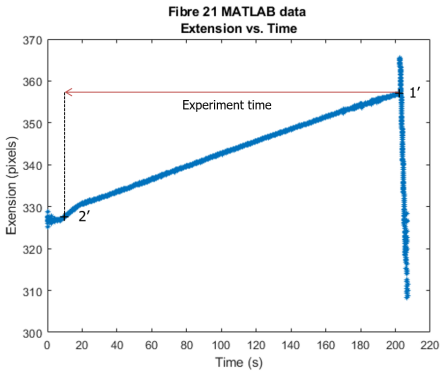
The elongation is then calculated by finding the difference between the averaged movement of the beads in the y axis direction in pixels, allowing for the calculation of the average strain when divided by the initial distance between the two of them in pixels. Data acquisition frequency of the tensile testing equipment is between 15 and 20 s^{-1} while the video camera captures 50 frames per second. To match the data points between strain from the processed videos and force from the tensile machine, for every strain value, tensile force is found using a linear interpolation, so the force-extension graph can be obtained.

In order to match the timing between the video of the test and the data from the test an experiment time is defined, t_e. This experiment time is defined in the data obtained from the equipment in the force-time chart, as the time between 1 and 2, as shown in Fig. 3.7a. Point 1 is when the fibre breaks, which is clearly visible as either the equipment stops recording or the jump between point 1 and the next one is very sharp, with the force dropping to zero. Point 2 is defined as when the force starts to increase, which is when the experiment starts, with the fibre getting loaded. The breaking point of the fibre is also easily identified in the video because of the jump in the function, and is represented by 1' in the extension-time chart in Fig. 3.7b. Once the experiment time

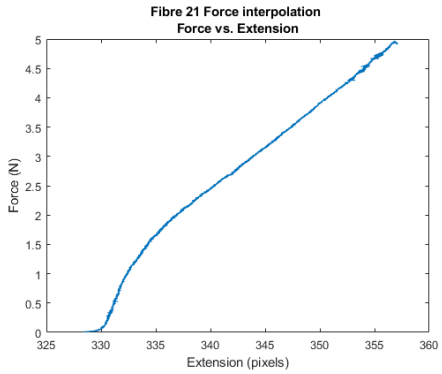
and the breaking point are identified from the equipment data (force-time chart in) and the video (extension-time chart) respectively, the experiment time is subtracted from point 1' in the video, to find point 2', which is when the fibre starts getting loaded. Once this is done, the aforementioned interpolation is done to have the same number of force values as extension points from the video, allowing to built the force-extension graph, combining both, equipment and video information as shown in Fig. 3.7c. The last step is to obtain the force elongation chart, in which the displacement of the top bead is divided by the initial distance between to beads at the beginning of the experiment, finding the force-elongation chart as shown in Fig. 3.7d.



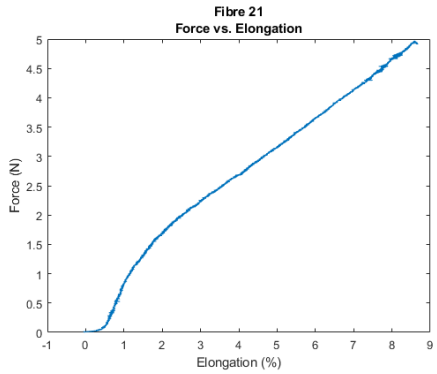
(a) Experiment time t_e defined from the equipment data between breaking point (1) and start of fibre loading (2).



(b) Breaking point identified in the time-extension chart from the video as 1', from which t_e is subtracted to find the starting point, 2'.



(c) Force-extension chart where the force data from the equipment reading is combined with the extension data from the video after an interpolation has been done.



(d) Force-elongation chart after the beads displacement is divided by the initial distance when the experiment started.

Figure 3.7: Graphs explaining the step-by-step process of matching the information gathered by the equipment with the information on displacement gathered from the video recording.

The slope of the initial linear part of the stress-strain curve, 1 to 3%, for each fibre is used to find the Young's modulus [27], with two values obtained for each fibre, one per area calculation method. The impact of the area is especially relevant when calculating the Young's modulus following the traditional indirect strain measurement method, as it is one of the parameters used. The stress values are found by dividing the peak force during the test by either the apparent or directly measured cross-sectional area, as stress values directly change depending on the area used.

If a test is valid or not is decided by direct observation of the sample and the force curve plotted. When the fibre breaks close to a bead or to the edge, this is discarded as a valid test through visual inspection of the breaking point, since the force-displacement curve will not show any peculiarity as shown in Fig. 3.8. When there is slippage from the edges, it is very hard to see through visual inspection, but the force-displacement curve arrives to a point and then the curve starts to go down, as the red dashed curve in Fig. 3.8. This shows that the fibre is not undergoing loading anymore. Once the test is stopped because of this, it can be checked by simply pulling the fibre and by it coming away easily, proving that slippage was actually occurring. So, results of fibres breaking very close to the beads or to the cardboard edges were discarded as well as those that showed slippage at the end tab during the test. This led to 24 fibres of 10 mm, 29 fibres of 20 mm, 50 fibres of 40 mm, 46 fibres of 100 mm and 49 fibres of 200 mm, considered as valid tests over a total of 306 fibres tested, as shown in Table 3.2.

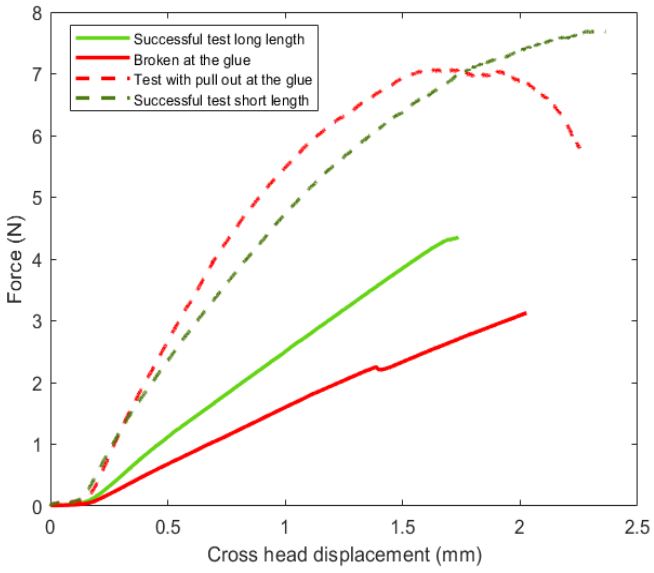


Figure 3.8: Typical curves seen during the experimental part. Green curves, solid and dashed, are successful cases for long and short gauge lengths respectively; while red curves, solid and dashed, are representative of not valid samples due to breaking at the card edge (which has a perfect normal curve and is discarded due to visually seeing where the breaking happens) and pull out respectively.

Table 3.2: Number of tested fibres and valid tests corresponding to each gauge length and the total.

Gauge length (mm)	Number of fibres tested	Number of valid tests
10	42	24
20	84	29
40	60	50
100	60	46
200	60	49
Total	306	198

3.4 Results and discussion

3.4.1 Cross section area

Using the apparent diameter shows a peak in the distribution of the area values seen for fibres with cross sectional area between 10×10^3 and 15×10^3 µm^2 as shown in Fig. 3.9; while for the CSA approach it can be seen that the measured value has more uniform frequency from 5×10^3 to 20×10^3 µm^2 with relatively similar frequency. Assumption of circularity does not accurately represent well the area of the fibres as studied by [4] on flax and sisal fibres, where the conclusion achieved is that apparent diameter measurement is not the most attractive method for cross-sectional area estimation of natural fibres, although it has been widely used due to its ease of implementation in comparison to the direct observation of the CSA.

Average values of the areas calculated and measured for each gauge length as well as the total average are shown in Table 3.3, along with the standard deviation and the coefficient of variation. The total averaged area for circularity assumption is 18.4 x10^3 μm^2, while for the measured cross-sectional area this value is 17.1 x10^3 μm^2. The coefficient of variation is 20 points lower for the measured cross-sectional area compared to using the apparent diameter of the fibre to estimate its area assuming its circularity. The equivalent apparent diameter for the circularity assumption is 147 μm, while for the cross-sectional area is 147.5 μm.

In the Fig. 3.10 values from the measured area are presented against the area estimated by assuming circularity. On it, it can be seen that sometimes the apparent

diameter approach for area estimation leads to under or overestimation by assuming a circular section, which although it can be found, it is not the most common shape. The average values obtained for each case compared to the overall values, shown in Table 3.3, can suggest that if many fibres are sampled, this over and underestimation may balance each other, leading to a very similar average area values, but with the one from the apparent diameter being higher in this case. The fact that the standard deviation is lower when it comes to the CSA means that although variation exists, CSA technique reduces the range, meaning some more accuracy. If the area of the fibres were the main subject of study of this work, both methods could be considered appropriate if the average of area values was the concern, always recommending to make measurements at three different locations along the fibre, as for the lengths that it was not done like that the difference between techniques clearly increases. This is shown by calculating the error following Eq. (3.7) when considering the directly measured cross-sectional area the true area value. Calculating this error when one picture is taken for the apparent diameter technique gives a value of 1.26, in contrast with the 0.91 obtained when three pictures along the length are taken. This is a 38% higher error, leading to the hypotheses that more pictures along the length allow for a closer value to the CSA following the apparent diameter approach.

$$\text{Root mean squared error} = \sqrt{\frac{1}{N}\sum(\frac{A_{AD} - A_{CSA}}{A_{CSA}})^2} \tag{3.7}$$

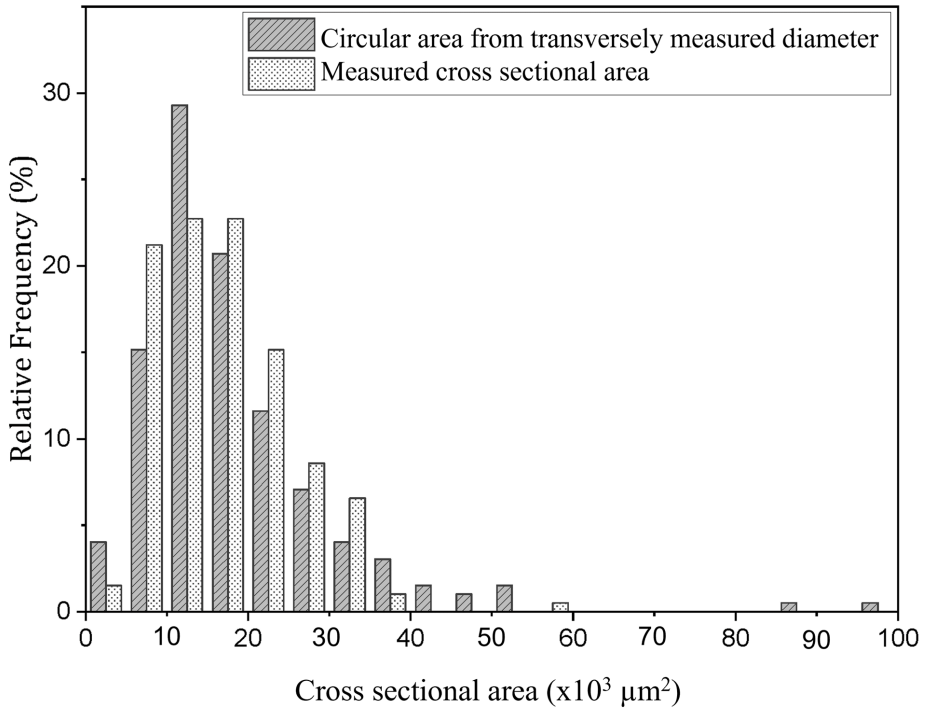


Figure 3.9: Fiber's cross sectional area frequency intervals for the two area estimation approaches, assuming circularity from the apparent diameter and measuring the cross-sectional area at the failure point.

Table 3.3: Area obtained from the apparent diameter (AD) approach assuming circularity compared to the area measured by the cross-sectional area (CSA) observation.

Gauge length (mm)		10	20	40	100	200	Average
Average area $\overline{A}$ ($x10^3$ μm^2)	AD	30.6	23.9	14.9	17.1	13.6	18.4
	CSA	16.9	18.2	19.1	18.2	13.3	17.1
Standard deviation s (x10^3 μm^2)	AD	22.6	13.6	8.3	7.3	5.7	12.5
	CSA	6.6	6.3	8.7	9.7	6.1	8.1
Coefficient of variation $s/\overline{A}$ (%)	AD	73.9	56.9	55.5	42.8	41.9	67.9
	CSA	39.1	34.7	45.7	53.6	45.8	47.4

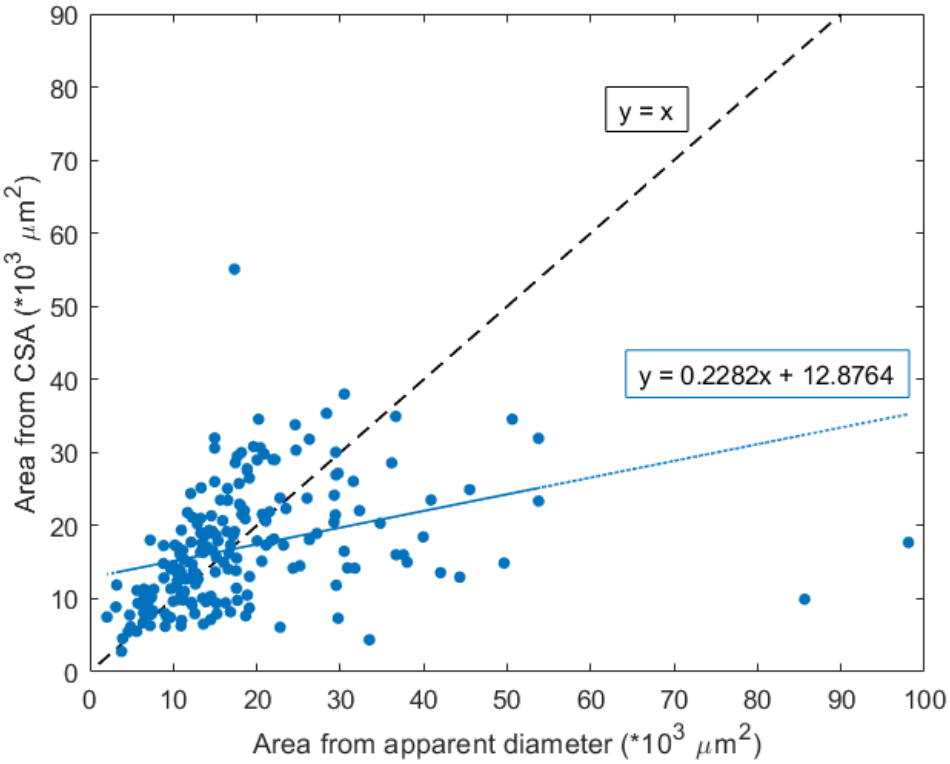


Figure 3.10: Comparison between the cross section area values calculated by using the apparent diameter and assuming circularity of the fibres and the cross section area measured at the microscope with its fitted line to compare it with the y=x that would follow if both values were the same.

For the study of other properties in which the area plays a role, the two different approaches are kept to understand how much it affects them. If it can be an appropriate method for some natural fibres depending on the general shape of their cross section can be discussed, as some other fibres can have a more consistent section that approximates to a circular area shape.

Fique area's shape

In the case of fique, a comparison between ellipse and Feret's diameters has been made in order to see if there are significant differences and if something can be said about the shape of fique fibres. Feret's diameters are defined in Fig. 3.11, and in Fig. 3.12 a comparison among the shapes found during the CSA measurement is shown. Here,

three different shapes that fit under three labels are shown: circular (a), ellipse (b), and bean like shape or more extreme shape (c). Ellipse and Feret's diameters are overlaid on top, and the comparison between both of them is presented in Fig. 3.13, showing that there is not a significant difference between these values, so approximating the area by an ellipse or Feret's diameters leads to approximately the same results.

With these, the circularity and solidity of these shapes has also been studied, following Eq. (3.8) and Eq. (3.9) alongside the definition of solidity also shown in Fig. 3.14. These present values between 0 and 1, being the closest to 1 the more circular and the less convex (or the more solid). Values for the case here are 0.54 for circularity and 0.86 for solidity. This leads to conclude that fique fibres are not circular. It also says that extreme shapes are not the most common ones, which agrees with the ellipse and Feret's diameter leading to the same results. Considering the figures (a), (b), and (c) in Fig. 3.12 and comparing the values of ellipse and Feret's diameters along with circularity and solidity as shown in Table 3.4 this becomes more clear.

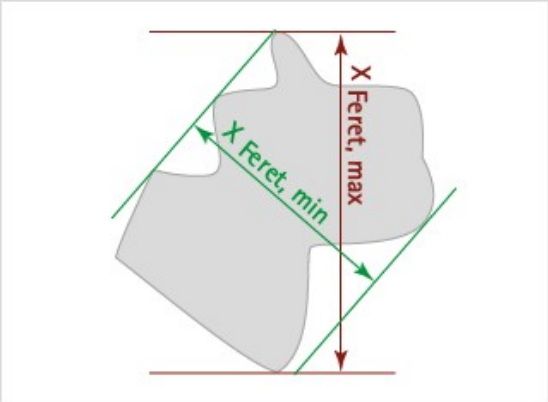
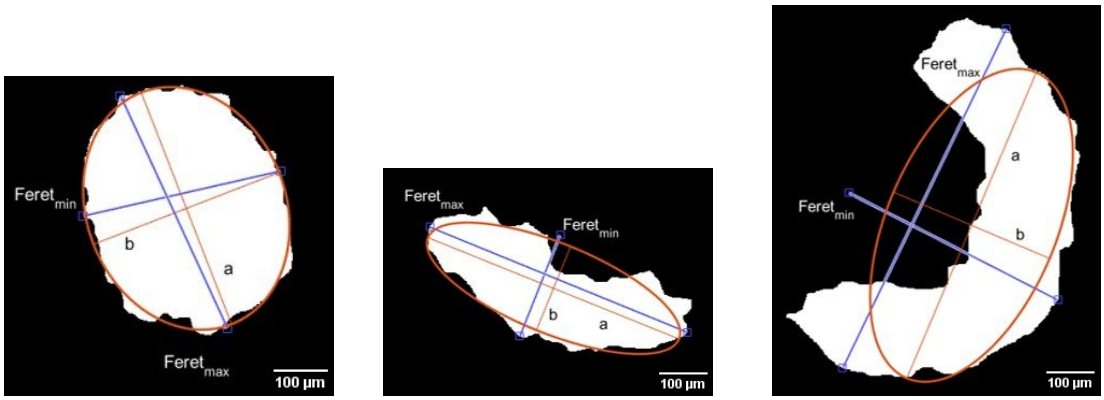


Figure 3.11: Feret's diameters definition.

$$\text{Circularity} = \frac{4\pi A}{\text{Perimeter}} \tag{3.8}$$

$$\text{Solidity} = \frac{A}{B} \tag{3.9}$$



(a) (b) (c)

Figure 3.12: Different shapes found in fique area's measurement, with (a) showing the closest to a circular cross section, (b) showing an elongated shape resembling more an ellipse, and (c) shwoing a bean like section considered an extreme shape.

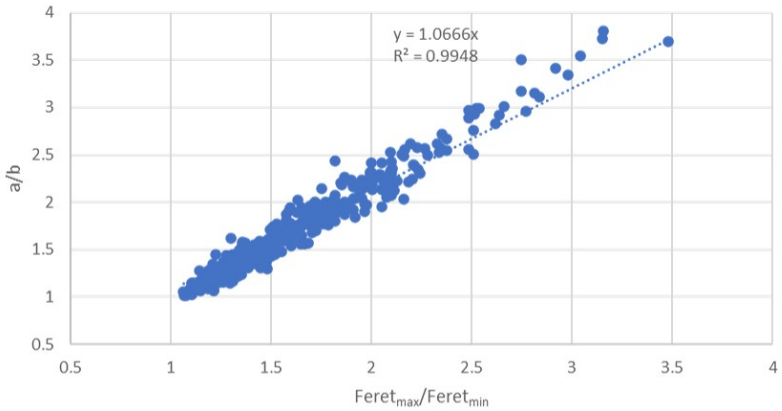


Figure 3.13: Feret's diameters definition.

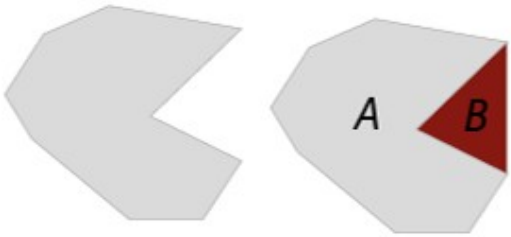


Figure 3.14: Solidity definition, where A is the measured area and B is the area of the convex region.

Table 3.4: Parameters for figures in Fig. 3.12 showing the differences between the shapes found.

	(a)	(b)	(c)
Ellipse axes ratio a/b	1.25	2.98	1.94
$\text{Feret}_{max}/\text{Feret}_{min}$	1.27	2.54	1.60
Circularity	0.73	0.43	0.33
Solidity	0.95	0.82	0.63

The ambition to calculate a correction factor seems appropriate, but the need to have enough fibre to represent different shapes and areas seems still a necessity. A correction factor based on a small sample can still be misleading, and more work needs to be done on this area.

3.4.1.1 Young's modulus

Two methods of indirect and direct strain measurement for finding the Young's modulus of the fibres are discussed below.

Indirect strain measurement

Fig. 3.15 (a) shows the results of the ASTM-C1557-20 standard method applied to all the valid tested fibres considering apparent diameter area measurement. Fig. 3.15 (b) shows the same standard applied using the measured cross-sectional area instead. The inverse of the slope of the line fitted to the data points represents the fibres average Young's modulus. For both area measurement techniques, the fitted line has a similar slope, giving a Young's modulus value of 17.3 GPa and 17.1 GPa respectively. The coefficient of determination, R^2, for each line is shown in both graphs of Fig. 3.15. Higher values of R^2 are an indication of lower variation in data and this shows that the variation is higher when using the apparent diameter from assuming circularity of the fibre instead of CSA.

Direct Strain measurement

On Fig. 3.16 it is shown how a line is fitted to the initial (1-3%) part of the stress-strain curve, and its slope, a, is identified as the Young's modulus. The averaged value of

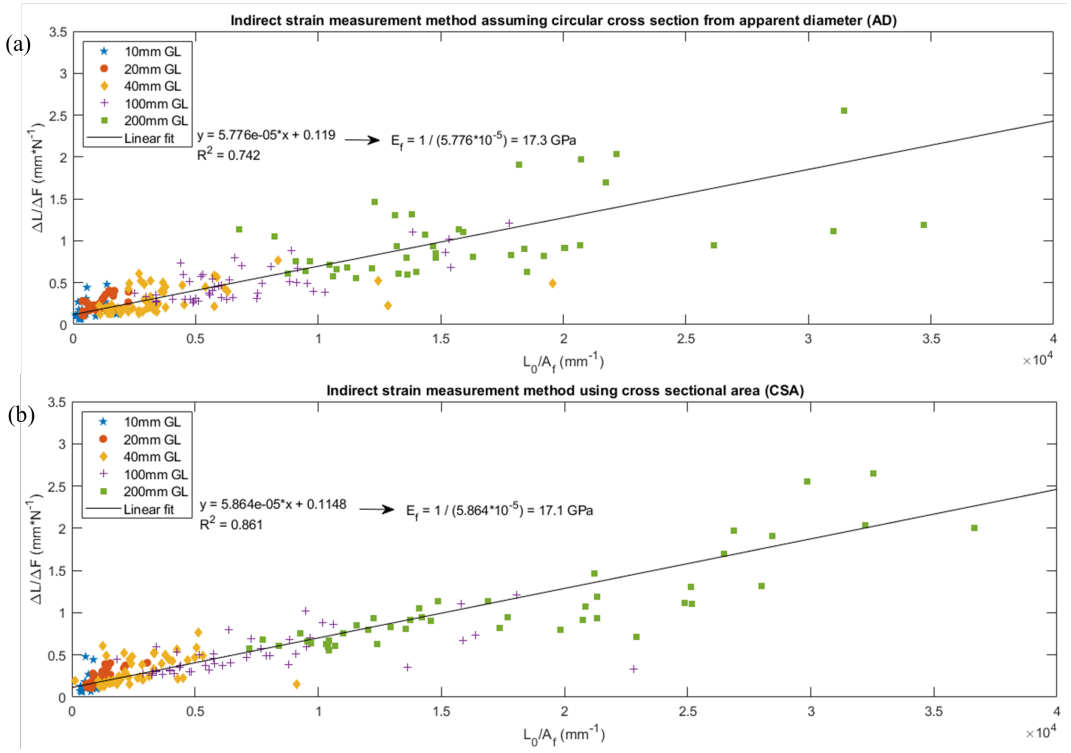


Figure 3.15: (a) shows the compliance theory applied by using area from apparent diameter using circularity assumption of the fiber; (b) shows the compliance theory applied by using the cross-sectional measured area of the fibers. The Young's modulus of the fibers is the inverse value of the fitted slope, giving very close values for both cases, 17.3 and 17.1 GPa respectively. Coefficient of determination R^2 is higher when using the cross-sectional area measured, suggesting a better fit for this case.

Young's modulus, standard deviation, and coefficient of variation for every gauge length are given in Table 3.5. Since fibre's area has a direct impact on the measured Young's modulus, two different values are provided: one using the measured apparent diameter for each fibre and another one using the measured CSA. Fig. 3.16 shows the stress-strain curve plotted with raw data as obtained from the equipment and as measured from the video. A toe shape can be seen at the beginning of it, which is associated with the fibre not being fully loaded. For visualization purposes and considering that the stress-strain curve theoretically starts in the origin, all curves have been shifted in the x-axis towards the origin, with the no loaded region removed.

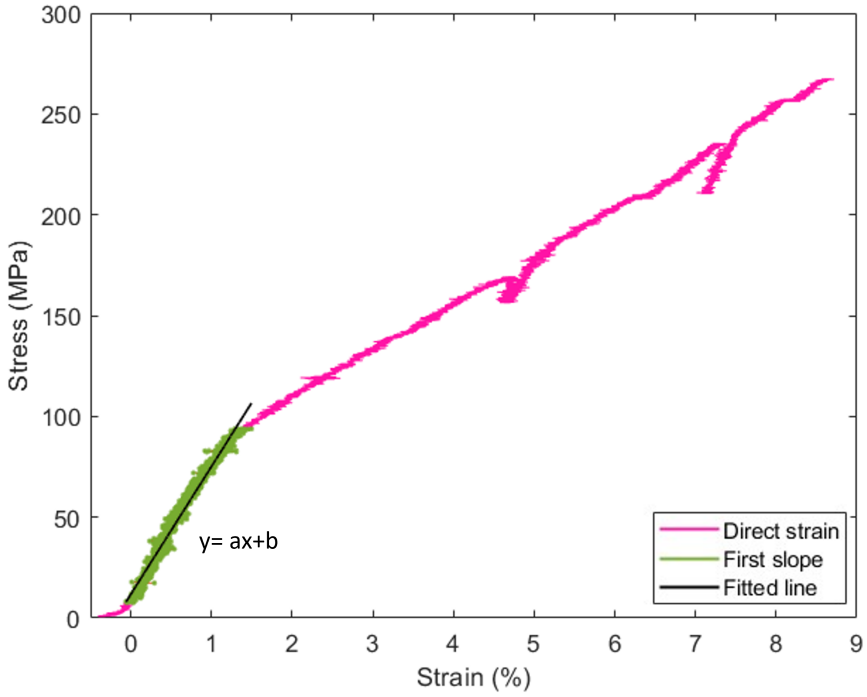


Figure 3.16: Stress-strain curve obtained from the direct strain measurement method, where the initial slope of the curve is used to calculate the Young's modulus of the fibre by fitting a line of which slope is taken as the Young's modulus, represented by a on the line equation.

Fig. 3.17 (a) and (b) compares the stress-strain curve found from the crosshead displacement of the equipment and the direct strain measurement tracking the beads on the fibres for two typical fibres with gauge lengths of 10 mm and 100 mm. Fig. 3.17 (a) shows that the 10 mm fibre has a clear non-linear stress-strain curve but the non-linearity in the 100 mm is less pronounced as shown in Fig. 3.17 (b). Also, the difference between the extension from the crosshead displacement and the direct strain measuring system is much higher for the 10 mm fibre. However, the extension found by both methods are quite similar in the 100 mm fibre. The responses shown in Fig. 3.17 for both gauge lengths are representative of each gauge lengths and other fibres with similar gauge length showed a similar stress-strain behaviour.

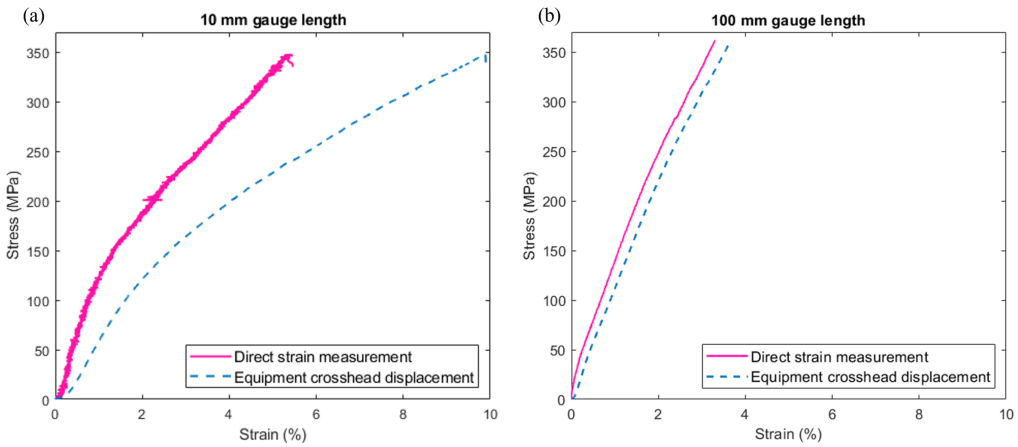


Figure 3.17: Two typical stress-strain curves of 10 and 100 mm fiber lengths for comparison. Both (a) and (b) show the differences between the direct strain measurement (solid line) vs. the equipment cross head displacement (dashed line), in both cases using the cross-sectional area (CSA).

As shown in Table 3.5, the values of the Young's modulus increase with the increase in the gauge length for the apparent diameter approach. A similar trend is observed for the measured CSA approach, although this is not true for every single increase in gauge length.

These values obtained by both, direct and indirect strain measurement methods, are higher than the ones found in the literature. Gañán and Mondragón [14] found a value between 8 and 12 GPa for fique's tensile modulus, while Delvasto [15] found a lower value between 8.2 and 9.1 GPa. Muñoz-Vélez *et al.* [17] obtained a value of 8.64 GPa in one study, and a lower value of 5.44 GPa in a later study [20]. Gómez *et al.* [21] obtained 4 GPa in their study of fique, while Muñoz-Blandón *et al.* [28] obtained a value of 11.54 GPa. The higher number of fibres evaluated, as well as the longer sample size, with the use of a direct strain measurement method, along with the actual measurement of the cross-sectional area can explain this difference.

Table 3.5: Young's modulus values, standard deviation, and coefficient of variation for different gauge lengths from the direct strain measurement method

Gauge length (mm)		10	20	40	100	200
Average Young's modulus $\overline{E}$ (GPa)	AD	6.9	7.9	16.6	17.8	18.5
	CSA	9.5	8.3	13.1	18.7	18.4
Standard deviation s (GPa)	AD	5.7	5.2	8.3	6.2	6.3
	CSA	4.3	3.2	10.3	13.0	4.9
Coefficient of variation $s/\overline{E}$ (%)	AD	82.1	66.1	49.9	34.7	33.9
	CSA	45.7	37.9	79.0	69.6	26.4

3.4.1.2 Tensile strength

The single fibre tensile test has also been used to calculate the tensile strength of fique fibre, σ_f, by using the force at peak, F_p, as measured by the equipment and the area value, A, for each fibre as calculated by either method following Eq. (3.10) [3], giving two tensile strength values per fibre, one for the apparent diameter calculated area, and another one for the directly measured cross-sectional area.

Values of tensile strength are stable, although slightly increasing when using the directly measured cross-sectional area, while having a higher variation when using the assumption of circularity approach, as shown in Fig. 3.18. In this latter case, the values go from 223.8 MPa for the 10 mm gauge length, increasing until an averaged peak of 449.6 MPa for the 40 mm gauge length fibres, and starts decreasing again until an average value of 364.4 MPa for 200 mm gauge length. The average value for this area approach is 359.4 MPa. Using the actual cross section of the fibres not only gives a more stable value for tensile strength, but standard deviation and hence coefficient of variation also decrease, as can be seen in Table 3.6. Values of tensile strength for the CSA approach are 329.7 MPa on average, with the lowest value of 300.3 MPa for the 10 mm gage length and the highest value for the 200 mm gauge length being 346.6 MPa.

$$\sigma_f = \frac{F_p}{A} \tag{3.10}$$

Table 3.6: Tensile strength values of fique fibres. AD=Area from apparent diameter, CSA=Cross section area.

Gauge length (mm)		10	20	40	100	200	Average
Average $\overline{\sigma_f}$ [MPa]	AD	223.8	288.9	449.6	369.2	364.4	359.4
	CSA	300.3	315.7	333.1	332.8	346.6	329.7
Standard deviation s [MPa]	AD	144.0	164.2	180.4	136.2	175.5	176.8
	CSA	106.4	87.7	116.6	105.0	113.7	108.2
CV $(s/\overline{\sigma_f})$ [%]	AD	64.3	56.8	40.1	36.9	48.2	49.2
	CSA	35.4	27.8	35.0	31.6	32.8	32.8

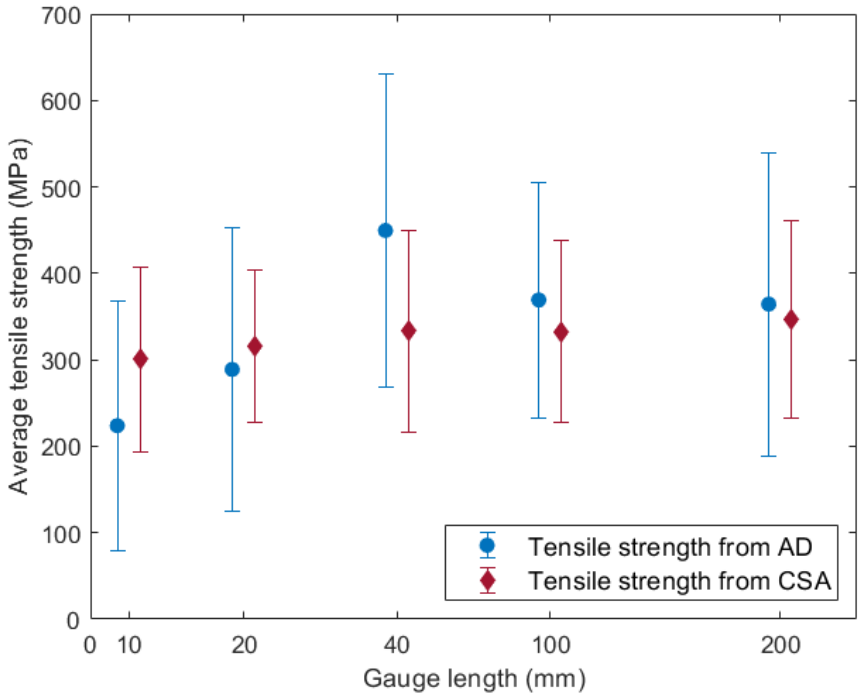


Figure 3.18: Average tensile strength for each gauge length for both methods of area calculation, AD= apparent diameter at the left hand side (in a blue circle) of every gauge length and CSA=cross section area observation at the right hand side (in a burgundy diamond) of every gauge length.

There is a wide range of values found in the literature, with Delvasto *et al* [15] reporting values between 43 and 571 MPa, with an average value of 132 MPa. Hoyos *et al* [16] have reported 197 ± 65 MPa. Luna *et al.* [18] have reported a value of 80 MPa as average tensile strength. Souza *et al* [19] reported a value of 320 ± 59 MPa. Muñoz-Blandón *et al.* [28] obtained a value of 355 ± 90 MPa for the ultimate

strength. Guzmán-López *et al.* [24] present average values for tensile strength between 72 and 208 MPa, with maximum values between 79 and 233 MPa; despite this wide values a 70 MPa tensile strength of fique is proposed. Values reported in this work are within the values reported previously, showing consistency across different gauge lengths, especially when the cross-sectional area is used, highlighting the importance of using a true representative area value.

3.4.1.3 Elongation at break

As for the tensile strength there is a wide range of values reported for elongation at break in fique, from the 4-6% [14] to the 4.8-23% found in other work [17], which was narrowed down to 9.3% by the same author couple of years later [20], similar to the 9.8% and 8.7% obtained somewhere else [15, 23]. These values contrast with the below 1.5% obtained by a variety of gauge lengths here [24]. As shown in Fig. 3.19, in this work values diverge between the direct and indirect strain measurements the shorter the fibre, and tend to converge the longer the fibre. This highlights how the equipment error is more significant the shorter the fibre. For 10 and 20 mm gauge lengths equipment values around 11% contrast with the 6% and below values for the direct strain method. These values become closer for 40 mm gauge length, going down to 5.7 and 4% respectively. When looking at the 200 mm gauge length, values are almost matching around 3% elongation at break. The differences between 10 and 100 mm gauge length stress-strain curves shown in Fig. 3.17 suggests that non-linear behaviour of fique is non neglectable, with this non-linearity being more significant when testing shorter fibres, between 10 and 20 mm lengths. These results show that at longer gauge lengths, direct strain measurement combined with CSA measurement give much closer results with less non-linear stress-strain curves.

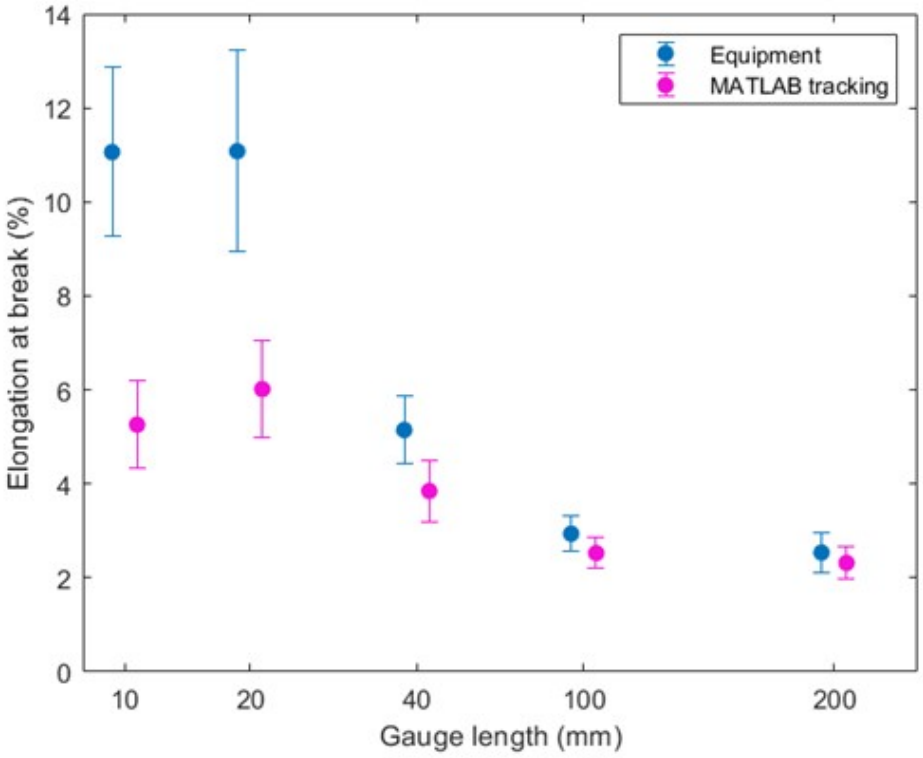


Figure 3.19: Average tensile strain (%) for each gauge length for both methods of strain measurement, equipment=indirect in blue circles to the left hand side of every gauge length and MATLAB=direct in pink circles to the right hand side of every gauge length.

3.5 Conclusions

The mechanical characterisation done in this chapter leads to suggest that direct strain measurement is more easily done in natural fibres than in synthetic fibres because of the significant size difference, increasing the feasibility of beads attachment, and this can help to reduce the impact of the system compliance in the measured mechanical properties, especially when using shorter fibres.

The indirect strain measurement gives a value of 17 GPa of the elastic modulus independently of the area used when calculating it. The direct strain measurement shows a trend in which the Young's modulus values increase with the fibre length, going from 6.9 to 18.5 GPa for the apparent diameter approach, and from 9.5 to 18.4 GPa when CSA is used. The interpretation for this is that fibres need to be long enough, so

the non-linearity is not the dominant phenomenon in the stress-strain behaviour.

Calculation of tensile strength has been done by using the two different area approaches, and using the CSA gives more stable values, with decreasing standard deviation. The average value for this case is 329.7 MPa, with the lowest value of 300.3 MPa for the 10 mm gauge length and the highest value for the 200 mm gauge length being 346.6 MPa. Using the apparent diameter approach for area calculation gives an average value of 359.4 MPa, with a lowest value of 223.8 MPa for the 10 mm gauge length, and a highest value of 449.6 MPa for the 40 mm gauge, with with 19 points different in the coefficient of variation over the CSA approach.

The elongation at break diverges significantly for the 10 and 20 mm gauge lengths between equipment displacement and beads tracking, suggesting that for shorter fibres the error in the equipment is significant enough to affect the results. Values converge the higher the gauge length.

Assuming circularity of fique can lead to inaccuracies, but given the logistics simplicity of measuring an apparent diameter and how much it facilitates the process of area calculation, the recommendation is to increase the number of fibres tested and the number of measurements per fibre. This means that instead of measuring at the fibre midpoint, at least three areas along the fibre are recommended with at least three measurements on each section, as this has contributed to reducing the values difference between apparent diameter and CSA approaches in the 100 and 200 mm gauge length fibres. This does not change the fact that CSA is always more accurate, especially when calculating tensile strength, but it does not appear to have a significant impact when the Young's modulus is calculated by using the indirect strain measurement method. For shorter fibres, given that compliance of the equipment can have more impact, CSA is recommended to reduce uncertainties when using the indirect strain measurement method. With this in mind and the results presented here fique is presented as a natural fibre with lower mechanical properties as flax or hemp, but with great potential for having higher mechanical properties than coir, sitting mid table in natural fibre's mechanical properties.

Bibliography

[1] ASTM International, "Standard Test Method for Tensile Strength and Young's Modulus for High-Modulus Single-Filament Materials," *ASTM International*, 1975 (Reapproved 1989). https://compass.astm.org/document/?contentCode=ASTM%7CD3379-75R89E01%7Cen-US.

[2] ASTM International, "Standard Test Method for Tensile Properties of Single Textile Fibers," *ASTM International*, 2014 (Reapproved 2020). https://compass.astm.org/document/?contentcode=ASTM%7CD3822_D3822M-14R20%7Cen-US.

[3] ASTM International, "Standard Test Method for Tensile Strength and Young's Modulus of Fibers," *ASTM International*, 2020. https://compass.astm.org/document/?contentCode=ASTM%7CC1557-20%7Cen-US.

[4] J. L. Thomason, J. Carruthers, J. Kelly, and G. Johnson, "Fibre cross-section determination and variability in sisal and flax and its effects on fibre performance characterisation," *Composites Science and Technology*, vol. 71, no. 7, pp. 1008–1015, 2011. https://doi.org/10.1016/j.compscitech.2011.03.007.

[5] F. Tomczak, K. G. Satyanarayana, and T. H. D. Sydenstricker, "Studies on lignocellulosic fibers of brazil: Part iii - morphology and properties of brazilian curauá fibers," *Composites Part A: Applied Science and Manufacturing*, vol. 38, pp. 2227–2236, 10 2007. https://doi.org/10.1016/j.compositesa.2007.06.005.

[6] W. Hu, M.-T. Ton-That, F. Perrin-Sarazin, and J. Denault, "An Improved Method for Single Fiber Tensile Test of Natural Fibres," *Polymer Engineering and Science*, vol. 50, pp. 819–825, 2010. https://4spepublications.onlinelibrary.wiley.com/doi/10.1002/pen.21593.

[7] N. Defoirdt, S. Biswas, L. De Vriese, L. Quan Ngoc Tran, J. Van Acker, Q. Ahsan, L. Gorbatikh, A. Van Vuure, and I. Verpoest, "Assessment of the tensile properties of coir, bamboo and jute fibre," *Composites: Part A*, vol. 41, pp. 588–595, 2010. https://doi.org/10.1016/j.compositesa.2010.01.005.

[8] M. E. A. Fidelis, T. V. C. Pereira, O. D. F. M. Gomes, F. D. A. Silva, and R. D. T. Filho, "The effect of fiber morphology on the tensile strength of natural fibers," *Journal of Materials Research and Technology*, vol. 2 (2), pp. 149–157, 2013. https://doi.org/10.1016/j.jmrt.2013.02.003.

[9] C. Jiang, X. Zhang, J. Zhao, J. Zou, and X. Zhang, "Evaluating the System Compliance in Testing Carbon Nanotube Fibres," 2017. https://doi.org/10.48550/arXiv.1706.00755.

[10] R. L. Moore and J. K. Lepper, "Strain Measurement Techniques for Fiber Modulus Determination," *Journal of Testing and Evaluation, JTEVA*, vol. 2, no. 3, pp. 173–175, May 1974. https://doi.org/10.1520/JTE10094J.

[11] D. Depuydt, K. Hendrickx, W. Biesmans, J. Ivens, and A. W. Van Vuure, "Digital image correlation as a strain measurement technique for fibre tensile tests," *Composites: Part A*, vol. 99, pp. 76–83, 2017. http://dx.doi.org/10.1016/j.compositesa.2017.03.035.

[12] J. Huether, P. Rupp, I. Kohlschreiber, and K. André, "An enhanced method to determine the Young's modulus of technical single fibres by means of high resolution digital image correlation," *Measurement Science and Technology*, vol. 29 045601, 2018. https://doi.org/10.1088/1361-6501/aaa0bb.

[13] R. B. Adusumalli, K. C. Venkateshan, C. Kunchi, and S. R. Vadlamani, "Tensile testing of single fibres," *Procedia Structural Integrity*, vol. 14, pp. 150–157, 2019. https://doi.org/10.1016/j.prostr.2019.05.020.

[14] P. Gañán and I. Mondragón, "Fique fiber-reinforced polyester composites: Effects of fiber surface treatments on mechanical behavior," *Journal of Materials Science*, vol. 39, pp. 3121–3128, 2004. https://doi.org/10.1023/B:JMSC.0000025841.67124.c3.

[15] S. Delvasto, E. F. T. Perea, F. Perdomo, and R. M. de Gutiérrez, "An appropriate vacuum technology for manufacture of corrugated fique fibre reinforced cementi-

tious sheets," *Construction and Building Materials*, vol. 24, pp. 187–192, 2010. https://doi.org/10.1016/j.conbuildmat.2009.01.010.

[16] C. G. Hoyos, V. A. Álvarez, P. G. Rojo, and A. Vázquez, "Fique fibers: Enhancement of the tensile strength of alkali treated fibers during tensile load application," *Fibers and Polymers*, vol. 13, pp. 632–640, 5 2012. https://doi.org/10.1007/s12221-012-0632-8.

[17] M. F. Muñoz-Velez, M. Á. Hidalgo-Salazar, and J. H. Mina-Hernández, "Fique fiber an alternative for reinforced plastics. influence of surface modification," *Biotecnología en el Sector Agropecuario y Agroindustria*, vol. 12 (2), pp. 60–70, 12 2014. https://www.researchgate.net/publication/317501110_FIQUE_FIBER_AN_ALTERNATIVE_FOR_REINFORCED_PLASTICS_INFLUENCE_OF_SURFACE_MODIFICATION.

[18] P. Luna, A. Mariño, J. Lizarazo-Marriaga, and O. Beltrán, "Dry etching plasma applied to fique fibers: influence on their mechanical properties and surface appearance," *Procedia Engineering, 3rd International Conference on Natural Fibers: Advanced Materials for a Greener World, ICNF 2017, 21-23 June 2017, Braga, Portugal*, pp. 141–147, 2017. https://doi.org/10.1016/j.proeng.2017.07.021.

[19] S. F. Souza, A. L. Leao, C. B. Lombello, M. Sain, and M. Ferreira, "Cytotoxicity studies of membranes made with cellulose nanofibers from fique macrofibers," *Journal of Materials Science*, vol. 52, pp. 2581–2590, 3 2017. https://doi.org/10.1007/s10853-016-0551-y.

[20] M. F. Muñóz-Vélez, M. Á. Hidalgo-Salazar, and J. H. Mina-Hernández, "Effect of Content and Surface Modification of Fique Fibers on the Properties of a Low-Density Polyethylene (LDPE)-Al/Fique Composite," *Polymers*, vol. 10, 2018. https://doi.org/10.3390/polym10101050.

[21] T. Gómez, S. Zuluaga, M. Jiménez, M. A. Navacerrada, M. M. Barbero-Barrera, D. de la Prida, A. Restrepo-Osorio, and P. Fernández-Morales, "Evaluation of colombian crops fibrous byproducts for potential applications in sustainable

building acoustics," *Polymers*, vol. 13 (1), 101, 2020. https://doi.org/10.3390/polym13010101.

[22] K. G. Bastidas, M. F. R. Pereira, C. A. Sierra, and H. R. Zea, "Study and characterization of the lignocellulosic Fique (Furcraea Andina spp.) fiber," *Cellulose*, vol. 29, pp. 2187—-2198, 2022. https://doi.org/10.1007/s10570-021-04377-6.

[23] O. Muñoz-Blandón, M. Ramírez-Carmona, L. Rendón-Castrillón, and C. Ocampo-López, "Exploring the potential of fique fiber as a natural composite material: A comprehensive characterization study," *Polymers*, vol. 15, 6 2023. https://doi.org/10.3390/polym15122712.

[24] R. E. Guzmán-López, A. M. P. Cavada, F. de Isidro Gordejuela, and R. A. González-Lezcano, "Physical and mechanical properties of fique: Thermal conductivity and breaking strain," *Journal of Strain Analysis for Engineering Design*, vol. 60, pp. 323–335, 7 2025.

[25] B. Casares-Fernández and M. Jalalvand, "Effect of gauge length, cross sectional area and strain measurement methods on stiffness characterization of fique natural fiber," *Journal of Natural Fibers*, vol. 21, 2024. https://doi.org/10.1080/15440478.2024.2433056.

[26] J. Thomason, L. Yang, and F. Gentles, "Characterisation of the anisotropic thermoelastic properties of natural fibres for composite reinforcement," *Fibers*, vol. 5, no. 4, 2017. https://doi.org/10.3390/fib5040036.

[27] I. Toray Carbon Fibres America, "Ty-030B-01 Test Method Method for Determination of Tensile Strength Tensile Modulus of Elasticity, and Elongation at Break," 2003. https://wenku.baidu.com/view/cd01810a4a7302768e9939f8.html?_wkts_=1697088029617&needWelcomeRecommand=1//https://www.google.com/url?sa=t&rct=j&q=&esrc=s&source=web&cd=&cad=rja&uact=8&ved=2ahUKEwif5M-74e-BAxXfTkEAHZ0VARcQFnoECBQQAQ&url=http%3A%2F%2Fwww.kordcarbon.cz%2Fdownload%2F144%2Ftoray.pdf&usg=AOvVaw1CuOZeBdYDsHrZhhZlTL4E&opi=89978449.

[28] O. Muñoz-Blandón, M. Ramírez-Carmona, L. Rendón-Castrillón, and C. Ocampo-López, "Exploring the potential of fique fiber as a natural composite material: A comprehensive characterization study," *Polymers*, vol. 15, 6 2023. https://doi.org/10.3390/polym15122712.

Chapter 4

Thermo-chemical characterisation of fique and its chemical modifications

4.1 Introduction

In this chapter chemical and thermal characterisation of fique and treated fique fibres are explored, with a focus on Fourier Transform Infrared Spectroscopy (FT-IR), Thermogravimetric Analysis (TGA) and Derivative Thermogravimetric Analysis (DTG), as well as Differential Scanning Calorimetry (DSC). A literature review on the chemical and physical treatments applied to the fibres is carried out, followed by these characterisation techniques applied to natural fibres and more specifically to fique. Results on the tests done are presented and commented.

4.2 Literature review

Thermal stability of natural fibres in the manufacturing of composite materials needs to be accounted for to avoid degradation during the manufacturing processes, specially if these require to be carried out at high temperatures. Natural fibres of vegetable origin are composed of mainly three components: cellulose, hemicellulose and lignin. Fibre

degradation starts with its components degradation, with lignin and cellulose degradation typically occurring between 300 and 450°C, but degradation has been reported to start even earlier for lignin at 200°C, leading to changes in mechanical and thermal properties. If some proportions of lignin and hemicellulose are removed within some range, thermal stability can be enhanced, but lower lignin content may lead to thermal damage, causing secondary cell walls to be deteriorated [1].

As explained by several authors [1–3], there are two main treatments to modify natural fibre's surface. The physical treatments change the surface properties without altering the structural chemical composition and are those such as plasma, corona, ultraviolet, heat treatments, electron radiation, and fibre beating. The chemical treatments remove waxy components, impurities, and increase the proportion of cellulose in the fibres, as well as increasing its crystallinity. Chemical treatments are commonly used to enhance the chemical bonding or the mechanical interlocking between the fibre and the matrix by increasing the interface adhesion. The most commonly used chemical treatments are sodium hydroxide, silane, acetic acid, benzoyl chloride, maleated coupling agents, isocyanates, peroxide, and stearic acid.

Physical treatments aim, in general, to enhance the contact surface and the interlocking capability of the fibre surface by increased roughness, but can also alter the fibre internal structure by thermal degradation, that can affect physical properties of the fibres like weight, strength, colour and crystallinity [2].

More specifically, ultrasound treatments enhance mass transfer and dispersion phenomena. The micro-bubbles created during the process can facilitate, due to the effect of shear forces, the disintegration of solid particles, contributing to significantly increase the surface area, but it can also act as initiator of chemical cleavage, and catalytic or radical reactions [4]. Although ultrasound is considered a physical treatment, the fact that it contributes to break down carbohydrates, and when applied at different temperatures can remove lignin, pectin, hemicelluloses and other surface impurities, contributing to improve the fibre-matrix interaction [3], makes it stay in between the two broader type of treatments.

In general, chemical treatments increase the thermal stability of fibres, but some-

times this gain can have a negative impact in the composite performance, while in other cases these surface treatments lower the temperatures at which degradation happens, leading also to an increased thermal instability in the composite material. Sometimes, the combination of chemical treatments can lead to an increase in thermal stability, although this can impact the mechanical properties of the fibre. In any case, improving the thermal stability of the natural fibres will depend on the type of treatment and for how long the fibre is subjected to it [1, 5].

Hydrolysis is one of the most common chemical treatments. This can be acid or alkaline hydrolysis. In this chapter, acid hydrolysis is referred as hydrolysis, and alkaline hydrolysis as alkaline treatment or mercerisation, named after John Mercer, who in 1850 treated cotton with a solution of sodium hydroxide (NaOH) [6]. On the one hand, the hydrolysis is used to effectively break down the rigid structure of lignocellulosic materials and hydrolyses the hemicellulose fraction of the biomass. The acid treatment has also been found to hydrolyse the amorphous fraction of cellulose to hexose sugars, leaving behind the crystalline cellulose fraction. The alkaline treatment, in the other hand, is normally aimed at the removal of the lignin fraction via the degradation of the ester and glycosidic side chains, while contributing to the de-crystallization/depolymerization and swelling of the cellulose fraction, while also contributing to partial hydrolysis of hemicellulose [7]. The alkaline treatment also contributes to the surface roughness of the fibres by interrupting the hydrogen bonds and eliminating surface impurities improving its adhesive features by exposing cellulose microfibrils. This swelling of the cellulose fraction is induced by microporosity that allows diffusion of other chemicals, while the de-crystallization comes from transformation of cellulose I into cellulose II, changing the crystal structure from parallel to antiparallel [8]. Water molecules fill the spaces in the amorphous region of cellulose after cellulose particles are detached, and the alkaline treatment mainly contributes to the dissolution of lignin and hemicellulose as pointed out earlier [2, 3, 9], and as shown in Fig. 4.1.

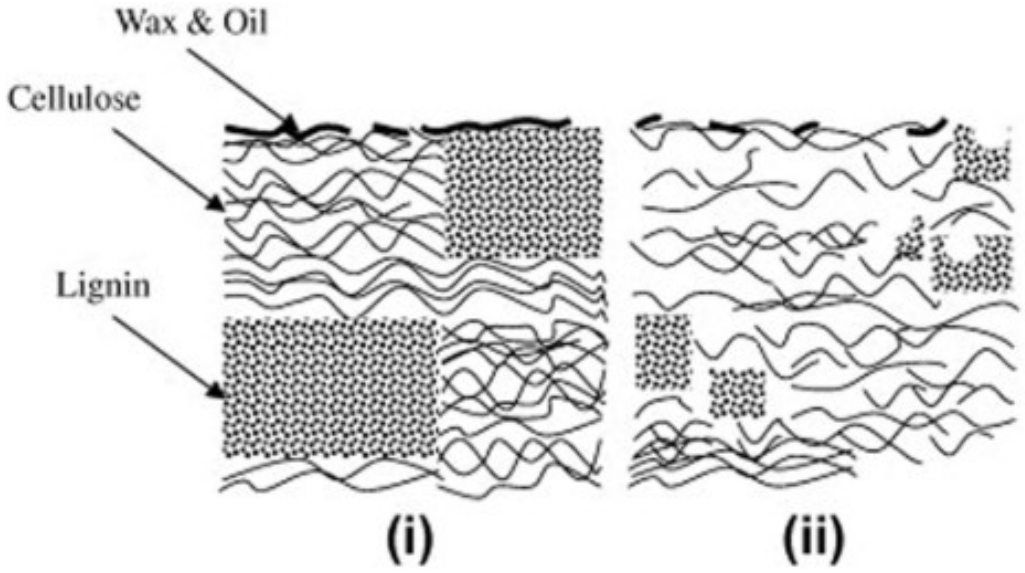


Figure 4.1: Untreated fibre (i) and alkaline treated fibre (ii), showing the effects on removal of surface components as well as its effects on cellulose and lignin removal [2].

4.2.1 Natural fibres FT-IR analysis

FT-IR is widely used in materials characterisation as a mean to provide a qualitative characterisation of materials composition, and as such, it has also been widely used in natural fibres [10].

Sgriccia *et al.* [11] applied FT-IR to kenaf, hemp, henequen, and flax, which were subjected to two different treatments. These fibres were treated with a 1% solution of 3-glycidoxypropyltrimethoxysilane in deonized water and ethanol in 1:1 ratio, and washed in deionized water after the silane treatment. After that, they were dried for 12 h in air and then in a convection oven for 5h. They were also treated in an alkali solution of 5% sodium hydroxide for 1 h at room temperature, and rinsed with tap water. They were let to dry at room temperature for 24 h. The FT-IR showed the CH- stretch at 2900 cm^{-1} is present in all fibres. All fibres not treated with alkali solution present the carbonyl (C=O) stretching peak at 1730 cm^{-1}, which corresponds with hemicellulose, and it dissapears after the alkali treatment. The 1500 cm^{-1} peak, deeply connected with the presence of lignin, is present in kenaf but not present in hemp fibres. The peak

at 664 cm^{-1} corresponding with the COOH bending peaks is present on all fibres as is the peak at 1432 cm^{-1} corresponding with CH_2 symmetric bending peaks. A peak at 1625 cm^{-1} is found in raw hemp and is reduced and removed in alkali treated hemp and kenaf respectively. This peak corresponds with the C=O bonds in the hemicellulose, and its change shows hemicellulose removal with the alkali treatment. A peak at 1239 cm^{-1} corresponding with C-O stretch is much larger for kenaf and silane treated kenaf than for the alkali treated fibre. This last peak is connected to the presence of lignin, so its reduction for the alkali treated kenaf fibres is explained by the lignin removal by the alkali treatment. Peaks corresponding to silane are expected at 766 and 847 cm^{-1}, but there is no evidence of silane presence, possibly due to the concentration being too small for being detected by FT-IR.

In the work presented by Abidi *et al.* [12] the study of cotton and its structural changes depending on the different developmental stages is studied using FT-IR analysis as the main tool. The peaks located at 2918 and 2850 cm^{-1} are attributed to CH_2 asymmetric vibrations due to the presence of wax substances present on the surface of the primary cell wall. These peaks' intensities decrease with further development. This is explained by the increased of the secondary cell wall with fibre maturity, since as the wall thickness increase, the contribution of the primary cell wall to the total weight of the fibre decreases, and here is where the waxy substances are mostly found, explaining the decrease on these two peaks. Bending of the O-H in adsorbed water molecules is located at 1627 cm^{-1}, and it decreases the older the fibre gets; this is explained by the decreased surface area and the reduced accessibility of water molecules to the internal hydroxyl groups to establish hydrogen bonds, explained by the polymerization reaction that leads to cellulose macromolecules and an increased crystallinity. The two vibration bands at 3280 and 3335 cm^{-1} are attributed to O-H stretching. The older the fibres the lower the intensity of the first band and the higher the intensity of the second one. The peak located at 1733 cm^{-1} is associated to the vibration of the C=O stretching vibration and it is associated with the presence of esters or amides, and its variation at different stages shows structural changes. During fibre development, while a band at 1236 cm^{-1} disappears another one at 1204 cm^{-1} appears, being attributed to the C-O-C stretching

mode of the pyranose ring. Almost simultaneously, a band at 900 cm^{-1} also appears, this one being attributed to the β-linkage, and making these two bands the secondary cell wall's fingerprint. The peak at 710 cm^{-1} is also attributed to the β-linkage, showing that cellulose synthesis during the development of the secondary wall is accompanied by increased crystallinity. Other peaks are found at 1105 cm^{-1} (anti-symmetric in-plane ring stretching band), 1056 cm^{-1} (C-O stretching mode), while others like the one at 1017 cm^{-1} shifts over to 1031 cm^{-1} (C-O stretch) the later the harvest is done. This work shows that the development of secondary wall can be tracked by the changes presented in the FT-IR bands.

The work done by Fernandes *et al.* [13] uses sisal to reinforce cork-polymer composites. As part of this work sisal fibre is chemically treated with a surface alkali treatment consisting on immersing the fibres in sodium hydroxide solution at 5% w/v for 2 h at room temperature. Fibres were then washed with distilled water and air-dried at room temperature before going on a vacuum oven at 70 °C. FT-IR was used to confirm the chemical treatment and composition of the fibres after treatment. The disappearance of the carbonyl band between 1660 and 1760 cm^{-1} after the fibres had undergone the alkali treatment is aligned with the partial dissolution of hemicellulose, directly linked with the significant weight loss after treatment of the fibres. A slight decrease of intensity around 1610 cm^{-1} in the treated fibres is attributed to the removal of aromatic-lignin impurities.

Khusairy Bin Bakri and Jayamani [14] work focus on bamboo, betel nut, and hemp fibres, which are subjected to an alkali treatment in a solution of 5% wt of NaOH with distilled water for 30 minutes. All fibres were dried in an oven at 60 °C for 2 days. FT-IR results show here how for bamboo fibres the alkaline treatment makes the band at 2118 cm^{-1} disappear, due to the break of the triple bond structure of alkynes into a double bond structure, as well as for the nitriles. In untreated fibres, the C=C stretching bond is seen at 1641 cm^{-1}, linked to lignin, while the peak at 1431 cm^{-1} represents the bending bond of C-H present in cellulose, hemicellulose, and lignin. Stretching bond of the C-O group of alcohol is present at 1099, 1036, and 1011 cm^{-1} peaks. For betel nut fibres, a band at 2146 cm^{-1} for the alkynes and nitriles triple bonds is found, while the

C=C stretching bond is shown in 1728 and 1605 cm^{-1} peaks linked to the presence of lignin. Cellulose, hemicellulose, and lignin presence are seen in peaks at 1331 and 1242 cm^{-1} linked to the C-H bending bond. The main changes identified for treated betel nut fibres are the intensity decrease at 1331 and 1242 cm^{-1} bands, since the alkaline treatment breaks C-H bending bond structure promoting hydrogen bonding. For hemp, a peak at 2893 is attributed to the C-H and O-H stretching bonds for untreated and treated fibres respectively, present in cellulose and lignin.In the case of treated hemp, bands at 1433, 1329, and 1253 cm^{-1}present a reduced intensity when compared with the untreated fibres. Interestingly, a band at 905 cm^{-1}, linked to the aromatic group present in lignin shows a reduction in the treated fibres, causing the smell of hemp fibres to disappear when treated. For all fibres peaks at 3500 and 3000 cm^{-1} are present for O-H stretching. In general, the alkaline treatment modified the natural cellulose by bond structure or its functional groups, increasing the amount of amorphous cellulose.

Ilyas *et al.* [15] study sugar palm fibre and how chemical treatments such as mercerisation with NaOH and delignification with sodium chlorite ($NaClO_2$), them referred as alkali and bleaching treatments respectively, affect the fibre. FT-IR is used to get spectra of the untreated and treated fibres to assess chemical changes. The ester groups in the hemicellulose or the ester linkage of the carboxylic groups in hemicellulose and lignin are identified by the 1719 cm^{-1} peak attributed to the C=O stretching. While the alkali treatment makes this band disappear, the bleaching treatment does not, and this is attributed to the alkaline treatment partly removing hemicellulose and lignin from the fibre. Lignin aromatic skeletal vibrations are seen in 1520 and 1510 cm^{-1} peaks, with peaks at 1227, 1507, and 1593 cm^{-1} also associated with the presence of lignin, with these peaks disappearing after the bleaching treatment. Other bands such as the ones found at 1650, 1630, 2900, 1030 cm^{-1} and some others detailed in their work are seen in all spectra regardless of the chemical treatment of the fibres.

Jayamani *et al.* [16] use kenaf fibres treated, among others, with an alkali treatment 5% wt of NaOH for 1 h at 25 °C. In kenaf raw fibres 8 predominant peaks are identified. Reduction and shift of the bands at 3350, 1443, and 1054 cm^{-1} after the alkaline treatment are related to the reduction of O-H bonds stretching, predominant in cellulose

along with the C-O bending, as well as the lignin predominant O-CH_3, O-H and C-H bending. The most significant change is the disappearance of the band at 1267 cm^{-1}, which highlights the removal of the C-O-C and C-C stretching bonds found in lignin. Peaks at 2835, 1823, 1665, and 851 cm^{-1}, despite suffering some shifting after the chemical treatment do not show any significant reduction.

In the work done by Tenazoa *et al.* [17] cabuya fibres treated in alkaline solution are studied. The alkaline treatment is done in 0.5 M NaOH solution at 70 °C for a period of 30, 60, and 120 minutes. Fibres are washed in distilled water and dried in an oven for 12 h at 60°C. The main difference between treated and untreated cabuya fibres is that after the treatment, the band around 1730 cm^{-1} attributed to the C=O bond in hemicellulose completely disappears. On top of this, the peaks around 750 cm^{-1} attributed to the C-H (para)bonds associated with the presence of lignin are removed for the treated fibres, although the presence of lignin is still strong with the C=C peak around 1500 cm^{-1} still present.

Freitas *et al.* [18] use rice straw to study how ultrasound treatments compared to alkali and bleaching treatment. For the sonication treatment a high-intensity ultrasonic homogenizer is used over an aqueous dispersion of 5% w/v of the fibre at 750 W power, 20 kHz frequency, and 40% sonication amplitude for 30 minutes. For the alkali treatment a 4.5% w/v NaOH solution is used at 100 °C for 3h. The bleaching treatment uses a 1.7% w/v solution of sodium chlorite. A combination of ultrasound and bleaching is also done to the fibres. Drying conditions vary between treatments. Following FT-IR results, the peak at 1730 cm^{-1} corresponding with the C=O stretching vibration of the carboxylic groups and esters disappears partially and totally for alkali and alkali+bleached treated fibres respectively, but was still present in the fibres that had undergone sonication and sonication+bleaching treatments. The lower intensity of the band at 1645 cm^{-1} for the alkali and bleached treated fibres, assigned to the O-H bending vibration of adsorbed water, shows a partial removal of hemicellulose for these fibres. Lignin removal is visible in alkali only treated fibres and all bleached samples by the absence of the peak at 1511 cm^{-1}, which corresponds to the C=C stretching vibration of the aromatic rings present in lignin. The band at 1033 cm^{-1} linked to the stretching vibration of acetal linkage

present in cellulose and hemicellulose is present on all fibres. Finally, the band at 898 cm^{-1} becomes more visible for the bleached samples, since the cellulose concentration is increased after the removal of hemicellulose and lignin fractions, as it is associated to the β-glycosidic linkage in cellulose I structure which shows in the C-O-C stretching vibration.

Prosopis juliflora is the fibre used in the work done by Yadav and Singh [19]. Fibres were extracted by immersing some stems in water and some others in an alkali medium for 30 days. This soaking process facilitates the fibre extraction. After drying them, fibres were alkali treated in a 6 % wt solution of NaOH for 24 h at room temperature, and later dried in an oven for another 24 h at 40 °C. The FT-IR is used to have a look at the chemical composition of treated and untreated fibres. Some peaks are found in both cases, with slight shifts, and other peaks completely disappear. In the first group, a band at 3331 cm^{-1} associated with the O-H stretching vibration shows the presence of cellulose; at 2919 cm^{-1} a band associated to the C-H stretching vibration; 1420 and 1437 cm^{-1} are the peaks for untreated and treated fibres for the CH_2 symmetrical bending; a peak at 1315 cm^{-1} for the C-H bending vibration; the β-glycosidic linkage peak appears around 1025 cm^{-1}; while a peak at 512 cm^{-1} appears for the pyranose ring present in cellulose. In the second group the peak at 1740 for the C=O stretching vibration disappears for the treated fibres, as well as the one found 1214 cm^{-1} for the anti symmetrical bridge of C-O-C stretching vibration, due to the removal of lignin and hemicellulose due to the chemical treatment.

4.2.1.1 Fique FT-IR analysis

In the work by Gañán and Mondragon [20] the surface modification of fique fibres is explored as well as the impacts on some of its properties. Sodium hydroxyde is used here for mercerisation, and maleic anhydride, acrylic acid and γ-methacryloxy propyl trimethoxy silane as coupling agents. In this case a 20 wt% sodium hydroxide was used for one hour. Before being submerged into the solution the fibres were pre-dried at 105°C for 24 h. After the treatment the fibres were thoroughly washed with distilled water with some drops of acetic acid until neutral pH was measured. After that, fibres

were dried again at 105°C for 24 h.

For applying the maleic anhydride, this was solved in acetone, and fibres that had been previously pre-dried were soaked in this treatment at 55°C. After the application, the fibres were washed with acetone and distilled water, and dried for 24 h at 105°C. Similarly for acrylic acid, but in this case the solvent was distilled water. The γ-methacryloxy propyl trimethoxy silane was also dissolved in water, that had been acidified to a pH of 3.5 with acetic acid. Fibres were soaked in this solution for 1 h at room temperature, and later dried for 24 h at 105°C. The highlighted changes to the fibres are the reduction or disappearance of the peak at 1737 cm^{-1}, associated with the reduction of the carbonyl group; the reduction of the peak at 1268 cm^{-1}, related to the C-O ring in lignin. The bonding agents react with the fibre's surface, inducing visible changes in the FT-IR results too. The thermal stability of the fibres is modified, with silanization reducing the water intake, decreasing the hydrophilic behaviour of the fibres. The most effective treatments for thermal stabilization are the aforementioned silanization and the esterification using acrylic acid. The mercerisation process has a clear effect in reducing the fibre size, which is not appreciated for the other treatments. Mechanical properties wise, the mercerisation process clearly increases the fibre strength, by increasing the proportion of cellulose and reducing the fibre's size. Added on top of this is that the removal of hemicellulose leads to a more homogeneous structure with minor voids, and the change in orientation of the molecular chains of cellulose, increasing its crystallinity. In general, all treatments introduce changes in the fibre surface that lead to a reduction on the hydrophilicity of the fibre allowing for a better compatibility with polymeric matrices.

Gómez *et al.* [21] characterize fique fibres after treating them with alkali treatment on slack and under a 1 N load. In both cases the fibres are treated with NaOH solution 5% w/v for 4 and 24 h with the fibre weight to alkaline solution volume ratio being 1:4 in all cases. In this study, it is found that treating the fibre under load does not significantly change its chemical structure, since FT-IR results are very similar. In general, the peak at 2918 cm^{-1}, corresponding to the O-H stretching of methyl and methylene groups in cellulose hemicelluloses and lignin do not show variations across

the spectra. The peak at 2850 cm^{-1} is associated here to lignin and waxes through the C-H stretching, and in this case it becomes sharper after the treatments. The vibrations at 1735 $^{-1}$ corresponding to acetyl and uronic ester groups in hemicellulose and in the ester linkage of carboxylic group of lignin shows a significant decrease after both treatments; as it is the band around 1230 cm^{-1} associated with the C-O-C stretch of ether groups present in lignin and hemicellulose. The conclusion here is that the alkali treatment is very effective in removing hemicellulose, but the presence of lignin after treatment is shown by the 1510 and 1460 cm^{-1} that corresponds to the aromatic rings and C-H deformations respectively, highlighting that the alkali treatment is not as effective in removing lignin which is resistant to chemical attack due to the strong C-C linkages.

Muñoz-Vélez *et al.* [22], in the work done with surface modifications of fique use the alkalinization treatment with a water solution of sodium hydroxide (NaOH), with a 2% w/v at a 25°C for 1 h. After the treatment the fibres are washed with distilled water to remove any remains of the treatment, and then dried in two stages: first, at ambient temperature for 12 h, and later at 60°C in an oven for 24 h. In this work silanization treatment is also studied. The FT-IR analysis shows typical peaks, with 3335, 2923 and 1029 cm^{-1} associated to OH, C-H and aromatics linked to cellulose, hemicellulose and lignin structures. The application of the alkalinization treatment brings about some changes in the surface composition, with peaks at 2865, 1370, and 1243 cm^{-1} linked to the disappearance of associated lignin links. In the figure number 2 in their work it can be seen that peaks at 2923 and 2865 merge in a less sharper peak. The peak at 1732 cm^{-1} also disappears, this one associated with carbonyl groups present in hemicellulose and pectins.

In the work done by Luna *et al.* [23], dry etching plasma treatment is used to modify the surface of the fique fibres. By using a DC sputtering system and employing Argon gas, exposing the fibres to the same energy at different exposure times, with these being 200, 400, 600, 800 and 1000 s. The SEM analysis of the fibre's surfaces shows a rougher and coarser surface, even with the formation of some cracks. These changes are attributed to the ion bombardment, which starts removing material surface

atoms, giving place to small and isolated microcracks that tend to coalescence with the increase in treatment time above 800 s. In this case, FT-IR analysis is not undertaken, so assessment of components exposed by the treatment is not explained, but this roughness increase with mechanical properties affectation is aimed at increased compatibility of the fibres with polymeric matrices, but that has not been explored in this work.

Alkali treated fibres are the focus of study for Guzmán *et al.* [24], where fique fibres were immersed in a NaOH solution at room temperature for 30 minutes. After being washed with water, they were dried in an oven at 60 °C for about 6 h. The FT-IR study shows that for treated fibres, the peak at 1730 cm^{-1} attributed to the C=O stretching vibration disappears due to the removal of hemicellulose. A significant reduction is seen in the peak at 1240 cm^{-1} attributed to the C-O stretching vibration of the acetyl group in lignin. The peak at 2915 cm^{-1} attributed to the C-H stretching vibration in cellulose and hemicellulose is also reduced after treatment, again due to the removal of hemicellulose. The following peaks are present for untreated and treated fibres: 3330 cm^{-1} attributed to the water molecules trapped in the cellulose structure; a band at 2850 attributed to the C-H stretching vibration in cellulose and hemicellulose materials; and the peak attributed to glycosidic linkage in cellulose at 1026 cm^{-1}.

In the work done by Salinas *et al.* [8] fique dust is used. The dry dust was obtained by immersing fique dust in water for two days and later drying it in an oven for two more days at 80 °C. After the drying stage, dust was immersed into a 8% p/v NaOH solution for four days and then dried again the same way as before. This is the alkaline fique dust. The alkaline treatment successfully removes hemicellulose, which is proved by the removal of the bands at 1742 and 1242 cm^{-1}, corresponding to the C=O stretching vibration and the C-O stretching of esters present in hemicellulose.

4.2.2 Thermogravimetric analysis of natural fibres

Ray *et al.* [25] studied jute fibre thermal behaviour along with the alkali treated fibres. The alkali treatment consisted of immersion for 2, 4, 6 and 8 h in a 5% NaOH solution at 30°C, and then washed to remove any remaining NaOH. A 48 hours drying period at room temperature was followed by 6h drying in the oven at 100°C. The findings from

this study are that alkali treated fibres shifted moisture release to a lower temperature than the non treated fibres. This tendency is explained by the surface area increase in the treated fibres, hence facilitating evaporation at lower temperatures. This shift to lower temperatures is also observable in the cellulose and hemicellulose degradation, that went from 362.2 and 297 °C to 348 and 274.3 °C respectively. While cellulose percentage of degradation remained almost constant, hemicellulose degradation saw a 41% reduction, showing that the mercerisation treatment reduces the hemicellulose significantly. This reduction creates a lignin-cellulose complex that is more stable than the original fibre, causing the residual char left to be increased by 7%.

Joseph *et al.* [26] studied the effect of chemical treatments on banana fibres, with alkaline treatment being one of them. A 2h treatment in a 4% NaOH solution at room temperature, with fibres being washed with distilled water before being dried in the oven. The TGA analysis shows how the treated fibres weight loss at 100°C was slightly higher than for the non treated fibres, suggesting that fibre fibrillation after the treatment facilitates water evaporation. From the derivative analysis, one degradation step is seen for both treated and untreated fibres, between 230 and 350°C. For the treated fibres, the degradation peak is 32°C higher than for untreated ones, with a higher percentage of thermal residue, suggesting an increase in thermal stability for the alkaline treated fibres.

Mofokeng *et al.* [27] study the thermal properties of sisal fibre, poly-lactic acid (PLA), and polypropylene (PP), as well as sisal reinforced PLA and PP. The TGA was done under nitrogen flow (20 ml/min) and heated from 30 to 600°C at a rate of 10°C/min, with samples being between 5 to 10 mg. Sisal moisture loss happens around 100°C, showing a two-step degradation process, with the first significant mass loss happening at 285°C, and the second one at 357°C, these being due to thermal depolymerization process of hemicellulose and the breaking of glycosidic linkages of cellulose, and to cellulose decomposition respectively.

Alvarez *et al.* [28] studied the combustion of biomass through thermogravimetric analysis and differential thermogravimetry, from which degradation of different natural fibres, as well as some components are obtained. Cellulose is shown to start oxidative

degradation between 300 and 360°C, while lignin chard combustion occurs between 450 and 600°C. In the biomass studied here, pineapple leaf may be also relevant, with oxidative degradation occurring between 250 and 380°C.

Kiziltas *et al.* [29] studied the thermal stability of flax, hemp and kenaf as part of their characterisation of natural fibres reinforced polyamide. The TGA was done under a nitrogen atmosphere (20 ml/min) from room temperature to 600°C at a heating rate of 10°C/min. For the three natural fibres and their blends three mass loss stages were identified. The first one extends to 120°C and corresponds to moisture loss. The second one is located between 270 and 290°C and corresponds to the thermal depolymerization or decomposition of hemicellulose. The third and last weight loss is located between 350 and 375°C and corresponds to cellulose degradation.

In the review made by Asim *et al.* [30] it is well presented the three stages of thermal degradation followed by natural fibres according to different sources, as shown in Fig. 4.2, and it can be summarized as follows. The first weight loss stage occurs between 50 and 100°C and is associated with moisture evaporation from the fibres. The second stage occurs between 200 and 300°C and is mainly attributed to the depolymerization of hemicellulose, although in some of the works this is extended to 370°C to include the division of glycosidic linkages in the cellulose, as well as pectins degradation. In the third and last stage, between 350 and 500°C, degradation of cellulose and lignin at higher temperatures takes place. Other authors [1,31] talk about three stages of degradation but with the second stage having a wider window (200-500°C), where degradation of hemicellulose, cellulose and lignin is placed within the third stage, this being the formation of active coal as a form of residue. This approach is not common and this same author, in the review done for different natural fibres used in composites manufacturing reported on a first stage that can start as early as 25°C until 200°C associated with water evaporation; a second stage from 190 to 350°C associated mostly with hemicellulose, but also with cellulose and lignin degradation; and a third stage that goes from 280 to 600°C associated mostly with α-cellulose and lignin degradation, although lignin is reported to start degrading from 210°C [31].

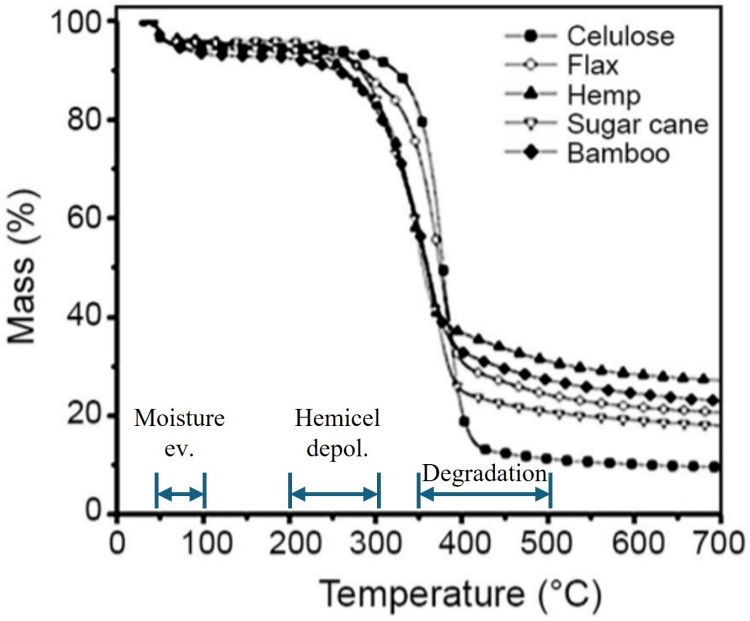


Figure 4.2: TGA curves of different natural fibres and cellulose from [30], adapted with the thermal degradation stages identified in the literature for natural fibres.

The thermal analysis by Thomason and Rudeiros-Fernández [32] carried out on as received coir and date palm fibres was done under both nitrogen and air atmospheres at a 60 ml/min flow rate at a heating rate of 10°C/min up to 600°C. The results show very similar mass loss behaviour by both fibres, with a higher mass loss at higher temperatures for the oxidative atmosphere. Under nitrogen three main regions are identified for both fibres. The region below 150°C is attributed to the loss of moisture in the fibres; between 150 and 300°C this second region is associated with the degradation of hemicellulose and pectins; the third region between 300 and 400°C corresponds to the degradation of cellulose. These last two regions are identified by two peaks in the DTG, with the first one being like a shoulder in the curve to the second one. Lignin degradation is expected to happen at higher temperatures, but a fourth peak in the DTG is only found under the oxidative atmosphere experiments and it is attributed to the oxidative decomposition of the charred residue.

In the analysis done by Song *et al.* [33] on willow bark, an alkali treatment in different concentrations (2%, 5%, 10%, and 15%) at 30°C during 5h was applied to the fibres in

order to study the impact on their thermal properties as well on the crystalline structure of cellulose. The TGA analysis was done under nitrogen atmosphere with a 20 ml/min flow rate, at a heating rate of 10°C/min up to 500°C, at which the samples were held for 5 minutes. In this case, the introduction of the alkali treatment lead to a reduction in the thermal stability of the natural fibres, with the onset degradation temperature going from 297.62°C to 284.5°C and the temperature at the highest degradation speed decreasing from 350.63°C to 329°C.

Heckadka *et al.* [34] study the thermal stability of jute and flax fibres and their composites, as well as the alkali treated fibres with a 10% NaOH treatment. Samples of 15 to 18 mg are heated from 50 to 700°C at a heating rate of 10°C/min under nitrogen flow. The findings on thermal stability and fibre behaviour are quite similar for both fibres, which present three events of mass loss during the test: the first event is associated with hemicellulose degradation, which happens at 276°C for flax and at 288°C for jute, with mass losses of 13.95% and 11.61% respectively; the second mass loss is associated with cellulose, which degradation happens at 360°C for both fibres with mass losses of 48.99 and 56.09% respectively; the last mass loss associated with lignin degradation happens at 600°C for both fibres, with mass losses of 15.31 and 17.92% respectively. For both cases, the alkali treated fibres see a thermal stability increase, with the first degradation happening now at 360°C for the treated flax, and at 354.47°C for the treated jute, with mass losses of 54.43 and 62.5% respectively; the second degradation peak happens for the treated flax at 419°C with a 16.97% mass loss appearing more like a shoulder in the curve, also visible in the non treated flax, with no peak in this region for jute, that presents only two events when treated; the last mass loss event happens at 605 and 604.47°C for flax and jute respectively, with mass losses of 18.84 and 23.12% respectively too.

Begum *et al.* [35] study the thermal degradation of jute and fire retardant treated jute fibres. Seven different woven structures made of 100% jute are analysed in this study through a TGA of 10 mg samples, heated from ambient temperature to 600°C at a heating rate of 10°C/min. For jute, hemicellulose degradation occurs between 250 and 290°C with the weight loss rate changing between 250 and 270°C shown in the

DTG as a shoulder just before a sharp weight loss rate change occurring between 350 and 370°C and corresponding to cellulose degradation. A distinct weight rate change up until 490 or 500°C corresponds to the degradation of the lignin component.

Full thermal degradation of lignocellulosic fibres is expected above 400 °C, but the three main components are affected at different temperatures range, with the proportion of them present on the fibre affecting the overall degradation effect. Hemicellulose has earlier degradation than cellulose because despite the higher degree of branching of hemicellulose, the degree of polymerization is higher in cellulose, but its reduced presence in comparison will affect degradation proportionally. Similarly, the presence of lignin will limit the effect of the fibre degradation, with this component starting to thermally degrade earlier than cellulose and hemicellulose but extending to higher temperatures [36].

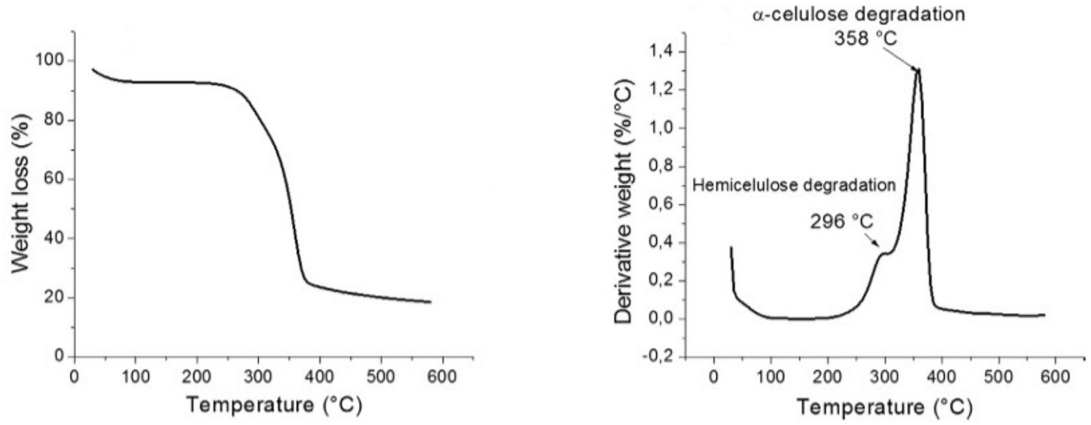
4.2.2.1 Fique fibre thermogravimetric analysis

In the work done by Gómez *et al.* [21] cited earlier, where chemically treated fique fibres are characterised the thermogravimetric analysis shows weight loss below 100°C that is linked to water evaporation. Then, three thermodegradation processes are identified: (i) around 300°C hemicellulose degradation; (ii) a peak at 360°C is attributed to cellulose decomposition; (iii) lignin decomposition occurs slowly in a wide range as it is the most difficult to decompose.

In the work done by Muñoz-Vélez *et al.* [22], fique fibres are subjected to an alkalinization treatment with a water solution of sodium hydroxide (NaOH), with a 2% w/v at a 25°C for 1 h. After the treatment the fibres are washed with distilled water to remove any remains of the treatment, and then dried in two stages: first, at ambient temperature for 12 h, and later at 60°C in an oven for 24 h. The thermal analysis shows a first loss of weight attributed to water evaporation between 23 and 100°C. In the untreated fibres, between 200 and 325°C depolymerization of hemicellulose takes place, with the peak loss at 304.82°C. The biggest mass loss takes place between 325 and 400°C for untreated fibres, and for the treated fibres it happens between 200 and 400°C. This corresponds to cellulose degradation, and it is 11% higher for the treated

fibres, showing that there is an apparent increase in cellulose, which effectively is the proportional increase of cellulose/fibre ratio as a consequence of hemicellulose and lignin removal due to the alkalinization treatment.

The thermal stability study of fique by Hidalgo-Salazar and Correa [37] was carried out at 10°C/min under nitrogen flow and shows three weight loss regions. The first one, under the 100°C is attributed to the evaporation of superficial water. The other two regions are associated with the degradation of the fibre constituents. In the DTG curve, as shown in Fig. 4.3 (b), a shoulder in the curve at 296°C corresponds to maximum weight loss rate of hemicellulose, while the clear peak at 358°C is associated with the maximum weight loss of α-cellulose. The residual weight is almost 16% at 600°C for this case.

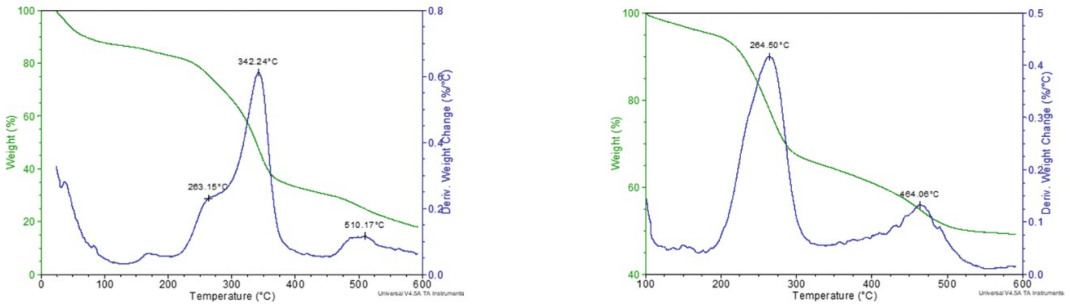


(a) (b)

Figure 4.3: Weight loss (a) and DTG (b) curves of fique at 10°C/min heating under nitrogen flow as presented in the work by Hidalgo-Salazar et al. [37], showing the hemicellulose and α-cellulose peak degradation temperatures.

In the work done by Salinas *et al.* [8] fique dust was chemically treated with an alkaline solution and then thermally characterised. The fique dust was submerged in the NaOH solution at a 8% p/v for four days and then washed with distilled water until a neutral pH was obtained. This dust was then dried in the oven at 80°C for 48h. The thermal characterisation of the dust and the treated dust shows the disappearance of the shoulder in the DTG curve associated with hemicellulose degradation as shown in Fig. 4.4. In this case, it is argued that the alkaline treatment has removed hemicellu-

lose, and through the structural transformation of cellulose I in cellulose II, made this last component more thermally unstable, leading to a lower temperature at which the decomposition rate is the highest for cellulose, which goes from 342°C to 264°C.



(a) (b)

Figure 4.4: Weight loss and DTG curves of fique dust (a) and fique alkaline dust (b) at 20°C/min heating under nitrogen flow as presented in the work by Salinas et al. [8], showing the shoulder disappearance for the alkaline dust associated with hemicellulose and the increased thermal instability for the treated dust.

4.2.3 Differential Scanning Calorimetry (DSC) of natural fibres

Differential scanning calorimetry is a thermo-analytical technique used to study glass transition, melting, crystallization and decomposition temperatures as well as crystallinity, phase changes and stability in materials. It measures the heat flow difference between the sample and a reference sample, as shown in Fig. 4.5, having as an output a thermogram of heat flow vs. temperature, where baseline changes as well as endotherms and exotherms show the material behaviour.

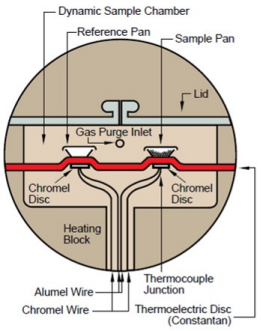


Figure 4.5: Diagram of the functioning principle of the DSC technique [38].

Wielage *et al.* [39] study the thermal stability and behaviour of retted flax and cellulose through DSC at a heating rate of 10 K/min in nitrogen atmosphere. From this, an endothermic peak in the range between 303 and 345°C is clearly visible for the cellulose, although not so distinctive for the flax, since the curve is much more flat for the latter, which presents an onset of a baseline change at 345°C. In the curves presented in Fig. 4.6, for both cases a baseline change between 60 and 150°C occurs, which is generally linked with the water molecules evaporation. The endothermic peak in cellulose is explained by means of the decomposition of this component via two competing pathways: a depolymerization process and a dehydration process.

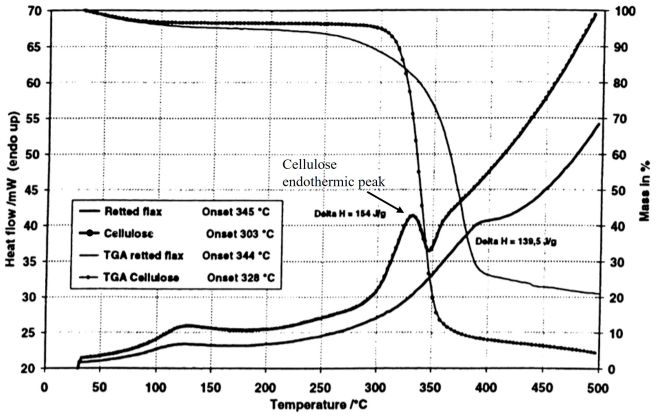


Figure 4.6: DSC and TGA of retted flax and cellulose from [39], where the cellulose endothermic peak can be clearly seen in contrast with the more flat evolution for the flax case.

Yeng *et al.* [40] study the thermal properties of cellulose and regenerated cellulose for the production of biocomposites. This regenerated cellulose is obtained by means of cellulose dust being added to a solution of NaOH and urea, where the cellulose is dissolved. Then, distilled water was used to remove any remaining NaOH and urea and the solution in water filtered with filter paper. The remaining residue of cellulose was centrifugated and the process repeated three times before the regenerated cellulose was dried at room temperature. The DSC was done on samples between 6 and 12 mg, at a heating rate of 10°C/min under a continuous nitrogen flow at a flow rate of 20 ml/min. In the thermograms of cellulose and regenerated cellulose a first endothermic event is visible from 40 to 80°C for the former and from 60 to 120°C for the latter.

This range difference is justified by the higher amount of amorphous components in the regenerated cellulose than in the cellulose. The cellulose presents a second endothermic event at 319.67°C, while the regenerated one presents it at a slightly lower temperature of 314.83°C. This small difference is explained by this endotherm being associated with the crystalline part of cellulose, its melting and depolymerization due to the breakage of the glycosidic bonds. In the regenerated cellulose the breakage of more intra-molecular and inter-molecular hydrogen bonding in the molecular chain during the dissolution process leads to lower crystallinity. This change in the molecular structure is also proved by the TGA results presented in their work.

4.2.3.1 Differential Scanning Calorimetry of fique fibre

In the work done by Souza Oliveira *et al.* [41] fique fibre thermal analysis is carried out via DSC in the range between 80 and 200°C at a heating rate of 10°C/min, under a nitrogen atmosphere. The results show a visible but not very pronounced endothermic peak at 147.4°C. This is compared with the results obtained by Ovalle *et al.* [42] where DSC is run at 10°C/min from 35 to 500°C under nitrogen atmosphere too. In here water evaporation is reported between 30°C and 130°C, with 90°C being the value for raw fique, which is slightly higher than what is reported elsewhere. This higher value is justified by the higher presence of amorphous components like hemicellulose and lignin which retain moisture by chemi- and physisorption processes in contrast with the delignified fibres that show this peak at 79°C. From 165 to 260°C shows here a change in baseline linked with the degradation of hemicellulose, followed by an exothermic peak, related to α-cellulose depolymerization, with the formation of 1,6-anidroglucose from 270 to 320°C. The raw/clean fibres also presented a endothermic peak at 360°C linked to the fusion and degradation cellulose's crystalline fraction. For the delignified fibres, an exothermic process taking place between 325 and 365°C is associated with the thermal transition of cellulose decomposition. After the delignification treatment, the cellulose peak changes from endothermic to exothermic, and it is suggested that this is due to the disruption of chemical linkages after the removal of non-cellulosic components, affecting the degradation behaviour of cellulose. From Souza Oliveira's

study it could be said that although the temperature range used can be useful to study the level of cure in the epoxy resin, in the study of fique fibres, the requirement of the full range from room temperature to allow moisture to evaporate to be able to see cellulose degradation clearer in the higher end too may be required, so better conclusions could be draw regarding fique characterisation.

García Sánchez *et al.* [43] study fique fibre morphology and thermal characteristics for its use as insulator. For this, raw fibre and fibre washed with fabric softener (one with the softener removed instantaneously and the other being soaked in softener for 24 hours) were used. DSC tests were carried at a heating rate of 10°C/min from -50 to 330°C as can be seen from Fig. 4.7. In all fibres it can be seen a first step from -14 to -7°C is linked to the glass transition temperature. This is followed by an endothermic reaction between 2 and 130°C, associated with dehydration of the fibre. Finally, an exothermic reaction between 293°C (soaked for 24h) and 301°C (raw fibre), which is associated to the combustion of the material due to the high temperatures reached, which tells the tests were carried out in oxygen reach atmosphere. This exothermic peak is attributed in other works to the depolymerization of cellulose [42] or hemicellulose degradation [44]. For the fibres washed with softener, another, smaller, endothermic event becomes visible between 134 and 149°C, and it is associated with structural water release, after this becomes more accessible after lignin is removed during the washing process, leaving cellulose microfibrils more exposed.

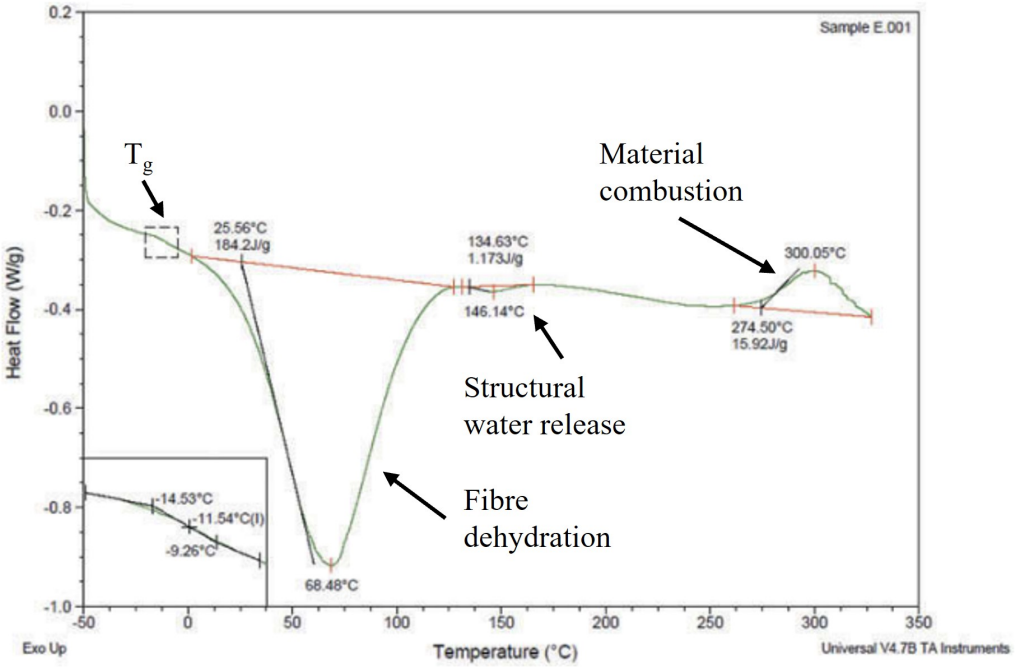


Figure 4.7: DSC of fique treated with softener from [43], where the different transitions are identified for this case.

Idarraga *et al.* [44] characterised fique fibre thermally in order to determine the appropriate temperature for hot pressing in manufacturing of fique reinforced polypropylene composite sheets. In this characterisation DSC was done on the fique fibres where two exothermic peaks are identified. The first peak happens at 295°C, with the onset at 260°C, and it is linked to hemicellulose degradation. The second one, with its peak at 390°C and starting at 360°C is reported due to cellulose degradation. Lignin degradation cannot be linked to one event, as its temperature range degradation is very wide, from 115 to 500°C.

Muñoz-Blandón [45] undertook a DSC analysis of fique over a temperature range of 0 to 350°C at a heating rate of 10 °C/min in an nitrogen atmosphere with a 50 ml/min flow rate. In their thermal characterisation of fique a first endothermic peak is reported at 142°C,and a second, more pronounced peak, at 193°C, attributed to vaporization of water absorbed in the fibres and fibre dehydration respectively, with nothing reported above 200°C.

The treatment of natural fibres, either chemical, physical, or the combination of both

alters their thermo-chemical characteristics impacting their mechanical properties and interaction with different matrices. Because of this, the study of differently treated fique fibres and their thermo-chemical characterisation to evaluate their potential uses and their use in different manufacturing methods is explored along the rest of this chapter.

4.3 Experimental

4.3.1 Materials

Fique fibres were provided by Compañía de Empaques through Universidad Nacional de Colombia in raw condition, and washed on arrival as explained in Section 3.3.1. Treated fibres were provided by Universidad Nacional de Colombia were the treatments took place and are explained as follows. These treatments, choses by Universidad Nacional, respond to the need of improvement of the fibre-matrix interface further along the manufacturing process of composites, and their choice corresponds to trialling treatments that have worked for other natural fibres and that have not been extensively studied on fique fibre.

4.3.1.1 Alkaline treated fibres

The alkaline treatment is a delignification process. In this case it is carried out at room temperature of ∼25-30°C. Firstly, a hydrogen peroxide, H_2O_2, (10% by weight) solution is prepared by pouring 180 grams of distilled water in a glass beaker, and adding 20 grams of hydrogen peroxide, mixing the solution manually. Secondly, the fique fibres (30 grams) are added to the solution and mixed, until they are completely immersed. Third, sodium hydroxide (NaOH) is added in flakes to the mixture to achieve a pH of 11.5, which requires 4.9 grams, making it a 2.4% by weight solution. Fourth, the fibres are left immersed in the mixture for 1h, with manually mixing every 15 minutes to avoid them to come to surface as froth is formed due to the delignification process. Fifth, the fibres are washed with abundant distilled water to remove any chemical residue before being dried for 3h at 105°C in an oven.

4.3.1.2 Acid hydrolysis treated fibres

The acid hydrolysis process, also called from here onwards as hydrolysis, requires, first, a sodium hydroxide (NaOH) solution to be prepared (17.5% by weight), for which to 247.5 grams of distilled water, 52.5 grams of NaOH are added, and mixed manually. Second, the fique fibres (30 grams) are added and fully immersed in the mixture, in which they are left for 2h. After that, the fibres are washed with abundant distilled water to remove any residual sodium hydroxide. The next step involves preparing another solution, this time of hydrochloric acid (HCl) 1M. This requires 289,05 grams of distilled water in a glass beaker, to which 10,95 grams of hydrochloric acid are added and then manually mixed. The solution is heated up until it reaches 80 °C, and at this point the fibres are added and let at that temperature in the solution for 2h. After that time, the fibres are washed with abundant distilled water to eliminate any residues. The last solution used is a sodium hydroxide (2% by weight), for which 6 grams of sodium hydroxide are added to 294 grams of distilled water in a glass beaker. This solution is then heated up to 80 °C, and fibres again immersed and left at this temperature in the solution for 1 additional hour. After that, the fibres are washed with abundant distilled water to remove any remaining chemicals on their surface before being dried in an oven for 3h at 105 °C.

4.3.1.3 High intensity ultrasonication (HIUS) treated fibres

This treatment is applied as complementary to the chemical treatments presented above, so some of the fibres that have undergone the alkaline and the hydrolysis treatments are also undergoing the High Intensity Ultrasonication (HIUS) treatment before the drying step described earlier. A 90% amplitude signal is used during 1h. Since it is not recommended to use the application of the sound energy in a continuously way, for every 59 seconds of activation there are 15 seconds of rest. After that, the drying stage of 3h at 105 °C takes place.

4.3.2 Methods

4.3.2.1 Fourier Transform Infrared Spectroscopy (FT-IR) analysis

An Agilent Technologies 4500 Fourier Transform Infrared (FT-IR) system was used, which was supported by a docking station and connected to a laptop for operation, to identify functional groups in the different materials analysed, so material identification could be performed. The interface used was a diamond-attenuated total internal reflectance (ATR), which required ensuring maximum contact with the interface by clamping the sample. A penetration depth of 2-4 μ m was established for all cases and a background scan was taken before each measurement after the contact area had been cleaned with acetone. For each differently treated fibre studied, ten samples were taken, which were later averaged and normalized. Data were processed using OriginLab software. Washed fique has been used as the baseline to compare the effect of the chemical and mechanical treatments on fique fibres.

4.3.2.2 Thermogravimetric analysis

A TA instruments Q50 TGA was used to analyse the thermal stability of fique fibres. Thermogravimetric analysis (TGA) was carried out under nitrogen flow (50 ml/min) on three samples per case, with them being close to 5 mg. Heating was done from 20 to 700°C at a heating rate of 10°C/min. Results presented are the averaged values from the three samples.

4.3.2.3 Differential Scanning Calorimetry (DSC) analysis

A TA Instruments Q20 DSC was used to identify endo and exothermic events in the fique fibre. A heating rate of 10°C/min from 20 to 450°C in nitrogen atmosphere with a flow rate of 50 ml/min. Three samples per fibre type above 5 mg were tested, and representative averaged values obtained.

4.4 Results and discussion

4.4.1 Fourier Transformed Infrared Spectroscopy (FT-IR)

The received fique presents a big lump peak at 3337 cm^{-1}, which appears for every other treated fibre, as shown in Fig. 4.8. This peak is associated with the OH stretching of the water molecules absorbed by the cellulose structure, and is commonly found in hydrophilic natural fibres [24]. This lump is consistent across all the different treated fibres, showing that water absorption is present in all cases.

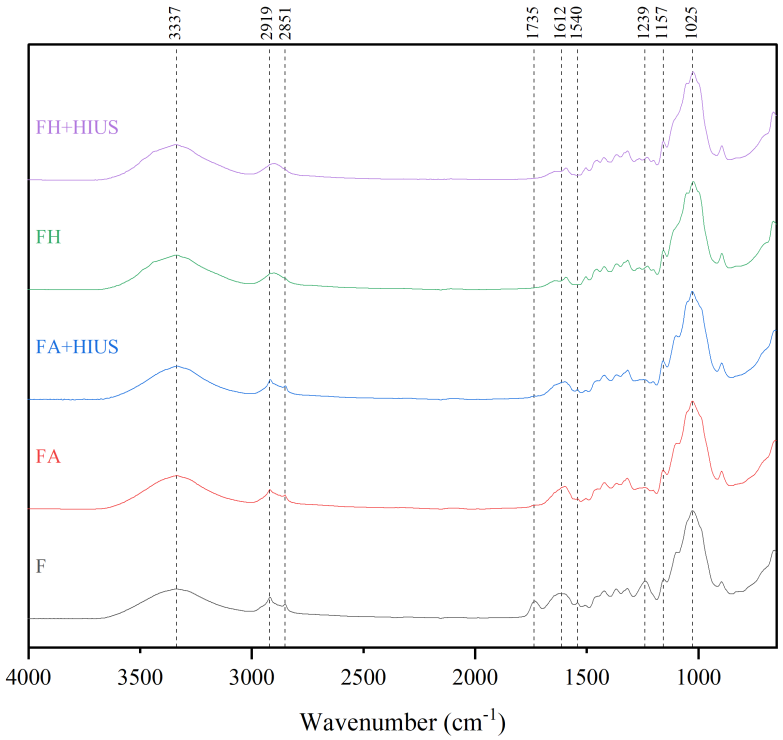


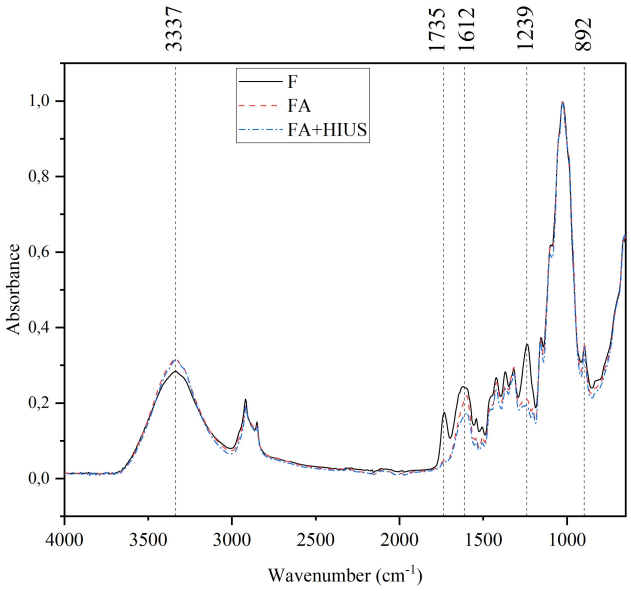
Figure 4.8: FT-IR results of washed fique (F) ready to use, and alkaline (FA), alkaline and high intensity ultrasonication (FA+HIUS), hydrolysis (FH), and hydrolysis and high intensity ultrasonication (FH+HIUS) treated fibres with lines highlighting the main areas of the analysis.

Two small peaks appear at 2919 and 2851 cm^{-1} in the raw fique and these are identified as CH stretching of cellulose and hemicellulose [24]. While these two peaks

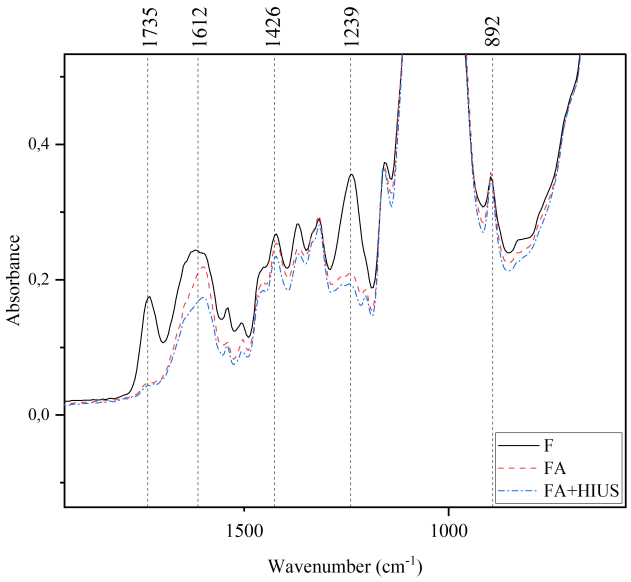
remain clear in the fique after the alkaline treatment, they become one more rounded peak when the fibre is treated with hydrolysis. At 1735 cm^{-1} there is a clear peak in the washed fique spectrum, that is identified with the stretching vibration of the carbonyl group, present in ester type bonds in the hemicellulose [24, 46]. This peak disappears for every treated fibre. The peak at 1612 is identified with the bending vibration of OH in the water molecules [18, 47], and although present for all the treated fibres it clearly reduces its intensity for the alkaline treatment, and even further in the fibres treated with hydrolysis, since there is a reduction in hemicellulose, the water trapped on it is also reduced. A peak at 1239 cm^{-1} identified with the stretching vibration of the C-O of the acetyl group is linked to the presence of hemicellulose and lignin [8, 24, 48], and its intensity significantly decreases for the treated fibres. The peak at 1157 appears for all fibres, washed and treated, and it is linked to the stretching vibration of C-O-C in cellulose and hemicellulose [48]. The biggest and most prominent peak for all fibres is the one at 1025 cm^{-1}, and it identifies the glycosidic linkage through the stretching vibration of the C-O-C bond, which is the backbone of the cellulose [24, 49]. The intensity of this peak allows for identification of cellulose as the main component for these fibres. The peak at 1371 cm^{-1} is associated with polysaccharides. Polysaccharides are found in the wall structure of leaves, which are composed of cellulose, microfibrils and hemicellulose, being this last one the major contributor of polysaccharides in leaves [50].

The disappearance of the peak at 1239 for both chemical treatments with very little effect by the high intensity ultrasonication treatment shows the effectiveness of the chemical treatments on reducing hemicellulose and lignin components [8, 16]. The complete reduction of the peak at 1735 cm^{-1}, associated with the C=O in the carbonyl group present in hemicellulose, furthers the effectiveness of the chemical treatments in removing hemicellulose [8, 17, 24]. The reduction and shift of peaks at 2919 and 2851 after the chemical treatments also suggests the reduction of hemicellulose which is more acute for hydrolysis treated fibres. This is explained by the chemical changes that hydrolysis introduces in the CH_2 environment, that leads to the presence of fewer types, making their vibrations less distinct (symmetrical and asymmetrical), causing the merge on a less sharp peak; this is also helped by the reduction of hemicellulose and

lignin components due to the treatment which also contributes to these peaks and once degraded a single broader band can appear as a result of cellulose signals overlapping. The intrinsic similarity in structure and composition of cellulose and hemicellulose gives place to similar patterns in their respective FT-IR analysis, leading to peak overlapping and shift when they are together as part of the fibre [51]. The peaks at 2919 and 2851 cm^{-1} belong to this group as being present in FT-IR analysis of both components, but these peaks have also been attributed to the CH_2 present in other substances in natural fibres [12]. The removal of waxes and hemicellulose from the chemical treatment suggests to leave the fibre surface cleaner when the hydrolysis treatment is used than oppose to the alkaline treatment, that although effective, does not remove so effectively CH_2 rich components from the fibre surface.



(a) Washed fique (F) with both alkaline (FA) treated fibres and alkaline plus high intensity ultrasonication (FA+HIUS) treated fibres.

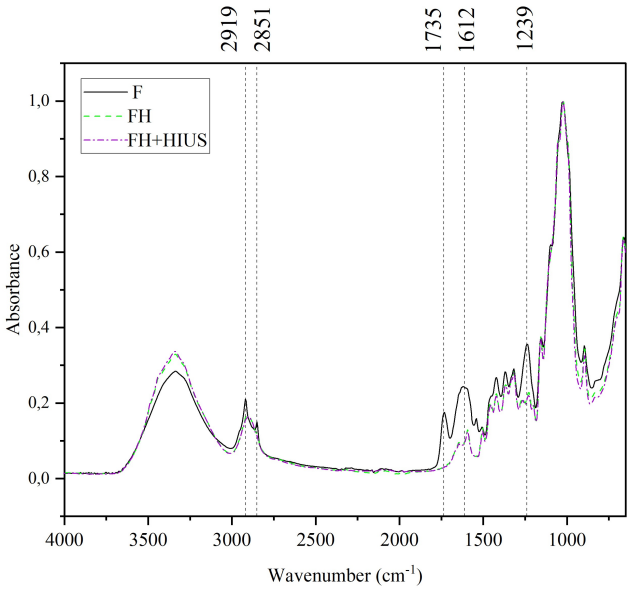


(b) Zoom in the 1750-1200 cm^{-1} region, where it is clearly visible the reduction of the 1735 cm^{-1} associated with the C=O in the carbonyl group, showing the effectiveness of hemicellulose removal. The significant reduction of the peak at 1239 cm^{-1} also shows the removal of hemicellulose and lignin components.

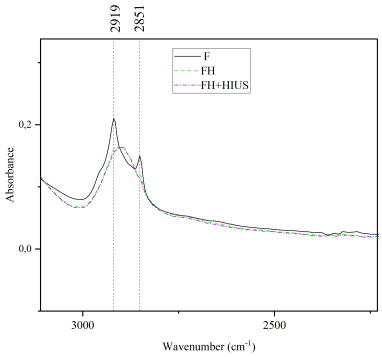
Figure 4.9: Washed fique (F) with both alkaline (FA) treated fibres and alkaline plus high intensity ultrasonication (FA+HIUS) treated fibres (a), with a zoom into the peak differences (b) to better evaluate how the fibre composition is affected.

The peak at 1508 cm^{-1}, along with the ones at 1540 and 1600 cm^{-1} are identified with the C=C aromatic ring of lignin [18, 47, 49, 52], and in both cases of chemically treated fibres a significant reduction is seen at these peaks, as shown in Fig. 4.9 and Fig. 4.10, where the comparison of washed fique with alkaline and hydrolysis treatments plus the ultrasonication process is shown, with a zoom into the range that suffer the greatest changes. A summary of band assignment can be found in Table 4.1.

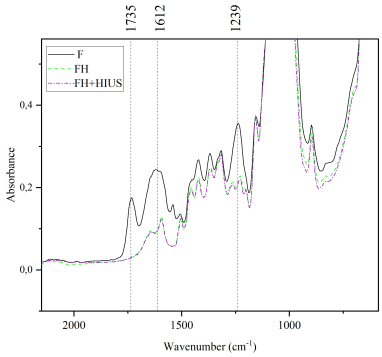
Peaks associated with the crystalline and amorphous cellulose structure are the ones at 1426 and 892 cm^{-1} respectively [53]. While the one at 1426 cm^{-1} sees a slight reduction for the hydrolysis treated fibres, the one at 892 cm^{-1} remains quite stable for all treated fibres. This suggests that the hydrolysis treatment may remove a small proportion of crystalline cellulose, maybe due to alkaline pretreatment, and against the expectation of removing the amorphous one with no significant changes for the alkaline only treated ones. On the crystallinity study of Song *et al.* [33], the impact of solution concentration and temperature on the crystallinity structure of willow bark is studied, and it shows that a 5wt% alkali solution reduced the amorphous phase, while a higher alkali solution contributed to break the cellulose structure, enlarging the amorphous phase and shortening the crystal grain size. This can explain how a too low concentration for fique of alkali treatment does not lead to significant changes, while a very large concentration in the pretreatment for the hydrolysis treated fibres leads to a slight increase in the amorphous phase proportion.



(a) Washed fique (F) with both hydrolysis treated fibres (FH) and hydrolysis plus high intensity ultrasonication treated fibres (FH+HIUS).



(b) Zoom in the 3000-2500 cm^{-1} region, where it is clearly visible the reduction of the 2919 and 2851 cm^{-1} associated with the C-H stretching present in cellulose and hemicellulose. The significant reduction these peaks and the shift towards a one more rounded peak is visible here.



(c) Zoom in the 2000-1200 cm^{-1} region. The reduction of the 1735 cm^{-1} associated with the C=O in the carbonyl group shows the effectiveness of hemicellulose removal. The significant reduction of the peak at 1239 cm^{-1} shows the removal of hemicellulose and lignin. The reduction of the 1612 cm^{-1} peak suggests a reduction in the water trapped in hemicellulose [18, 47].

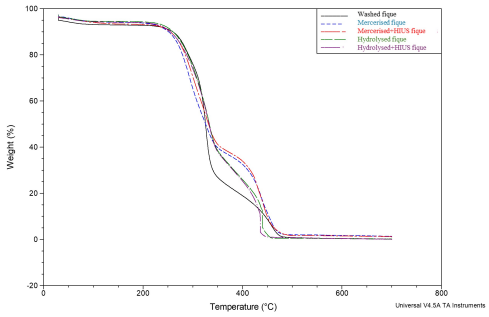
Figure 4.10: Zoom into two regions to explore the peak differences between the cleaned fique and both, hydrolysis and hydrolysis+HIUS treated fibres.

Table 4.1: FT-IR band assignment for the fique fibres analysed, including washed fique, fique treated with alkaline solution, fique treated with hydrolysis, and fique fibres treated chemically and exposed to high-intensity ultrasonication.

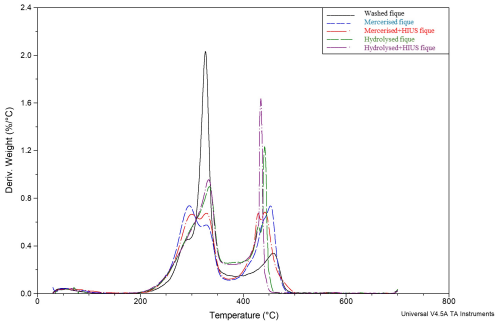
Wavenumber (cm^{-1})	Vibration type	Band assignment	Associated component	Reference
3337	Stretching	OH	Water molecules absorbed in cellulose structure	[24]
2919	Stretching (asymmetric)	C-H_2 and C-H_3	Cellulose and hemicellulose	[18, 24, 48, 53, 54]
2851	Stretching (symmetric)	C-H in CH and CH_2	Hemicellulose, lignin and waxes	[18, 21, 24, 54]
1735	Stretching	Carbonyl group C=O, ester type bonds	Hemicellulose	[18, 24, 46]
1612	Bending	OH	Water molecules and adsorbed moisture in hemicellulose	[18, 47]
1540, 1508	Symmetrical stretching	C=C aromatic ring	Lignin	[18, 47, 49, 52]
1426	Stretching	CH and CH_2	Crystalline structure of cellulose	[53]
1371	Bending	C-H group of the aromatic ring in the polysaccharides	Hemicellulose	[49, 50]
1321		Syringyl ring breathing	Lignin monomer	[49]
1239	Stretching	C-O of acetyl group and C-H	Hemicellulose and lignin	[8, 24, 48]
1157	Stretching	C-O-C	Cellulose and hemicellulose	[48]
1025	Stretching	C-O-C, glycosidic linkage	Backbone of cellulose	[24, 49]
892	Bending	OH and C-O bonds	Amorphous region of cellulose	[53]

4.4.2 Thermogravimetric analysis

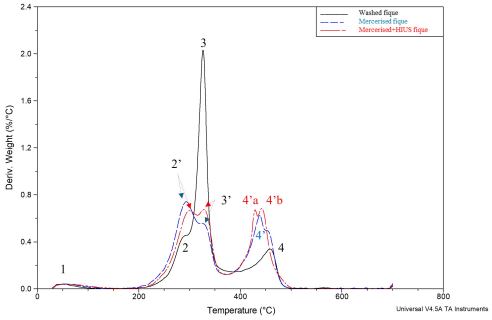
The TGA results for fique show a behaviour change between the washed fique and the treated fibres as shown in Fig. 4.11. On the washed fique's TGA the onset point for the first significant weight loss is found at 262 °C, while it reduces to 251 °C for fibres which underwent the alkaline treatment, while it starts at 254 °C for fibres with the alkaline treatment plus high intensity ultrasonication. For fibres treated with hydrolysis the onset temperature is also around 254 °C, while it is further decreased to 250 °C for those treated with hydrolysis and high intensity ultrasonication. The removal of some fibre components may facilitate this onset temperature reduction by exposing less stable fibre components [55].



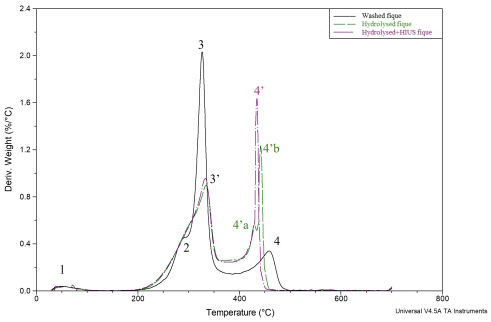
(a) TGA of washed and treated fibres.



(b) DTG of washed and treated fibres.



(c) DTG peaks in the washed fique and mercerised fibres with and without HIUS treatment, showing clear differences in the weight loss rate.



(d) DTG peaks in the washed fique and hydrolysed fibres with and without HIUS treatment, showing clear differences.

Figure 4.11: TGA and DTG results for the washed fique and the different treatments, showcasing the differences among them and how different treatments affect when peak degradation happens to different treated fibres. These curves are specific to each test, and do not represent the average values represented in the tables.

From the weight loss curves three regions are clearly seen, as presented in Fig. 4.11a, but when having a look at the DTG curves, as shown in Fig. 4.11c and Fig. 4.11d, in general four peaks are distinctive, corresponding to different thermal events, as also summarized in Table 4.2. In the case of washed fique, peaks 1, 2, 3, and 4 are identified, with number 2 being more a shoulder on the curve, but distinctive. On the mercerised fibres, peaks 1, 2', 3', and 4' are identified, with 2' and 3' being clearly distinctive now. For the mercerised plus ultrasonication treated fibres peaks 1, 2', and 3' are clearly identified as before, but two small peaks appear in the highest temperature region, named 4'a and 4'b present in most of the samples, although it can appear as a smaller shoulder, making it 5 peaks as identified in Fig. 4.11c. When looking at the hydrolysed

fibres, with or without ultrasonication treatment, the 2/2' peak disappears; but for the hydrolysed only fibres a second peak in the highest temperature region appears again, as for the mercerised plus ultrasonication treated fibres, again sometimes as a shoulder, but shows some overlapping degradation in this area. These peaks are again shown as 4'a and 4'b. For the hydrolysis and ultrasonication treated fibres three peaks are identified as, 1, 3' and 4', as shown in Fig. 4.11d.

Table 4.2: Thermogravimetric analysis with temperature peaks on the DTG as identified in Fig. 4.11c and Fig. 4.11d.

Peak	DTG peak temperature (°C)				
	Washed fique	Mercerised fique	Mercerised+ HIUS fique	Hydrolysed fique	Hydrolysed+ HIUS fique
1	42.8	51.3	58.9	60.7	53.2
2/2'	287.3	293.9	298.1	-	-
3/3'	326.1	363.2	320.8	333.6	331.2
4/4'/4'a	458.5	447.9	427.3	434.2	431.8
4'b	-	-	433.7	444.9	-

In the first region A, as summarized in Table 4.3 and shown in Fig. 4.12, between 40 and 60°C, and below 150°C, the weight loss is attributed to water molecules evaporation, and this goes from 1.9% for the hydrolysed fibres to the 3.0% of the mercerised plus ultrasonication treated fibres, being the value for the washed fibres of 2.8%, and corresponds to peak 1 for all cases. It is quite common that treated fibres absorb less water water than untreated ones, due to the elimination of fibre components that tend to absorb more moisture [36].

Table 4.3: Weight loss at the different stages identified from the TGA and DTG for the washed fique and each treatment, following nomenclature as used in Fig. 4.12.

Region	Weight loss (%)				
	Washed fique	Mercerised fique	Mercerised +HIUS fique	Hydrolysed fique	Hydrolysed+ HIUS fique
A	2.8	2.5	3.1	1.9	2.1
B/B'	17.6	38.1	32.7	-	-
C/C'	45.9	16.2	21.3	56.5	56.5
D/D'	28.9	33.5	18.2	24.2	36.5
E/E'	-	-	19.4	13.4	-
Chard	4.6	5.9	5.2	4.0	4.9

In the second region in the weight loss curve peaks 2/2' and 3/3' are present in the DTG curve. Peak 2/2' has a T_{max} on 287°C for the washed fique; 294°C for the mercerised fique; 298°C for the mercerised plus ultrasonication treated fique; and does not appear for any hydrolysis treated fibre. First, this peak is delayed for the mercerised fibres, and further delayed for the mercerised plus ultrasonication treated fibres, which makes them more thermally stable, since hemicellulose, component to which this peak is associated, degrades later for the treated fibres. Second, the weight loss associated with this stage is 17.6%, 38.1%, and 32.7% respectively. This increase on weight loss of hemicellulose is explained by how the chemical treatment reduces the waxes, pectins, and lignin presence, which makes that lignin-linked hemicellulose degrades in higher proportion [4]. For the hydrolysed fibre this peak associated with hemicellulose does not appear, highlighting the effectiveness of the hydrolysis treatment in removing hemicellulose more effectively than mercerisation only as mentioned in Section 4.4.1. The peak 3/3' has T_{max} on 326°C for the washed fibres; 363°C for the mercerised fibres; 321°C for the mercerised plus ultrasonication treated fibres; 334°C for the hydrolysed fibres; and 331°C for the hydrolysed plus ultrasonication treated fibres. This peak is associated with the cellulose degradation and it is the most characteristic one in the washed fique's DTG, being sharp and high, with a weight loss in this C' region of 45.9% for the washed fique. For the mercerised fibres this 3' peak becomes much

shorter, shorter even than the 2', while for the mercerised plus ultrasonication treated fibres peak 3' becomes a double peak with 2', being broader than for the washed fibres, with a weight loss of 16.2 and 21.3% respectively. For the hydrolysis and hydrolysis plus ultrasonication treated fibres this 3' peak remains sharper, but much shorter than for the washed fibres, but higher than for the other treatments, having its T_{max} further to the right, again, proving an increase in the thermal stability of the treated fibres, and with a weight loss in this C' region of 56.5% in both cases. The tail in the curve at higher temperatures corresponds to lignin degradation only, which does not mean lignin degradation does not occur earlier, as it is well known that its temperature degradation range is quite wide, from 150 to 600°C, as shown by García *et al.* [4] in their work, where it is also discussed how the application of ultrasound contributes to the cleavage of the lignin. The weight loss in this region of the TGA is of 28.9% for the washed fique, with a T_{max} at 454.5°C ; 33.5% for the mercerised only fique with highest degradation rate at 447.9°C; 37.6% for the mercerised plus HIUS treated fibres, split into two peaks, as it is the case for hydrolysis treated fibres with the T_{max} at 427.3°C and 433.7 for the former, and 434.2°C and 444.9°C for the latter; and 36.5% for the hydrolysis plus HIUS treated fibres with a T_{max} at 431.8°C. The appearance of the 4'a and 4'b peaks in the mercerised plus HIUS treated fibres is explained by the ultrasound having that effect of lignin cleavage, leading to a weight loss percentage where D' plus E' is higher than the D' in the mercerised only fibres. In this case, the latest stage of lignin degradation happens the latest for the washed fique, and not for the treated fibres.

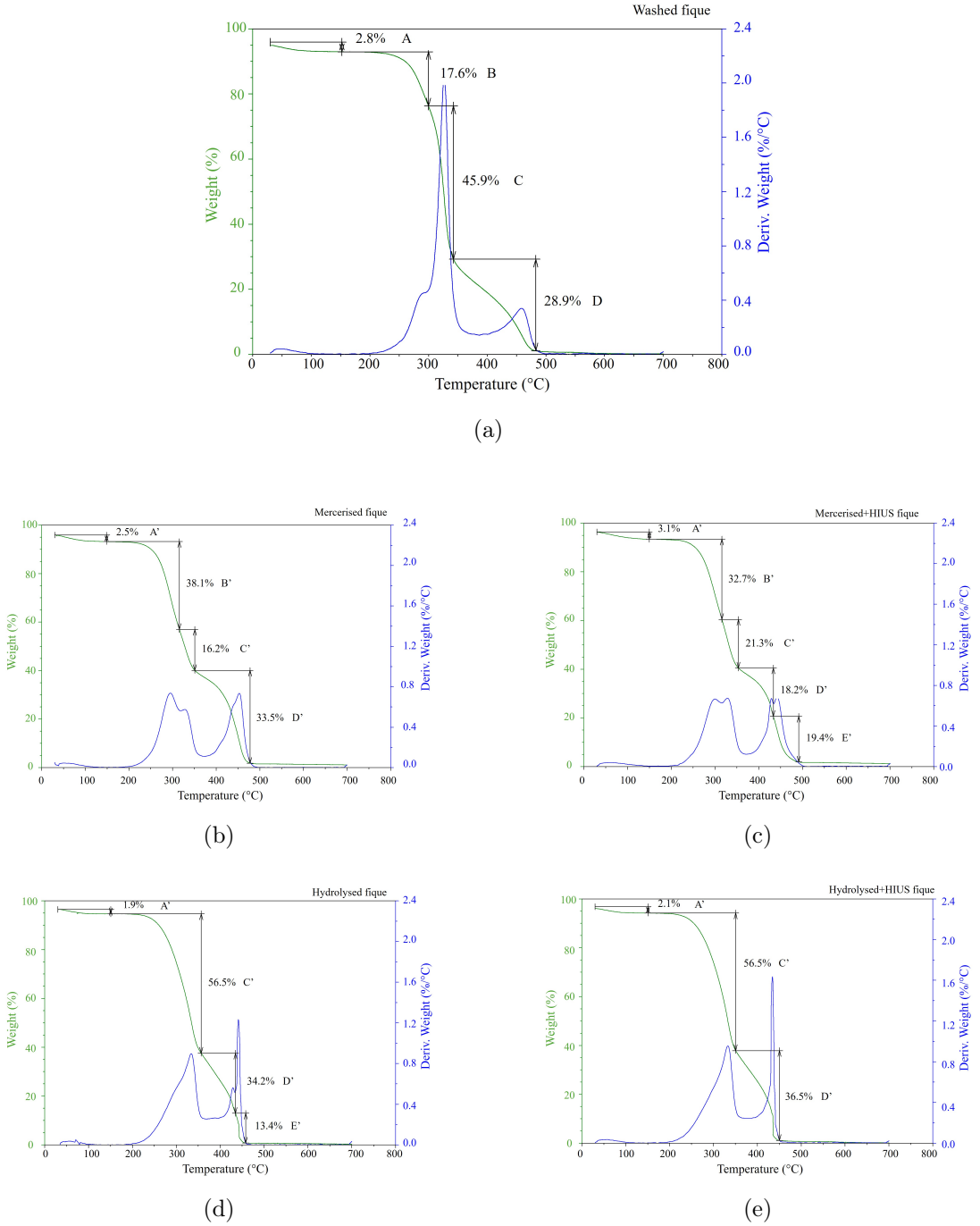


Figure 4.12: TGA results for the washed fique (a) and the different treatments: mercerised (b), mercerised+HIUS (c), hydrolysed (d), and hydrolysed+HIUS (d), showcasing the differences among them and how they affect fibre degradation. These curves are specific to particular tests but the values on each figure are the averaged ones.

The different treatments affect the different components of the fibres differently. The mercerisation process degrades the ester and glycosidic side chains, which leads to the structural alteration of the lignin (delignification is one of the main aims of this chemical treatment), but it also leads to the de-crystallization and swelling of the cellulose, as well as some hydrolysis in the hemicellulose. If the cellulose I, more thermally stable, transforms into cellulose II, which is less thermally stable after the mercerisation treatment of fique, what is shown in Fig. 4.11c can be a peak 2' for the chemically treated fibres corresponding to the hemicellulose and cellulose II degradation, and the 3' peak a slower degradation of the remaining cellulose I [7, 8]. The earlier degradation of the lignin components, as well as faster, after the chemical treatments, becoming more obvious for the fibres also treated with the ultrasonication, is not excessively surprising, since these treatments lead to lignin cleavage. It is the acid hydrolysis the one with a higher impact on the hydrolyzation of hemicellulose, which can happen more easily after an alkaline bath where the lignin structure disruption leaves the hemicellulose fraction more accessible [55].

4.4.3 Differential Scanning Calorimetry (DSC)

The DSC results show, in general, for all fibres, three events. The first endothermic event happens between 30 and 100°C, with peaks between 67 and 81°C, and it is associated with water evaporation. The second event is an exothermic baseline change, more abrupt for the mercerised and mercerised+HIUS treated fibres than for the hydrolysed or hydrolysed+HIUS treated fibres. This second event happens between 250 and 325°C, with the washed fique having the peak at 273°C while all the others have it around 265°C. This event is related to hemicellulose degradation [41, 44]. The next event happens around the 360°C for both mercerised fibres, and it is an exothermic event, although for some mercerised and mercerised+HIUS treated fibres an endothermic peak is found, and this is reported on Table 4.4. It does not mean that these treated fibres present both peaks, it means that some present the endothermic and the majority presents an exothermic peak, as it is shown in Fig. 4.13. This behaviour can be explained by the chemical treatment not being homogeneously applied to all fibres

meaning that the effect caused on some of then has not been as intense as to create the same chemical bond disruptions. For the washed fique and both the hydrolysed fibres an endothermic event happens around the 360°C. This shift from endothermic to exothermic peak upon the mercerisation treatment has also been observed in Ovalle-Serrano's work [42], and the disruption in the chemical linkages after the delignification process might be the cause for this change, modifying cellulose degradation behaviour. In the pyrolysis analysis of cellulose, hemicellulose and lignin [56], it is shown that cellulose has an obvious and big endothermic peak around 355°C, while hemicellulose and lignin have an exothermic peak around 275 and 365°C respectively. In the DSC results presented here the degradation of hemicellulose with that exothermic baseline change corresponds well with that, while the exothermic peak for the mercerised fibres can be justified, as commented in Section 4.4.2, with the cellulose I transformed into the less stable cellulose II due to the chemical treatment, making the case for that disruption in chemical linkages of this component. The endothermic peak for the fibres that underwent hydrolysis and hydrolysis+HIUS may show an overlap of lignin with cellulose degradation.

Table 4.4: DSC results with peak temperatures (°C) of events and their nature.

Fique / Event	Washed	Mercerised	Mercerised +HIUS	Hydrolysed	Hydrolysed +HIUS
Water evaporation	67	81	80	68	73
Hemicellulose degradation	273	264	265	265	267
Endothermic event	358	334	337	358	359
Exothermic event	-	350	354	-	-

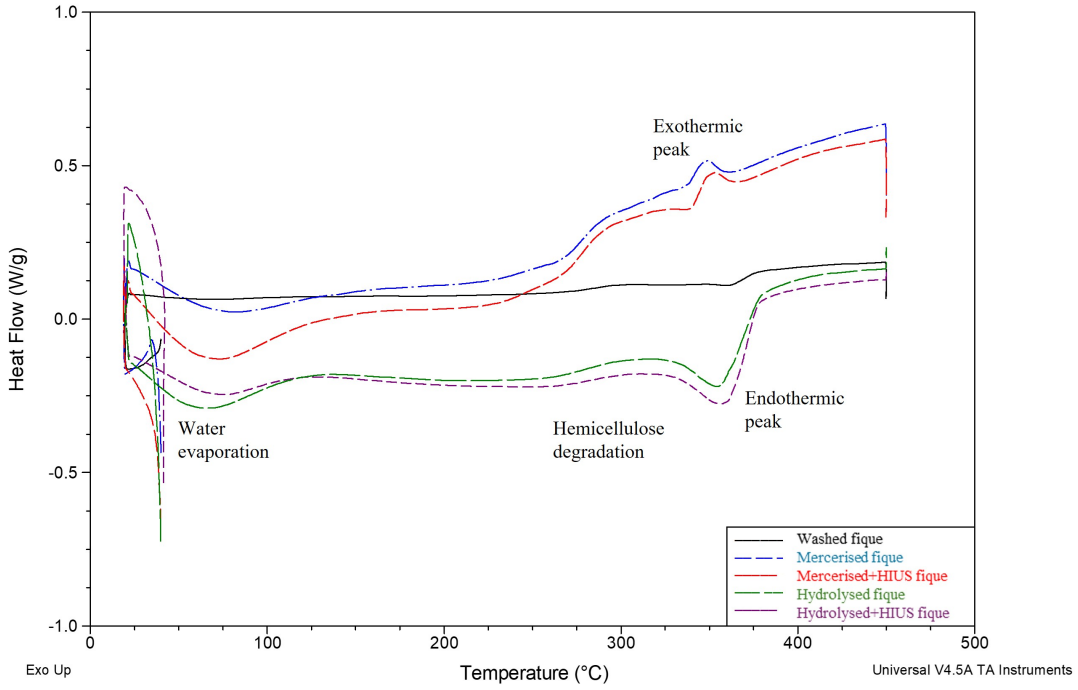


Figure 4.13: DSC curves for washed fique and the different treatments, showing the differences especially in the shift from endothermic to exothermic peak upon the mercerisation treatment.

4.4.4 Conclusions

The study of the impact of chemical treatments in fique fibre shows chemical and thermal changes in the fibre. On one hand, the alkali treatment with sodium hydroxide is expected to remove lignin and dissolve hemicellulose, but it can also induce the change of cellulose I into cellulose II, decreasing the crystallinity phase, and leading to a decrease in thermal stability of the fibres. On the other hand the hydrolysis treatment is expected to target hemicellulose and the amorphous phase of cellulose, leaving the crystallinity phase of cellulose intact, therefore, increasing the proportion of crystalline cellulose in the fibre, leading to increase mechanical properties and thermal stability. The hydrolysed fibres here undergo an alkali treatment before the acid hydrolysis, with this alkali treatment being at a much higher concentration than the fibres that only undergo the alkali treatment. This can explain the results found here, where the FT-IR proves the elimination of hemicellulose and lignin components, but where the crystalline

phase of cellulose sees a decrease in the hydrolysis treated fibres, and not in the alkali treated ones, with the amorphous phase not seeing any indication of decrease. This can be further explained with the TGA results, which show a shift to lower temperatures in terms of hemicellulose and cellulose degradation for the chemically treated fibres, which can be explained by a higher proportion of amorphous phase, which is less stable than the crystal phase, which presence in higher proportion has shown to increase the thermal stability of natural fibres as opposed to what is presented here. And this point is further made with the DSC results pointing in the same direction, with peak temperatures shifting down or remaining stable, but not increased, after the chemical treatments. For all treated fibres the addition of high intensity ultrasonication to the treatment does not add significant visible changes through the tests carried out here beyond further lignin cleavage that leads to a higher weight loss during thermal degradation. In general, washed fique shows the expected behaviour in a natural fibre, with representative FT-IR peaks and expected thermal degradation phases within the temperatures found in the literature. Regarding the chemical treatments, it seems from these results that an iterative study to find ideal chemical treatment conditions accounting for varying concentrations of alkali and acid solutions is required. Despite this, the thermal degradation of these fibres starts above 200°C, showing there is room for composites manufacturing at temperatures below that.

Bibliography

[1] J. S. Neto, H. F. de Queiroz, R. A. Aguiar, and M. D. Banea, "A review on the thermal characterisation of natural and hybrid fiber composites," 12 2021. https://doi.org/10.3390/polym13244425.

[2] M. Samanth and K. S. Bhat, "Conventional and unconventional chemical treatment methods of natural fibres for sustainable biocomposites," 1 2023. https://doi.org/10.1016/j.scca.2023.100034.

[3] M. Mohammadi, M. R. Ishak, and M. T. H. Sultan, "Exploring chemical and physical advancements in surface modification techniques of natural fiber reinforced

composite: A comprehensive review," 2024. https://doi.org/10.1080/15440478.2024.2408633.

[4] A. García, X. Erdocia, M. G. Alriols, and J. Labidi, "Effect of ultrasound treatment on the physicochemical properties of alkaline lignin," *Chemical Engineering and Processing: Process Intensification*, vol. 62, pp. 150–158, 12 2012. https://doi.org/10.1016/j.cep.2012.07.011.

[5] A. Vinod, R. Vijay, D. L. Singaravelu, M. R. Sanjay, S. Siengchin, and M. M. Moure, "Characterization of untreated and alkali treated natural fibers extracted from the stem of catharanthus roseus," *Materials Research Express*, 2019. https://doi.org/10.1088/2053-1591/ab22d9.

[6] C. L. Luchese, J. B. Engel, and I. C. Tessaro, "A review on the mercerization of natural fibers: Parameters and effects," *Korean Journal of Chemical Engineering*, vol. 41, pp. 571–587, 3 2024. https://doi.org/10.1007/s11814-024-00112-6.

[7] A. Ranjan, S. Singh, R. S. Malani, and V. S. Moholkar, "Ultrasound-assisted bioalcohol synthesis: Review and analysis," *RSC Advances*, vol. 6, pp. 65541–65562, 2016. https://doi.org/10.1039/c6ra11580b.

[8] O. A. Salinas, R. B. Benítez, and J. M. Franco, "Chemical modification of fique fiber by alkalization and esterification utilizing fique fiber dust as residue of the fiquera industry," *Journal of Natural Fibers*, vol. 19, pp. 3186–3194, 2022. https://doi.org/10.1080/15440478.2020.1841061.

[9] A. L. Naidu, Duppala, and A. Kumar, "A study on different chemical treatments for natural fiber reinforced composites," *International Journal of Mechanical and Production Engineering Research ad Development (IJMPERD)*, vol. 8 (5), pp. 143–152, 10 2018. PaperID: JMPERDOCT201818, www.tjprc.org.

[10] M. Fan, D. Dai, and B. Huang, *Fourier Transform Infrared Spectroscopy for Natural Fibres, Fourier Transform - Materials Analysis*. InTech, 2012. Accessed 19/03/2025.

[11] N. Sgriccia, M. C. Hawley, and M. Misra, "Characterization of natural fiber surfaces and natural fiber composites," *Composites Part A: Applied Science and Manufacturing*, vol. 39, pp. 1632–1637, 10 2008. https://doi.org/10.1016/j.compositesa.2008.07.007.

[12] N. Abidi, L. Cabrales, and E. Hequet, "Fourier transform infrared spectroscopic approach to the study of the secondary cell wall development in cotton fiber," *Cellulose*, vol. 17, pp. 309–320, 4 2010. https://doi.org/10.1007/s10570-009-9366-1.

[13] E. M. Fernandes, J. F. Mano, and R. L. Reis, "Hybrid cork-polymer composites containing sisal fibre: Morphology, effect of the fibre treatment on the mechanical properties and tensile failure prediction," *Composite Structures*, vol. 105, pp. 153–162, 11 2013. https://doi.org/10.1016/j.compstruct.2013.05.012.

[14] M. K. Bakri and E. Jayamani, "Comparative study of functional groups in natural fibers: Fourier transform infrared analysis (FTIR)," *International Conference on Futuristic Trends in Engineering, Science, Humanities, and Technology (FTESHT-16)*, pp. 167–174, 1 2016. https://www.researchgate.net/publication/298793407_Comparative_Study_Of_Functional_Groups_In_Natural_Fibers_Fourier_Transform_Infrared_Analysis_FTIR.

[15] R. A. Ilyas, S. M. Sapuan, M. R. Ishak, and E. S. Zainudin, "Delignification of palm fibre," *BioResources*, vol. 12 (4), pp. 8734–8754, 2017. https://doi.org/10.15376/biores.12.4.8734-8754.

[16] E. Jayamani, T. G. Loong, and M. K. Bakri, "Comparative study of fourier transform infrared spectroscopy (ftir) analysis of natural fibres treated with chemical, physical and biological methods," *Polymer Bulletin*, vol. 77, pp. 1605–1629, 4 2020. https://doi.org/10.1007/s00289-019-02824-w.

[17] C. Tenazoa, H. Savastano, S. Charca, M. Quintana, and E. Flores, "The effect of alkali treatment on chemical and physical properties of ichu and cabuya fibers," *Journal of Natural Fibers*, vol. 18, pp. 923–936, 2021. https://doi.org/10.1080/15440478.2019.1675211.

[18] P. A. Freitas, C. González-Martínez, and A. Chiralt, "Applying ultrasound-assisted processing to obtain cellulose fibres from rice straw to be used as reinforcing agents," *Innovative Food Science and Emerging Technologies*, vol. 76, 3 2022. https://doi.org/10.1016/j.ifset.2022.102932.

[19] D. Yadav and G. P. Singh, "Sem, ftir study on natural fibers of plant prosopis juliflora and biodegradable composites reinforced with natural fibers," *International Journal of Creative Research Thoughts (IJCRT)*, vol. 11 (2), pp. 389–393, 2023. eLocator: IJCRT1134915 https://www.ijcrt.org/papers/IJCRT1134915.pdf.

[20] P. Gañán and I. Mondragon, "Surface modification of fique fibers. effects on their physico-mechanical properties," *Polymer Composites*, vol. 23 (3), pp. 383–394, 6 2002. https://doi.org/10.1002/pc.10440.

[21] C. G. Hoyos, V. A. Álvarez, P. G. Rojo, and A. Vázquez, "Fique fibers: Enhancement of the tensile strength of alkali treated fibers during tensile load application," *Fibers and Polymers*, vol. 13, pp. 632–640, 5 2012. https://doi.org/10.1007/s12221-012-0632-8.

[22] M. F. Muñoz-Velez, M. Á. Hidalgo-Salazar, and J. H. Mina-Hernández, "Fique fiber an alternative for reinforced plastics. influence of surface modification," *Biotecnología en el Sector Agropecuario y Agroindustria*, vol. 12 (2), pp. 60–70, 12 2014. https://www.researchgate.net/publication/317501110_FIQUE_FIBER_AN_ALTERNATIVE_FOR_REINFORCED_PLASTICS_INFLUENCE_OF_SURFACE_MODIFICATION.

[23] P. Luna, A. Mariño, J. Lizarazo-Marriaga, and O. Beltrán, "Dry etching plasma applied to fique fibers: influence on their mechanical properties and surface appearance," *Procedia Engineering, 3rd International Conference on Natural Fibers: Advanced Materials for a Greener World, ICNF 2017, 21-23 June 2017, Braga, Portugal*, pp. 141–147, 2017. https://doi.org/10.1016/j.proeng.2017.07.021.

[24] R. E. Guzmán, S. Gómez, O. Amelines, and G. M. Aparicio, "Superficial modification by alkalization of cellulose fibres obtained from fique leaf," *IOP Conference*

Series: Materials Science and Engineering, vol. 437, 2018. https://doi.org/10.1088/1757-899X/437/1/012015.

[25] D. Ray, B. K. Sarkar, R. K. Basak, and A. K. Rana, "Study of the thermal behavior of alkali-treated jute fibers," *Journal of Applied Polymer Science*, vol. 85, pp. 2594–2599, 9 2002. https://doi.org/10.1002/app.10934.

[26] S. Joseph, M. S. Sreekala, and S. Thomas, "Effect of chemical modifications on the thermal stability and degradation of banana fiber and banana fiber-reinforced phenol formaldehyde composites," *Journal of Applied Polymer Science*, vol. 110, pp. 2305–2314, 11 2008. https://doi.org/10.1002/app.27648.

[27] J. P. Mofokeng, A. S. Luyt, T. Tábi, and J. Kovács, "Comparison of injection moulded, natural fibre-reinforced composites with pp and pla as matrices," *Journal of Thermoplastic Composite Materials*, vol. 25 (8), pp. 927–948, 12 2012. https://doi.org/10.1177/0892705711423291.

[28] A. Álvarez, C. Pizarro, R. García, J. L. Bueno, and A. G. Lavín, "Determination of kinetic parameters for biomass combustion," *Bioresource Technology*, vol. 216, pp. 36–43, 9 2016. https://doi.org/10.1016/j.biortech.2016.05.039.

[29] E. E. Kiziltas, H. S. Yang, A. Kiziltas, S. Boran, E. Ozen, and D. J. Gardner, "Thermal analysis of polyamide 6 composites filled by natural fiber blend," *BioResources*, vol. 11, pp. 4758–4769, 5 2016. https://doi.org/10.15376/biores.11.2.4758-4769.

[30] M. Asim, M. T. Paridah, M. Chandrasekar, R. M. Shahroze, M. Jawaid, M. Nasir, and R. Siakeng, "Thermal stability of natural fibers and their polymer composites," 7 2020. https://doi.org/10.1007/s13726-020-00824-6.

[31] R. Kumar, A. Ganguly, and R. Purohit, "Thermogravimetric analysis of natural fiber reinforced hybrid composites – a review," *Materials Today: Proceedings*, 8 2023. https://doi.org/10.1016/j.matpr.2023.08.025.

[32] J. L. Thomason and J. L. Rudeiros-Fernández, "Thermal degradation behaviour of natural fibres at thermoplastic composite processing temperatures," *Polymer*

Degradation and Stability, vol. 188, 2021. eLocator 109594 https://doi.org/10.1016/j.polymdegradstab.2021.109594.

[33] X. H. Song, C. M. Huang, H. Qin, W. F. Guan, and Y. S. Ye, "Effects of alkali treatment on properties of willow bark fiber as potential fillers for polymer composites," *Journal of Engineered Fibers and Fabrics*, vol. 17, 1 2022. https://doi.org/10.1177/15589250221138105.

[34] S. S. Heckadka, R. P. Ballambat, P. Bhagavath, M. V. Kini, R. K. Sinha, M. K. Sonali, and D. Sen, "Thermogravimetric analysis of flax, jute, and uhmwpe fibers and their composites with melamine and phenol formaldehyde resins," *Cogent Engineering*, vol. 10, 2023. https://doi.org/10.1080/23311916.2023.2209990.

[35] M. S. Begum, M. Hummel, S. Mandal, S. Mahmood, M. R. Repon, and R. Milašius, "Thermal degradation and chemical analysis of flame-retardant-treated jute fabrics," *Polymers*, vol. 16 (14), 7 2024. https://doi.org/10.3390/polym16142049.

[36] N. M. Nurazzi, M. R. Asyraf, M. Rayung, M. N. Norrrahim, S. S. Shazleen, M. S. Rani, A. R. Shafi, H. A. Aisyah, M. H. Radzi, F. A. Sabaruddin, R. A. Ilyas, E. S. Zainudin, and K. Abdan, "Thermogravimetric analysis properties of cellulosic natural fiber polymer composites: A review on influence of chemical treatments," 8 2021. https://doi.org/10.3390/polym13162710.

[37] M. A. Hidalgo-Salazar and J. P. Correa, "Mechanical and thermal properties of biocomposites from nonwoven industrial fique fiber mats with epoxy resin and linear low density polyethylene," *Results in Physics*, vol. 8, pp. 461–467, 3 2018. https://doi.org/10.1016/j.rinp.2017.12.025.

[38] TA Instruments, "DSC 2920 differential scanning calorimeter," tech. rep.

[39] B. Wielage, T. Lampke, G. Marx, K. Nestler, and D. Starke, "Thermogravimetric and differential scanning calorimetric analysis of natural fibres and polypropylene," *Termochimica Acta*, pp. 169–177, 1999. https://doi.org/10.1016/S0040-6031(99)00161-6.

[40] L. C. Yeng, M. U. Wahit, and N. Othman, "Thermal and flexural properties of regenerated cellulose(rc)/poly(3- hydroxybutyrate)(phb)biocomposites," *Jurnal Teknologi*, vol. 75 (11), pp. 107–112, 9 2015. https://doi.org/10.11113/jt.v75.5338.

[41] M. S. Oliveira, A. C. Pereira, S. N. Monteiro, F. da Costa Garcia Filho, and L. C. da Cruz Demosthenes, "Thermal behavior of epoxy composites reinforced with fique fabric by dsc," in *Green Materials Engineering An EPD Symposium in Honor of Sergio Monteiro* (S. Ikhmayies, J. Li, C. M. F. Vieira, J. I. Margem, and F. de Oliveira Braga, eds.), pp. 101–106, 2019. https://doi.org/10.1007/978-3-030-10383-5_11.

[42] S. A. Ovalle-Serrano, C. Blanco-Tirado, and M. Y. Combariza, "Exploring the composition of raw and delignified colombian fique fibers, tow and pulp," *Cellulose*, pp. 151–165, 2017. https://doi.org/10.1007/s10570-017-1599-9.

[43] G. F. García Sánchez, R. E. Guzmán Lopez, A. M. Restrepo Osorio, and E. Hernandez Arroyo, "Fique as thermal insulation morphologic and thermal characterization of fique fibers," *Cogent Engineering*, vol. 6, pp. 1–11, 1 2019. https://doi.org/10.1080/23311916.2019.1579427.

[44] G. Idarraga, J. Vargas, M. Jalalvand, J. Meza, and L. Yang, "Manufacturing and mechanical characterisation of unidirectional fique fibres reinforced polypropylene composites," *Conference: Composites Meet Sustainability – Proceedings of the 20th European Conference on Composite Materials, ECCM20. 26-30 June, 2022, Lausanne, Switzerland*, 2022. https://doi.org/10.5075/epfl-298799_978-2-9701614-0-0.

[45] O. Muñoz-Blandón, M. Ramírez-Carmona, L. Rendón-Castrillón, and C. Ocampo-López, "Exploring the potential of fique fiber as a natural composite material: A comprehensive characterization study," *Polymers*, vol. 15, 6 2023. https://doi.org/10.3390/polym15122712.

[46] J. H. M. Hernandez, E. F. T. Perea, K. C. Mejía, and C. A. M. Jacobo, "Effect of fique fibers in the behavior of a new biobased composite from renewable

mopa-mopa resin," *Polymers*, vol. 12, pp. 1–15, 7 2020. https://doi.org/10.3390/polym12071573.

[47] J. Summerscales, "FTIR spectral bands for natural fibres," tech. rep., Plymouth Univeristy, 2014. https://ecm-academics.plymouth.ac.uk/jsummerscales/mats347/FTIR_of_natural_fibres.htmAccessed September 16, 2025.

[48] K. Ramalingam, S. M. K. Thiagamani, T. Theivasanthi, M. Chandrasekar, C. Santulli, K. Senthilkumar, and S. Siengchin, *Characterization of fiber surface treatment by Fourier transform infrared (FTIR) and Raman spectroscopy*, pp. 115–127. Elsevier, 1 2022. https://doi.org/10.1016/B978-0-323-90125-3.00020-3.

[49] O. Muñoz-Blandón, M. Ramírez-Carmona, L. Rendón-Castrillón, and C. Ocampo-López, "Exploring the potential of fique fiber as a natural composite material: A comprehensive characterization study," *Polymers*, vol. 15, 6 2023. https://doi.org/10.3390/polym15122712.

[50] E. Morgan, T. J. Foxon, and A. Tallontire, "'i prefer 30°'?: Business strategies for influencing consumer laundry practices to reduce carbon emissions," *Journal of Cleaner Production*, vol. 190, pp. 234–250, 7 2018. https://doi.org/10.1016/j.jclepro.2018.04.117.

[51] A. M. Raspolli Galletti, A. D'Alessio, D. Licursi, C. Antonetti, G. Valentini, A. Galia, and N. Nassi O Di Nasso, "Midinfrared ft-ir as a tool for monitoring herbaceous biomass composition and its conversion to furfural," *Journal of Spectroscopy*, vol. 2015, 2015. Article ID 719042 https://doi.org/10.1155/2015/719042.

[52] K. Jin, Z. Ling, Z. Jin, J. Ma, S. Yang, X. Liu, and Z. Jiang, "Local variations in carbohydrates and matrix lignin in mechanically graded bamboo culms," *Polymers*, vol. 14 (1), 1 2022. https://doi.org/10.3390/polym14010143.

[53] V. Hospodarova, E. Singovszka, and N. Stevulova, "Characterization of cellulosic fibers by ftir spectroscopy for their further implementation to building materials," *American Journal of Analytical Chemistry*, vol. 09 (06), pp. 303–310, 2018. https://doi.org/10.4236/ajac.2018.96023.

[54] R. M. Salim, J. Asik, and M. S. Sarjadi, "Chemical functional groups of extractives, cellulose and lignin extracted from native leucaena leucocephala bark," *Wood Science and Technology*, vol. 55 (2), pp. 295–313, 3 2021. https://doi.org/10.1007/s00226-020-01258-2.

[55] J. Chen, X. Ma, M. Liang, Z. Guo, Y. Cai, C. Zhu, Z. Wang, S. Wang, J. Xu, and H. Ying, "Physical–chemical–biological pretreatment for biomass degradation and industrial applications: A review," *Waste*, vol. 2, pp. 451–473, 11 2024. https://doi.org/10.3390/waste2040024.

[56] H. Yang, R. Yan, H. Chen, D. H. Lee, and C. Zheng, "Characteristics of hemicellulose, cellulose and lignin pyrolysis," *Fuel*, vol. 86, pp. 1781–1788, 8 2007. https://doi.org/10.1016/j.fuel.2006.12.013.

Chapter 5

Fique fibre and matrix interaction: fique-recycled polypropylene

5.1 Introduction

Natural fibre-polymer interphase has proven to have its own challenges, due to the different natures of these components, the first one being polar and hydrophilic, the second non-polar and hydrophobic, making interface adhesion generally weak. Despite the use of natural fibres reinforced composites can be a real challenge in structural applications, the use of natural fibres reinforced polymers has shown to have a place in industries like automotive, civil engineering and construction, sports goods, or aerospace with hybrid natural/synthetic fibres composites.

In general, the low abrasion to equipment, their renewability and biodegradability leading to a lower carbon footprint, manufacturing flexibility, high mechanical strength, low cost, non-corrosive, non-toxic, and non-hazardous nature makes natural fibres reinforced composites relevant to study, especially how adhesion works and how it can be improved in natural fibres and how surface properties may vary with different treatments. [1].

In this chapter thermo-chemical characterisation of recycled and virgin polypropylene (PP) is done, identifying differences and signs of degradation via FT-IR and DSC.

The study of the matrix/fibre interaction is done only between the recycled polypropy-

lene (rPP) and the different treated fibres, since the woven virgin PP supplied would degrade under temperature when forming them into film/sheets. Still, the study of the differences between recycled and virgin PP was deemed relevant.

Fique's wettability is characterised here via the Owen and Wendt method alongside the Young-Laplace equation by immersing each type of fibre in four different liquids in order to obtain the surface energy and its polar and dispersive components. Direct interaction between the different treated fibres and rPP is done via a hot stage microscope test, from which contact angle between both elements is directly measured.

Lastly, the stress transfer capability between the rPP and the differently treated fibres is studied via the single fibre fragmentation test, which allows for calculation of the interfacial shear strength and the critical length of the fibre.

5.2 Literature review

5.2.1 Polypropylene and recycled polypropylene

Polypropylene is a thermoplastic polymer widely used in the commodities manufacturing, ranging from orthopaedic applications to packaging, holding a 16% share in this latter industry [2], to flat filaments used in industrial bags and outdoor carpets, home appliances, air management systems, automotive bumpers and interior panels [3]. Besides injection moulding, other manufacturing processes like blow moulding, extrusion, film casting and thermoforming are also used when processing this material [4]. This polymer is manufactured by polymerizing the propylene monomer. It has three possible chemical structures isotactic, atactic, and syndiotactic, although the main one is the isotactic, with all the methyl groups to the same side of the polymer chain, which is semicrystalline and shows good mechanical properties, normally improved by fillers like calcium carbonate. To this, it can be added that polypropylene is manufactured as homopolymer and copolymer, with the former presenting a higher melting point, while the latter normally includes some fraction of ethylene, which essentially lowers the crystallinity fraction of the polymer, leading to a higher impact strength even at low temperatures as well as an increased flexibility, but at a lower melting point [3].

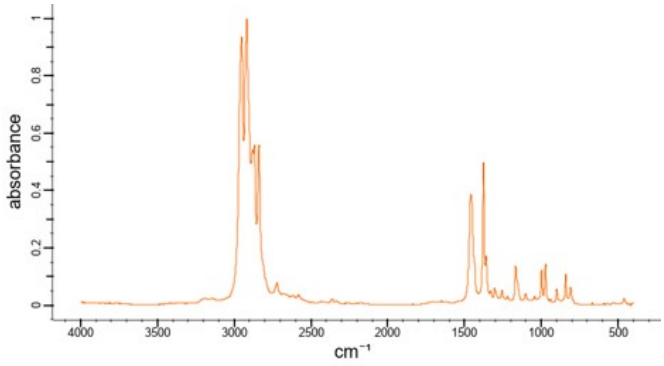
It is a very versatile polymer with good mechanical and thermal properties and it is commonly used to evaluate new systems, study the relationships between internal polymeric characteristics and resulting fibre characteristics, but also in simulation and modelling [5].

With polypropylene being one of the most widely used polymers, there has also been great efforts in recycling it and finding applications for this recycled polymer. This has been also encouraged from a legislation point of view, with the European Union pushing for increased recycling rates in post consumer plastic, aiming to reduce landfill use as well as decreasing the requirement of virgin materials along with the resources and energy consumption. This recycling process can be done as mechanical or chemical recycling. The most common approach in polymers recycling is mechanical recycling, but due to some of its challenges chemical recycling of polymers is getting more and more attention, especially when having heterogeneous and contaminated plastic waste material, where separation is many times not technically feasible, or if it is, at a very high cost [6]. Mechanical recycling normally includes separation and sorting; baling, if transport is required between steps; washing and cleaning, to remove normally organic contaminants; grinding, to reduce products/parts into flakes; and compounding and pelletizing, to convert the flakes intro granulates to ease their later use. The main challenges regarding the mechanical recycling is the material's degradation. The degradation during the lifetime of the product, which can be exposed to heat, light, oxygen, moisture during its service, and the thermo-mechanical degradation due to the recycling process itself, as the exposure to heat and mechanical shear can lead to chain scission and chain branching, affecting the molecular weight of the polymer and impacting the physical and mechanical properties of the recyclate. Chemical recycling aims to recover monomers, effectively a depolymerization process, or petro-chemical feedstocks [6].

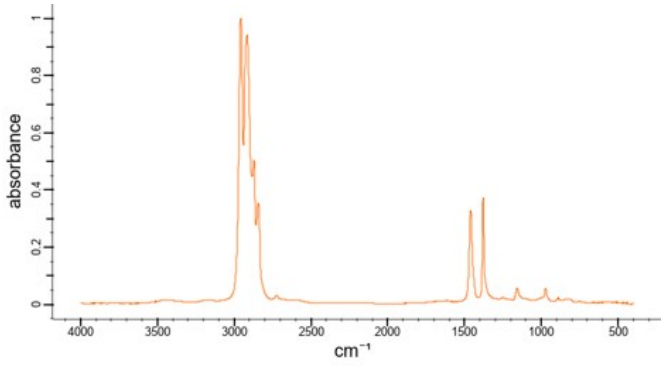
In this project, mechanically recycled polypropylene is used to explore the interaction with natural fibres, more specifically fique fibre, for which first a thermo-chemical characterisation of the polymer is made to explore possible degradation or contamination in the material.

5.2.1.1 Fourier Transform Infrared Spectroscopy (FTIR)

Different chemical structures of polypropylene can present significant differences in their FT-IR spectra [7,8], as shown in Fig. 5.1, where isotactic and atactic polypropylenes are shown. Independently of its chemical structure, peaks that allow for clear identification of polypropylene via FT-IR fall in three main regions. The first one, within the 3000 and 2750 cm^{-1}, where four peaks are found, all associated with the methyl and methylene stretching vibrations. The second region has two main peaks around 1460 and 1380 cm^{-1}, which correspond with asymmetrical and symmetrical bending of the methyl (CH_3) groups. In the region between 1300 and 750 cm^{-1} is where the main differences between the two structures arise. The characteristic peaks of isotactic polypropylene are at 1166, 998, 974, and 841 cm^{-1}, while the atactic PP presents two smaller ones around 1155 and 970 cm^{-1} [9–11].



(a) Isotactic PP FTIR spectrum [12].



(b) Atactic PP FTIR spectrum [13].

Figure 5.1: FTIR spectrum of isotactic and atactic polypropylene, showcasing how the structural chemical differences can be appreciated through FTIR.

When looking at FT-IR spectra of recycled polypropylene, these mentioned peaks are also found, but besides them, it is not uncommon to find peaks that point towards some sort of degradation in the material. A subtle peak at 1730 cm^{-1}, as shown in Fig. 5.2, characteristic of the carboxyl (C=O) stretching vibrations from saturated aldehydes is associated with the thermal and shear degradation of polypropylene in the recycling process [10], which is seen to increase in the presence of impurities [14], which can be aided by biodegradation with the formation of ether and ketone, which become visible in the 1730 cm^{-1} peak [15].

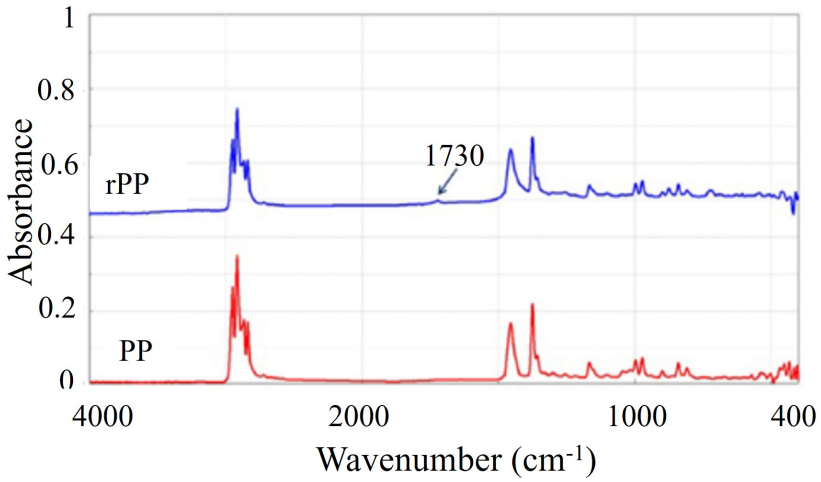


Figure 5.2: Virgin and recycled PP FT-IR spectra from [10], showing the 1730 cm^{-1} in the recycled material.

5.2.1.2 Differential Scanning Calorimetry (DSC)

Differential scanning calorimetry is typically used to thermally characterise materials by obtaining the glass transition temperature, the melting temperature and heat of fusion, and the crystallization temperature, which are important characteristics for polymer applications, as it will help define the temperature range within a material that can fulfil its role without degradation of properties.

Partially crystalline polypropylene has been found to have glass transition temperatures between -13 and 7°C [16]. Glass transition temperature of isotactic polypropylene has been calculated at -1°C [17], while atactic's glass transition temperature is a bit

lower at -7°C, due to the chemical structure.

Melting temperature of polypropylene has been observed at 162°C with a melting enthalpy of 95.4 J/g, with the recrystallization peak at 120°C. The degree of crystallinity in this case is 46% [18]. Further thermal characterisation by DSC has found melting temperature of virgin polypropylene at 167°C and 86.5 J/g melting enthalpy [19], with crystallization peaks at around 119°C. In a different study the melting peak was found at 166°C with a melting enthalpy of 63.2 J/g [20]. The crystallites found in the polymer will impact the melting temperature, which for the stable α-PP form is between 155°C and 160°C, while for the unstable β-PP form is lower, in the 120°C to 130°C [21]. The crystal structure affects the DSC curves, showing that polypropylene that has been heat treated at a certain temperature, shows in the heating cycle a change in the baseline, like a glass transition temperature type of change, at the same temperature the material was isothermally treated [22]. This type of treatment belongs to the thermal history of the material, so it would appear in the first heating cycle, but not in the second heating cycle after thermal history has been erased.

In the case of recycled polypropylene from technological waste a melting peak at 160°C and a smaller one at 109°C are seen in the second heating cycle, as shown in Fig. 5.3. The fact that the peak at 109°C remains in the second heating cycle, as it is also present in the first one suggest the presence of polyethylene [23], although in recycled PP is not uncommon the presence of copolymer, which shows as a shoulder that can extend into the 80°C [24]. In the post consumer recycled PP, DSC presents a peak at 123°C, associated with contamination of polyethylene; a double peak around 160°C, showing the presence of different type of PP crystals formed during cooling; plus a small peak at 146°C associated with typical PP polymorphism. Crystallinity associated with both cases is between 38% and 42%, these values being slightly higher when explored by wide angle X-ray scattering [23]. Gall *et al.* [25] studied the thermal characteristics of four recycled PP blends, and major melting peaks were in the range of 159°C to 164°C. All materials showed a minor melting peak between 124°C and 127°C, associated with both low and high density polyethylene contamination. Melting enthalpies calculated here range between 57 J/g to 74 J/g, presenting a crystallinity

degree between 28% and 36%, which in this case is argued this value to be higher due to the unknown contaminants in the recyclate. In the work done by Jones *et al.*. [26] virgin and recycled PP are thermally characterised by DSC. The virgin PP presents a melting peak at 167.4°C, while the recycled one has it at 164.9°C with crystallization peak temperature happening at 122°C for both cases. Melting enthalpy is 64.4 J/g for the virgin polymer and 42.8 J/g for the recycled PP with crystallinities of 31.1% and 19.6% respectively. According to this study recycled blends can have higher crystallinity than virgin blends, and this is due to the increase mobility due to decrease molecular weigh in the recycling process. This increased mobility allow chains to fold giving place to thicker lamella increasing the crystallization rate.

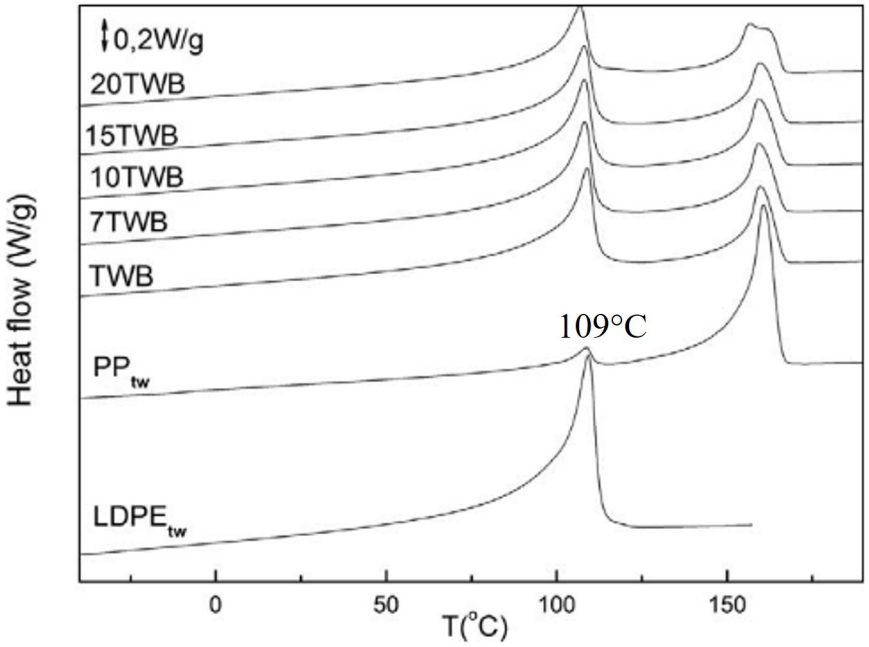


Figure 5.3: Second heating DSC results from [23] on recycled polypropylene from technological waste and the peak at 109°C suggesting the presence of low density polyethylene.

5.2.2 Fibre-matrix interface

How fibre and matrix interact and predicting the affinity in this interaction as well as measuring how strong is the load transfer from matrix to fibre has been intensively

studied. In the case of natural fibres this is especially interesting due to the diverging nature of fibres and matrices, with the former being of polar and hydrophilic in contrast with the non-polar and hydrophobic nature of the latter [27]. Different ways to study this interaction include pull out tests, wettability tests, contact angle interaction and single fibre fragmentation tests.

5.2.2.1 Contact angle: fibre-matrix interface affinity

Measuring the hydrophilic or hydrophobic nature of a material can be done through contact angle measurements. Different approaches can be seen, with the most common being the Wilhelmy and dynamic contact angle (DCA) techniques, although approaches where the droplet is set on top of the fibre surface and the contact angle measured through imaging software are also found. Van De Velde and Kiekens [28] study the wettability of four different types of flax. Two of them taken from two kinds of dew retted flax combings, presenting different thickness, another one take from a flax/polypropylene yarn, and the last one taken from a flax/aramid yarn. Advancing contact angles in water go from 68.46° for the latter to 79.75° for the former. Regarding the fibre surface energy and the polar and dispersive components with the first type of flax presenting two very similar polar and dispersive components, 14.73 and 10.82 mN/m, while for the other three cases these values are around 30 and 3 mN/m respectively as shown in Table 5.1. In general, a contact angle hysteresis is observed, connected with the hydration of the surface of the fibres.

The study of non-treated jute fibres [29] through the DCA shows a decrease in the contact angle with repetitive cycles for water, diiodomethane and glycerol, showing the impact of the adsorption of the test liquid has on the results. In here it is also found that the dispersive and polar components of the surface energy depend on the test liquid diffusion, although total surface energy stays around 30 mN/m. Corona treated fibres see their polarity increased while the dispersive part of the surface energy does not see any changes. This increase is due to the oxidation process that takes place during the treatment and due to the increase in hydroxyl and carboxyl groups in the fibre surface. While the dispersive part of the surface energy stays around 23 mN/m, the polar part

increases from 10 mN/m with no corona treatment to 46 mN/m. This polarity increase leads to a higher adsorption rate of the resin. For this case, single fibre modification was more effective than yarn modification and this was attributed to the limited efficiency of treating a bigger and thicker yarn.

Cantero *et al.*. [30] studied the impact of surface treatments in flax fibre. Contact angles were studied through the Wilhelmy equation. Treatments of 5 and 10% maleic anhydride (Ma) and MaPP copolymer, as well as 2.5% of vinyl tri-methoxy silane (VTMO). In all cases these treatments increase the contact angle of the flax fibre with water, which means the polarity of the fibre is decreased. The treatment with MA decreases the polar component of the surface energy but not as significantly as the MaPP treatment, which achieves a polar component in the surface energy very similar to the one on polypropylene which is naturally non-polar. The VTMO treatment also reduces significantly the polar component in flax fibres. Assessing how this affects the mechanical properties of flax reinforced polypropylene the finding show that the effect is not so evident, and it is associated with the presence of hemicellulose and how interferes with the contact of cellulose in the fibre and the polypropylene matrix.

Baley *et al.* [31] studied the wettability of flax fibres via the study of the contact angle. Untreated flax fibres and NaOH treated flax fibres as well as fibres treated with acetic anhydride after the NaOH treatment and fibres only treated in a formic acid solution. The latter shows the lowest polar component of the surface energy with a value of 22.1 mN/m, while the treated flax with NaOH and acetic anhydride shows the highest value of 36.8 mN/m, which is in line with the other two cases. For the dispersive component a value of 28.2 mN/m is obtained for the formid acid treated while 26.6 mN/m for the untreated fibre. The total surface energy is 62.5 mN/m for untreated flax; 61.7 mN/m for flax treated with NaOH; 60.1 mN/m for the NaOH plus acetic anhydride treated flax; and 50.3 mN/m for the formic acid treated flax. Interface shear strength was characterised in this work via microbond test, and what was found is that while flax treated with NaOH and anhydride acid has significant different surface energy values compared to flax treated with formic acid as well as the nature of the chemical species found in the surface, they showed identical mechanical performance. On top

of this, despite very similar energy values between the two treated flax with NaOH, the ones only treated with that solution shows very poor adherence. The highlights of this research show that although chemistry plays an important role in load transfer and adhesion, mechanical anchorage may be more successful in more regular, clean and with high microporosity surface fibres. Added to this, poor interfacial shear strength resistance in the NaOH only treated flax fibres may be due to the structural degradation suffered by the fibres during treatment.

Hemp and jute fibres' wettability are studied by Park *et al.* [32], both untreated and chemically treated with NaOH and a silane coupling agent. The dynamic contact angle is measured here following the Wilhelmy plate technique, showing an advancing contact angle of 78.46 and 67.05° for untreated jute and hemp respectively. These angles remain quite stable for the treated fibres. Regarding the fibres' surface energies the biggest change is seen for the NaOH treated fibres, which has a general increase on both its components. The decrease in contact angle with water for NaOH treated fibres in contrast with the increase for silane treated fibres is explained by the increase in surface area after the mercerization process by the removal of waxes, lignin, and pectin.

Contact angle via DCA technique on untreated coir fibres has also been studied with PET fibres acting as control samples [33]. This showed that while advancing contact angles are stable for coir fibre, the receding ones are not, in contrast with the PET fibre, for which both angles are stable. This difference is associated with the nature of the fibre surface and it is known as contact angle hysteresis, commonly found in natural fibre due to their increased roughness over synthetic fibres. For both types of fibres the advancing contact angles are speed dependant and for coir they are between 80 to 105° in water, 55 to 64° in diiodomethane, and between 29 to 36° in benzyl alcohol respectively. In this case surface energy of coir fibres is 38.5 mN/m with a dispersive fraction of 31-33 mN/m and a low polar contribution. This value of the surface energy is just slightly above the value range for hydrophobic materials (28 to 34 mN/m), which can be explained by the presence of waxes, fatty substances and lignin in the fibre surface.

Untreated and treated jute fibres and their interaction with epoxy matrices have

been studied by Doan *et al.*. [34]. Fibres treated with NaOH only; with NaOH, 3-Aminopropyl-triethoxy-silane solution (APS) and epoxy dispersion (ED); NaOH and 3-Phenyl-aminopropyl-trimethoxy-silane (PAPS) aqueous solution have been part of this study where contact angles through dynamic contact angle and Wilhelmy approach were used to obtain the surface energy with its polar and dispersive components. On the one hand the contact angle changes significantly for alkali treated fibres in the case of water compared to the untreated fibres, from 67 to 50°, while remaining very stable for less polar liquids. On the other hand, fibres treated with NaOH and silane coupling agent or a combination of silane and epoxy dispersion on top of the NaOH treatment see a decrease of contact angles for all liquids except for water, for which a significant increase is appreciated. This contact angle increase with water shows that these treatments increase the hydrophobicity of the fibres. Regarding the surface energy, the untreated fibres show a total value of 37 mN/m with a dispersive component of 23 mN/m. The dispersive component increases to 25 mN/m for NaOH only treated fibres, to 29 mN/m for NaOH/(APS+ED) treated fibres, and to 30 to NaOH/PAPS treated jute. For the alkali only treated fibres not only the total surface energy is increased, but both the polar and dispersive components too, while for the other two treatments while the dispersive component is increased the polar one decreases leaving a total surface energy very similar to untreated fibres. The cleaner and rougher surface of alkali treated fibres permits the formation of a strong interface with the epoxy, allowing for a mechanical interlocking with the matrix while increasing the wettability of the fibre. The other treatments enhance the adhesion further since the coupling agents can penetrate in the porous surface of the alkali treated fibre, again contributing to the mechanical interlocking.

Orue *et al.* [35] study the wettability of sisal and how chemical treatments affects it. Alkali treatment, silane treatment and a combination of both are used to modify the fibre's surface before contact angles in water, ethylene glycol and diidomethane are measured. For this, an amount of sisal was compressed in a mould to the shape of a disc and a droplet of each liquid deposited on the surface before the contact angle was measured. Higher contact angles were measured on water for silane and the combination

of both treatments. After the silane treatment the polarity component in the surface energy was reduced from 9.4 mN/m for untreated fibres to 3.1 mN/m. This reduction was higher for the combination of treatments, 2.4 mN/m, and contained for the NaOH only treatment, 7.6 mN/m. For the dispersive component big differences when compared to the untreated fibre were not found, staying between 25.3 mN/m and 27.6 mN/m for untreated fibres and the ones with the combined treatments.

5.2.2.2 Fique contact angles and wettability

Gañán and Mondragón [36] in their study of fique and its surface modifications use the Wilhelmy plate technique with the Owens and Wu methods to study the fibres wettability. Contact angles are measured for 2 mm length of immersed fibre in water, ethylene glycol and α-bromonaphthalene, with the fibre diameter measured before each wettability measurement by using an optical microscope. Fibres studied here are untreated fique, mercerised fique, fibres treated with a esterification process with maleic anhydride (MA), with acrylic acid, and with γ-methacryloxy propyl trimethoxy silane, with different combinations that include a mercerization pre-treatment. The contact angle of the untreated fibre with water is 47°, and with the treatments increases up to 67.3° for the mercerization pre-treatment plus silane, while being 62.7° for mercerization only. With contact angles being higher in water for treated fibres, and the opposite for the α-bromonaphthalene case the treatments introduce changes in the fibre's surface that lead to an increase hydrophobicity, which would enhance the compatibility with polymeric matrices. Both methods used for calculating the surface energy and polar and dispersive components give significantly different values, with total surface energy being 44.4 mN/m for untreated fibres using the Owens-Wendt method, while for the Wu method this value is 102.7 mN/m, with polar components being 22.6 mN/m and 67 mN/m respectively. For the mercerized fibres the total surface energies are 43.3 mN/m and 71.3 mN/m, with polar components being 11.5 mN/m and 32.4 mN/m for these two methods. Independently of the method used what is clear is that for all treatments the polar contribution to the surface energy is reduced.

Muñoz-Vélez *et al.* [37], in their work about surface modifications of fique fibre study

the hydrophobicity of the fibres by looking at the contact angle of distilled water on the fibre surface. In general, the lower the contact angles the higher the affinity of the fibre to be wet by the liquid. So, fibres without treatment showed a contact angle around 57°. The treated fibres with NaOH showed a lower contact angle, showing an increase in the fibre polarity due to hydroxyl groups exposed after the chemical treatment that interact with the water molecules through the hydrogen bonds. Fibres treated with NaOH and silane showed an increased contact angle showing a decrease polarity of the fibre, since the hydroxyl groups have reacted with OH groups from the silane, diminishing the compatibility between fibre and water, making the fique more hydrophobic.

Schellbach *et al.*. [38] developed an alternative approach for contact angle measurement which was applied to eight different natural fibres: curaua (*Ananas erectifolius*), fique (*Furcraea andina*), hemp (*Cannabis sativa*), jute (*Corchorus capsularis*), piassava (*Attalea funifera*), pineapple (*Ananas cosmosus*), ramie (*Boehmeria nivea*) and sisal (*Agave sisalana*), all used as received. Indirect contact angle measurement is done by the analysis of spherical menisci formed between two parallel fibres bridged by a small amount of water as shown in Fig. 5.4.

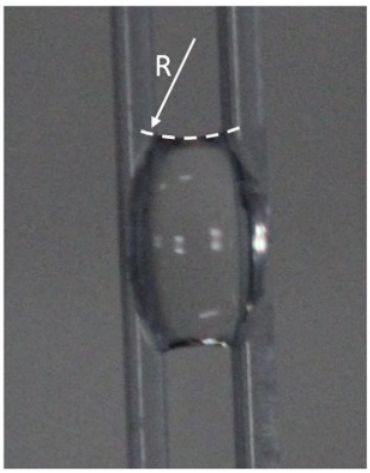


Figure 5.4: Contact angle measurement approach through fibres bridged with water from [38] with the radius of curvature of meniscus formed by water signalled.

Advancing contact angles are reported in Table 5.1 along the surface energy, for each fibre, with these values being respectively 44/34° for curaua; 47/16° for fique; 50/43° for

hemp; 39/38° for jute; 52/30° for piassava; 49/43° for pineapple; 42/35° for ramie; and 41/30° for sisal. Nylon was used as control sample with contact angles being 71/52°. With the advancing contact angles in the range between 41 and 52° all natural fibres show a weakly hydrophilic nature, which means they tend to be wet more than the Nylon fibre which presents a higher contact angle, showing its hydrophobic tendency. The quality of the fibres, i.e. not split fibres, impacts the ability to form a meniscus preventing from an accurate measurement.

Table 5.1: Surface free energy for natural fibres.

Fibre (treatment)	Water advancing contact angle (°)	Polar component (mN/m)	Dispersive component (mN/m)	Surface energy (mN/m)	Reference
Flax	79.75	14.73	10.82	25.55	[28]
Flax	70.12	33.34	2.67	36.01	
Flax	75.80	32.14	1.13	33.27	
Flax	68.46	31.47	4.36	35.83	
Jute		10	24	34	[29]
Jute (corona treatment)		46	24	70	
Flax	53	19	26.6	43	[30]
Flax (5%Ma)	59	13	33	46	
Flax (10%Ma)	61	12	35	47	
Flax (5%MaPP)	82	2	30	32	
Flax (10%MaPP)	84	1.5	29.5	31	
Flax (silane)	78	3.5	34.5	38	
Flax	-	35.9	26.6	62.5	[31]
Flax (NaOH)	-	36.0	25.7	61.7	
Flax (NaOH+acetic anhydride)	-	36.8	23.3	60.1	
Flax (formic acid)	-	22.1	28.2	50.3	
Jute	78.46	8.8	20.7	29.5	[32]
Jute (silane)	79.74	9.0	19.6	28.6	
Jute (NaOH)	71.10	12.3	24.1	36.4	
Hemp	67.05	35.9	15.2	20.0	
Hemp (silane)	68.90	14.1	20.5	34.6	
Jute (NaOH)	65.10	15.4	21.9	37.3	
Coir	80-105	7.5-5.5	31-33	38.5	[33]
Jute	67	12	20	32	[34]
Jute (NaOH)	50	18	26	44	
Jute (NaOH+silane+epoxy)	74	22	26	48	
Jute (NaOH+silane)	73	28	30	58	
Sisal	70.6	9.4	25.3	34.7	[35]
Sisal (NaOH)	74.6	7.6	26.6	34.2	
Sisal (silane)	86.7	3.1	25.8	28.9	
Sisal (NaOH+silane)	89.6	2.4	27.6	30.0	
Curaua	44	-	-	-	[38]
Hemp	50	-	-	-	
Jute	39	-	-	-	
Piassava	52	-	-	-	
Pineapple	49	-	-	-	
Ramie	42	-	-	-	
Sisal	41	-	-	-	
Fique	47.0	22.6	21.8	44.4	[36]
Fique (NaOH)	62.7	11.5	31.8	43.3	
Fique	47.0	67.0	35.7	102.7	
Fique (NaOH)	62.7	32.4	38.9	71.3	
Fique	57.3	-	-	-	[37]
Fique (NaOH)	54	-	-	-	
Fique (NaOH+silane)	70	-	-	-	
Fique (NaOH+silane+PE)	86.7	-	-	-	
Fique	47	-	-	-	[38]

5.2.2.3 Interfacial shear strength measurement and single fibre fragmentation test in natural fibres and thermoplastic matrices

Interfacial shear strength is a measurement of load transfer between the matrix and the fibre in isolation, to predict the behaviour for the fibre reinforced matrix in the manufactured composite. Although it is not uncommon to find the nouns interphase and interface interchanged, it is worth clarifying how they are generally understood in the research community of this area. The term interphase is referred to the 3-D zone, different from the 2-D interface [39,40]. The interphase leads to a gradation of properties from one phase to another, in contrast with the abrupt change that a 2-D interface would require, with its own chemical, physical, and mechanical properties, unique from the reinforcement and the matrix [41]. As described by Drzal [42], this interphase starts at the point in the fibre where the properties differ from those of the bulk filler and ends at the point in the matrix where its properties become equal to those of the bulk matrix. How to measure the mechanical, thermal, and chemical properties of this interphase has taken a lot of attention, since understanding the behaviour of this region directly contributed in predicting composites behaviour and failure. The ability to transfer load from matrix to fibre across the interphase is normally discussed in terms of adhesion, as it is used to describe a complex combination of phenomena. The measure of this adhesion is normally made in terms of the mechanically measured interfacial shear strength [43]. This measurement is normally done in single fibre experiments, with micromechanical tests divided into four main categories: pull-out, microbond, fragmentation, and push out tests as shown in Fig. 5.5 [44].

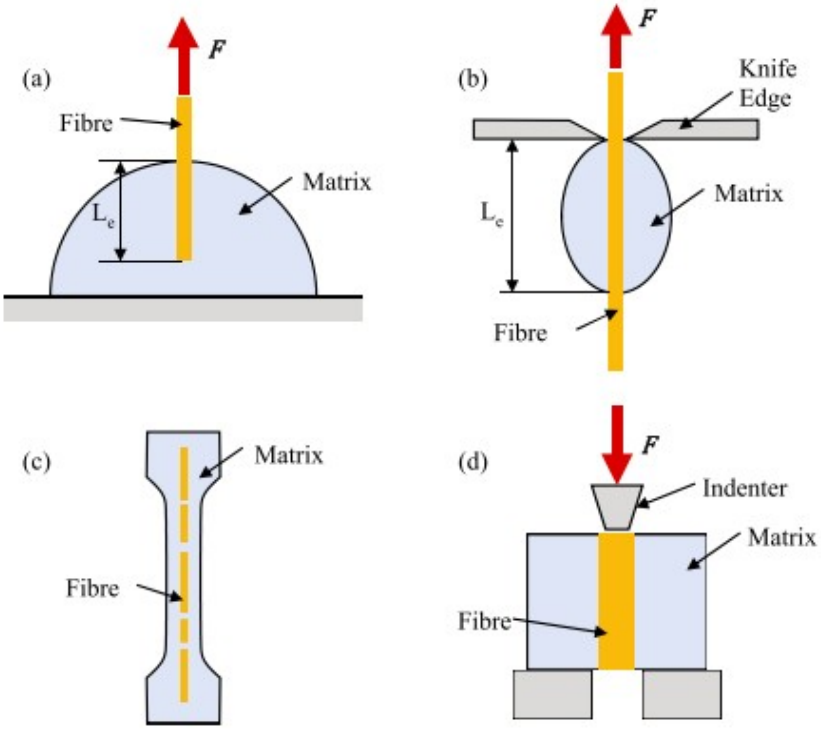


Figure 5.5: Micromechanical tests: (a) pull-out, (b) microbond, (c) fragmentation, and (d) push-out from [44].

When applying any of these characterisation techniques to natural fibres and their interaction with thermoplastic matrices different challenges arise for each of them as explained by Thomason and Rudeiros-Fernández [44]. In general, the nature of the internal structure of natural fibres and its weakness would make them unsuitable for the push-out test where this internal structure needs to be robust enough to transmit the stress applied homogeneously through the cross-section of the fibre. Microbond tests are often used in the study of fibre-matrix systems with high levels of adhesion, which require short embedded length fibre to obtain an interfacial failure instead of a fibre failure. Despite the low level of adhesion expected between fique fibre and the polypropylene matrix, the initial exploration of the microbond test on fique fibres indicated difficulty of forming a polymer drop in the fibres surface making it not viable. The pull-out test set up as presented by Thomason and Rudeiros-Fernández [44] was explored, but difficulties in ensuring a good fibre alignment and having difficulties demoulding without sample rupture made this approach non viable. This led to the choice

of single fibre fragmentation test to study the interaction between fique fibre and recycled polymer matrix. Besides this, the study of artificial isolated systems with single fibres, which do not include the presence of neighbour fibres in a composite may lead to different results than what is presented later on in a manufactured composite.

Bos [45] explores the use of flax as reinforcement for composite materials, more particularly using polypropylene as matrix. Measurement of the interfacial shear strength is done using the single fibre fragmentation test on elementary and technical fibres with PP and PP with maleic anhydride grafted polypropylene compatibilizer (PP/MaPP) to increase adhesion. Critical fibre length is reported here with values of 0.98 mm and 0.52 mm with apparent interfacial shear strength of 13 MPa and 28 MPa for the elementary fibres with PP and PP/MaPP respectively. For the technical fibres with PP and PP/MaPP the critical fibre length is 3.8 mm and 2.8 mm and the apparent interfacial shear strength is 8 MPa and 12 MPa respectively.

Park *et al.* [32,46] study interfacial shear strength of jute, hemp and modified fibres with polypropylene and MaPP copolymers, 1%, 3%, and 5%, via microdoplet experiments. Values of interfacial shear strength between 5.4 MPa to 6.3 MPa for jute fibres, and 4.5 MPa and 6 MPa for hemp fibres, always increasing with the increasing amount of MaPP in the PP matrix are reported in this work, with the alkaline and silane treatments also having an effect in enhancing the interfacial shear strength via different mechanisms. While the MaPP and the silane treatment contribute to creating a chemical bridge, the alkaline treatment removes the weak boundary layers and increases the surface area, with fibre roughness and polarity being enhanced.

Huber and Müssig [47] use the single fibre fragmentation test to study the interfacial shear strength of flax, hemp and cotton reinforced polypropylene with 2% maleic anhydride (MaPP) coupling agent. Test are done under 0.2 mm/min with 15.5 mm and 30 mm gauge lengths. Number of specimens is between 7 and 9. Critical fibre length for flax and hemp is 3.20 mm and 3.16 mm respectively, which do not differ significantly from each other, while for cotton this is 5.03 mm, which is significantly higher. The values for the IFSS are 14.33 MPa for flax, 12.03 MPa for hemp, and 0.664 MPa for cotton. The 30 mm specimens used for flax/MaPP showed a critical length of 3.62

mm, which was not considered significantly different from the 15.5 mm specimens. The presence of maleic anhydride is thought to facilitate the interaction between the polar and hydrophilic fibres with the non-polar and hydrophobic matrix, with the anhydride groups forming hydrogen and covalent bonds with the fibre surface. It is hypothesized here that not only the fibre mechanical properties have or not an impact in the IFSS, but also the chemical structure and how that affects adhesion, arguing that the presence of lignin has an important role to play in the interface, but also how crystalline cellulose does not bond well with other substances and the fact that cotton fibres in this case, consisting mainly of crystalline cellulose, presents the lowest IFSS, having an impact on the fibre/matrix adhesion.

Flax and ramie fibres with nominal tensile strengths of 874 MPa and 1250 MPa respectively and their interaction with polypropylene and polypropylene with 2% maleic anhydride compatibilizer were studied by using the single fibre fragmentation test at 0.1 mm/min by Awal *et al.* [48]. Gauge lengths of 15, 30, and 70 mm were used, finding that the 70 mm gauge length increased the coefficient of variation significantly, showing significant differences in fragments length and concluding that ideal test conditions are at 15.5 mm gauge length. For the 15.5 mm gauge length for flax/MaPP samples critical fibre lengths were obtained between 2.42 and 2.60 mm for different speed rates (0.1-2 mm/min), with interfacial shear strengths between 11.2 and 13.9 MPa. For flax/PP the critical fibre length is 4.86 mm while the interfacial shear strength is 4.5 MPa. For the case of ramie/PP no fragments were found, while for ramie/MaPP critical fibre length is found at 0.98 mm and the interfacial shear strength is 24.9 MPa. These results show how the interfacial properties are greatly affected by the presence of a coupling agent and the fibre type.

Orue *et al.* [35] study the sisal fibre, its surface modifications and how that affects it mechanical properties as well as measuring the IFSS of reinforced PLA via a pull-out test. Fibre tensile strength is calculated at 366 MPa, and for each treatment it decreases to 341 MPa, 352 MPa, and 212 MPa for silane, NaOH, and a combination of both treatments respectively, with the elastic modulus decreasing from 9 GPa to 5 GPa, and the elongation at break increasing from 3.9% up to 6%. Despite the decrease

in the tensile strength of the fibres, the IFSS increases from 2.4 MPa to 5.3 MPa for the silane treated fibre, to 6 MPa for the alkaline treated fibres, and to 5.8 MPa for the combination of both treatments. The IFSS increase for the alkali treated fibres is justified by the increase in contact surface area, which allows for a better mechanical interlocking, aided by the increase in roughness of the surface due to removal of non-cellulosic components. This removal also exposes the OH groups in cellulose, which may contribute to the hydrogen bonds with PLA. In the case of the silane treatment, the IFSS increase is linked to the chemical bond between PLA matrix and amino groups linked to the fibre surface, with stress transfer happening from PLA chains to the fibre through the bonded silane agent.

Seghini *et al.* [49] study the interaction of flax fibre with two thermosets, epoxy and vinylester resins. The single fibre fragmentation test is carried out at 0.005 mm/min. Flax embedded in epoxy led to more fragments than when embedded in the vinylester matrix, leading to a lower value in the critical fibre length, these being 2.02 mm with epoxy and 2.96 mm with vinylester, indicating that adhesion is better for the first system than for the second. This is confirmed by the interfacial shear strength values calculated, which are reported around 19 MPa and 14 MPa respectively. These results conclude that the lower the critical length, the higher the interfacial shear strength for the flax/thermoset system, showing a better load transfer from matrix to fibre.

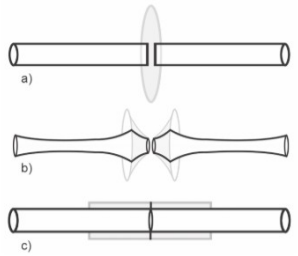
Candiotti *et al.* [50] use the SFFT to explore the interface properties between *Peruvian Stipa Obtusa* technical fibres both, raw and alkali treated, with transparent unsaturated polyester resin. A gage length of 16 mm and a number of 6 samples per treatment were tested at a speed rate of 0.2 mm/min taking steps of 0.1 mm, with 5 min of pause afterwards to reach saturation in the specimen. The treated fibres were immersed in the alkali treatment for 1.5 h, 3.5 h, and 5 h, with the first case giving a longer critical length, 0.87 mm, in the SFFT compared to the other two treatment times, 0.7 mm and 0.8 mm respectively. The 5 h treatment leads to lowered mechanical properties than the 3.5 h, but it also leads to a lower level of non-cellulosic components, exposing the cellulose crystallites, which are reactive sites. The interfacial shear strength is 28 MPa, 35 MPa, and 43 MPa, respectively with the fibres with the 5 h

treatment showing the highest value and the lowest variation.

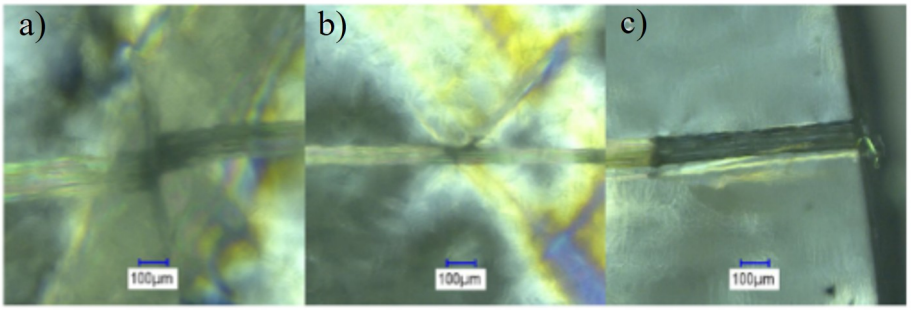
The study of coir fibre and its interaction with homopolymer and copolymer polypropylene and low density polyethylene (LDPE) as they are and modified with maleic anhydride grafted polypropylene (MaPP) and maleic anhydride modified high-density polyethylene (MaPE) respectively was carried out by Thomason and Rudeiros-Fernández [44] via single fibre pull-out test at a cross-head displacement rate of 0.5 mm/min. Interfacial shear strength values for coir-cPP and the MaPP variation are 1.67 MPa and 5.02 MPa. The IFSS value shows a continuos increase with MaPP content up to 10%, 4.9 MPa, showing no significant difference to coir embedded in 100% MaPP. Despite these values being equivalent, the debonded areas of both types of samples showed different characteristics suggesting different behaviours on how the cracks propagate along the interface, and how the matrix behaviour can be different due to the presence of a rubbery phase in the PP copolymer. For the coir with LDPE matrix the IFSS values are 1.5 MPa and 3.97 MPa when it is the modified matrix, again with a clear increase to MaPE modified samples. For all cases clear scattering in results was observed.

Brodowsky and Hennig [51] use flax reinforced epoxy to study how enzymatic treatments of the fibre's surface impact the interfacial shear strength of the fibre-matrix system. There are four enzymatic treatments: laccase enzyme in presence of its substrate dopamine in malonate buffer (DL), malonate buffer only (R), laccase in buffer without dopamine (RL), and dopamine in buffer without laccase (RD). Single fibre fragmentation test at a cross-head speed of 0.2 mm/min as well as single fibre pull-out test with a embedded length of 100 μm and at 10 nm/s during interface fracture and 1μm/s in the friction phase, were used to study the matrix-fibre stress transfer. For the single fibre fragmentation tests fractures were classified according to the fracture mode as identified by other authors [52–54] and as shown in Fig. 5.6, where the level of adhesion can be determined by the type of fracture. From this is obtained that the percentage of disc cracks that would correspond to the highest level of adhesion is mostly independent of the treatment method, between 12 and 15%. For double cone cracks and debonding DL and R fibres showed comparable values, indicating comparable levels of adhesion for these two treatments. RD fibres show a percentage for double cone crack of 67%, while

this is 61% and 55% for R and D fibres respectively. Regarding debonding RD fibres show an 18%, which is lower than the 24% for RL and the 27% for R fibres, being this an indication of poor adhesion. The calculation of the critical fibre length via the single fibre fragmentation test poses a more objective method of adhesion measurement. From this, DL fibres show the lowest fragment lengths,∼1.1 mm, with RD showing higher median fragment lengths, ∼1.8 mm, indicating lower interface adhesion, contradicting the observations through the analysis of the fracture. The apparent shear strength values obtained through the microbond tests are 34 MPa for DL fibres and 24 MPa for the R fibres, which supposes a 30% increase in the treated DL fibres, in accordance with the critical fibres lengths calculated via the SFFT. One of the challenges highlighted here when calculating the IFSS in natural fibres comes from the irregular cross-section from where the circumference is meant to be obtained to calculate the IFSS, since these microexperiments are made on fibre bundles or technical fibres, which are individual fibres bound together by lignin.



(a) Fracture modes schematic from [53].



(b) Example of each fracture mode on flax/epoxy microcomposites from [51].

Figure 5.6: Schematic and example of the fracture modes on single fibre fragmentation tests from [51, 53], with (a) disk crack indicating high adhesion, (b) double cone crack indicating intermediate adhesion, and (c) debonding indicating weak adhesion.

5.2.2.4 Fique fibre interfacial shear strength

Ardila [55] as cited in Vargas *et al.* [56] studies the interfacial shear strength of fique reinforced polyester by using a pull-out test with 5 mm of embedded length, presenting a IFSS of 2.4 MPa.

Mina [57] studies the interfacial shear strength of fique and alkaline treated fique when reinforcing a thermoplastic starch matrix obtained from plasticization with glycerol of native cassava starch. Raw fique and alkaline treated fique were used. The alkaline treatment was done on 2% NaOH for 1 h at 25°. The interface study is made via pull-out test for which specimens were manufactured via heat compression. From these tests, highest IFSS values were obtained for the alkaline treated fibres with values around 2.1 MPa for 5 mm embedded fibre length decreasing to 1.4 MPa for 10 mm embedded length. For the untreated fibres there is also a reduction which in this case reaches a plateau, from 1.25 MPa to 1.1 MPa. This increase in the IFSS with the treated fibres is explained by the lower moisture adsorption compared to the untreated fibres and a better adhesion shown by the traces left by the matrix in the treated fibres in contrast with no matrix residue found on the untreated fique.

Minty *et al.* [58] explore the IFSS of fique fibre reinforced polypropylene via the single fibre fragmentation test via the same manufacturing route used in the work of this thesis. Single fibre fragmentation tests were run at 0.4 mm/min with samples being polished for observation of the fragments. The average critical fibre length is 10.83 mm with a standard deviation of 3.06 mm, which leads to an average value of IFSS of 2.5 MPa with a standard deviation of 0.7 MPa.

Vargas *et al.* [56] study the interfacial shear strength via a pull-out test of fique and fique coated with a styrene-acrylic resin in an unsaturated polyester resin. Embedded length of 5 mm resulted in higher values of IFSS than lengths between 2 and 4 mm, although success rate was 34% lower in the interfacial fracture, so 5 mm length results are reported. Fibres as received and washed present a tensile strength of 355 and 297 MPa respectively. Critical fibre lengths go from 6.2 mm for unwashed and coated fibre to 15.20 mm for only unwashed fique. Washed fique presents a critical fibre length of 13.07 mm, while for its coated version this is 6.50 mm. This leads to the highest value

for IFSS for the unwashed and coated fibre at 5.45 MPa, while the unwashed only fique shows a 2.57 MPa. For the washed fibre, IFSS is 2.38 MPa while when coated increases up to 5 MPa. In the uncoated fibres the main mechanism of adhesion is mechanical anchoring, while with the styrene-acrylic coating the new interface chemical properties through an esterification reaction promotes a chemical bond, enhancing the adhesion as proven by the pull-out test results. Added to this, the change in polarity of the fibre surface allows for the London dispersion forces, part of the van der Waals forces, to interact with the resin.

5.3 Experimental

5.3.1 Materials

Fique fibres were provided by Compañía de Empaques through Universidad Nacional de Colombia in raw condition, and washed on arrival as explained in Section 3.3.1. Treated fibres were provided by Universidad Nacional de Colombia were the treatments took place as explained in Section 4.3.1.

The fabric polypropylene was also provided by Compañía de Empaques and it corresponds to a plain homopolymer PP fabric. The yarns of the fabric are manufactured in a drawing process and they correspond to a flat tape of PP with a width of 2.5 mm and a thickness of 0.041 mm.

The source of the recycled polypropylene is big bags, Fig. 5.7a, which are collected and reprocessed to obtain a recycled material called Granuplas in the form of spherical like pellets as shown in Fig. 5.7b.



(a) (b)

Figure 5.7: Bags made of polypropylene (a), and the pellets resulted from the recycling of those bags (b).

5.3.2 Methods

5.3.2.1 Fourier Transform Infrared Spectroscopy (FT-IR)

An Agilent Technologies 4500 FT-IR system was used, which was supported by a docking station and connected to a laptop for operation, to identify functional groups in the different materials analysed, so material identification could be done. The interface used was a diamond-attenuated total internal reflectance (ATR), which required ensuring maximum contact with the interface by clamping the sample. A penetration depth of 2-4 μ m was established for all cases and a background scan was taken before each measurement after the contact area had been cleaned with acetone. For each material studied, ten samples were taken, which were later averaged and normalised. Data were processed using OriginLab software.

5.3.2.2 Differential Scanning Calorimetry (DSC)

A TA instrument Q20 DSC was used to identify the glass transition temperature and the degree of crystallinity present in each material following ISO 11357 [59,60]. Sample materials in the form of pellets between 5 and 20 mg were weighed and placed in aluminium crucibles and placed with an empty crucible (reference) within the measuring cell, consisting of a furnace and an integrated sensor. Samples underwent two heating

and cooling cycles at 10 K/minute from -30°C to 200°C. The first cycle is used to erase the thermal history of the material, and the second cycle is used to thermally characterised the material. Tests were run in an inert atmosphere of nitrogen with a flow of 50 mL/min. Crystallinity of the samples was calculated following Eq. (5.1):

$$X_c = \frac{\Delta H_m}{\Delta H_m^0} \cdot 100 \tag{5.1}$$

where ΔH_m is the heat of fusion for the material, and ΔH_m^0 is the heat of fusion of the 100% crystalline polymer.

5.3.2.3 Wettability and contact angle

Contact angle and surface energy measurements were made using the Attension sigma 700/701 by immersing the fibres in n-Hexane, ethanol, ethylene glycol and water, with n-hexane being the least polar and water being the most polar as presented in Table 5.2. Fibres were attached to a small ring that was hooked to an electro micro-balance. The free end of the fibre was immersed into the liquid (final depth of immersion 3 mm, speed 4 mm/min, mean of at least 10 measurements) and then brought up in the same conditions, as shown in Fig. 5.8. From the test, the force versus position loop was recorded and the force was converted to the advancing and receding contact angles (θ_A and θ_R) using the Wilhelmy equation, and presented in Table 5.2. The force in the balance is theoretically equal to the wetting force, the weight of the probe and the buoyancy force, as put in Eq. (5.2).

$$F_{total} = P\gamma cos\theta + mg + \rho gAh \tag{5.2}$$

where F_{total} is the total measured force on the electrobalance, P is the fibre wetted perimeter; γ or $\gamma_{LV}$is the liquid surface tension; θ is the contact angle -A for advancing and R for receding-; m is the mass of the fibre; g is the acceleration of gravity; ρ is the liquid density; A is the fibre cross sectional area; and h is the immersion depth. Because the electrobalance can have the weight tared when the probe is put in and the effect of buoyancy can be removed by extrapolating the force back to zero immersion

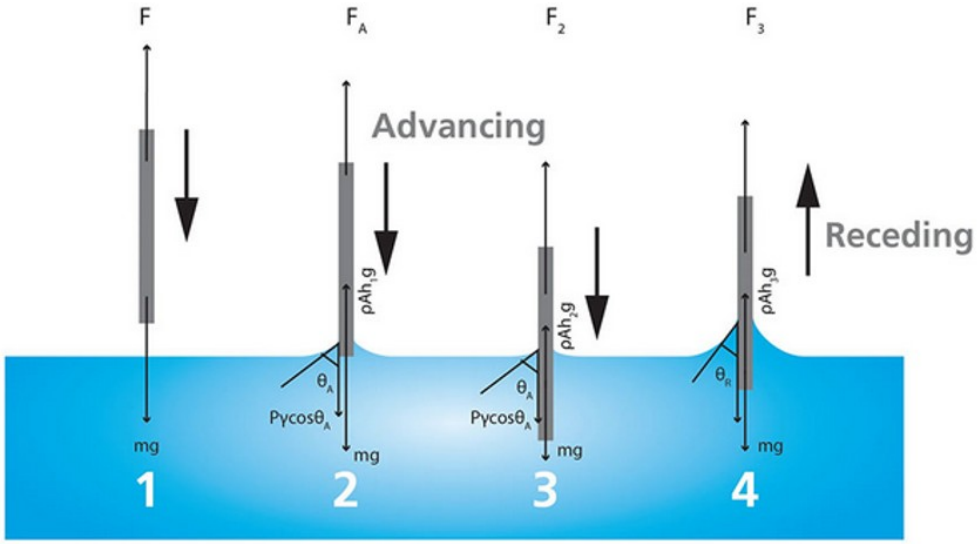


Figure 5.8: Diagram showing the forces acting on the fibre when immersed in the different liquids, with advancing and receding angles identified [61].

depth, the remaining force is the wetting force only as shown in Eq. (5.3) [33].

$$F_{total} = P\gamma cos\theta \tag{5.3}$$

The fibre perimeter is obtained from assuming circular cross section of the fibres and measuring their apparent diameter before the test is done as explained in Section 3.3.3, and the perimeter calculated from it, with two pictures taken along the fibre and ten measurements across each picture.

Following the Owen and Wendt method the surface energy of the solid, γ_{SV}, is divided into a polar, γ_{SV}^{p}, and a dispersive, γ_{SV}^{d}, components as shown in Eq. (5.4)

$$\gamma_{SV} = \gamma_{SV}^{p} + \gamma_{SV}^{d} \tag{5.4}$$

The interfacial energy between two phases, γ_{SL}, can be approximated by Eq. (5.5) which combined with the Young-Laplace equation in Eq. (5.6) can then be linearly rearranged into Eq. (5.7), allowing for a least square method to be applied once at least three liquids have been tested, leading to obtaining γ_{SV}^{p} and γ_{SV}^{d} as the slope and interception respectively [33, 62] as shown in Fig. 5.9, taken from the work done here

for fique.

$$\gamma_{SL} = \gamma_{SV} + \gamma_{LV} - 2(\sqrt{\gamma_{SV}^{d}\gamma_{LV}^{d}} + \sqrt{\gamma_{SV}^{p}\gamma_{LV}^{p}}) \tag{5.5}$$

$$\gamma_{SV} = \gamma_{SL} + \gamma_{LV}cos\theta \tag{5.6}$$

$$\frac{\gamma_{LV}(1+cos\theta)}{2\sqrt{\gamma_{LV}^{d}}} = \sqrt{\gamma_{SV}^{p}}(\frac{\sqrt{\gamma_{LV}^{p}}}{\sqrt{\gamma_{LV}^{d}}}) + \sqrt{\gamma_{SV}^{d}} \tag{5.7}$$

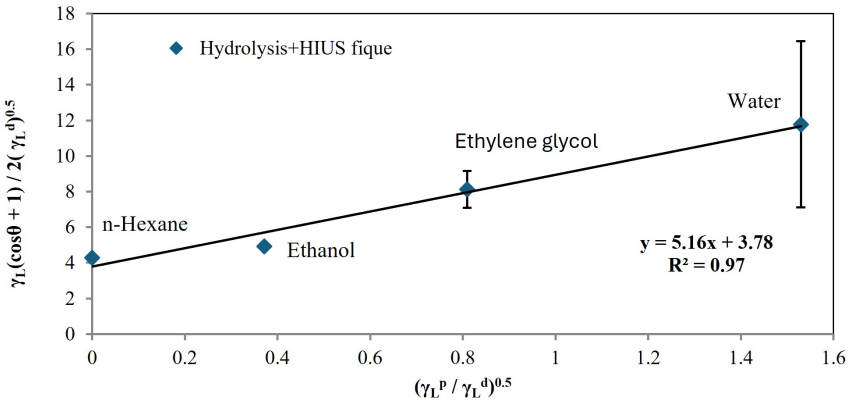


Figure 5.9: Least squares method applied to the three liquids used to measure the contact angle of differently treated fique fibres, in this case for delignified fique, showing how the line interception allows for calculation of the dispersive component of the surface energy, while the slope allows for the calculation of the polar component.

Table 5.2: Summary of surface tension and the polar and dispersive components of the liquids used in the wettability characterisation of fique

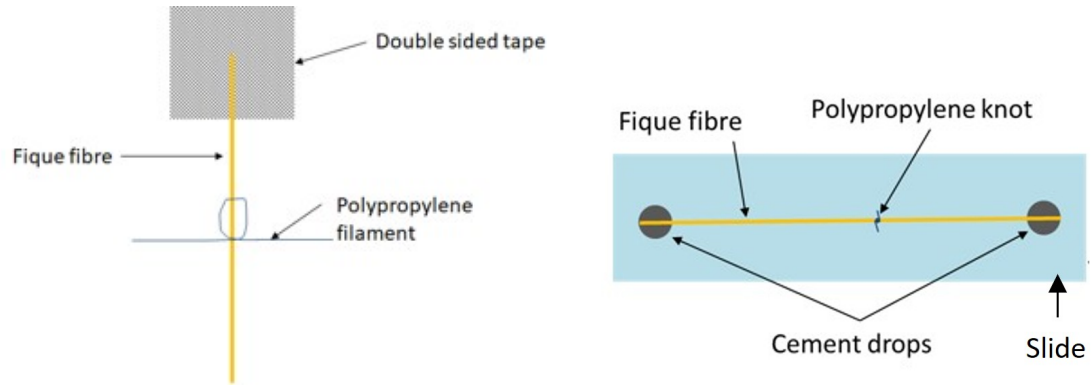
Liquid	γ_{LV} (mN/m)	γ_{LV}^{p} (mN/m)	γ_{LV}^{d} (mN/m)
Water	72.8	51	21.8
Ethylene glycol	48	19	29
Ethanol	21.4	2.6	18.8
n-Hexane	18.4	0	18.4

5.3.2.4 Fique-PP contact angle: hot stage microscope

The hot stage microscope was used to see how the recycled polypropylene behaved when put in direct contact with the different treated fique fibres.

Polypropylene filaments were tied to the individual fibres. To create the recycled polypropylene filaments, a pellet was placed onto a slide on top of a hot plate. The hot plate is heated up to 200°C. While the polypropylene is melting, up to 45 s before it degrades, a pair of tweezers is used to produce filaments by drawing.

Once the PP filaments are available, an individual fique fibre is taken and hung, in order to tie a knot around it with one of those filaments, as can be seen in Fig. 5.10a. Because this procedure was initially thought for being used with glass fibre, more than one knot is necessary for achieving a visible droplet around fique, one to two orders of magnitude thicker than glass fibre. Later, the fibre with the rePP tied to it is placed on a slide, where it is attached to by two cement droplets, which fix the fibre, but that can also undergo the temperature range it will be subjected to. This is let to dry for a 24 h period to allow for the cement solidification and hardening as shown in Fig. 5.10b. After the cement has settled, the sample is ready to be put into the hot stage.

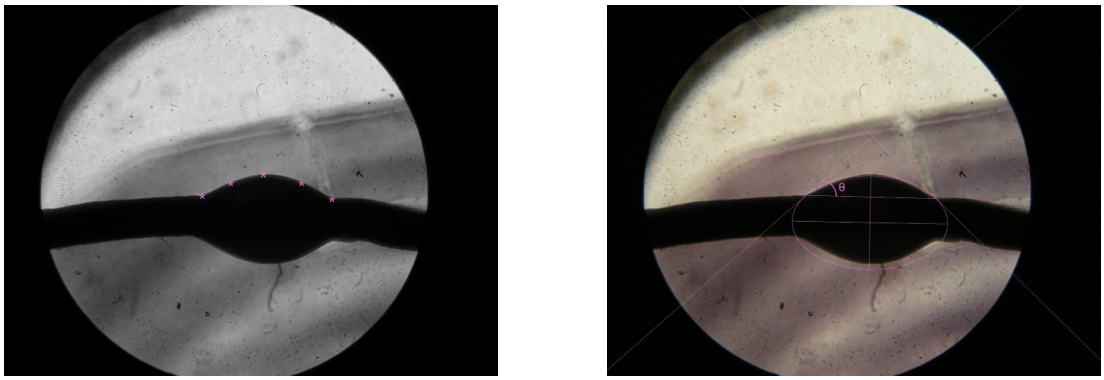


(a) (b)

Figure 5.10: (a)Shows the fibre hung and how the rePP filament is made a knot around it; (b) shows the sample finished with the cement drops to keep the fibre in place when subjected to temperature.

The sample is then placed in a hot stage, where it will be heated up to 220°C at a rate of 2°C per minute. The process is photographed all the way through with a camera

attached to the optical microscope at x100 magnification, pictures being taken every minute. The contact angle of the droplet with the fibre is measured since the droplet is formed till the end of the experiment by using ImageJ software and the plug-in "contact angle" as shown in Fig. 5.11. Average contact angles from 10 samples are reported.



(a) (b)

Figure 5.11: (a) Shows how 5 points around the droplet are selected; (b) shows the software fitting the best match between an ellipse and a circumference and giving the contact angle θ as an outcome.

5.3.2.5 Single Fibre Fragmentation Test (SFFT)

The single fibre fragmentation test was performed in a Testometric M250-2.5CT testing machine with a 100 N load cell. Cross-head speed was established at 0.4 mm/min. For each specimen tested, Windtest analysis software, which controls the Testometric testing machine recorded the load as a function of the cross-head displacement and time. If the specimen failed or fragmentation saturation was achieved the loading was removed and the test stopped, with the test evolution represented in an schematic in Fig. 5.12 [48]. To avoid sliding of the samples in the clamping area, sanding paper was glued at both ends of the specimens as shown in Fig. 5.13. In this case the recycled PP is not transparent, it is actually of a grey colour, which means that despite the small thickness of the specimens it is not possible to directly see through it, so early samples were put against the light to observe the number of fragments, giving a clear picture of how does the fibre break looks like, so in final samples, which are slightly thicker the number of fragments could be identified. This is helped by the stress whitening occurring

in the matrix where the fibre has failed. This was confirmed by sample polishing and a close look taken at the microscope.

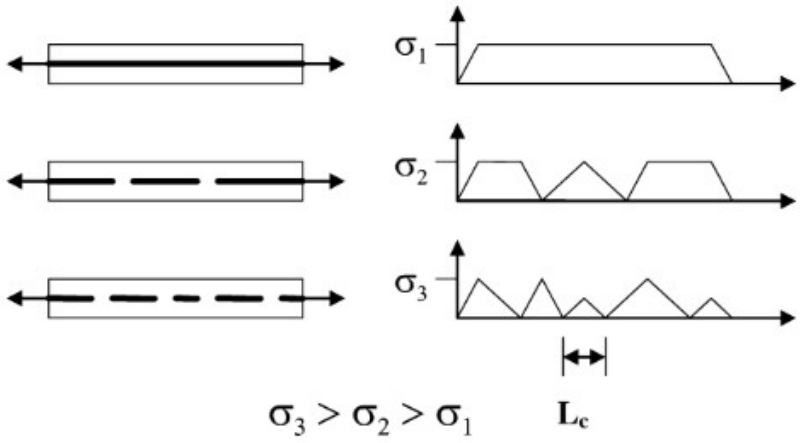


Figure 5.12: Schematic of the single fibre fragmentation test [48].

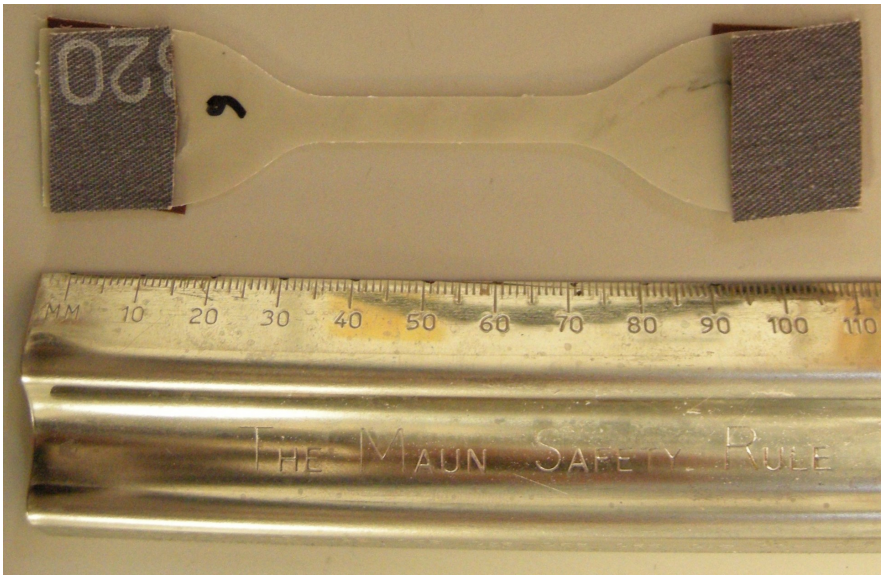


Figure 5.13: Specimen for the SFFT where the sand paper has been glued to both ends of the sample to prevent sliding in the clamping area.

The critical fibre length, l_c is calculated according to Eq. (5.8) [63].

$$l_c = \frac{4}{3} * \frac{\text{Sample gauge length}}{\text{Number of fragments within gauge length}} \tag{5.8}$$

Interfacial shear strength can then be calculated according to Eq. (5.9)

$$IFSS(\tau) = \frac{r_f \sigma_f}{l_c} \tag{5.9}$$

where r_f is the radius of the fibre, σ_f is the average tensile strength of the fibre, and l_c the critical fibre length defined previously. Before sample manufacturing ten pictures were taken along the fibre the length to measure the apparent diameter three times from each picture and obtain an average value representative of the fibre radius. In here, the average tensile strength used is the one obtained from the mechanical characterisation of fique as explained in Chapter 3, with a value of 330 MPa.

5.3.2.6 SFFT sample manufacturing

Several steps are followed in order to prepare the single fibre fragmentation samples based on the procedure explained by Awal *et al.*. [48]. At this stage the fabric PP is discarded for this endeavour due to high structural degradation when using the hot press. A specialized mould, manufactured from 8 mm thick aluminium 6082-T6 using water jet cutting was used to press mould PP films with individual fique sample sandwiched in between. A exploded diagram of the mould is shown in Fig. 5.14.

1. Preparation of PP film: For the recycled PP, 7 g of rPP pellets where measured and put on top of an aluminium plate that had been previously cleaned with anti-adherent. These pellets were place in the hot press at 200°C for 10 minutes and let to melt before putting another plate on top and applying a 20 bar pressure for other 10 minutes. After this the plates were removed from any heat source and let to cool before separating them, between which a circular film was formed.

2. The PP film is cut on rectangular shape of the dimensions of the mould and two films are put in the mould on top of anti-adherent film.

3. Double sided tape is put on the top and bottom sides and individual fique fibres placed on top of the PP film and kept aligned by being stuck on the tape.

4. Another two films of PP cut out to the shape of the mould are put on top of the fique fibres, and covered with anti-adherent film.

5. The top plate is then put in place and the nuts and bolts fastened.

6. Six kg were put on top of the top plate before the mould being introduced in the oven, where it stayed for 40 min at 180°C.

7. After that time the mould was removed from the oven and let to cool at ambient temperature.

8. The mould was dismantled to removed the samples, all together in a rectangular shape, and then they were cut to the desired dogbone shape for testing.

Some of the challenges faced in sample preparation were the fibres alignment, especially with the treated fibres, since they were shorter and wavier than the untreated fibres; and the trapped air in the polypropylene film, which lead to bubbles in the specimens

ITEM No.	PART NAME	ITEM No.	PART NAME
1	BASE	6	SPACER
2	BASE WITH CUT-OUT	7	TOP PLATE
3	PP SHEET	8	M6 BOLT
4	FIBRES	9	M6 NUT
5	SHIM		

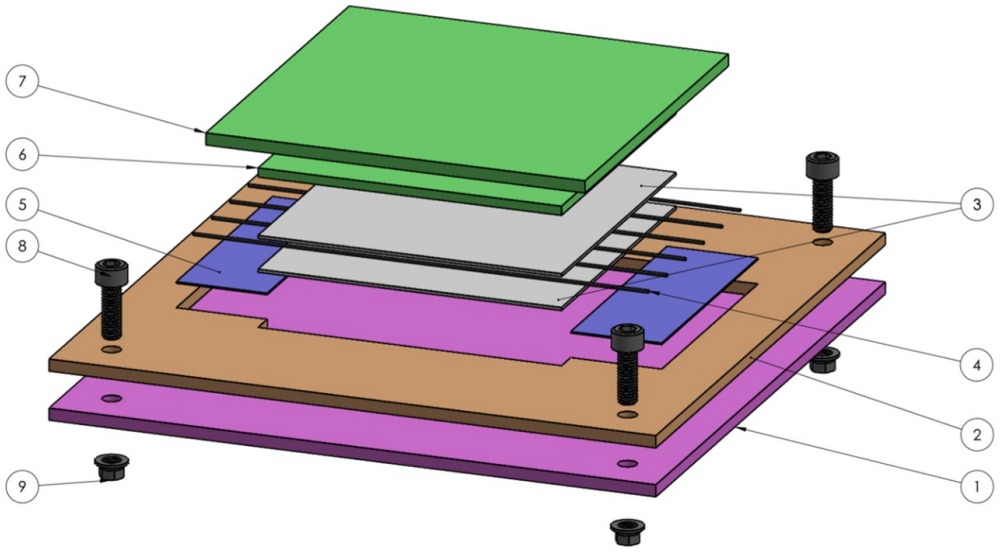


Figure 5.14: Exploded diagram with different parts identified of the mould used in the manufacturing of the SFFT samples [58].

5.4 Results and discussion

5.4.1 Polypropylene and recycled polypropylene FT-IR

As commonly found in polypropylene FT-IR absorbance bands, as detailed in Table 5.3, three main regions are identified for both materials tested. The first one, in the region between 2950 and 2839 cm^{-1} presents four clear peaks associated with C-H stretching. The one at 2950 cm^{-1} is linked to the asymmetric stretching of methyl (-CH_3) groups, while the one at 2915 cm^{-1} is associated with the asymmetric stretching of the methylene (-CH_2) groups. In the second region two peaks are found at 1453 and 1375 cm^{-1}, corresponding to C-H bending in the methyl groups, both symmetric and asymmetric [11, 14, 64].

The third region contains what are the characteristic peaks of polypropylene, within the 1250 - 715 cm^{-1} region. The peaks at 1167, 998, 974, and 838 cm^{-1} are characteristic of isotactic partially crystalline polypropylene . The peak at 1167 cm^{-1} is associated with C-H wagging, -CH_3 rocking, and C-C stretching in the polymer backbone. The peak at 998 cm^{-1} is associated with the crystalline fraction of the polymer, while the peak next to it as can be seen in Fig. 5.15, corresponding to 974 cm^{-1}, is associated with both amorphous and crystalline phases, being very similar for both blends. The peak at 838 cm^{-1} is associated with the rocking vibrations of the methyl groups in the polymer backbone, while the peak at 715 cm^{-1} is linked to the out-of-plane vibration of the methylene groups [11, 64].

One of the main differences in the FT-IR absorbance spectra of the two polypropylenes is the much higher peak at 874 cm^{-1} for the fabric PP. This is associated with the presence of calcium carbonate, typically used as a filler in polypropylene to increase its whiteness and opacity, as well as to reduce the production costs. Not only the peak at 874 cm^{-1} but also the higher peak in the fabric PP at 715 cm^{-1} [25, 65] suggests a higher presence of calcite in this blend. The shoulder present at 1434 cm^{-1} in the fabric PP is associated with the stretching vibration of CO_3 [66], also linked to the presence of calcium carbonate, which, if present as a filler in the recycled PP, its presence cannot be clearly confirmed from FT-IR. In the recycled PP blend two small peaks at 1730 cm^{-1}

and just before the second region referred to earlier is associated with the carboxyl acid group (C=O) stretching vibrations of saturated aldehydes and ketones, linked to the blend degradation after the recycling process [10, 14, 15]. The peak at 1644 cm^{-1} also pointed out in Fig. 5.15 is also associated with the stretching vibration of C=O typically found in polyolefins. Its appearance in the recycled PP can suggest degradation or some polyethylene contamination [23], although the presence of polyethylene is hard to confirm through FT-IR only, as its peaks and the ones corresponding to PP overlap to each other [8].

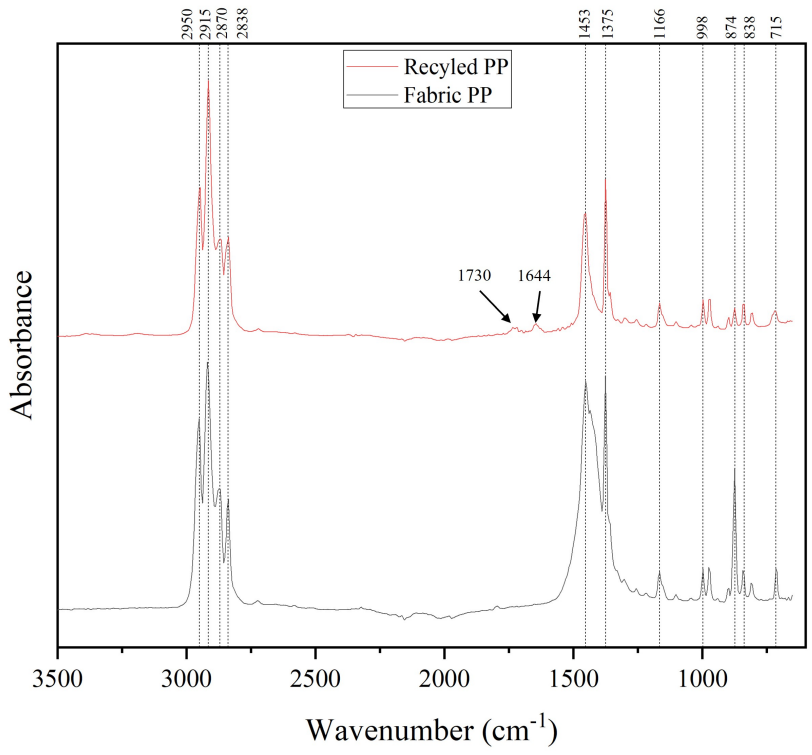


Figure 5.15: FTIR absorbance bands with identified peaks of fabric and recycled PP in black at the bottom and in red at the top respectively.

Table 5.3: FT-IR band assignment for the fabric and recycled PP.

Wavenumber (cm^{-1})	Vibration type	Band assignment	Reference
2950	Asymmetric stretching	-CH_3	[11, 14, 64]
2915	Asymmetric stretching	-CH_2	[11, 14, 64]
2870	Symmetric stretching	-CH_3	[11, 64]
2838	Symmetric stretching	-CH_2	[9, 11, 14]
1730 1644	Stretching	C=O	[23]
1453	Symmetric bending	-CH_3	[64]
1434	Asymmetric stretching	CO_3	[66]
1375	Symmetric bending	-CH_3	[11, 14, 64]
1167	Wagging Asymmetric rocking Asymmetric stretching	C-H -CH_3 C-C	[11, 14, 64]
998	Asymmetric rocking Bending Wagging	-CH_3 C-H -$CH_3$2	[11, 14]
974	Rocking Stretching	-CH_3 C-C	[14]
874	Out-of-plane bending	CO_3	[66]
838	Rocking	C-H -CH_2 -CH_3	[11, 14, 64]
715	Out-of-plane bending	-CH_3 CO_3	[11, 64, 66]

5.4.2 Polypropylene and recycled polypropylene DSC

From the DSC results the glass transition temperature cannot be obtained, as it is not appreciated. This can be either because a lower temperature should have been used as the starting point or because there is not so much amorphous phase. Both materials show an onset temperature of 150°C. For the PP in fabric shape there is a sharp melting peak at 163°C, showing the presence of a crystalline phase as presented in Fig. 5.16. For the recycled PP there are two endotherms, one very subtle at 125°C, and a broader and deeper one at 167°C. The fact that this first endotherm is still present in the second heating, shows that is not due the crystallization process or previous treatment given to the material, but instead shows the presence of a small amount of polyethylene [23], which melting temperature is around 125°C, in accordance with what was mentioned in the FT-IR results in Section 5.4.1. The second and broader peak corresponds to the polypropylene itself. The shift towards the right in the melting peak centre can be attributed to two different reasons. The first one, the pellet shape and mass, which induces temperature gradients in the sample, leading to recrystallization process while temperature is increasing, broadening the melting peak as the process takes place along a wider range of temperatures; the second, the crystalline structure of the polymer, since polypropylene homopolymer, block copolymer, and random copolymer show slightly different DSC curves as shown in Fig. 5.17.

For both cases an exothermic peak happens in the cooling cycle at 120°C for the fabric PP and at 119°C for the recycled one, this last one with a shoulder around the 109°C, which is associated with the polyethylene contaminating fraction that can show a crystallization peak between 94 and 113°C [67], as shown in Fig. 5.18.

Values of heat of fusion or melting enthalpy for 100% crystalline polypropylene have been reported at 170 J/g [68] and 207 J/g [69], depending on the polymer structure. By using these two values as a range, crystallinity of the materials studied here are between 34% and 42% for the fabric PP and between 35% and 43% for the recycled material.

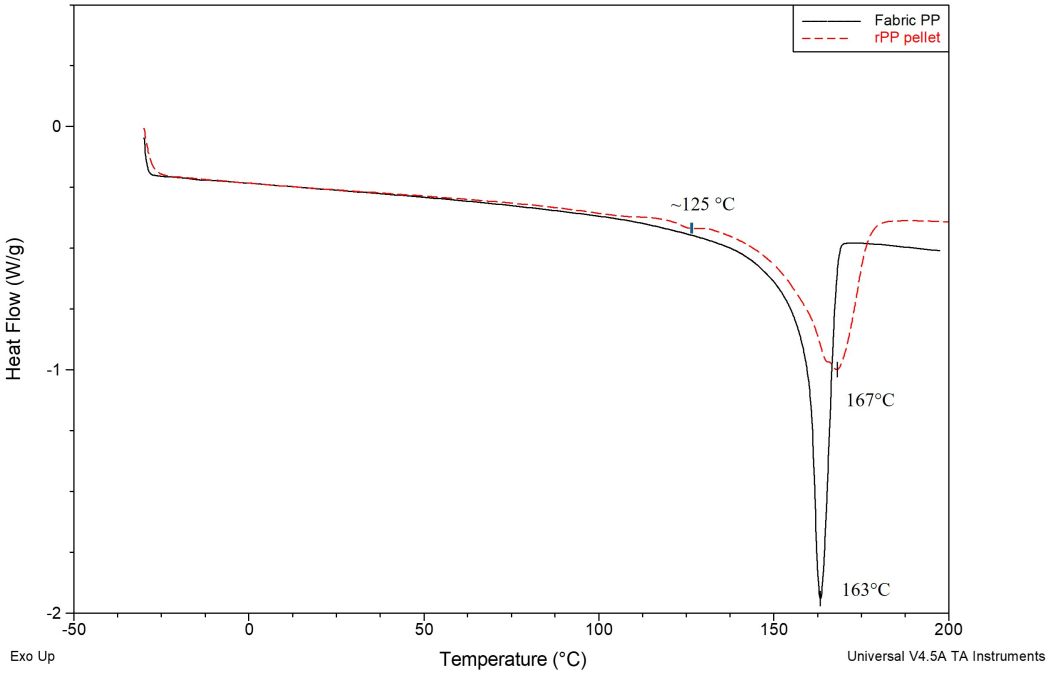


Figure 5.16: DSC results of fabric and recycled PP with melting peaks identified for the second heating cycle.

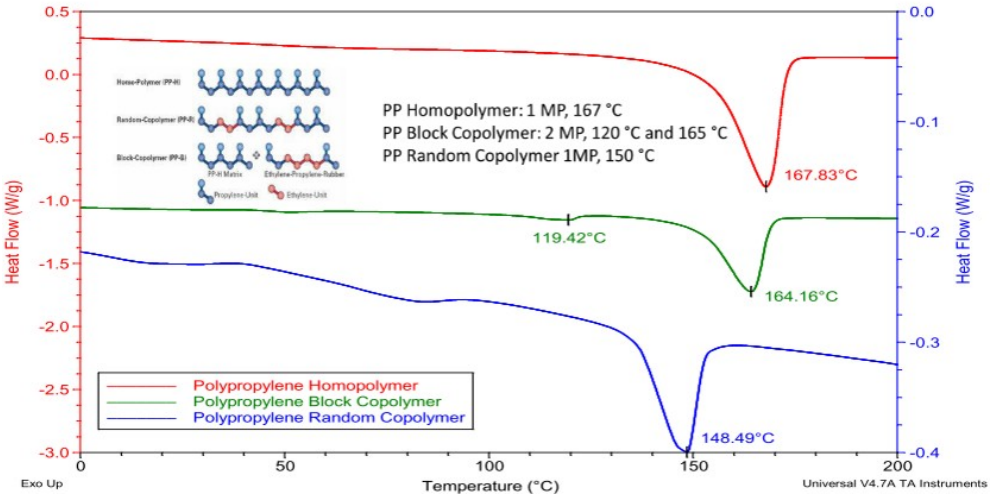


Figure 5.17: DSC of polypropylene homopolymer, block copolymer and random copolymer, showcasing how the chemical structure impacts the melting behaviour, from [70].

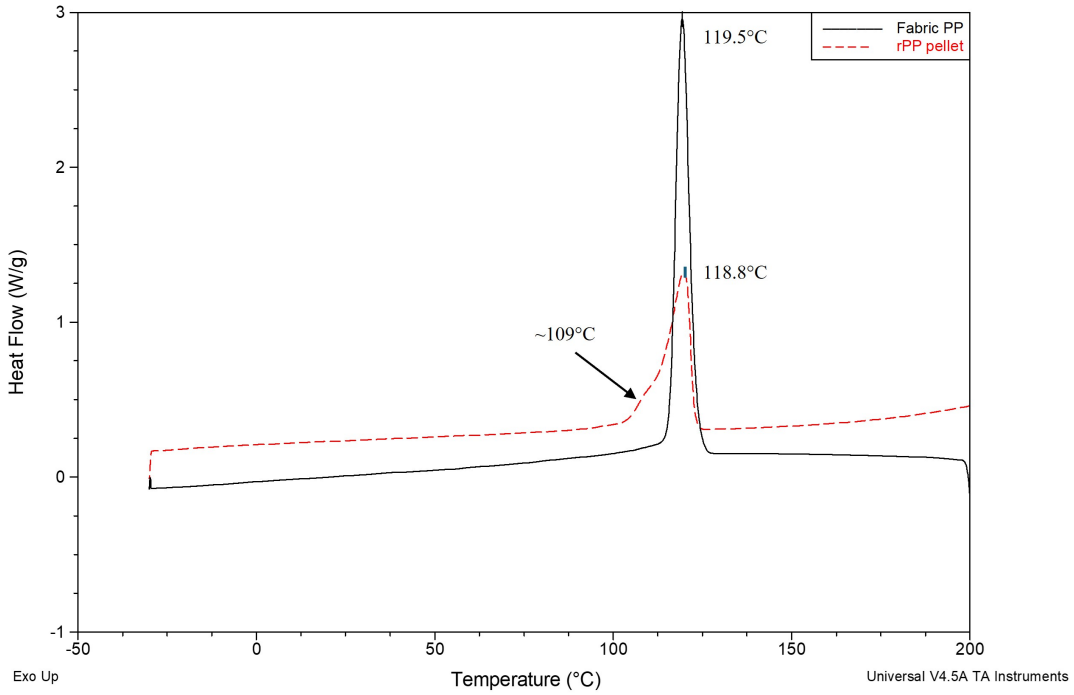


Figure 5.18: DSC results of fabric and recycled PP with crystallization peaks identified for the second cooling cycle.

5.4.3 Contact angle and wettability of fique fibres

The contact angle is measured when immersing the fibre in the liquids and when retreating it at the same speed. Advancing and receding contact angles for fique are clearly different for all cases, presenting hysteresis, as commonly found in cotton and rayon [71], coir and PET fibres [33], jute [34], and cellulosic fibres [62], and as shown in Fig. 5.19. The nature of hysteresis can be explained from thermodynamic or kinetic reasons [28]. The roughness and heterogenous nature of the fibre's surface [72], as well as surface contamination and molecular structure [71] fall under the former, while surface deformation when penetrating the liquid [73], liquid penetration, and surface mobility or reorientation fall under the latter.

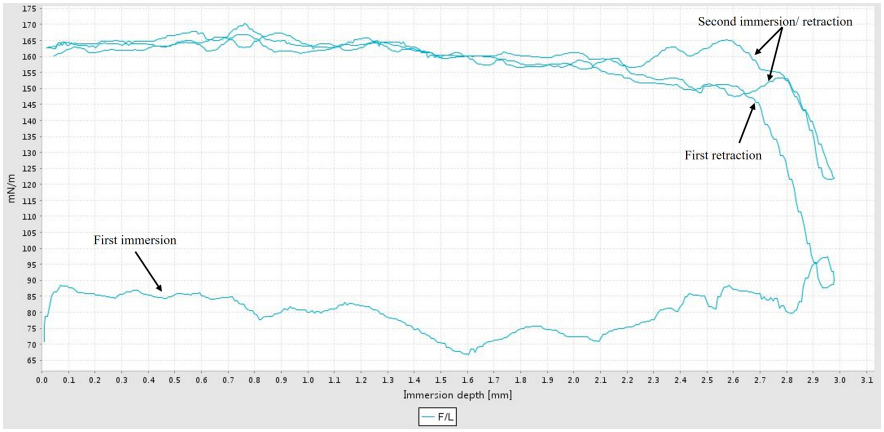


Figure 5.19: Graph obtained directly from the OneAttension measuring equipment, where the hysteresis between advancing and receding angle can be seen between the first immersion and the retraction, as well as for the second cycle.

The advancing contact angles for the differently treated fibres changes significantly for both the mercerised and hydrolysed fique when immersed in water, with a contact angle that goes from 54.1° for untreated fibres to 14.5° and 27.4° for the chemically treated fibres respectively, as collected in Table 5.4. For the high intensity ultrasonication treatment, for the previously mercerised fibres the contact angle decreases to 36.8°, but for the previously hydrolysed fibres this decreased is less pronounced, to 47.8°. This decreased in contact angle shows a polarity increase in the fibre as well as an increase hydrophilicity; with the untreated fibres presenting the highest contact angle for water, being them the more hydrophobic ones, although hydrophobic as such would mean a contact angle above 90° [74]. For the ethylene glycol the contact angle is 64.8°, and decreases for every treatment to 31.1° for the mercerised fibres and further to 20.2° for the mercerised+HIUS treated fibres, with this remaining around 24° for both hydrolysed cases. For the ethanol, the untreated fibres show a 49.7° contact angle, which slightly increases for the mercerised fibres and abruptly decreases to around 0° for the other treated fibres. Contact angles with n-hexane are close to 0° for all cases. These contact angles are translated into the polar and dispersive components of the surface energy as explained in Section 5.3.2.3. In general, the surface energy values show a tendency where the polar component is increased when the water contact angle decreases, with the exception of hydrolysed+HIUS treated fibres, which show a lower contact angle with

water than the untreated fibres, but a slight decrease in the polar component which goes from 33.2 for untreated fibres to 26.6 mN/m for hydrolysed+HIUS treated fibres, with a small decrease in the total surface energy from 41.4 mN/m to 40.9 mN/m respectively. Mercerised and hydrolysed only treated fibres show the highest polar component with 57.5 mN/m and 48.0 mN/m respectively, and a total surface energy of 64.4 mN/m and 58.3 mN/m respectively. For all the treated fibres the polar energy component changes with the dispersive component increasing for all cases except the mercerised only fibres. For the chemically plus sonication treated fibres the dispersive component reaches 12.5 mN/m and 14.3 mN/m values for mercerised and hydrolysed respectively as shown in Fig. 5.20, with the polar component being reduced after the HIUS treatment on the chemically treated fibres.

Table 5.4: Advancing contact angles (°) for fique and its different treatments for the four used liquids

Liquid	Fique fibres				
	Untreated	Mercerised	Mercerised +HIUS	Hydrolysed	Hydrolysed +HIUS
Water	54.1± 23.8	14.5±19.8	36.8±28.0	27.4±17.6	47.8±46.9
Ethylene glycol	64.8±14.5	31.1±15.2	20.2±20.3	24.1±28.9	24.0±27.5
Ethanol	49.7±10.5	52.6±8.7	0±0	4.4±15.2	0.7±2.4
n-Hexane	7.0±22.3	8.8±28.0	0.0±0.0	2.3±7.7	0.0±0.0

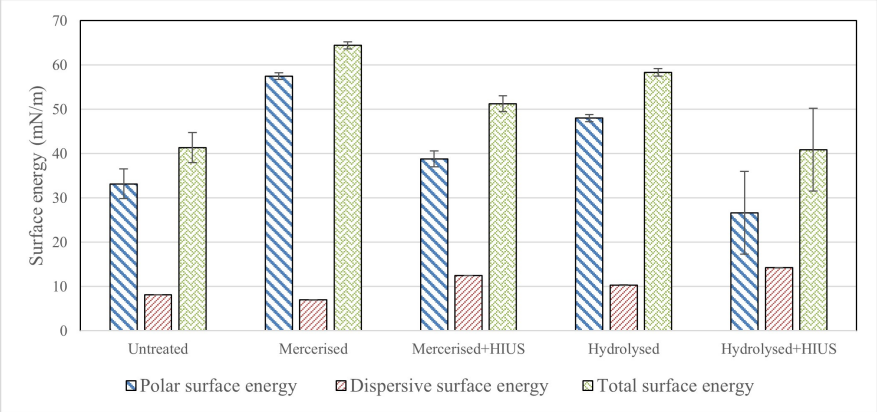
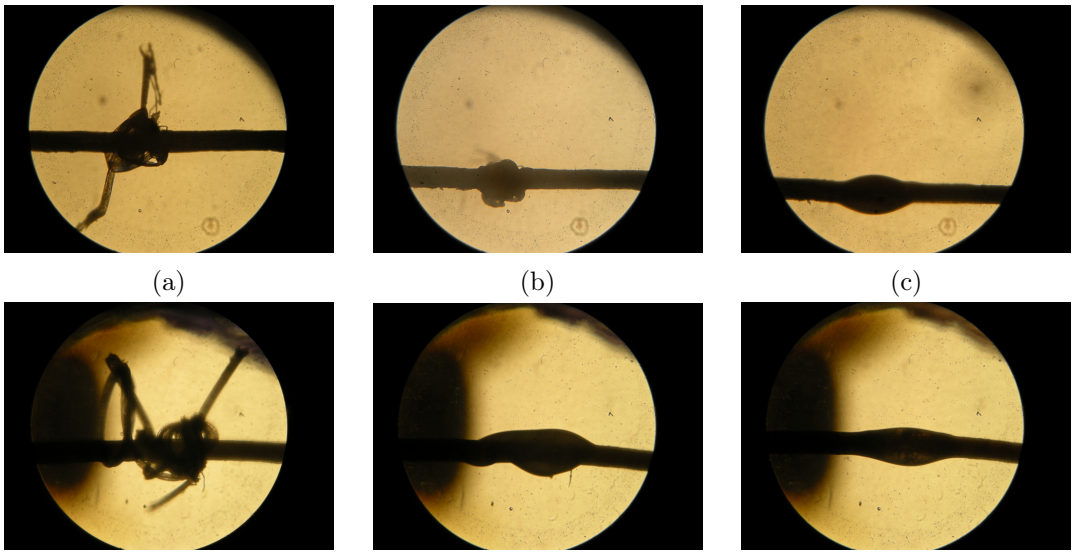


Figure 5.20: Surface energy and its polar and dispersive components for the untreated fique and the different treatments, showing how these impact the polarity of the fibres.

5.4.4 Fique-PP contact angle

The hot stage microscope allowed to see the evolution of the recycled PP when subjected to temperature on top of the fibre's surface. In Fig. 5.21 it is shown how a knot is visible at ambient temperature and how as the temperature increases the rPP starts to melt to finally form the droplet on which the contact angle will be measured.



(a) (b) (c)

(d) (e) (f)

Figure 5.21: (a) and (d) show a rPP knot around washed and hydrolysis treated fique respectively, (b) and (e) show how the rPP starts melting, and (c) and (f) show how a droplet is finally formed around the fibre.

The contact angle is measured every 2°C from 177°C to 219°C, and the values for each treated fibre are presented in Table 5.5, with a graph showing and evolution complementing this table in Fig. 5.22.

Table 5.5: Advancing contact angles (°C) for fique and its different treatments with recycled polypropylene with temperature increase.

(°C) / Fique	177	179	181	183	185	187	189	191 (...)	199	201	203	205	207	209	211	213	215	217	219
Untreated	55	48	44	43	42	46	40	41	42	41	41	39	38	39	40	40	38	38	40
Mercerised	60	53	50	44	44	45	43	42	42	43	48	45	41	43	36	33	27	24	12(→0)
Mercerised+HIUS	54	53	48	51	48	44	44	45	51	45	41	38	39	39	40	34	34	35	30
Hydrolysed	61	49	48	45	45	45	46	47	49	46	47	47	45	43	45	46	34	22	20(→0)
Hydrolysed+HIUS	62	59	59	49	50	54	51	54	55	53	54	55	54	58	50	46	50	27	23(→0)

While for the untreated fique a clear droplet is visible at the end of the thermal process, only the mercerised+HIUS treated fibres present this behaviour with a lower angle value, but a still visible droplet. For the other three cases the contact angle decreases significantly until the point that no droplet is visible any more with a tendency towards a zero angle, i.e. what would equate to full wettability by the matrix. For the mercerised+HIUS treated fibre, its polar surface energy is the most similar to the untreated fibre, but with an increase in the dispersive component. This zero contact angle behaviour is quite unexpected, so a further look was taken with a scanning electron microscope to have a look at the surface of the fibre and the contact with the recycled polypropylene. It is worth noticing how in Fig. 5.22 the hydrolysis+HIUS treated fibre shows the highest contact angle value until 215°C, after which it decreases significantly, signalling that differently treated fibres may need temperature adjustments when processing to maximize the fibre-matrix interaction, as this significant decrease is also visible for the hydrolysis treated fibres.

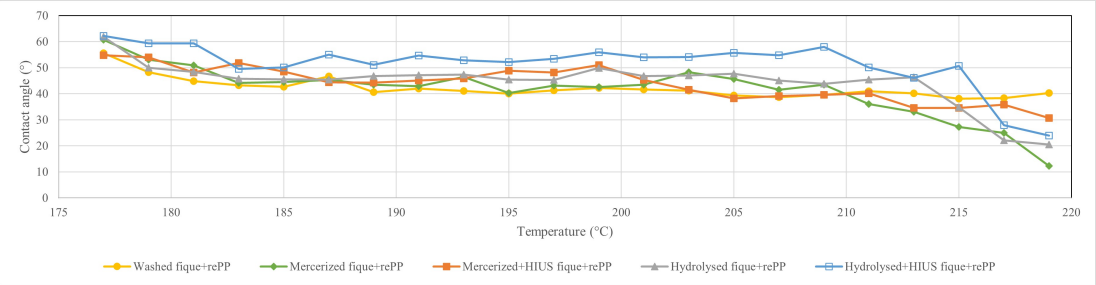
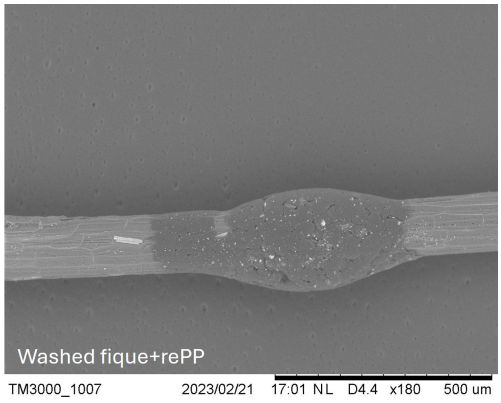
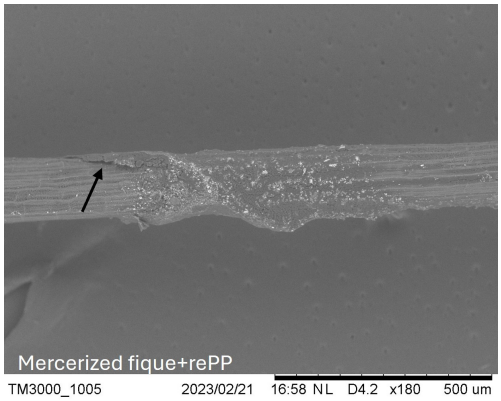


Figure 5.22: Graph showing the evolution of the contact angle of rPP on the different treated fique fibres.

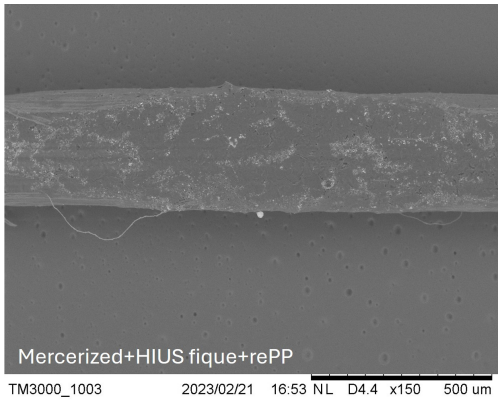
In Fig. 5.23 it is shown how a droplet of rPP forms around untreated fique fibre after the thermal process in the hot stage microscope. The contact angle is measured at 40°, remaining the highest one, and also the most stable along the whole temperature raising process. For the mercerized treated fique, the droplet disappears with the rPP spread along the fibre with that contact angle tending to zero. Interestingly, as pointed out with a black arrow in Fig. 5.23b, a gap between the matrix and the fibre can be seen. For mercerized+HIUS and hydrolysis treated fibres the matrix is visible around the fibre, again spread along it, with the contact angle tending to zero. For the case of



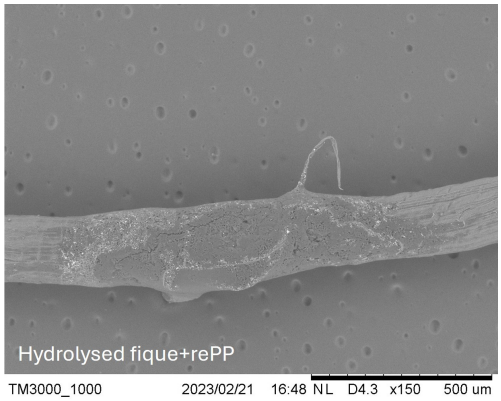
(a)



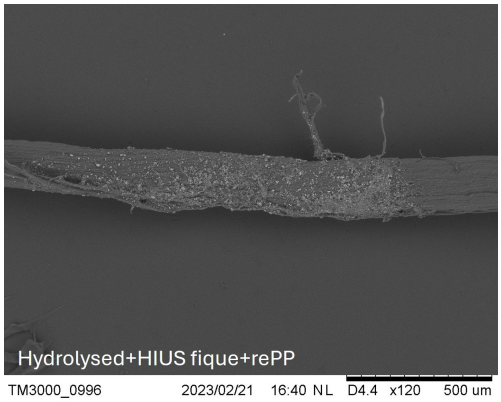
(b)



(c)



(d)



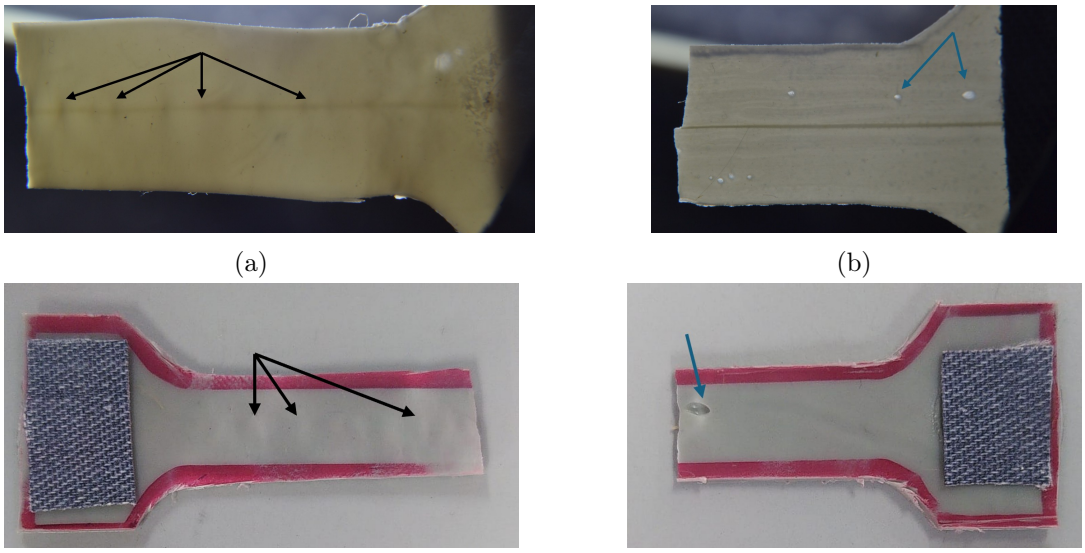
(e)

Figure 5.23: (a) Washed fique and a rPP well formed droplet; (b) mercerized fique with rPP, with a gap between polymer and fibre; (c) mercerized+HIUS treated fibre with matrix visible on the fibre's surface; (d) hydrolysed fique with rPP on the fibre surface; (e) hydrolysed+HIUS fique with rPP matrix showing a discontinuous matrix surface on top of the fibre.

hydrolysed+HIUS treated fique, the matrix on the fibre's surface is visible, but discontinuity on it is worth highlighting, as this can be a problem when it comes to transfer load from the matrix to the fibre. The reason why the contact angle decreases with the chemical treatments can be partly explained because of the interaction between the fibre and the matrix due to the chemical changes in the fibre's surface. But not only that, as the hydrolysis treatment, while removing waxes and non-cellulosic components, also exposed the microfibrils that conform the technical fibres more, effect increased by the ultrasonication treatment, potentially contributing to facilitate the spread of the matrix along these smaller microfibrils, breaking the continuity of the matrix surface.

5.4.5 Single fibre fragmentation test

For each type of fibre at least 16 specimens were manufactured, sometimes with only 25% of success when testing, with specimens presenting debonding or matrix breaking earlier than interfacial failure due to trapped air with bubbles acting as stress concentrators, and how bubbles were present during samples manufacturing and on final samples as shown with blue arrows in Fig. 5.24b and Fig. 5.24d. These bubbles are believed to have formed during the manufacturing process of the polypropylene film, when heating and pressing the pellets. This led to 5 valid samples for the washed fique, 4 for the mercerised fique, 3 for the mercerised+HIUS treated fique, and 4 for both hydrolysed and hydrolysed+HIUS treated fique. On Fig. 5.24 it is shown the difference between a case with no fragmented fibre in contrast with one with a fragmented fibre with black arrows pointing to some of the breaking points. In Fig. 5.24c it can be seen one of the tested specimens, and how the same breaking pattern as in the initial samples as shown in Fig. 5.24a can be seen and how the matrix sees a change in colour due to the strain sustained.



(a) (b)

(c) (d)

Figure 5.24: (a) Initial specimen with some fragments signalled by black arrows after testing, (b) initial specimen with no fragments after testing, with bubbles pointed out by blue arrows, (c) tested specimen with some fragments signalled by black arrows with visible stress whitening, and (d) failed specimen, with no fragmentation and a visible superficial defect signalled by a blue arrow.

On average, the higher number of fragments is obtained for the mercerized+HIUS treated fique fibres, which leads to the lowest critical fibre length, this being 7.13 mm, and the highest IFSS with a value of 3.32 MPa. The lowest IFSS value is obtained for the mercerized fique, 1.12 MPa, which presents the lowest number of fragments leading to a 16.5 mm critical fibre length, followed by the 1.64 MPa obtained by the hydrolysed+HIUS treated fique. Values of critical fibre length and interfacial shear strength for all fique fibre treatments are detailed in Table 5.6.

These values are well within values in the literature for studies about fique. The starch reinforced with untreated fique 1.25 and 1.1 MPa [57] is in good agreement for the values obtained here for the mercerized and hydrolysed+HIUS treated fique, while in the work presented here the untreated fique shows a higher level of adhesion with polypropylene than in the starch case. The 2.5 MPa obtained by Minty *et al.* [58] with virgin polypropylene and untreated fibres is in very good agreement with the values obtained in this case with recycled polypropylene for the washed fique. The same

happens when comparing these values with the work done by Vargas *et al.* [56], with 2.38 MPa and 2.57 MPa for washed and unwashed fique, in this case in a polyester matrix. The coating with styrene-acrylic resin increases these values up to 5 MPa through the esterification reaction that promotes a greater chemical bond. Similar values are obtained with polypropylene and polyethylene reinforced coir, which find a maximum IFSS of 5 MPa when adding a compatibilizer to the PP matrix [44]. Other fibres like jute or hemp present values around 5 MPa of IFSS when reinforcing polypropylene with MaPP and silane treatments increasing these values [32, 46], although hemp reinforced polypropylene with 2% MaPP has achieved values on the 12 MPa range [47]. Higher IFSS values are generally obtained for matrices reinforced by flax fibre with values going above the 10 MPa or higher when matrix compatibilizers are used. In these cases, where the fibre tensile strength is significantly higher than fique's, mechanical properties besides the adhesion with the matrix are considered to have a significant impact on the measured interfacial properties. Flax and ramie fibres with reported tensile strengths of 874 and 1250 MPa, well above the 330 MPa calculated for fique in this work can lead to values well above the 20 MPa for the IFSS [45, 48]. High values are also obtained when thermosetting matrices are used instead of thermoplastics [49] even when no fibre treatment or matrix compatibilizer are used.

Table 5.6: Critical fibre length (mm) and shear strength (MPa) for different fibre treatments.

Fique fibres	l_c (mm)	IFSS (MPa)
Washed fique	7.95±2.39	2.77±0.81
Mercerized fique	16.5±3.67	1.12±0.64
Mercerized fique+HIUS	7.13±3.37	3.32±0.59
Hydrolysed fique	8.56±4.23	2.73±1.11
Hydrolysed fique+HIUS	9.85±2.21	1.64±0.29

In the work presented here there is a clear inconvenient, which is that treated fibres have not been mechanically characterised in any way and definitely not as thoroughly as the washed fique has, as discussed in Chapter 3. From others work natural fibres subjected to chemical treatments can see their tensile strength increased or decreased,

as is the case for their ability to interact with the matrix, depending on type and time of treatment. *Stipa obtusa* fibres shown a tensile strength increase of approximately 100 MPa for a 3 h of NaOH treatment in comparison to the 1.5 h treatment, and this property goes back to the same values obtained at 1.5 h treatment for a 5 h treatment, showing that while a mid duration treatment time can increase the proportion of cellulose, and hence increasing the mechanical properties, a too long treatment can contribute to the degradation of the crystalline cellulose, in addition to the loss of pectin, hemicellulose and lignin during the prolonged chemical reaction [50]. Sisal fibres characterised prior pull-out test in reinforced PLA showed a decrease in tensile strength after silane, alkaline and a combination of both treatments, going from 366 MPa when untreated to 212 MPa when both treatments were combined. A lower decreased was shown when the treatments were applied independently, finding a tensile strength of 341 MPa for silane treated fibres, and 352 MPa for alkaline treated fibres [35], showing that although the mechanical properties of the fibre may decrease, and improvement on the interface characteristics can lead to an increase of the IFSS. In the case of jute fibre, the modulus has been reported to increase by 33% after 2 h alkaline treatments, after which the increase was by 50% and 78% after 4h and 8 h treatments respectively. At the same time, the strain at break saw a reduction of 44%, 55.5%, and 72.2% respectively, showing that alkali treated fibres are stiffer and more brittle than untreated fibres. Nothing is mentioned about the tensile strength, but given how proportionally the modulus and the strain at break change, it is expected that the tensile strength does not see significant changes in this case [75], although this is not true in other study, where jute was treated with alkaline and silane treatments, besides being boiled. For all cases, untreated and treated boiled jute saw a decrease in the tensile strength. But alkaline and silane treated jute went from 1233 MPa for the untreated case to 1287 MPa and 1331 MPa respectively, with small or no significant changes in the fibres elastic modulus and elongation [46].

In the case of fique, just the fact of washing the fibres has been reported to reduce the tensile strength from 355 MPa to 297 MPa [56], but when it comes to treated fibres it has been reported in the past that a 1 h alkaline treatment saw the tensile strength of

the fibres increasing from 262 MPa to 340 MPa, with an increase in the elastic modulus from 8.4 GPa to 12.5 GPa that corresponds with an increase in the strain at break from 6.3% to 8% [57]. In the work done by Gañán and Mondragón [36] the effect of different treatments on fique is also studied and from a tensile strength of 237 MPa for the untreated fique this values increases up to 373 MPa when a mercerization treatment is applied, and is further increased to 400 MPa when mercerization and a silane treatment are combined. In this case the process of esterification with maleic anhydride leads to a decrease in tensile strength to a value of 141 MPa, while the process using acrylic acid reduces it to 190 MPa. The silane only treatment led to an increase in the tensile strength of fique up to 265 MPa, with the combination of mercerization with maleic anhydride achieving a value of 242 MPa, while the combination of mercerization with acrylic acid reduces the value from the untreated fibres in 3 MPa. This just shows that prediction of how the chemical or surface treatments can impact the mechanical properties is going to depend on the type of fibre, the type of treatment, the treatment duration, and the physical properties of the fibre such as cross-section area, which are at the same time dependent on origin and harvest time and location.

5.5 Conclusion

In this chapter a closer look via FT-IR and DSC was taken into recycle and virgin polypropylene, which has contributed to understand the polymer behaviour and to see the differences between virgin and recycled PP, helping to identify degradation. This has also helped to understand different compositions and fillers used in polypropylene manufacturing. The investigation on matrix-fibre interface has been done looking solely at rPP, since the virgin PP, which was provided in woven shape and thin sheets would degrade under temperature very easily, not allowing to form films to manufacture the single fibre fragmentation samples.

Wettability of the washed and treated fibres was studied by the Owen and Wendt method combined with the Young-Laplace equation using four different liquids, n-Hexane, ethanol, ethylene glycol, and water, from less to most polar. From this the

surface energy of fique was calculated along with the polar and dispersive components showcasing how the different treatments impact the surface properties of the fibres beyond roughness, with the ultrasonication treatment clearly reducing the polar component of the surface energy after the chemical treatments.

The study on the hot stage microscope is used to directly measured the contact angle of the recycled PP on top of the fibre's surface, showing this evolution with the increasing temperature. The washed fique shows here the most stable values after the droplet is formed, with contact angle values significantly decreasing for mercerized, hydrolysed, and hydrolysed+HIUS treated fibres, with this drop being smoother for the mercerized+HIUS treated fique. Through a closer look via SEM, it can be appreciated how a clear gap between the rPP and the mercerized fique surface exists, which can help to explain this treated fibre presenting the lowest value of IFSS in the single fibre fragmentation test, as with the existence of a gap a stress transfer from the matrix to the fibre would fail. The next lowest value of IFSS is obtained by the hydrolysed+HIUS treated fique, which in the SEM image shows a discontinuous matrix, also unable to successfully transfer load to the fibre. This discontinuity is explained by the microfibrils contributing to spread the matrix along the microfibrils surface, as after the chemical and ultrasonication treatments these are more exposed. The significant drop of contact angle after 213°C in some cases suggests the need to adjust the temperature range for manufacturing when having chemically treated fibres.

In the IFSS results, the mercerized+HIUS treated fique shows the highest number of fragments leading to the highest IFSS values, followed by the washed fique and the hydrolysis treated fique with values of 3.32 MPa, 2.77 MPa, and 2.73 MPa. The manufacturing technique used for these samples has proven to be less efficient than expected., with many bubbles forming through the matrix, and specimens not failing inter-facially. On top of this, mechanical characterisation of the treated fibres with the same detail as for the washed fibres, which tensile strength as calculated in Chapter 3 is used here could potentially change these results and help understand better how the IFSS and the interaction fibre-matrix changes with fibre mechanical properties modification.

Bibliography

[1] N. E. Ajayi, S. Rusnakova, A. E. Ajayi, R. O. Ogunleye, S. O. Agu, and A. N. Amenaghawon, "A comprehensive review of natural fiber reinforced polymer composites as emerging materials for sustainable applications," *Applied Materials Today*, vol. 43, 4 2025. https://doi.org/10.1016/j.apmt.2025.102666.

[2] L. T. Sin and B. S. Tueen, "2 - eco-profile of plastics," in *Plastics and Sustainability* (L. T. Sin and B. S. Tueen, eds.), pp. 45–89, Elsevier, 2023. https://doi.org/https://doi.org/10.1016/B978-0-12-824489-0.00010-6.

[3] E. A. Campo, *1. Polymeric Materials and Properties.* William Andrew Publishing/Plastics Design Library, 2008. https://app.knovel.com/hotlink/pdf/id:kt013JV0F4/selection-polymeric-materials/polymeric-materials-properties.

[4] S. Gohil, S. Suhail, J. Rose, T. Vella, and L. Nair, "Chapter 8 - polymers and composites for orthopedic applications," in *Materials for Bone Disorders* (S. Bose and A. Bandyopadhyay, eds.), pp. 349–403, Academic Press, 2017. https://doi.org/10.1016/B978-0-12-802792-9.00008-2.

[5] M. Lanaro, L. Booth, S. K. Powell, and M. A. Woodruff, *Electrofluidodynamic technologies for biomaterials and medical devices: Melt electrospinning*, pp. 37–69. Elsevier Inc., 1 2018. https://doi.org/10.1016/B978-0-08-101745-6.00003-7.

[6] K. Ragaert, L. Delva, and K. V. Geem, "Mechanical and chemical recycling of solid plastic waste," *Waste Management*, vol. 69, pp. 24–58, 11 2017. https://doi.org/10.1016/j.wasman.2017.07.044.

[7] X. Zhu, D. Yan, and Y. Fang, "In situ ftir spectroscopic study of the conformational change of isotactic polypropylene during the crystallization process," *Journal of Physical Chemistry B*, vol. 105 (50), pp. 12461–12463, 12 2001. https://doi.org/10.1021/jp012165f.

[8] R. A. Ozzetti, A. P. D. O. Filho, U. Schuchardt, and D. Mandelli, "Determination of tacticity in polypropylene by ftir with multivariate calibration," *Journal of Applied Polymer Science*, vol. 85, pp. 734–745, 5 2002. https://doi.org/10.1002/app.10633.

[9] N. Chibani, H. Djidjelli, A. Dufresne, A. Boukerrou, and S. Nedjma, "Study of effect of old corrugated cardboard in properties of polypropylene composites: Study of mechanical properties, thermal behavior, and morphological properties," *Journal of Vinyl and Additive Technology*, vol. 22 (3), pp. 231–238, 9 2016. https://doi.org/10.1002/vnl.21437.

[10] S. A. Stoian, A. R. Gabor, A. M. Albu, C. A. Nicolae, V. Raditoiu, and D. M. Panaitescu, "Recycled polypropylene with improved thermal stability and melt processability," *Journal of Thermal Analysis and Calorimetry*, vol. 138 (4), pp. 2469–2480, 11 2019. https://doi.org/10.1007/s10973-019-08824-2.

[11] R. Caban, "Ftir-atr spectroscopic, thermal and microstructural studies on polypropylene-glass fiber composites," *Journal of Molecular Structure*, vol. 1264, 9 2022. https://doi.org/10.1016/j.molstruc.2022.133181.

[12] Wiley Science Solutions, "Isotactic polypropylene ftir spectrum." https://spectrabase.com/spectrum/6KzAseIX4o1, 2025. SpectraBase Spectrum ID: 6KzAseIX4o1. Accessed September 16, 2025.

[13] Wiley Science Solutions, "Atactic polypropylene ftir spectrum." https://spectrabase.com/spectrum/62hSXgHLxzz, 2025. SpectraBase Spectrum ID: 62hSXgHLxzz. Accessed September 16, 2025.

[14] L. Prior, M. S. Oliveira, and T. Zhiltsova, "Assessment of the impact of superficial contamination and thermo-oxidative degradation on the properties of post-consumer recycled polypropylene," *Materials*, vol. 16 (3), 2 2023. https://doi.org/10.3390/ma16031198.

[15] A. Khoironi, H. Hadiyanto, S. Anggoro, and S. Sudarno, "Evaluation of polypropylene plastic degradation and microplastic identification in sediments at tambak

lorok coastal area, semarang, indonesia," *Marine Pollution Bulletin*, vol. 151, 2 2020. https://doi.org/10.1016/j.marpolbul.2019.110868.

[16] J. Grebowicz, S.-F. Lau, and B. Wunderlich, "The thermal properties of polypropylene," *Journal of Polymer Science: Polymer Simposia*, vol. 71 (1), pp. 19–37, 1984. https://doi.org/10.1002/polc.5070710106.

[17] J. Cowie, "Glass transition temperatures of stereoblock, isotactic and atactic polypropylenes of various chain lengths," *European Polymer Journal*, vol. 9, no. 10, pp. 1041–1049, 1973. https://doi.org/10.1016/0014-3057(73)90081-5.

[18] J. Cao and I. Sbarski, "Determination of the enthalpy of solid phase transition for isotactic polypropylene using a modified dsc technique," *Polymer*, vol. 47 (1), pp. 27–31, 1 2006. https://doi.org/10.1016/j.polymer.2005.10.144.

[19] A. Kpeusseu, K. Yeo, B. Ernest, B. Bi, P. Magloire, E. Koffi, and P. Gbaha, "Polypropylene characterization by differential scanning calorimetry (dsc)," *International Journal of Innovation and Applied Studies*, vol. 40 (1), pp. 12–19, 2023. Article ID: IJIAS-23-151-06http://www.ijias.issr-journals.org/abstract.php?article=IJIAS-23-151-06.

[20] J. P. Mofokeng, A. S. Luyt, T. Tábi, and J. Kovács, "Comparison of injection moulded, natural fibre-reinforced composites with pp and pla as matrices," *Journal of Thermoplastic Composite Materials*, vol. 25 (8), pp. 927–948, 12 2012. https://doi.org/10.1177/0892705711423291.

[21] L. Baltes, L. Costiuc, S. Patachia, and M. Tierean, "Differential scanning calorimetry—a powerful tool for the determination of morphological features of the recycled polypropylene," *Journal of Thermal Analysis and Calorimetry*, vol. 138 (4), pp. 2399–2408, 11 2019. https://doi.org/10.1007/s10973-019-08679-7.

[22] Hitachi High-Tech, "TA no.86 DSC Measurement of Polypropylene: The effects of heat treatment on polymer crystallinity," tech. rep., Hitachi High-Tech Corporation, 2008. https://www.hitachi-hightech.com/file/global/pdf/products/science/appli/ana/thermal/application_TA_086e.pdf.

[23] I. Borovanska, T. Dobreva, R. Benavente, S. Djoumaliisky, and G. Kotzev, "Quality assessment of recycled and modified ldpe/pp blends," *Journal of Elastomers and Plastics*, vol. 44 (6), pp. 479–497, 11 2012. https://doi.org/10.1177/0095244312441731.

[24] Åge G. Larsen, K. Olafsen, and B. Alcock, "Determining the PE fraction in recycled pp," *Polymer Testing*, vol. 96, 4 2021. https://doi.org/10.1016/j.polymertesting.2021.107058.

[25] M. Gall, P. J. Freudenthaler, J. Fischer, and R. W. Lang, "Characterization of composition and structure–property relationships of commercial post-consumer polyethylene and polypropylene recyclates," *Polymers*, vol. 13 (10), 5 2021. https://doi.org/10.3390/polym13101574.

[26] H. Jones, J. McClements, D. Ray, C. S. Hindle, M. Kalloudis, and V. Koutsos, "Thermomechanical properties of virgin and recycled polypropylene—high-density polyethylene blends," *Polymers*, vol. 15 (21), 11 2023. https://doi.org/10.3390/polym15214200.

[27] I. Elfaleh, F. Abbassi, M. Habibi, F. Ahmad, M. Guedri, M. Nasri, and C. Garnier, "A comprehensive review of natural fibers and their composites: An eco-friendly alternative to conventional materials," *Results in Engineering*, vol. 19, 9 2023. https://doi.org/10.1016/j.rineng.2023.101271.

[28] K. Van De Velde and P. Kiekens, "Wettability of natural fibres used as reinforcement for composites a," *Die Angewandte Makromolekulare Chemie*, vol. 272, pp. 87–93, 1999. https://doi.org/10.1002/(SICI)1522-9505(19991201)272:1%3C87::AID-APMC87%3E3.0.CO;2-Q.

[29] J. Gassan, V. S. Gutowski, and A. K. Bledzki, "About the surface characteristics of natural fibres," *Macromolecular Materials and Engineering*, vol. 283, pp. 132–139, 2000. https://doi.org/10.1002/1439-2054(20001101)283:1<132::AID-MAME132>3.0.CO;2-B.

[30] G. Cantero, A. Arbelaiz, R. Llano-Ponte, and I. Mondragon, "Effects of fibre treatment on wettability and mechanical behaviour of flax/polypropylene composites," *Composites Science and Technology*, vol. 63 (9), pp. 1247–1254, 2003. https://doi.org/10.1016/S0266-3538(03)00094-0.

[31] C. Baley, F. Busnel, Y. Grohens, and O. Sire, "Influence of chemical treatments on surface properties and adhesion of flax fibre-polyester resin," *Composites Part A: Applied Science and Manufacturing*, vol. 37 (10), pp. 1626–1637, 10 2006. https://doi.org/10.1016/j.compositesa.2005.10.014.

[32] J. M. Park, S. T. Quang, B. S. Hwang, and K. L. DeVries, "Interfacial evaluation of modified jute and hemp fibers/polypropylene (pp)-maleic anhydride polypropylene copolymers (pp-mapp) composites using micromechanical technique and nondestructive acoustic emission," *Composites Science and Technology*, vol. 66 (15), pp. 2686–2699, 12 2006. https://doi.org/10.1016/j.compscitech.2006.03.014.

[33] L. Q. Tran, C. A. Fuentes, C. Dupont-Gillain, A. W. V. Vuure, and I. Verpoest, "Wetting analysis and surface characterisation of coir fibres used as reinforcement for composites," *Colloids and Surfaces A: Physicochemical and Engineering Aspects*, vol. 377 (1-3), pp. 251–260, 3 2011. https://doi.org/10.1016/j.colsurfa.2011.01.023.

[34] T. T. L. Doan, H. Brodowsky, and E. Mäder, "Jute fibre/epoxy composites: Surface properties and interfacial adhesion," *Composites Science and Technology*, vol. 72 (10), pp. 1160–1166, 6 2012. https://doi.org/10.1016/j.compscitech.2012.03.025.

[35] A. Orue, A. Jauregi, C. Peña-Rodriguez, J. Labidi, A. Eceiza, and A. Arbelaiz, "The effect of surface modifications on sisal fiber properties and sisal/poly (lactic acid) interface adhesion," *Composites Part B: Engineering*, vol. 73, pp. 132–138, 2015. https://doi.org/10.1016/j.compositesb.2014.12.022.

[36] P. Gañán and I. Mondragon, "Surface modification of fique fibers. effects on their physico-mechanical properties," *Polymer Composites*, vol. 23 (3), pp. 383–394, 6 2002. https://doi.org/10.1002/pc.10440.

[37] M. F. Muñoz-Velez, M. Á. Hidalgo-Salazar, and J. H. Mina-Hernández, "Fique fiber an alternative for reinforced plastics. influence of surface modification," *Biotecnología en el Sector Agropecuario y Agroindustria*, vol. 12 (2), pp. 60–70, 12 2014. https://www.researchgate.net/publication/317501110_FIQUE_FIBER_AN_ALTERNATIVE_FOR_REINFORCED_PLASTICS_INFLUENCE_OF_SURFACE_MODIFICATION.

[38] S. L. Schellbach, S. N. Monteiro, and J. W. Drelich, "A novel method for contact angle measurements on natural fibers," *Materials Letters*, vol. 164, pp. 599–604, 2 2016. https://doi.org/10.1016/j.matlet.2015.11.039.

[39] J.-K. Kim, Y.-W. Mai, and Y.-W. Mai, *Chapter 1 - Introduction*, pp. 1–4. Elsevier Science Ltd, 1998. https://doi.org/10.1016/B978-008042695-2/50002-6.

[40] D. A. Jesson and J. F. Watts, "The interface and interphase in polymer matrix composites: Effect on mechanical properties and methods for identification," 7 2012. https://doi.org/10.1080/15583724.2012.710288.

[41] S. Huang, B. Wang, and L. Yan, *Interphase and interfacial properties of composite materials*, pp. 151–177. Elsevier, 1 2021. https://doi.org/10.1016/B978-0-12-820512-9.00020-4.

[42] L. T. Drzal, M. J. Rich, and P. F. Lloyd, "Adhesion of graphite fibers to epoxy matrices: I. the role of fiber surface treatment," *The Journal of Adhesion*, vol. 16 (1), pp. 1–30, 1983. https://doi.org/10.1080/00218468308074901, issn = 15455823.

[43] J. L. Thomason, "Interfacial strength in thermoplastic composites-at last an industry friendly measurement method?," *Composites: Part A*, vol. 33, pp. 1283–1288, 2002. https://doi.org/10.1016/S1359-835X(02)00150-1.

[44] J. L. Thomason and J. L. Rudeiros-Fernández, "Characterization of interfacial strength in natural fibre–polyolefin composites at different temperatures," *Composite Interfaces*, vol. 29 (2), pp. 175–196, 2022. https://doi.org/10.1080/09276440.2021.1913901.

[45] H. Bos, *The Potential of Flax Fibres as Reinforcement for Composite Materials*. Technische Universiteit Eindhoven, 2004. https://doi.org/10.13140/RG.2.1.1540.4643.

[46] J. M. Park, P. G. Kim, J. H. Jang, Z. Wang, B. S. Hwang, and K. L. DeVries, "Interfacial evaluation and durability of modified jute fibers/polypropylene (pp) composites using micromechanical test and acoustic emission," *Composites Part B: Engineering*, vol. 39 (6), pp. 1042–1061, 9 2008. https://doi.org/10.1016/j.compositesb.2007.11.004.

[47] T. Huber and J. Müssig, "Fibre matrix adhesion of natural fibres cotton, flax and hemp in polymeric matrices analyzed with the single fibre fragmentation test," *Composite Interfaces*, 2008. https://doi.org/10.1163/156855408783810948.

[48] A. Awal, G. Cescutti, S. B. Ghosh, and J. Müssig, "Interfacial studies of natural fibre/polypropylene composites using single fibre fragmentation test (sfft)," *Composites Part A: Applied Science and Manufacturing*, 2011. https://doi.org/10.1016/j.compositesa.2010.10.007.

[49] M. Seghini, F. Touchard, F. Sarasini, D. Mellier, J. Tirillò, M. Seghini, F. Touchard, F. Sarasini, and D. Mellier, "Interfacial adhesion assessment in flax / epoxy and in flax / vinylester composites by single yarn fragmentation test : Correlation with micro-ct analysis.," *Composites Part A: Applied Science and Manufacturing, Elsevier*, vol. 113, pp. 66–75, 2018. https://doi.org/10.1016/j.compositesa.2018.07.015.

[50] S. Candiotti, J. L. Mantari, C. E. Flores, and S. Charca, "Assessment of the mechanical properties of peruvian stipa obtusa fibers for their use as reinforcement in composite materials," *Composites Part A: Applied Science and Manufacturing*, 2020. https://doi.org/10.1016/j.compositesa.2020.105950.

[51] H. M. Brodowsky and A. Hennig, "Micromechanical tests on natural fibre composites with enzymatically enhanced fibre–matrix adhesion," *Materials Circular Economy*, vol. 4 (1), 12 2022. https://doi.org/10.1007/s42824-021-00040-4.

[52] L. T. Drzal and M. Madhukar, "Fibre-matrix adhesion and its relationship to composite mechanical properties," *Journal of Materials Science*, vol. 28 (3), pp. 569–610, 2 1993. https://doi.org/10.1007/BF01151234.

[53] A. Asadi, M. Miller, R. J. Moon, and K. Kalaitzidou, "Improving the interfacial and mechanical properties of short glass fiber/epoxy composites by coating the glass fibers with cellulose nanocrystals," *Express Polymer Letters*, vol. 10 (7), pp. 587–597, 7 2016. https://doi.org/10.3144/expresspolymlett.2016.54.

[54] J. Goswami, E. Haque, D. M. Fox, J. W. Gilman, G. A. Holmes, R. J. Moon, and K. Kalaitzidou, "The effect of cellulose nanocrystal coatings on the glass fiber-epoxy interphase," *Materials*, vol. 12 (12), 6 2019. https://doi.org/10.3390/ma12121951.

[55] C. A. Ardila Rodríguez, "Pruebas mecánicas para la estandarización y caracterización del método de pull-out-prueba de extración de fibras-para materiales compuestos de resinas poliméricas reforzadas con fibras de fique," 2009. https://hdl.handle.net/1992/16679.

[56] J. Vargas, M. Jalalvand, and J. M. Meza, "Improving interfacial shear strength of fique fibres using an acrylic coating," *Science Progress*, vol. 106 (4), 10 2023. https://doi.org/10.1177/00368504231207199.

[57] J. Mina, "Physico-mechanical characterization of thermoplastic cassava starch (tps) and interfacial analysis with fique fibers," *Biotecnología en el Sector Agropecuario y Agroindustrial*, vol. 10 (2), pp. 99–109, 2012. https://www.researchgate.net/publication/262515383.

[58] R. Minty, D. Martínez de Luca, and M. Jalalvand, "Interfacial characterisation of natural fique fibre / polypropylene composites using single fibre fragmentation test," *SAMPE Europe Conference*, pp. 1–8, 11 2022. https://www.researchgate.net/publication/373197002_Interfacial_Characterisation_of_Natural_Fique_FibrePolypropylene_Composites_using_Single_Fibre_Fragmentation_Test.

[59] British Standard Instituion, "Plastics - Differential scanning calorimetry (DSC) - Part 2: Determination of glass transition temperature and step height," standard, British Standard Institution, 2020.

[60] British Standard Instituion, "Plastics - Differential Scanning calorimetry (DSC) - Part3: Determination of temperature and enthalpy of melting and crystallization," standard, British Standard Institution, 2018.

[61] nanoScience Instruments, "Contact angle measurements and wettability." https://www.nanoscience.com/techniques/tensiometry/contact-angle-measurements-and-wettability/. Accessed June 17, 2026.

[62] M. F. Pucci, P. J. Liotier, and S. Drapier, "Tensiometric method to reliably assess wetting properties of single fibers with resins: Validation on cellulosic reinforcements for composites," *Colloids and Surfaces A: Physicochemical and Engineering Aspects*, vol. 512, pp. 26–33, 1 2017. https://doi.org/10.1016/j.colsurfa.2016.09.047.

[63] D. Tripathi and F. R. Jones, "Single fibre fragmentation test for assessing adhesion in fibre reinforced composites," *Journal of Materials Science*, vol. 33 (1), pp. 1–16, 1998. https://doi.org/10.1023/A:1004351606897.

[64] J. Fang, L. Zhang, D. Sutton, X. Wang, and T. Lin, "Needleless melt-electrospinning of polypropylene nanofibres," *Journal of Nanomaterials*, vol. 2012, 2012. https://doi.org/10.1155/2012/382639, issn = 16874110.

[65] M. Ni and B. D. Ratner, "Differentiating calcium carbonate polymorphs by surface analysis techniques - an xps and tof-sims study," *Surface and Interface Analysis*, vol. 40 (10), pp. 1356–1361, 10 2008. https://doi.org/10.1002/sia.2904.

[66] S. Hajji, T. Turki, A. Boubakri, M. B. Amor, and N. Mzoughi, "Study of cadmium adsorption onto calcite using full factorial experiment design," *Desalination and Water Treatment*, vol. 83, pp. 222–233, 7 2017. https://doi.org/10.5004/dwt.2017.21079.

[67] D. Li, L. Zhou, X. Wang, L. He, and X. Yang, "Effect of crystallinity of polyethylene with different densities on breakdown strength and conductance property," *Materials*, vol. 12 (11), 6 2019. https://doi.org/10.3390/ma12111746.

[68] F. J. Lanyi, N. Wenzke, J. Kaschta, and D. W. Schubert, "On the determination of the enthalpy of fusion of α-crystalline isotactic polypropylene using differential scanning calorimetry, x-ray diffraction, and fourier-transform infrared spectroscopy: An old story revisited," *Advanced Engineering Materials*, vol. 22 (9), 9 2020. https://doi.org/10.1002/adem.201900796.

[69] R. L. Blaine, "THERMAL APPLICATIONS NOTE Polymer Heats of Fusion," tech. rep., TA. https://docslib.org/doc/6777890/thermal-applications-note-polymer-heats-of-fusion.

[70] J. Jansen, "DSC Practical Interpretation with Examples for Polymer Development," tech. rep., The Madison Group, 2024.

[71] H. S. Whang and B. S. Gupta, "Surface wetting characteristics of cellulosic fibers," *Textile Research Journal*, vol. 70 (4), pp. 351–358, 2000. https://doi.org/10.1177/004051750007000412.

[72] J. Y. Heng, D. F. Pearse, F. Thielmann, T. Lampke, and A. Bismarck, "Methods to determine surface energies of natural fibres: A review," *Composite Interfaces*, vol. 14 (7-9), pp. 581–604, 9 2007. https://doi.org/10.1163/156855407782106492.

[73] C. Rulison, Ph.D, Krüss GmbH, "Contact angle determinations by the "straw" method and packed cell method:," tech. rep., 2019. https://www.kruss-scientific.com/files/kruss-ar206-en.pdf.

[74] I. Rea, P. Giardina, S. Longobardi, and L. D. Stefano, *Protein-modified porous silicon films for biomedical applications*, pp. 104–128. Elsevier Ltd., 2014. https://doi.org/10.1533/9780857097156.1.104, isbn = 9780857097118.

[75] E. Sinha and S. K. Rout, "Influence of fibre-surface treatment on structural, thermal and mechanical properties of jute fibre and its composite," *Bull. Mater. Sci*, vol. 32 (1), pp. 65–76, 2009. https://doi.org/10.1007/s12034-009-0010-3.

Chapter 6

Conclusions and future work

According to the research objectives specified at the beginning of this thesis, there were different aims for this work, all connected around fique and its properties, gaining a deeper understanding on its variation. Not only this, but also to gain understanding on its interaction with a recycled polypropylene matrix, within natural fibres reinforced thermoplastics, and how differently treated fibres impact this interaction. The mechanical properties of the fibre are going to partly define the end properties of the composite, alongside the fibre-matrix interface behaviour, which will define the ability of the matrix to transfer the load onto the fibre.

The aim of this chapter is to present the key findings and conclusions established from the research carried out in this thesis, alongside recommendations following this work, as well as recommended future work.

6.1 Key findings

In view of the research carried out to reach the objectives described in Chapter 1, the contents of each chapter are summarised, analysing the subsequent implications from the perspective of the mentioned goals.

In Chapter 2, the area variation along two fique fibres is studied by means of a CT-scan, which is a non-destructive technique. Given the variability that cross-sectional area can induce in further studying the mechanical properties of the fibres, this aimed

to quantify this variation better as well as characterised the proportion of lumen versus fibre cell walls, which is the structure of the technical fibres actually carrying the load. From the two fibres analysed clear differences in shape, size and morphology can be seen. The average area values for both fibres are 1.5 x 10^4 and 6.3 x 10^3 μm^2, showing one order of magnitude difference between the two areas, added to the two different shapes, one being kidney like and the other being closer to a circular cross-section. Along the 11 cm of fibre, there is a variation of 6.2 and 12.2% in the measured areas, while the variation for the cell walls is 6.6 and 11.8%, and for the lumen's area is 10.2 and 16.8%, respectively for each fibre. Apparent diameters derived from those averaged area values assuming circularity of fibres lead to 140.2 μm and 89.8 μm respectively.

Porosity values are in both cases below 46%, being 41.0% the lowest value for fibre *a*, and 45.3% the highest porosity values. Meanwhile, for fibre *b* these values are 33.4 and 39.5%. These porosity values are relatively close, specially considering the great variation in the area values, showing that porosity and cell wall areas vary proportionally, giving an approximate porosity value for fique fibre.

In Chapter 3 the mechanical properties of fique are studied through tensile testing with two different methods and compared. Alongside that two cross-section area calculation approaches are used in order to being able to compare how this affects the mechanical properties calculated.

The two area calculation approaches are: one, assuming circularity of the fibres and by means of measuring the transverse diameter of the fibres calculate the area value; two, after the test has been performed, directly measuring the cross-sectional area of the fibre relatively close to where it broke.

Young's modulus is obtained via two ways. The first one, through an indirect strain measurement, which also calculates the compliance of the system. This method requires several gauge lengths of fibre to be tensile tested and establishing a linear relationship between the force and cross-head displacement and the Young's modulus of the fibre and the compliance of the system. When plotting the cross-head displacement over the force against the initial gauge length over the area of at least three different gauge lengths, the inverse of the linear slope is the Young's modulus and the constant is the compliance

of the system. For this method, where the area of the fibre is used, the two approaches of area calculation are used, giving two values for the Young's modulus. The second way for obtaining the Young's modulus is via a direct strain measurement technique by which two beads are attached to each fibre and their movement tracked. By doing this, a stress-strain curve is obtained by every fibre and the Young's modulus obtained from the initial slope of these curves. Because again, two area calculation approaches are used, two values are obtained per each. The two values obtained from the first method are 17.3 and 17.1 GPa, with a higher variation obtained for the area approach that considers fibres to be circular. For the second method, values are averaged per gauge length and show an increasing trend with gauge length, going from 6.9 GPa to 18.5 GPa when the area is obtained from the assumption of circularity, and from 9.5 GPa to 18.4 GPa when the area considered is the one directly measured after the test has taken place. The values obtained in this case are higher than what is found in the literature. These differences found in the direct strain measurement suggest that fibres need to be long enough, so non-linear behaviours are not dominant, and hence, the stress-strain behaviour represents more accurately the elastic modulus of the fibres.

Similarly, tensile strength is also calculated, in this case by using the peak force measured and the area of the fibre tested, leading only to two values, each of them coming from the different approach followed in obtaining the value of the area. Again, averaged values are given per gauge lengths, following an increasing trend with the gauge length. Values that go from 223.8 MPa to 364.4 MPa, with and average value of 359.4 MPa for the assumption of circularity when calculating the cross-sectional area of the fibre are obtained. While for the direct measurement of the cross-sectional area approach values go from 300.3 MPa to 346.6 MPa with and average value of 329.7 MPa. In this case, values obtained by the measured cross-sectional area are more stable than when the area is assumed to be circular, with reported values within what is found in the literature.

Similarly to the tensile strength, the elongation at break results present two values per gauge length, but in this case based on the equipment measured displacement or the elongation as calculated from tracking the beads on the fibre. Values decrease

with increasing gauge length, more notably for the equipment measured displacement, showing how the equipment error becomes more significant the smaller the fibre. Values go from 11% to 3% for equipment measured displacement, while the go from 6% to 3% for displacement obtained from tracking the beads attached to the fibre, with values converging for both methods the longer the fibre.

From the study of the cross-sectional area shape of all the fibres tested in the mechanical characterisation one of the main outcomes is that fique cross-sectional area is not circular, although extreme shapes are not common. Given the time consuming requirements of measuring the actual cross-sectional of the fibre, the recommendation is that the circularity assumption can be used only and only if enough measurements along the fibre are taken, that can prevent big over and underestimation measurements. The recommendation is that at least three transverse pictures of the fibre are taken, with at least three measurements on each section of the fibre. This does not change that direct CSA measurement is more accurate and recommended in all cases.

When calculating mechanical properties in natural fibres, it is suggested that a large enough number of fibres is tested, and potentially in different gauge lengths, as this helps in understanding different phenomena that can influence the measurement of these mechanical properties. From the experience with fique, longer fibres lead to values that converge for different methodologies, suggesting that equipment influence and measuring errors become less and less significant the longer the fibres. If the nature of the fibres tested is that they are short, a recommendation for direct strain measurement technique is done when possible.

In Chapter 4 thermo-chemical characterisation of fique is done. Raw fique as well as chemically and physically treated fique are studied in this work. Fibres undergoing alkaline and hydrolysis treatments as well as high intensity ultrasonication are studied via FT-IR, TGA, and DSC analysis. These analysis help to deepen the understanding of the chemical changes that the fibres undergo after the treatments and how that affects their thermal stability. Thermal stability is key to ensure that these fibres can be used in manufacturing processes to be used as reinforcement of polymer matrices, with the focus on thermoplastic ones in this work.

The FT-IR analysis shows the effectiveness of the NaOH treatment in removing hemicellulose and lignin, with no significant changes in the cellulose composition. For the hydrolysis treated fibres, which underwent a previous alkaline treatment, hemicellulose and lignin are also removed in a more acute manner than for alkali only treatment, alongside some proportion of the crystalline cellulose, leading to a higher proportion of amorphous cellulose. This is believed to be due to the higher solution concentration in the previous alkaline treatment, which can lead to break the cellulose structure. The high intensity ultrasonication treatment does not induce significant changes on the already chemically treated fibres.

The TGA analysis supports the case for the previous alkaline treatment to the hydrolysed fibres contributing to the degradation of crystalline cellulose or its transformation into an amorphous phase due to the shift down in temperature for cellulose degradation, supporting the idea of a higher proportion of the amorphous phase. The DSC analysis points in the same direction, with chemical treatments shifting down degradation temperatures, with HIUS non inducing great changes besides inducing a higher weight loss during thermal degradation due to the increased cleavage of lignin. Thermal degradation of these fibres is still above the 200°C, proving their thermal requirements allow them to be used as reinforcement for thermoplastic matrices.

In Chapter 5 the composition and thermal stability of virgin and recycled PP is studied, furthering the understanding in the degradation mechanisms as well composition differences and chemical changes in the recycled blend compared to the virgin polymer.

The wettability of fique fibres has been studied in this chapter via two different methods. The first one, by the Owen and Wendt method combined with the Young-Laplace equation using four different liquids covering the spectrum of liquid polarity to obtain the polar and dispersive components of fique's surface energy for the raw and the treated fibres. The second method used has been a direct contact angle measurements of the rPP with the fibres via a hot stage microscope, where a droplet forms under the heat, and the contact angle is directly measured. In this case, the surface energy measurement indicated that the HIUS treatment clearly reduces the polar component

after the chemical treatments on the fique fibre. From the second method, the contact angle shows stable values for the washed fique, while it significantly decreases for the treated fibres, with a smoother reduction for the mercerized+HIUS treated fibres. In general, contact angle reduction after 213°C is shown via SEM imaging as matrix discontinuity due to the higher microfibrils exposure, making the point of needing to tune the temperature to ensure good contact between fibre and matrix.

On top of this, the interfacial shear strength recycled polypropylene reinforced with fique is characterised by the single fibre fragmentation test giving values of 3.32 MPa, 2.77 MPa and 2.73 MPa for the mercerized+HIUS treated fique, washed fique, and hydrolysis treated fique respectively. The lowest IFSS value is obtained by the mercerized only fique, which can be explained by the gap appreciated via SEM imaging in the contact angle study via hot stage microscope with rPP droplets on the fibre's surface. For the case for the hydrolysed+HIUS treated fibre, the low value can be explained by the atomization the matrix suffers over the fibre surface as seen in the SEM imaging from measuring the contact angle, which would prevent load from been transferred effectively.

The mechanical characterisation of the interface presents some challenges, especially when using recycling polymers. In the case of rPP and other recycled blends, they are opaque in contrast with transparent virgin polypropylene as used in other works. This restricts significantly the access to see through and accurately count the segments, so strategies such as understanding the whitening behaviour of the matrix, or developing a polishing process if the polymer is opaque is considered an investment for further measurements.

On top of this, when using chemically or physically treated fibres, the recommendation is to apply the same mechanical characterisation than the one used for raw fibres, as if as seen here the cellulose structure is changed, the expectation is that mechanical properties will change, which will impact the final mechanical properties of the composite itself. A way of accounting for that potential change in mechanical properties is also recommended to increase accuracy in the measured interfacial values.

6.1.1 The future of fique

With the method developed in this work used in fique fibre, the mechanical properties of this natural fibre have been more accurately measured, giving an updated data source for future works in fique aimed at using it in technological applications, with a representative number of fibres. This puts fique in the map for such applications, as it shows where is sits as an averaged performing fibre, below flax and hemp, but well above fibres like coir, suggesting its good disposition to be reinforcement for biodegradable matrices for composite components of medium requirements.

6.2 Future work

6.2.1 Cross-sectional area of fique and other natural fibres

Having access to scan more fique fibres, and other natural fibres, along all their length and in greater numbers, statistically significant numbers while also measuring them via apparent diameter to calculate their areas assuming their circularity, and via direct cross-sectional area examination can lead to obtain correction factors. Correction factors obtained from accurately measured areas along fibres through X-Ray CT-scan can significantly enhance accuracy in later calculating mechanical properties. The reason why is that using the apparent diameter of fibres is by far the cheapest and fastest way to estimate their areas, but this still brings a lot of error when the area is required to calculate other properties. Having correction factors on each fibre from a statistically significant pool of data is relevant to increase accuracy, while allowing the use of apparent diameter for fibre area estimation, which would have a direct application when moving to use natural fibres into industry, significantly reducing the time required for quality control and properties estimation.

6.2.2 Mechanical behaviour of fibres

Mechanical characterization of natural fibres will continue to be relevant for the future of more sustainable composite materials. Methods like direct strain measurement combined with more accurate ways of obtaining the cross-sectional area of fibres will con-

tribute to the expansion of natural fibres into more technical products. Extrapolating new methodologies currently used in synthetic fibres, like the direct strain measurement into natural fibres will contribute to a more accurate pool of properties data and help close the gap found when in the mechanical properties of different natural fibres.

6.2.3 Interfacial properties

In the work done in this thesis when characterising the interfacial properties of chemically or/and physically modified fibres with a polymer matrix are taken as the mechanical properties calculated for the raw fibre. Future work will require to apply the same mechanical characterisation method to all the fibres in order to use more accurate values after proving if these change or not significantly. Studying the topography of treated fibres can contribute to the understanding of the fibre-matrix adhesive strength. Potentially drying the PP and the fibres before making the samples, to remove moisture, that can lead to bubbles as seen in this work.

Finding a way to study the interfacial properties with other methods, like it could be the pull-out test can lead to a better understanding of fibre-polymer interface as well as a good comparison of IFSS values, while implementing the use of MaPP to enhance the interface can be another thing to implement.

6.2.4 Natural fibre reinforced composites

In a further step, the manufacturing of composites reinforced with fique fibre and their characterisation via bending, tensile/compression, and fatigue tests can significantly contribute to the expansion of natural fibres reinforced matrices. It will add significant value to the understanding of mechanical properties and interface interaction to connect between the micro, the meso, and the macro scales. The study of matrices with bio origins that are also biodegradable will be a further step in ensuring the sustainability of these materials significantly contributing to their end of life solutions.

Part I

Appendix A: MATLAB code for direct strain measurement as part of the mechanical characterization of fique.

The content of this appendix is the MATLAB code developed for the direct strain measurement from which the mechanical properties of fique have been measured.

6.3 Main: Inputs, variables, output files definition and different functions call.

The code is divided into a main, from which different functions are called in, and the different functions. Here, the main is shown as a section, and the following subsections are the different functions.

```
close all
clear all
clc

video_name = 'Fibre_30.MP4'; %Video that has to open
fibre_number = 'Fibre 30';
file_name = 'Fibre_30.xlsx';%File where it has to read the Time and
↪  Force data from the equipment
sheet_name = 'Test Curve Data';
C_t = 'C'; %This C_t stands for column time from the data from the
↪  equipment.
C_f = 'D'; %This C_f stands for column of force from the data from the
↪  equipment. They are both used
%for reading the data obtained and identify the breaking points, and
↪  later
%used for the interpolation.
txt_filename_top = 'Fibre_30_points_position_by_frame_top.txt'; %in this
↪  txt it is saved
%the data correspondent to each point identified by Matlab in the
```

```
%Tracking_points_mean_y function. It is saved the x and y of each point
↪ for
%each frame at the top bead.
txt_filename_bottom = 'Fibre_30_points_position_by_frame_bottom.txt';
↪ %in this txt it is saved
%the data correspondent to each point identified by Matlab in the
%Tracking_points_mean_y function. It is saved the x and y of each point
↪ for
%each frame at the bottom bead.
filename = 'Matlab_results_10mm.xlsx'; %file
%where the data from matlab and the interpolation data is stored
sheet = 30; %sheet of the excel file where it will store the data for
↪ this
%fibre. Name it as the fibre number.
R=-1;%R=-1 by default.Sometimes the breaking point is not so easy to
↪ recognize.In that case it will be seen
%from the graph that something went wrong. If R=-1, the breaking point
↪ will
%be identified by the function breaking points. If it goes wrong, the
%breaking point can be identified manually, and introduced here. R=536
%means that on row 536 of the reading the breaking point happens.

%Calling function for tracking the points in the video
[t_mat,ext_mat,l_0]=Tracking_points_mean_y(video_name,fibre_number,txt_
↪ filename_top,txt_filename_bottom,filename,sheet);

%Calling the function for identifying the breaking points from the data
[t_equ_origin,f_equ_select,t_mat_origin,ext_mat_select]=...
    Identifying_breaking_points(ext_mat,t_mat,file_name,sheet_name,C_t,
    ↪ C_f,R);
```

```
%Calling the function for interpolate in the force data for having as
↪ many
%values as for the elongation extracted from the video processing.
[f_mat_interpol,ext_mat_interpol]=...
    Interpolation_force_elongation(t_equ_origin,f_equ_select,t_mat_orig
    ↪ in,ext_mat_select,fibre_number,filename,sheet,l_0);
```

6.3.1 Function tracking points

Once the code starts running, a window with the first frame of the video is opened and the top bead area is selected first, and when it finishes going through all the frames, it opens again the first frame so the bottom bead can now be selected to go over the same process again, so movement of both beads can be tracked.

```
function [t_mat,ext_mat,l_0]=Tracking_points_mean_y(video_name,fibre_nu
↪ mber,txt_filename_top,txt_filename_bottom,filename,sheet)
%%
%This function does:
%1. Reads the first frame of the video

%2. The area of interest can be selected (here, the top bead first, and
↪ the
%bottom bead later).

%3. Identifies m points in the top bead and follows them along the whole
%video, frame by frame. So the x and y data of those points is saved.

%4. The mean of all the points is calculated, first for the top bead and
%later for the bottom bead.
```

```
%5. The distance between the beads is calculated as the difference
↪  between
%the mean_y_bottom and mean_y_top. This is called dis_mat.

%6. The extension is calculated as l-l_0, i.e. the distance between
↪  beads
%on each frame minus the initial distance. This is called ext_mat.

%7. l_0 is defined and used in the last function called from the main,
↪  in
%order to calculate the elongation, since the whole code was developed
%using the extension.

%8. The coordinates for each point identified are saved in txt files.

%9. The mean values are saved in the excel where the rest of data will
↪  be
%also saved.


%% Track a bead in a tensile test for single fibre
% Create System objects for reading and displaying video and for drawing
↪  a bounding
% box of the object.

videoReader = VideoReader(video_name);
%next line in case I want to specify time (s) from the video where to
↪  start
%different from the first frame
%videoReader.CurrentTime = 10;
```

```
%This line cuts the image size to the interest region
videoPlayer = vision.VideoPlayer('Position',[100,100,680,520]);
%%
% Read the first video frame, which contains the object, define the
↪  region.
% If I know the region of the bead, enter coordinates in object region.
% Matlab places de origin in the left top corner, with x to the right
↪  and y
% to the bottom.
%%
objectFrame = readFrame(videoReader);
%objectRegion = [930,171,38,30]; if the position is known.

% As an alternative, you can use the following commands to select the
↪  object
% region using a mouse. The object must occupy the majority of the
↪  region:
% this allows you to draw the rectangle around the bead.
%
figure; imshow(objectFrame);
objectRegion=round(getPosition(imrect));
%
% Show initial frame with a red bounding box.
%%
objectImage =
↪  insertShape(objectFrame,'Rectangle',objectRegion,'Color','red');
figure;
imshow(objectImage);
title('Red box shows object region');
```

```
%%
% Detect interest points in the object region.
%%
points =
↪  detectMinEigenFeatures(rgb2gray(objectFrame),'ROI',objectRegion);
%%
% Display the detected points.
%%
pointImage =
↪  insertMarker(objectFrame,points.Location,'+','Color','white');
figure;
imshow(pointImage);
title('Detected interest points');
%%
% Create a tracker object.
%%
tracker = vision.PointTracker('MaxBidirectionalError',1);
%%
% Initialize the tracker.
%%
initialize(tracker,points.Location,objectFrame);

%the next two lines give the coordinates for the first and for the last
%frame.
%point_0 = points.Location;
pnts=points.Location;
%%
% Read, track, display points, and results in each video frame.
%%
```

```
%initialize frame count and cell array
num_frame_t=1;
hist_points_Top = {};

%It gives the coordinates for all the points in each frame in a cell
↪  array,
%where each cell has two columns, x and y.
i = 1;
while hasFrame(videoReader)
      frame = readFrame(videoReader);
      [pnts,validity] = tracker(frame);


       %this should work no matter which dimension points has, and even
       ↪  if points is
    %a different size each iteration, which is not the case.
    hist_points_Top{num_frame_t} = pnts;

      out = insertMarker(frame,pnts(validity, :),'+');
      videoPlayer(out);

      %moves to next array location
    num_frame_t = num_frame_t+1;
end

%This next line gives the time in the video.
%disp([videoReader.CurrentTime    videoReader.Duration])
%disp([CurrentTime])
```

```
%Calculating the mean for x and y for each frame in a cell array
ss = size(hist_points_Top{:,1});
if ss(1)==1
    mean_x_y_Top = hist_points_Top;
else
    mean_x_y_Top = cellfun(@mean,hist_points_Top,'UniformOutput',false);
end

for i=1:(num_frame_t-1)
    %x_y_coordinate_bottom_per_frame: each two rows containe the x
    ↪  (first row)
    % and y (second row) coordinates of each point identified in each
    % frame. This means that the rows go as x_1,
    ↪  y_1,x_2,y_3,...,x_n,y_n,
    % being n the frame number; and the columns go as 1,2,3,...,m, being
    ↪  m
    % the number of points identified in each frame.Save in T1.
    x_y_coordinate_top_per_frame(2*i-1,:) = hist_points_Top{:,i}(:,1);
    x_y_coordinate_top_per_frame(2*i,:) = hist_points_Top{:,i}(:,2);
end

%%
[M,D] = size(mean_x_y_Top);
for i=1:D
    % Vector with x average for each frame
    mean_x_Top(i,:) = mean_x_y_Top{i}(1);
    % Vector with y average for each frame
    mean_y_Top(i,:) = mean_x_y_Top{i}(2);
    % Matrix with x average for each frame in the first column and y
    ↪  average in the second column
```

```
    Mean_x_y_Top(i,:) = mean_x_y_Top{i}(:);
end

%%


%% This is exactly the same but for the bottom bead
% Release the video player.
%%
release(videoPlayer);

%For the bottom bead

videoReader = VideoReader(video_name);

%This line cuts the image size to the interest region
videoPlayer = vision.VideoPlayer('Position',[100,100,680,520]);

%ojectFrame = readFrame(videoReader);
%objectRegion = [932,475,30,28];

% As an alternative, you can use the following commands to select the
↪  object
% region using a mouse. The object must occupy the majority of the
↪  region:
% this allows you to draw the rectangle around the bead.
%
figure; imshow(objectFrame);
objectRegion=round(getPosition(imrect));
```

```
objectImage =
↪  insertShape(objectFrame,'Rectangle',objectRegion,'Color','red');
figure;
imshow(objectImage);
title('Red box shows object region');

%%
% Detect interest points in the object region.
%%
points =
↪  detectMinEigenFeatures(rgb2gray(objectFrame),'ROI',objectRegion);

tracker = vision.PointTracker('MaxBidirectionalError',1);
%%
% Initialize the tracker.
%%
initialize(tracker,points.Location,objectFrame);

%initialize frame count and cell array
num_frame_b=1;
hist_points_Bottom = {};

%It gives the coordinates for all the points in each frame in a cell
↪  array,
%where each cell has two columns, x and y.
i = 1;
while hasFrame(videoReader)
      frame = readFrame(videoReader);
      [pnts,validity] = tracker(frame);
```

```
        %this should work no matter what dimension points is, and even if
        ↪  points is
    %a different size each iteration
    hist_points_Bottom{num_frame_b} = pnts;

      out = insertMarker(frame,pnts(validity, :),'+');
      videoPlayer(out);

      %moves to next array location
    num_frame_b = num_frame_b+1;
end

%This next line gives the time in the video.
%disp([videoReader.CurrentTime    videoReader.Duration])
%disp([CurrentTime])

%%
%Calculating the mean for x and y for each frame in a cell array
ss = size(hist_points_Bottom{:,1});
if ss(1)==1
    mean_x_y_Bottom=hist_points_Bottom;
else
    mean_x_y_Bottom =
    ↪  cellfun(@mean,hist_points_Bottom,'UniformOutput',false);
end
%%

for i=1:(num_frame_b-1)
```

```
    %x_y_coordinate_bottom_per_frame: each two rows containe the x
    ↪  (first row)
    % and y (second row) coordinates of each point identified in each
    % frame. This means that the rows go as x_1,
    ↪  y_1,x_2,y_3,...,x_n,y_n,
    % being n the frame number; and the columns go as 1,2,3,...,m, being
    ↪  m
    % the number of points identified in each frame. Save in T2.
    x_y_coordinate_bottom_per_frame(2*i-1,:) =
    ↪  hist_points_Bottom{:,i}(:,1);
    x_y_coordinate_bottom_per_frame(2*i,:) =
    ↪  hist_points_Bottom{:,i}(:,2);
end


[M,D] = size(mean_x_y_Top);%here the size is taken as the mean_x_y_Top
↪  because
%Matlab has trouble reading the last frame of the videos depending on
↪  the
%format, and for operating later on between the top and bottom y_mean
↪  the
%matrices need to be the same size.
for i=1:D
    % Vector with x average for each frame
    mean_x_Bottom(i,:) = mean_x_y_Bottom{i}(1);
    % Vector with y average for each frame
    mean_y_Bottom(i,:) = mean_x_y_Bottom{i}(2);
    % Matriz with x average for each frame in the first column and
    ↪  average y for each frame
    %in the second one % segunda columna
```

```
    Mean_x_y_Bottom(i,:) = mean_x_y_Bottom{i}(:);
end

release(videoPlayer);

%This is for plotting the extension (average y_bottom minus average
↪  y_top) for
%each frame against time
s = videoReader.Duration;
f = videoReader.FrameRate;
t = linspace(0,s,D);
t_mat = t';
AxesH = axes('Xlim', [0, s], 'XTick', 0:1/f:s);
x = t;
dis_mat = (mean_y_Bottom-mean_y_Top); %distance between bottom and top
↪  bead in pixels for each fram
ext_mat = (dis_mat-dis_mat(1)); %extension is equal to l-l_0, so to the
↪  distance of each
%frame the distance at the first frame is substracted.
l_0 = dis_mat(1);%this is the distance at the first frame. This is used
↪  in the next function call
%from the main script for calculating the elongation (strain).

%this adds a trendline
p = polyfit(x,ext_mat,1);
f = polyval(p,x);

figure (7);
plot (x,ext_mat);
plot(x,ext_mat,'b*',x,f,'r-');
```

```
xlim([0 s])
xlabel('Time (s)');
ylabel('Extension (pixels)');
title('Extension vs. Time');

fig8 = figure (8);
plot (x,ext_mat,'b*');
xlim([0 s])
xlabel('Time (s)');
ylabel('Exension (pixels)');
title('Extension vs. Time');

fig_name = sprintf('%s_ext_vs_t', fibre_number);
saveas(fig8,['figfolder/' fig_name],'fig');



T1 = table(x_y_coordinate_top_per_frame);
T2 = table(x_y_coordinate_bottom_per_frame);

writetable(T1,['datafolder/'
↪  txt_filename_top],'WriteVariableNames',false);
writetable(T2,['datafolder/'
↪  txt_filename_bottom],'WriteVariableNames',false);



T3 = table(mean_x_Top(:),mean_y_Top(:),mean_x_Bottom(:),mean_y_Bottom(:
↪  ));
T3.Properties.VariableNames =
↪  {'mean_x_top','mean_y_top','mean_x_bottom','mean_y_bottom'};
```

```
writetable(T3,['datafolder/' filename],'Sheet',sheet,'Range','A1');
end
```

6.3.2 Function Identifying breaking points

With the data gathered from tracking the beads, this function identifies when the fibre breaks by analysing the continuity of the motion of the beads. When a bigger difference between one position and the next happens, the breaking point is identified. Factor R defined in the main contributes to this identification, and can always be done manually.

```
function[t_equ_origin,f_equ_select,t_mat_origin,ext_mat_select]=Identif
↪  ying_breaking_points(ext_mat,t_mat,file_name,sheet_name,C_t,C_f,R)

%%
%This functions does:
%1.Reads the data from the equipment: time and force from the excel
%file...considering just the numbers and ignoring the rest of the column
%which is not a number (NaN). Not all columns of data have the same
↪  length.

%2.It identifies the breaking point from the equipment data based on
%the drop in the force measured: f_equ_break

%3.It takes the time at that moment: t_equ_break.

%4.It also identifies the time at which the experiment starts, when the
%force starts to increase, and takes this two data as f_equ_start and
%t_equ_start.

%5.From the extension and time data obtained from the video processed in
```

```
%the first function called (Tracking_points_mean_y),it identifies at
↪  what
%distance between beads the fibre breaks and the time at which this
↪  happens:
%ext_mat_break and t_mat_break.

%6.For identifying the start point at the video a t_experiment is
↪  defined as
%the difference between the t_equ_break and the t_equ_start. The start
↪  time
%at the video (MATLAB time) is then define as the differentce between
↪  t_mat_break and
%t_experiment, so the same time frame is taken for the experiment in the
%video and from the equipment data.

%7.It selects all the data from the start to the break.

%8.Finally, it sets a common time origin to zero by substracting to the
%t_equ_select and to the t_mat_select the first time values to the whole
%column of data giving a t_equ_origin and t_equ_origin.
%%

%1. Reads the data from the equipment
range = sprintf('%s:%s', C_t,C_f);
[D,S]=xlsread(file_name,sheet_name,range);
 %D(:,C_t:C_f);

t_equ=D(:,1);
f_equ=D(:,2);
%t_mat=D(:,6);
```

```
%e_mat=D(:,7);

%2. and 3.Breaking point from the equipment data: force and time of the
%event

for i=1:length(t_equ)
   if isnan(t_equ(i)) || isnan(f_equ(i))
       t_equ=t_equ(1:i-1,:);
       f_equ=f_equ(1:i-1,:);
       break
   end
end
[M,~] = size(f_equ);
[N,~] =size(ext_mat);

last=1;
for i=2:M
    if (f_equ(i-1)-f_equ(i))>(0.9)%this can be tuned depending on how
    ↪  your breakingpoint an be identified
        f_equ_break=f_equ(i-1);
        t_equ_break=t_equ(i-1);
        last=0;
        break
    end

end
if last ==1
    f_equ_break=f_equ(M);
    t_equ_break=t_equ(M);
end
```

```
%4. When the experiment starts: force and time of the event. The
↪  conditions
%can also be tuned depending on your case
for j=2:M
   if (f_equ(j)-f_equ(j-1))/(t_equ(j)-t_equ(j-1))>0 &&
    ↪  (f_equ(j+1))>f_equ(j);
       f_equ_start=f_equ(j);
       t_equ_start=t_equ(j);
       break
   end

end


%5. Breaking point identification from the MATLAB data on the extension:
%extension and time of the breaking event. Conditions to be tuned on
↪  your
%particular case.
last=1;
for i=2:N
         if (ext_mat(i)-ext_mat(i-1))>1.1 && i>N/10
          ↪  %%||(ext_mat(i)-ext_mat(i-1))<0 && i>N/1000
         ext_mat_break = ext_mat(i-1);
         t_mat_break=t_mat(i-1);
         last=0;
         break
         end
end
```

```
if R==-1
    if last ==1
    ext_mat_break=ext_mat(N);
    t_mat_break=t_mat(N);
    end
end

if R~=-1
    ext_mat_break=ext_mat(R);
    t_mat_break=t_mat(R);
end

%6. The t_experiment is defined and use to get the same time frame for
↪  the
%equipment data and the MATLAB data.Since there might be a slight
%variation in the decimals, the closest value is selected to be the
↪  starting point from
%the MATLAB data.

t_experiment=t_equ_break-t_equ_start;

t_mat_start=t_mat_break-t_experiment;

[t_mat_start_closest,idx_t_mat_start_closest] = min(abs(t_mat(:,1) -
↪  t_mat_start.'));


%7. Data selection between the start and the breaking event: first for
↪  the
%equipment data and second for the MATLAB data.
```

```
%8. Establishes the time origin at 0 for both cases.
for i=1:M;
    t_equ_ = t_equ(i);
    if t_equ(i)==t_equ_start
        index_1=i;
    end
    if t_equ(i)==t_equ_break
        index_2=i;
        break
    end
end
t_equ_select(:,1)=t_equ(index_1:index_2)';
f_equ_select(:,1)=f_equ(index_1:index_2)';
t_equ_origin(:,1)=t_equ_select(:,1)-t_equ_start;

for i=1:N
    if t_mat(i)==t_mat(idx_t_mat_start_closest)
        index_3=i;
    end
    if t_mat(i)==t_mat_break
        index_4=i;
        break
    end
end
t_mat_select(:,1)=t_mat(index_3:index_4)';
ext_mat_select(:,1)=ext_mat(index_3:index_4)';
t_mat_origin(:,1)=t_mat_select(:,1)-t_mat(idx_t_mat_start_closest);

end
```

6.3.3 Function Interpolation force elongation

In this case, the video provides more data points than the equipment, so an interpolation in the load measured by the equipment is required to match the data points, and this is what this function does.

```
function[f_mat_interpol,ext_mat_interpol]=Interpolation_force_elongatio
↪  n(t_equ_origin,f_equ_select,t_mat_origin,ext_mat_select,fibre_numbe
↪  r,filename,sheet,l_0)
%%
%Matlab data length is larger than equipment data, so this function
↪  does:
%1.The first loop is for considering only the actual data from the
%equipment and not the cells with not a number (NaN) value.

%2. Linear interpolation to calculate the force value at
%the same time that the elongation data from the video processing in
↪  Matlab

%3. The force-extension curve is plotted, as it is and smoothed.

%4. The force-elongation curve is plotted as it is.

%5. Data and figures are saved.

%%
%1.
for i=1:length(t_equ_origin)
   if isnan(t_equ_origin(i))
       t_equ_origin=t_equ_origin(1:i-1,:);
       f_equ_select=f_equ_select(1:i-1,:);
```

```
        break
    end
end
[M,~] = size(t_mat_origin);

%2.The next loop is the linear interpolation to calculate the force
↪  value at
%the same time that the elongation data from the video processing in
↪  Matlab

f_mat_interpol= zeros(M,1);
for i=1:M
    t=t_mat_origin(i);
        if i == 1
        f_mat_interpol(i,:) = f_equ_select(1);
    elseif i == M
        j = length(t_equ_origin);
        t_e = t_equ_origin(j);
        a=(f_equ_select(j)-f_equ_select(j-1))/(t_e-t_equ_origin(j-1));
        b=f_equ_select(j)-a*t_e;
        f_mat_interpol(i,:)=a*t+b;
    elseif i>1
        for j=1:length(t_equ_origin)
            t_e=t_equ_origin(j);
            if t==t_e
                f_mat_interpol(i,:)=f_equ_select(j);
                break
            elseif t<t_e
                a=(f_equ_select(j)-f_equ_select(j-1))/(t_e-t_equ_origin
                ↪  (j-1));
```

```
                b=f_equ_select(j)-a*t_e;
                f_mat_interpol(i,:)=a*t+b;
                break
            end
        end
    end
end

%3. This plots the force-actual extention curve.
ext_mat_interpol=ext_mat_select;
s=smooth(ext_mat_interpol);
x=ext_mat_interpol;
elon = (ext_mat_interpol/l_0)*100;

fig9 = figure (9);
plot (x,f_mat_interpol);
xlabel('Extension (pixels)');
ylabel('Force (N)');
title(fibre_number);

%This plots the force-actual extension curve smoothed.
fig10 = figure (10);
plot(s,f_mat_interpol);
xlabel('Extension (pixels)');
ylabel('Force (N)');
title(fibre_number);

%4. This plots the force-actual elongation curve.
fig11 = figure (11);
plot(elon,f_mat_interpol);
```

```
xlabel('Elongation (%)');
ylabel('Force (N)');
title(fibre_number);


%5. Saving
fig_name = sprintf('%s_1', fibre_number);
saveas(fig9,['figfolder/' fig_name],'fig');
fig_name = sprintf('%s_2', fibre_number);
saveas(fig10,['figfolder/' fig_name],'fig');
fig_name = sprintf('%s_3', fibre_number);
saveas(fig11,['figfolder/' fig_name],'fig')

T4 = table(t_equ_origin,f_equ_select);
T5 = table(t_mat_origin,ext_mat_select);
T6 = table(ext_mat_interpol,f_mat_interpol);
T7 = table(elon);
T4.Properties.VariableNames = {'t_equ_origin (s)','f_equ_select (N)'};
T5.Properties.VariableNames = {'t_mat_origin (s)','ext_mat_select
↪  (Pixel)'};
T6.Properties.VariableNames = {'ext_mat_interpol(Pixel)','f_mat_interpol
↪  (N)'};
T7.Properties.VariableNames = {'elongation_mat_interpol (%)'};
writetable(T4,['datafolder/' filename],'Sheet',sheet,'Range','F1');
writetable(T5,['datafolder/' filename],'Sheet',sheet,'Range','I1');
writetable(T6,['datafolder/' filename],'Sheet',sheet,'Range','L1');
writetable(T7,['datafolder/' filename],'Sheet',sheet,'Range','N1');

end
```